Development of Highly Efficient Perovskite-on-Silicon Tandem Solar Cells

Présentée le 28 septembre 2020

à la Faculté des sciences et techniques de l'ingénieur
Laboratoire de photovoltaïque et couches minces électroniques
Programme doctoral en chimie et génie chimique

pour l'obtention du grade de Docteur ès Sciences

par

Florent SAHLI

Acceptée sur proposition du jury

Dr A.-S. Chauvin, présidente du jury
Prof. C. Ballif, Dr Q. T. Jeangros, directeurs de thèse
Prof. B. Ruhstaller, rapporteur
Dr U. Paetzold, rapporteur
Prof. K. Sivula, rapporteur

École
polytechnique
fédérale
de Lausanne

2020

"If you have to skydive for the first time, would you prefer to do it solo or in tandem?"

Gianluca Coletti
EU PVSEC 2019, Marseille

Acknowledgements

Abstract

Crystalline Silicon (c-Si) solar cells are dominating the photovoltaic (PV) market, covering a market-share above 90%. Owing to their large cumulative manufacturing capacity, reliability and high power conversion efficiency, c-Si solar cells are now cost-competitive with other non-renewable electricity sources in most parts of the world. The price of c-Si PV modules has been decreasing drastically for the past decades. They now account for less than half of the cost of an installed PV system. System costs other than modules include labour, installation, mounting structure, inverters, grid connections, etc. As these costs are rather inflexible, increasing the power conversion efficiency of the solar modules is the most efficient approach to lower the levelized cost of PV electricity. One issue is that c-Si cells are approaching their practical efficiency limit. One strategy to increase efficiency beyond the limit of c-Si relies on adding, on the front of a c-Si cell, another solar cell featuring a complementary absorption profile to form a tandem solar cell. Stacking a wider-band gap absorber on c-Si enables carrier extraction with a higher voltage due to reduced thermalisation losses. Inorganic-organic lead halide perovskite solar cells are promising top cell candidates to combine with c-Si based on their sharp absorption edge with few sub-band gap defects, band gap tunability, high efficiencies, ease of manufacturing and low material costs. By combining both technologies, power conversion efficiencies in the range of 30-35% are realistic, well above best-in-class c-Si solar cells, which achieve a power conversion efficiency up to 26.7%.

This thesis aims to produce high efficiency perovskite solar cells specifically tailored for a 2-terminal monolithic tandem integration with a c-Si bottom cell. First, we develop a perovskite hybrid fabrication method, which employs thermal evaporation to produce a lead halide template and then a spin-coating step with an organohalide solution. By varying the composition of the template and solution, the perovskite band gap can be tuned in the 1.6-1.8 eV range, which are ideal values to produce sub-cells that are current-matched in a 2-terminal tandem. In addition, the use of a thermally evaporated lead halide template makes the perovskite deposition compatible with rough and textured substrates. Then, we develop a recombination junction connecting the c-Si and perovskite sub-cells that features highly doped nanocrystalline hydrogenated silicon layers (nc-Si:H). When used with a c-Si bottom cell featuring a planar front side, this recombination junction shows a superior optical performance compared to commonly used transparent conductive oxides thanks to a better matching of refractive indices. In addition, owing to the low conductivity of the nc-Si:H layers, the top cell leakage current is reduced as

Acknowledgements

the impact of shunts that may be present in the top cell is mitigated, which enables to scale-up the cell active area. Then, relying on these concepts, perovskite/c-Si tandems featuring a double-side textured c-Si bottom cell are processed, achieving a certified power conversion efficiency of 25.2%. This high efficiency, the highest at the time of publication, is enabled by low reflection losses and efficient infrared light trapping thanks to the pyramidal texture present on both sides of the device. More importantly, the use of front and rear side texture yields a close to optimum system that is also simpler and optically more efficient compared to alternatives (*e.g.* a textured antireflective foil placed on top of a front-side polished device). Furthermore, such double-side textured tandem design does not require any modification to existing c-Si manufacturing production lines as these rely on silicon wafers textured on their front side.

In the second part of the thesis, we intend to replace the spin-coating of the organohalides by a vapour transport deposition (VTD) step. First, we detail our home-made vapour transport deposition setup that offers a large flexibility in terms of processing parameters. Using a thermally evaporated lead iodide template and a methylammonium iodide vapour, perovskite solar cells with an efficiency $> 12\%$ are fabricated on 0.25 cm^2. Thanks to the presence of a showerhead and a large deposition chamber, a homogeneous and conformal perovskite growth is obtained on 6 inch textured c-Si substrates (> 220 cm^2), the industry standard. The VTD of formamidinium iodide (FAI) is more challenging. Only a limited amount of FAI molecules are introduced in the deposition chamber. Trimerisation reaction of the FAI molecule to form sym-triazine is identified as the main problem regarding FAI evaporation by VTD. The resulting sym-triazine vapour does not react with the lead template to form the perovskite. Nevertheless, it is found that in the presence of primary amines, the sym-triazine heterocycle is cleaved, resulting in the formation of formamidine, thus offering an alternative pathway to deposit perovskite layers.

Keywords: Inorganic-organic perovskite, tandem solar cell, silicon heterojunction solar cell, nanocrystalline silicon, vapour transport deposition of organohalides, methylammonium iodide, formamidinium iodide, sym-triazine.

Résumé

Les cellules solaires en silicium cristallin (c-Si) dominent le marché du photovoltaïque (PV) avec une part de marché supérieure à 90%. En raison du grand volume de leur production, de leur bonne stabilité et de leur haute efficacité, les modules en c-Si permettent désormais d'atteindre un prix de l'électricité compétitif en comparaison à d'autres sources non renouvelables dans la plupart des régions du monde. Le coût des modules PV à base de c-Si a considérablement baissé au cours des dernières décennies et celui-ci représente désormais moins de la moitié du prix total d'une installation solaire. Le reste des coûts d'un système solaire comprend la main-d'œuvre, l'installation, le support, les onduleurs, les connexions au réseau, etc. Le coût de ces derniers est difficile à réduire. Dès lors, augmenter l'efficacité des modules solaires est un excellent levier pour réduire l'impact de ces coûts additionnels et par conséquent le prix de l'électricité produite. Cependant, les modules à base de c-Si approchent de leur limite d'efficacité. Ainsi, la meilleure manière d'augmenter l'efficacité des modules de c-Si sur le long terme repose sur l'ajout sur leur face avant d'une autre cellule solaire ayant un profil d'absorption complémentaire afin de former une cellule tandem. En faisant directement croître un matériau à bande interdite plus large sur la cellule en c-Si, l'efficacité peut être augmentée moyennant des coûts additionnels de production relativement faibles. Cette augmentation de l'efficacité résulte du fait que les porteurs de charge peuvent être extraits avec une tension plus élevée du fait de la diminution des pertes de thermalisation. Les cellules solaires à base d'un matériau de type pérovskite inorganique-organique sont des candidates prometteuses du fait de leurs bonnes propriétés optiques et électroniques, haut potentiel d'efficacité, de la possibilité d'ajuster la taille de leur bande interdite, sans oublier leur facilité de fabrication à faibles coûts. En combinant les deux technologies, c-Si et pérovskite, une efficacité en cellule tandem de 30 à 35% est réaliste, ce qui est bien au-dessus du record de 26.7% obtenu en laboratoire pour les cellules en c-Si.

Cette thèse vise à développer des cellules en pérovskite à haute efficacité en vue de leur intégration de manière monolithique en tandem à 2 terminaux avec une cellule en c-Si. Dans un premier temps, nous avons développé une méthode hybride de fabrication de la pérovskite utilisant l'évaporation thermique d'iodure de plomb suivie d'une étape de revêtement par centrifugation pour les molécules organiques. En faisant varier la composition à chaque étape, des pérovskites avec des bandes interdites entre 1.6 à 1.8 eV sont ainsi obtenues, des valeurs idéales pour obtenir des sous-cellules qui produisent le même courant au sein d'une tandem. De plus, l'utilisation de la couche d'iodure de

plomb produite par évaporation thermique rend le dépôt de la pérovskite compatible avec des substrats rugueux ou texturés. Par la suite, nous avons développé une jonction de recombinaison comportant des couches de silicium nanocristallin dopé (nc-Si:H) afin de contacter les deux sous-cellules. Lorsqu'utilisée avec une cellule c-Si polie en surface, cette jonction de recombinaison offre une combinaison d'indices de réfraction plus optimale que les oxydes conducteurs transparents généralement utilisés. Cela se traduit par une réflectance réduite entre les deux cellules et ainsi un gain en courant dans la cellule en c-Si. Du fait de la faible conductivité de cette couche, le courant de fuite de la cellule pérovskite est diminué, ce qui permet la fabrication de cellules en tandem d'une taille plus grande. En s'appuyant sur ces concepts, des cellules en tandem pérovskite/c-Si dotées d'une cellule c-Si texturée sur ses deux faces sont fabriquées. Celles-ci atteignent une efficacité certifiée de 25.2%, un record lors de la publication de ces résultats. La présence de la texture microscopique sur la surface avant agit comme antireflet, permettant ainsi d'obtenir un système optiquement simple mais efficace, lui donnant un avantage optique en comparaison aux cellules polies en surface principalement utilisées actuellement. De plus, l'utilisation en tandem de cellules c-Si texturées sur leur surface avant ne nécessite pas d'étape de fabrication supplémentaire afin de polir la texture du c-Si, ce qui rend ce type de tandem plus adapté à l'industrie du c-Si (qui utilise une texture sur la face avant).

Dans la deuxième partie de cette thèse, nous tentons de remplacer l'étape de revêtement par centrifugation des organohalogénures par une étape de déposition par transport de vapeur (VTD), plus prometteuse en vue d'une industrialisation. Tout d'abord, nous décrivons le système de déposition par transport de vapeur utilisé durant cette thèse. Ce système offre une grande flexibilité concernant les paramètres de déposition. En utilisant un substrat d'iodure de plomb préalablement évaporé et une étape de dépôt en phase vapeur d'iodure de méthylammonium, des cellules solaires pérovskite avec des efficacités > 12 % pour 0.25 cm^2 sont fabriquées. Grâce au design du réacteur, une croissance homogène de la pérovskite est obtenue sur un substrat de c-Si texturé de 6 pouces (> 220 cm^2), le standard utilisé par l'industrie du c-Si. La VTD de l'iodure de formamidinium (FAI) est quant à elle plus difficile. Seule une quantité limitée de FAI est introduite dans la chambre de dépôt. La réaction de trimérisation de la molécule FAI formant de la sym-triazine est identifiée comme principal problème concernant l'évaporation du FAI par VTD. La vapeur de sym-triazine ne réagit pas avec la matrice de plomb pour former la pérovskite. Néanmoins, on constate qu'en présence d'amine primaires, l'hétérocycle sym-triazine peut être clivé pour former de la formamidine, offrant ainsi une alternative pour fabriquer des cellules en perovskite.

Mots clés : pérovskite inorganique-organique, cellule solaire en tandem, cellule solaire silicium à hétérojonction, silicium nanocristallin, déposition par transport de vapeur d'organohalogénure, iodure de méthylammonium, iodure de formamidinium, sym-triazine.

Contents

Contents

Introduction

Context and motivation

Currently, the vast majority of our energy supply comes from fossil fuels. Even though fossil fuel reserves are still sufficient to cover our needs, their use comes at a massive environmental cost. The temperature rise related to greenhouse gases is projected to be higher than 5-7°C at the end of 2100 if no action is taken. This is clear that renewable technologies must be widely deployed to avoid this catastrophic scenario. Amongst the possible options, solar energy has the biggest potential. The resource, sunlight, is abundant and solar technologies are compatible, at least on paper, with a terawatt/year deployment.

Wafer-based crystalline silicon (c-Si) solar cells represent more than 90% of the solar module market.[1] Since first commercialised, the cost of c-Si modules has declined drastically.[2] This trend mainly stems from improvements in fabrication processes, economy of scale effects thanks to the ever-growing cumulative capacity installed (1 MW in 1975 to 500 GW now[2,3]) and increasing efficiencies. As a result, the cost of a c-Si module represents today less than 50% of the overall price of a residential photovoltaic system. The other 50% arise from the balance-of-system costs (BOS), which include the mounting system, wiring, grid connection (inverters), labour and permits. These costs are difficult to reduce. Due to this cost distribution, increasing power conversion efficiency (PCE) at the cell level is the most straightforward approach to further lower the price of PV electricity. In other words, the aim is to produce more watts for the same BOS costs. This quest for efficiency can be observed today in the PV industry, where less efficient cell designs such as aluminium back surface field (Al-BSF) are being quickly replaced by passivated emitter and rear cell (PERC) or more advanced technologies based on passivating contacts (TOPCon, POLO, SHJ). However, there is a limit to this technological upgrade: the theoretical limit of c-Si solar cells (29.4%).[4] Best-in-class c-Si devices yield efficiencies close to their practical efficiency limit, with record devices reaching 26.7%.[5] The only validated approach to surpass the efficiency limit of single-junctions under 1 sun conditions, detailed by Shockley and Queisser, involves stacking several absorbers in a multijunction solar cell.[6] The band gap (1.1 eV), efficiency, industrial know-how and long-term stability make c-Si the ideal bottom cell of a tandem. While III-V materials can be used as top

1

cell to reach efficiencies higher than 30%,[7,8] their costs are prohibitive.

Recently, organic-inorganic lead halide perovskite solar cells have been identified as promising top cell candidates for c-Si cells due to their highly attractive optoelectronic properties, tunable band gap and potentially low processing costs. Over the years, the PCE of perovskite solar cells has increased from 3% to above 25% at the single-junction level. Besides, perovskite solar cells can be deposited by various techniques (from solution-based to vapour phase processes) at low temperature, enabling a monolithic integration on a bottom cell. By combining perovskite and c-Si cells in a tandem device, efficiencies beyond 30% may be achieved cost-competitively.

At the start of this thesis in 2016, only few reports presented perovskite/c-Si tandems and the highest power conversion was 21.5%, which was still way below the record efficiency of single-junction c-Si cells. Four years later, the PCE of such devices has risen to over 29%, and the first commercial module may not be too far ahead.

Objectives

The goal of this thesis was to develop monolithic perovskite/c-Si tandems exhibiting a high efficiency by designing a thin film process flow adapted to the constraints imposed by the c-Si cell.

More specifically, this work aimed to design:

1) a wide band gap perovskite absorber with improved stability by compositional engineering.

2) a recombination layer connecting both sub-cells that reduces optical losses and shows superior electrical properties by mitigating the impact of shunts that may be present in the top cell.

3) a perovskite top cell process flow yielding conformal and functional layers on the micron-sized pyramidal features present at the front side of the c-Si wafers. This texture reduces reflection losses and promotes light-trapping.

4) a monolithic perovskite/c-Si tandem that combines 1-3) to achieve a high efficiency over an active area of ≈ 1 cm^2

5) a novel perovskite processing route based on vapour transport deposition for compatibility with textured 6 inch c-Si bottom cells.

2

Structure of the thesis

This thesis is divided into two distinct parts. In the first part, a hybrid sequential physical vapour deposition/solution-processing (PVD/SP) process for perovskites deposition is presented. The aim of this method is to coat conformally the front side texture of the c-Si bottom cell. A recombination junction, based on hydrogenated nanocrystalline silicon (nc-Si:H), connecting the perovskite and the c-Si sub-cells, is developed. Thanks to these advances, perovskite/c-Si tandems on textured silicon bottom cells are fabricated. In the second part of the thesis, we develop a sequential physical vapour deposition/chemical vapour deposition (PVD/CVD) process for perovskites fabrication. To do so, a custom-made vapour transport deposition setup for organohalides deposition is presented.

Chapter 1 - In this chapter, we review some of the fundamentals of photo-voltaics and introduce the notion of multijunction devices. We then discuss why c-Si and perovskite absorbers hold a great potential for tandem devices. Finally, we review recent advances in the field of perovskite/c-Si tandems and discuss requirements for them to be economically viable.

Chapter 2 - This chapter deals with the development of the hybrid PVD/SP method and focuses on single-junction perovskite solar cells. The different perovskite solar cell structures used during the thesis are introduced.

Chapter 3 - This chapter details the development of a nanocrystalline recombi-nation junction for perovskite/c-Si tandems. The optical benefit of using this junction is evidenced along with its shunts quenching properties. Monolithic perovskite/c-Si tandems featuring this recombination junction and a wafer polished on its front side are demonstrated. The shunt quenching properties of the recombination junction enable to upscale the active area from 0.25 cm^2 to 13 cm^2.

Chapter 4 - In this chapter, we deposit the perovskite layer on top of the silicon texture to benefit from the reduced reflection. First, we analyse the perovskite formation on top of different silicon textures (from flat to 5-6 μm pyramids). Combined with evaporated charge carrier selective contacts and the use of the nanocrystalline silicon recombination junction, a certified > 25% monolithic perovskite/silicon tandem is produced. This is the first demonstration of a perovskite/c-Si tandem featuring a textured silicon bottom cell and, at the time of publication, this device was the most efficient one reported.

Chapter 5 - This chapter is a general conclusion on the first part of this

thesis dealing with the hybrid PVD/SP process and textured perovskite/c-Si tandems. We discuss the shortcomings of our design, potential pathways to improve it, and future directions or applications of the work. One key aspect is the need to upgrade the perovskite deposition process to upscale the active area of the tandem cell.

Chapter 6 - This chapter is the first of the second part of this thesis dealing with the process flow upgrade towards a fully vapour-based route. We first review the advances in the development of perovskite solar cells by vapour deposition methods. We focus on sequential methods, where the organohalides are deposited by vapour transport deposition. In a second step, we describe the vapour transport home-made setup designed here and introduce the characterisation methods for organohalides analysis.

Chapter 7 - Here, the deposition of methylammonium iodide by vapour transport deposition is investigated. The resulting perovskite morphology and growth are characterised. Perovskite solar cells are fabricated with a high yield. More importantly, homogeneous perovskite depositions are demonstrated on large areas, including on 6 inch textured c-Si wafers.

Chapter 8 - In this chapter, we discuss the deposition of formamidinium halides by vapour transport deposition. We find out that only limited quantities of formamidinium reach the deposition chamber and suspect the formation of a larger molecule (sym-triazine) during the evaporation process or transport to the chamber. Possibilities to prevent the formation of this side-product and to use it as a perovskite precursor are investigated.

Chapter 9 - This chapter is a general conclusion on the second part of this thesis. Results obtained with our custom-made vapour transport deposition setup are discussed and further optimisations needed are elaborated.

Concluding Remarks - This chapter is a general conclusion and outlook of the thesis.

4

Contributions to the research field

This research brought several key contributions to the field of perovskite/c-Si tandems. We developed a novel hybrid PVD/SP method to deposit mixed-cations, mixed-halides perovskite compositions by co-evaporating caesium-halides with PbI_2. This co-evaporation, combined with the use of formamidinium halides during a subsequent spin-coating step, brings several advantages. It enables to tune the perovskite band gap in view of a monolithic 2-terminal tandem integration, it improves the thermal and operational stability of the top cell, thanks to the replacement of methylammonium (MA) cations with formamidinium (FA) cations. More importantly, this sequential perovskite deposition process is compatible with various substrate topographies. This last feature was key to the development of perovskite/c-Si tandems that feature a c-Si bottom cell textured on both sides for optimal light management. By combining high-efficiency bottom cells, either silicon heterojunction solar cells or high-temperature passivating contacts cells developed in-house, a nanocrystalline silicon-based recombination junction and top cell charge carrier selective contacts deposited via vapour-based routes, perovskite/c-Si tandems with a double-side textured wafer achieved an efficiency $> 25\%$, a world record at the time of publication. The certified value of 25.2% made it to the NREL chart compiling record solar cells of each technology. These devices were the first ones reported to feature a c-Si bottom cell textured on its front side, one (of the many) important milestone likely needed in view of an industrial deployment of the technology. Indeed, this front-side c-Si texture makes the device optics close-to-optimal (without needing any additional light management scheme) and is already employed in the c-Si industry. Designing a perovskite top cell process compatible with such texture simplifies greatly any refurbishment of c-Si process lines with no extra process steps needed to include a perovskite top cell. In other words, commercial c-Si cells do not require any modifications to be upgraded into a tandem thanks to these top cell developments. Still, the path to a commercial product is long. One aspect is that the cell active area (about 1 cm^2 for these high-efficiency devices) needs to be up-scaled to industrially relevant ones: 6 inch c-Si wafers.

In that regard, we developed a vapour transport deposition setup for organohalide deposition over large areas. At this stage, methylammonium lead iodide perovskites can be deposited with this setup on textured 6 inch c-Si wafers. While next research will involve upgrading the reactor to deposit FA instead of MA and tune the perovskite band gap thanks to the introduction of another precursor source, the results presented here are a first step towards 30%-efficient 6 inch perovskite/c-Si tandems.

Overall, this doctoral work resulted in three peer-reviewed articles as main author or shared first author,[9–11] one article in preparation and several peer-reviewed articles as co-author.[12–21]

1 Literature review

1.1 The climate crisis: Photovoltaics as an option?

In 2015, parties at the United Nations Framework Convention on Climate Change held in Paris reached an agreement to combat climate change, stating that the increase in global average temperatures must be maintained well below 2°C compared to pre-industrial levels. In order to meet this requirement, greenhouse gas emissions related to human activities should tend to zero at the end of the century (Figure 1.1). In all the projections, this implies that emissions should sharply drop by the 2030 horizon (Figure 1.1). This change can only occur if our energy production shifts away from fossil-based energy sources. Solar energy, which produces today only a few percents of our energy, is one of the few renewable technologies that has the potential to replace fossil fuels at a low cost, especially when combined with wind and hydro electricity and some storage capacity.[2,22]

PV technologies, which directly convert sunlight photons into electricity, already reach a levelized cost of electricity (LCOE) < 0.05 \$/kWh for big solar farms, a value competing with fossil fuels electricity price in several countries.[24] Crystalline silicon (c-Si) solar cells represent more than 90% of the PV market today. Thanks to a combination of technological advances and increased installed capacity (> 500 GW worldwide at the end of 2018), the price of the c-Si PV modules has decreased drastically in the past years (by 84% from 2010 to 2016, Figure 1.2a).[24,25] 18-19% efficient c-Si modules sell typically at 0.2 \$/W in 2020.[26] However, this price goes up by a factor 3 to 4 in Switzerland or niche markets.

Nowadays, c-Si solar modules account for only $\approx$ 30-50% of the overall price of an installed PV system (Figure 1.2a-b). The rest of the costs are attributed to the balance-of-system (BOS) costs, which consist in grid connections (inverters, electrical wiring, interconnection), support structure, manpower (design, installation), administrative parts, etc. The price of the BOS has not decreased as drastically over the years in comparison to the one of c-Si modules (Figure 1.2b). In addition, most of the BOS costs (except
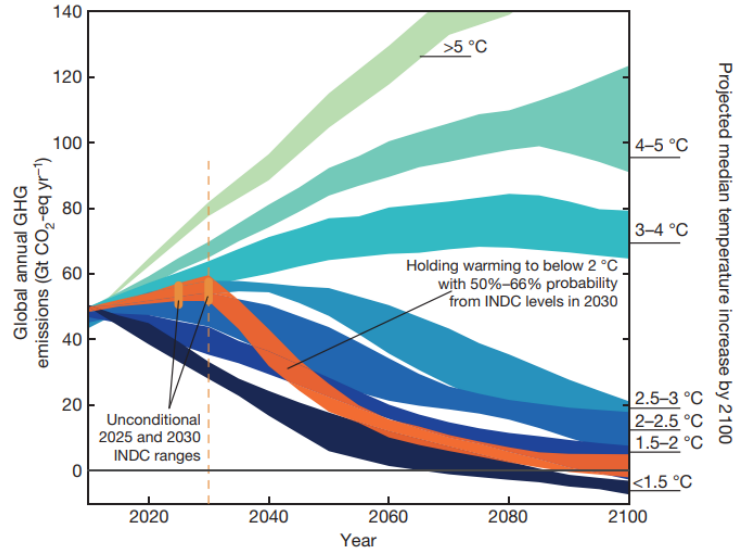
Figure 1.1 – Temperature increase projections due to greenhouse gas emissions. Global-mean temperature (20th–80th percentile) increase in 2100 relative to pre-industrial levels (1850–1900). Graph from ref.[23] Published in 2016.

inverters) are area-related. This implies that to further reduce the LCOE of c-Si PV, increasing the module efficiency is the most straightforward approach. For example, for residential PV in 2020, according to Figure 1.2 (module = 42\$ m^{-2}, BOS = 277\$ m^{-2}), a 20% decrease in the module price leads to a $\approx$ 3% LCOE decrease whereas an increase of 20% in efficiency leads to a LCOE decrease of $\approx$ 20%.
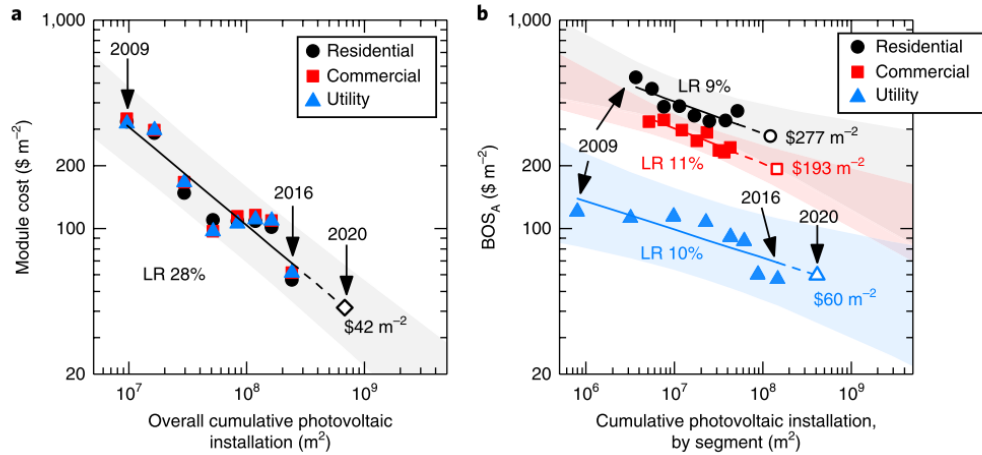
Figure 1.2 – Photovoltaic system learning curves (c-Si module and BOS). a) c-Si module learning curve, b) BOS learning curve. Open symbols represent predictions for 2020. The shaded areas represent the 95% prediction intervals for future values based on historical data. Graph from ref.[25] Published in 2016.

Various approaches can be applied to increase the power conversion efficiency (PCE) of c-Si modules. For instance, the PV market is currently moving towards the next generation of c-Si solar cells, meaning that historical aluminium back surface field (Al-BSF) designs are

being replaced by designs based on passivated emitter and rear cells (PERC), "passivating contacts", interdigitated back contacted (IBC) cells (to reduce shadow losses due to the front metallisation) or bifacial cells (sunlight reaches the cell from the front and back sides). However, the efficiency of monofacial c-Si cells is theoretically limited to 29.4%. With a current world record lying at 26.7%, there is only few tenths of a percent to gain before the practical efficiency limit is reached.[4,5] This means that a c-Si solar cell PCE in the range of 25-26% is likely the maximum attainable in a production line, leading to 22-24% modules depending on the assembly technique. Noticeably, current best commercial c-Si modules reach a PCE of 22.6% featuring individual cells with an efficiency of 25%.[27]

Several approaches, *i.e.* multiple carrier extraction and hot carrier solar cells, concentration PV and multijunction solar cells, are being investigated to reach efficiencies beyond the single-junction efficiency limit detailed by Shockley and Queisser.[28,29] Among those approaches, the concept of multijunction is the only one validated experimentally under 1 sun conditions and holds the greatest promise for an industrial implementation.

1.2 Multijunction solar cells

The theoretical maximum efficiency of a solar conversion system can be derived from the laws of thermodynamics. The Shockley-Queisser detailed balance limit for p-n junctions is strongly dependent on the band gap of the absorber material. Considering an ideal band gap of 1.34 eV, a maximum efficiency of 33.7% can be reached (under AM 1.5G illumination, *i.e.* 1 sun conditions) and 31.9% for c-Si (1.1 eV).[6] Including Auger recombination in the calculation lowers this value to 29.4% for c-Si.[4] This limit arises from the fact that the absorber is transparent to photons having energies below its band gap, and that the "excess" energy from photons with larger energies than the material band gap is lost by thermalisation (cooling of "hot" carriers to the band edge). These two types of losses can be mitigated by stacking absorbers with various band gaps on top of each other in a multijunction solar cell (Figure 1.3). An efficiency of 68.2% (under an AM 1.5G illumination) can be theoretically reached by stacking an infinite number of cells with different band gaps.[30,31] In a more realistic approach, stacking two different band gap absorbers to form a tandem device can lead to a PCE of 42.3% assuming ideal band gaps of 1.0 and 1.9 eV.[30]

Different strategies exist to construct a tandem solar cell. They can be separated into two categories: two terminal (2T) and four terminal (4T) tandem devices. 4T tandems are made of two cells which are processed and contacted separately. 4T cells can be made by several approaches. The first and most common 4T approach consists in mechanically stacking both sub-cells, the bottom cell being illuminated through the top one. A second 4T approach consists in splitting the solar spectrum (e.g. by using dichroic filters before the light reaches the cells).[33,34] Both configurations have the advantage of being

Figure 1.3 – **Losses in single- and multijunction solar cells.** Fractional losses and maximum power output for the ideal band gap energies under one sun illumination for one to six junction solar cells. Adapted from ref.[32]
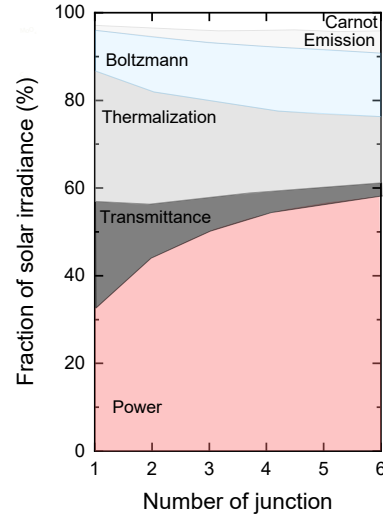
constraint-free regarding sub-cells fabrication and current matching conditions. The only requirement for the former design is to develop a semitransparent top cell which lets low energy photons through to the bottom cell. This implies employing transparent contacts. However, 4T designs come at additional costs as two junction boxes, inverters, two additional transparent conductive electrodes and filters in the case of spectral splitting are needed compared to 2T designs.

On the other hand, monolithically integrated 2T tandems, where the top cell is directly deposited on top of the other sub-cell, are more economically viable as they demand no extra BOS costs and transparent electrodes. However, the main disadvantage of 2T tandems lies in the need to reach current matching conditions. The current delivered by such series-connected tandems is limited by the cell with the smaller current. To reach high efficiencies, perfect light management is hence required. In addition, for a 2T integration, the top cell processing should be compatible with the underlying bottom cell (deposition temperature, presence of solvents, surface topography compatibility). 2T tandems are hence more challenging to produce than 4T tandems but likely hold greater industrial potential.

Figure 1.4 presents a sketch along with the spectrally resolved power output and current-voltage curves for a single-junction, 4T and 2T tandems. One can see that for the single-junction case in Figure 1.4a, thermalisation losses are significant (middle chart) and the open-circuit voltage (V_{oc}, no carrier extracted from the cell) is dependent on the band gap of the material. In opposition, a large current density is reached (a broader part of the spectrum is collected by the narrow band gap material). One can see that, in the J-V curve of a wide band gap material solar cell (E_{g2}, in blue in Figure 1.4b), the short-circuit density (J_{sc}) is reduced whereas the V_{oc} is increased (less carriers collected but higher voltage due to the wide band gap). In a 4T configuration, as the two sub-cells are measured independently, the total PCE is purely the sum of the power output of

each sub-cell. It is worth mentioning that sunlight that penetrates the bottom cell is first filtered by the top cell, lowering its current density. In the case of 2T tandems, the series-connection of the sub-cells intrinsically limits the current density of the tandem device to the one of the limiting sub-cell. Another effect of the series-connection is that the V_{oc} of both sub-cells sum up, whereas the overall PCE of the 2T device is determined by the tandem J-V curve (Figure 1.4c)
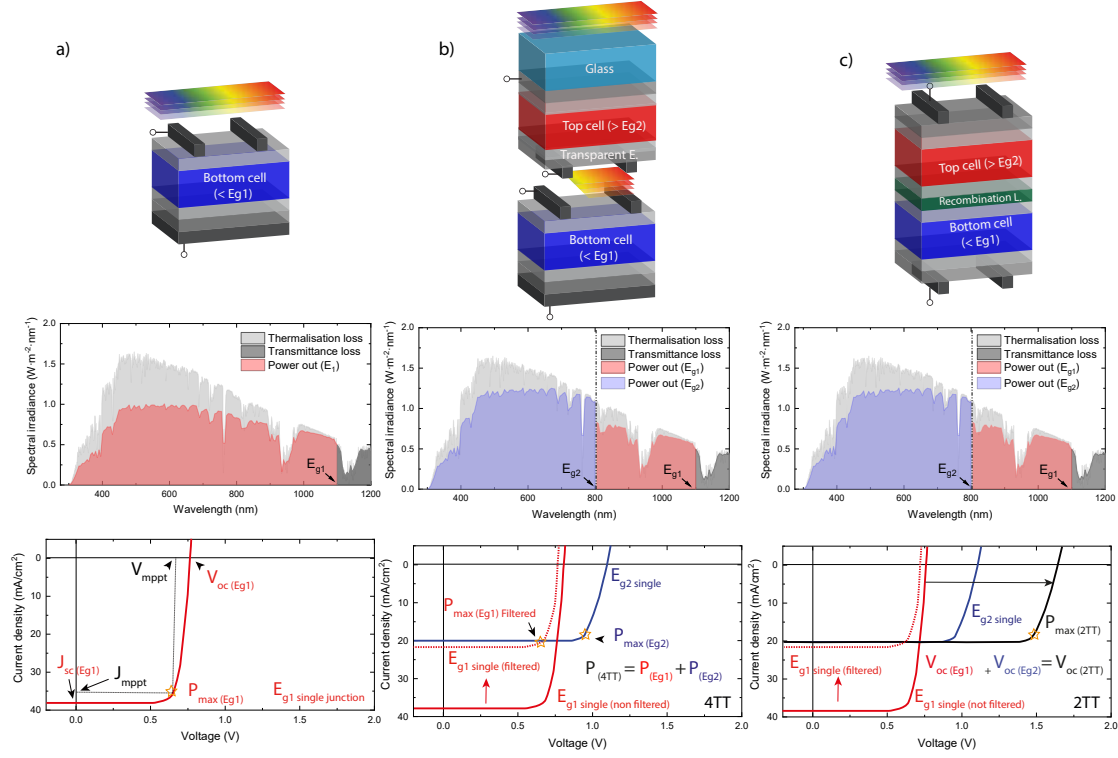
Figure 1.4 – Single-junction, 4T and 2T tandem solar cells. Sketches of the different solar cells (top), the spectral power output (middle) and typical J-V curves (bottom) are displayed for the 3 different configurations. a) single-junction solar cell, b) 4T tandem solar cell, c) monolithically integrated 2T tandem solar cell. The top and bottom band gaps are 1.1 eV and 1.55 eV in this particular case. V_{oc} stands for open-circuit voltage, J_{sc} for short-circuit current density and V_{mppt} and J_{mppt} for the voltage and current density at maximum power-point, respectively.

Over the years, various tandem devices have been developed. However, those devices either fall into low-cost, low-efficiency or high-efficiency, high-cost categories. A polymer (organic solar cell) multijunction with 14.2% efficiency was recently introduced (single-junction at 17.4%).[35, 36] Thin-film silicon tandem composed of an amorphous silicon (a-Si:H 1.6-1.8 eV) top cell and a microcrystalline silicon (μc-Si:H 1.1 eV) bottom cell reached an efficiency of 13%.[27, 37] Even though these technologies have potentially low fabrication costs, their modest power output prevents their deployment in the field. On the other hand, high-efficiency multijunction devices based on III-V semiconductor materials have demonstrated the highest PCEs so far: 47.1% under concentrated sunlight (monolithic six junctions solar cell under 143 suns) and 39.2% under 1 sun conditions.[27] In addition, 2T tandems using a GaInP and GaAs sub-cells have reached a PCE of 32.8% in

1 sun conditions. Nevertheless, the high cost and low abundance of III-V semiconductors prevent them from being produced at a reasonable cost and limit their market-share to niche applications such as space and concentrated PV.

Crystalline silicon solar cells are the best bottom cell candidates due to their high efficiency and stability, low toxicity and the fact that they already provide electricity at a competitive price. Several attempts have been made to combine c-Si and III-V absorbers in tandems, reaching close to 33% efficiency in a 4T design.[7] A monolithic III-V integration on c-Si would bring the costs down, but processing conditions of the III-V material directly on top of the c-Si cell is challenging.[8] In that sense, the development of tandem solar cells featuring an efficient top cell that can be deposited directly on the c-Si bottom cell at low cost is essential. Recently, organic-inorganic metal halide perovskites have emerged as promising light absorber materials for low-cost, high-efficiency tandem solar cells with a c-Si bottom cell.[38–40]

In the next section, we describe briefly these two solar cell technologies that will be combined in a tandem, c-Si and perovskites, and discuss their efficiency and commercial potential.

1.3 Crystalline silicon solar cells

Further improvements were achieved by introducing an insulating layer ($AlOx/SiN_x$) with localised openings on the rear side to reduce the overall metal/c-Si contact area.[41,42] Such cell design, called passivated emitter and rear cell (PERC), is currently taking over Al-BSF as the industrial workhorse due to their high PCE ($< 23\%$ for record 6 inch cells, and $< 22\%$ for some production lines) and relatively similar processing scheme. While PERC-like technologies rely on partial passivation (through localised contact openings), full area passivation is the most promising path to further increase the V_{oc} to values over 700 mV and push the PCE towards 25%. In that regard, passivating contacts using a thin silicon oxide (SiO_x) layer capped by doped poly-silicon deposited on both sides of the wafer appear as the main upgrade to PERCs. A high level of passivation, while still enabling carrier transport by tunnelling or through pinholes across the SiO_x layer, ensures high V_{oc}'s.[43,44]

Alternatively, another full area-passivation approach is to use hydrogenated amorphous silicon (a-Si:H) on both sides of the silicon wafer.[45–47] These a-Si:H layers are commonly deposited by plasma enhanced chemical vapour deposition (PECVD). By introducing p-type or n-type dopants (boron, phosphorous) into the gas mixture, charge carrier selective contacts can be deposited on each side. Silicon heterojunction solar cells (SHJ) using these passivation and contact layers yield a V_{oc} higher than 700 mV.[48] SHJ solar cells also show an improved response to near-infrared light compared to the standard diffused p-n junction solar cells, which makes the former an ideal candidate for tandem devices.[49]

When employing an interdigitated back-contacted design (charge carrier extraction on the rear side), SHJ solar cells yield an efficiency of 26.7% (by Kaneka), which is the best efficiency to date for c-Si solar cells.[27] However, due to the presence of a-Si:H layers, SHJ solar cells cannot be exposed to temperatures much more than 200°C or hydrogen will effuse from the film.[50] For 2T tandems, this limited thermal budget imposes some constraints on the top cell processing conditions. For 2T tandems, SHJs already feature a transparent conductive oxide (TCO) for carrier extraction on their front-side. Advantageously, this TCO can be used directly as a recombination layer in a 2T tandem. Due to these aspects (high efficiency, high near-IR response), most 2T tandems reported so far use a SHJ bottom cell. Figure 1.5 represents sketches of the different c-Si technologies described in the previous paragraphs.
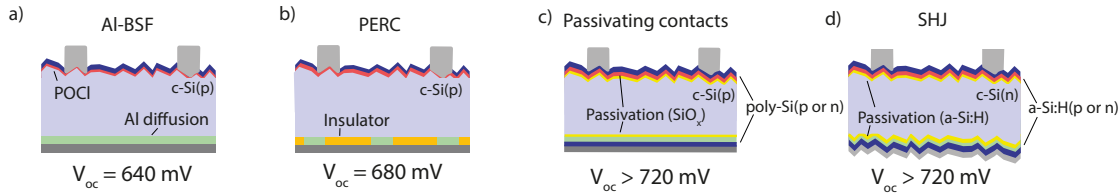
Figure 1.5 – **Evolution of c-Si solar cell technologies.** a) Aluminium back surface field (Al-BSF), b) Passivated emitter and rear cell (PERC), c) Passivating contact cell, d) Silicon heterojunction cell (SHJ).

1.4 Perovskite solar cells

Perovskites refer to a material crystallising with the ABX_3 crystal structure (Figure 1.6). The first inorganic perovskite mineral to be identified was $CaTiO_3$ in 1839. Since then, various perovskite materials have been discovered or synthesised such as $SrTiO_3$ and $BaTiO_3$. The first hybrid organic-inorganic halide perovskite structure was reported in 1978 by Weber.[51] The optoelectronic properties have been investigated by Mitzi *et al.* in the late 1990 when their applications as field-effect transistor and light-emitting diode were demonstrated.[52–55] The first application of an organic-inorganic perovskite as a solar absorber was reported in 2009.[56]
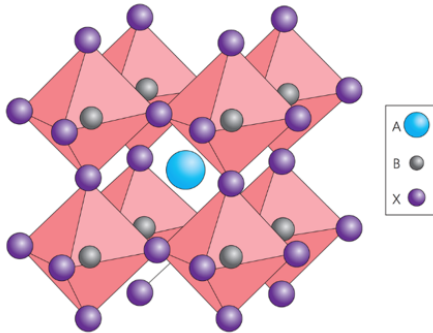
Figure 1.6 – **Perovskite crystal structure.** For organic-inorganic perovskites, the A-site is occupied by methylammonium (MA^+), formamidinium (FA^+) and/or cesium (Cs^+) cations, the B-site is occupied by bivalent metal cations (*e.g.* Pb_2^+ and/or Sn_2^+), and the X-site is occupied by a halide (*e.g.* I^-, Br^-, Cl^-). Image from ref.[38]

For mixed organic-inorganic perovskites the A site is an organic (mostly methylammonium,

formamidinium) cation, sometimes combined with an inorganic one (Cs^+), B is a bivalent metal (usually $Pb_2{}^+$, $Sn_2{}^+$), and X contains halide anions (I^-, Br^-, Cl^-).[57,58] The size of each ion determines whether the structure falls into a perovskite or non-perovskite crystal according to the Goldschmidt tolerance factor:[59,60]

$$t = \frac{r_A + r_B}{\sqrt{2}(r_B + r_X)} \tag{1.1}$$

where r_A, r_B and r_X are the atomic radii of the A-site cations, B-site bivalent metal cations and X-site halides, respectively.[1] A cubic perovskite structure (photo-active "black" phase) is obtained for t in between 0.9 and 1, whereas $t > 1$ and t < 0.9 results in a non-perovskite crystal structure (photo-inactive, "yellow" phase, for $t < 0.9$ orthorhombic phase, $t > 1$, hexagonal phase). Notably, as transitions between these phases depend on temperature, the same perovskite alloy might result in different phases depending on its fabrication or operational temperatures. The use of MA^+ leads to the black perovskite phase. On the other hand, pure FA^+-based perovskites ($FAPbI_3$) often crystallise in the hexagonal phase due to the bigger size of the FA^+ cation. However, phase stability can be obtained by alloying FA^+ with a smaller cation such as Cs^+ and/or MA^+.[60,62] It has been reported that methylammonium lead triiodide ($MAPbI_3$) perovskite absorbers are not intrinsically stable at temperatures higher than 85°C,[63] due to the volatile nature of the MA cations. While this might not be an issue for cells fabricated in the laboratory, some of the module fabrication processes used nowadays, such as encapsulation and screen-printing of the front metal grid (for tandems), require annealing steps > 100°C. As a result, methylammonium-free perovskites will be preferred in this thesis.

Even though the A-site cation is of major importance regarding crystal structure and its thermal stability, it plays a limited role in the energetic levels of the perovskite. The $[PbI_6]_4$ octahedra framework dominates carrier transport.[64,65] The valence band maximum of $MAPbI_3$ is formed by the anti-bonding coupling of the I(5p) and Pb(6s) orbitals, while the conduction band minimum is defined by the unoccupied Pb(6p) orbitals. This is also responsible for the direct band gap and strong absorption coefficient as the intra-atomic transition from Pb(6s) to Pb(6p) orbitals is favoured.[66,67]

The perovskite band gap depends on the size of its unit cell. For example, a smaller unit cell by replacing iodide by the smaller bromide anion (on the X-site) results in an increase in band gap from 1.55 eV for $MAPbI_3$ to 2.4 eV for $MAPbBr_3$.[68] However, certain alloys featuring high Br contents ($> 33\%$ of the I content) may segregate under light into low

---

[1]Notably, the expression of the tolerance factor was recently improved by using the relation:[61]

$$\tau = \frac{r_X}{r_B} - n_A(n_A - \frac{r_A/r_B}{ln(r_A/r_B)}) \tag{1.2}$$

Where n_A is the degree of oxidation of the cation. A τ below 4.18 should yield a perovskite photo-active structure.

band gap I-rich domains.[69] Similarly, the introduction of bigger A-site cations (such as FA^+) reduce the overall band gap, however, to a limited extent (1.48 eV for pure $FAPbI_3$). This band gap tunability is of major importance for tandem applications. In addition, the sharp optical absorption edge,[70,71] the long carrier diffusion lengths ,[72] low exciton binding energies[73] and ambipolar charge carrier transport observed in polycrystalline thin films deposited at low temperature[74,75] make organic-inorganic perovskites unique optoelectronic materials.

Moving on from the material itself to solar cells, perovskite solar cells emerged from dye-sensitised devices where they were used as an alternative to the dye.[39,56] However, the stability of those devices was limited due to the fact that the perovskite dissolved in the liquid electrolyte within a few minutes.[56] Further enhancements in efficiency and stability were made by replacing the electrolyte by a solid-state hole transporting layer (spiro-OMeTAD) used in dye-sensitised solar cells.[76] Removing the mesoporous scaffold present in dye-sensitised solar cells (TiO_2 or Al_2O_3) was made possible due to ambipolar transport of holes and electrons.[74] Planar heterojunction (absence of a mesoporous scaffold) structures can be made into either polarity depending on the deposition order of the selective layers. First, n-i-p configurations (where the electron transport layer (ETL) is deposited first) were developed by replacing the TiO_2 scaffold with other ETL, while spiro-OMeTAD was often used as hole transport layer (HTL) on top of the perovskite. However, due to the high manufacturing costs of spiro-OMeTAD and its poor stability (due to the presence of Li-dopants), considerable efforts have been made to develop HTL alternatives.[77] Inspired by organic PV research, perovskite solar cells in the p-i-n polarity (also called inverted structure) have also been developed.[78] Metal oxides (NiO_x,CuO_2), polymers (PTAA, PEDOT:PSS) and small organic molecules (SpiroTTB, CuPc) have been used as HTL in such device configuration, whereas fullerenes and derivatives (C_{60}, PCBM) have regularly been adopted as a top ETL. Figure 1.7 presents the different perovskite architectures (n-i-p, p-i-n) with few of the most commonly used charge transport layers.
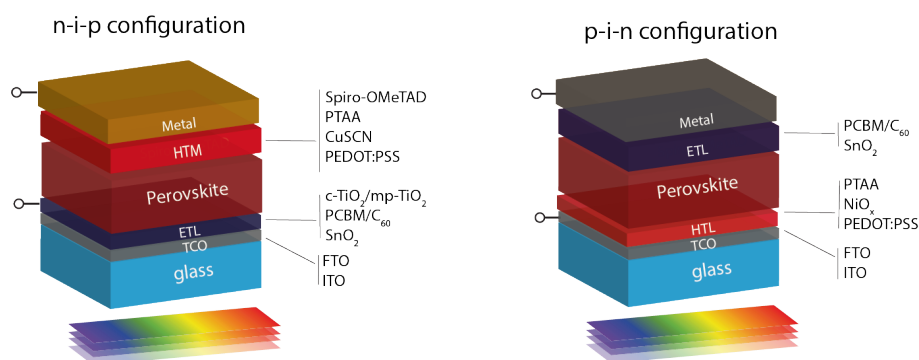
Figure 1.7 – Different perovskite architectures (n-i-p, p-i-n). FTO stands for fluorinated tin oxide, ITO for indium tin oxide, c- is for compact and mp- stands for mesoporous. PCBM is [6,6]-phenyl-C_{61}-butyric acid methyl ester, C_{60} fullerene, PEDOT:PSS is poly(3,4-ethylenedioxythiophene) polystyrene sulfonate, PTAA is poly[bis(4-phenyl)(2,4,6-trimethylphenyl)amine] and spiro-OMeTAD for 2,2',7,7'-Tetrakis-9,9'-spirobifluorene.

15

To produce high-quality perovskite absorber materials, various deposition methods have been developed. They can be divided into two main categories: one-step and two-step methods. For one-step methods, all the components are deposited at the same time,[79] whereas for two-step methods, a lead halide template is often deposited first, followed by a subsequent organohalide deposition.[80] Wet chemical methods, mostly spin-coating,[79,80] but in some cases inkjet printing,[81,82] blade coating,[83,84] or slot-die coating,[85,86] are generally the preferred routes for perovskite deposition as they enable precise control of composition and short processing times. In parallel, vapour-based techniques have emerged. These methods give high flexibility regarding material depositions and substrate choice as these do not involve any aggressive solvents that may dissolve underlying layers.[87–90]

Overall, due to their highly attractive optoelectrical properties, versatility of deposition route and device configurations, organic-inorganic lead halide perovskite single-junction solar cells have seen their efficiency increase from 3.8%[56] to a certified value of 25.2%.[27] in just over a decade. Considering the minimal volume of material required for their fabrication, the low deposition temperature involved and the various options for band gap, charge carrier selective contacts and deposition routes, perovskites solar cells are promising candidates for low-cost yet high-efficiency single-junction and tandem PV.

1.5 Perovskite/c-Si tandems

As explained in the section above, the band gap of the perovskite absorber can be readily tuned in between 1.6-1.8 eV, which is the optimal band gap for a tandem using a c-Si bottom cell. In addition, the perovskite features a sharp optical band gap onset with few sub-band gap absorption states and a high PCE, which makes it highly attractive for tandem applications. Furthermore, in opposition to III-V/c-Si tandems, the perovskite layer can be deposited directly on the bottom cell, even on a thermally sensitive SHJ. Simulations have shown that combining c-Si bottom cell and a perovskite top cell in a tandem device can yield an efficiency of 31-32%.[91,92] In the laboratory, 2T and 4T perovskite/c-Si tandem solar cell efficiencies now reach up to 28.2% for 4T designs and 29.1% for 2T configurations (Figure 1.8). Perovskite/chalcopyrite tandems achieve up to 25.9% for 4T and 24.2% for 2T.[93–97] Perovskite/perovskite tandems yield up to 23.1% for 4T tandems and 24.8% for 2T tandems.[98–101] Even though impressive efficiency results have been obtained using chalcopyrite and perovskite bottom cells, we will focus here exclusively on perovskite/c-Si tandem devices.

Figure 1.8 shows record efficiencies of single-junction silicon, perovskite cells and perovskite/c-Si tandems (both 4T and 2T). One can see that the 2T tandems now exhibit a higher PCE than 4T tandem cells. This is mainly attributed to the reduced parasitic absorption in 2T tandems due to the absence of the two transparent electrodes needed in 4T designs (at the top of the c-Si cell and at the bottom of the perovskite one).

It is still debatable whether 4T or 2T tandems have the highest potential towards commercialisation.[102] Various simulations have been carried out by several research groups to compare 4T and 2T designs. In standard test conditions (STC, AM1.5G, 1000W/m^2, 25°C), it was found that both 4T and 2T tandems could reach similar efficiencies around 31-32%.[19,91] Nevertheless, due to current-matching requirements in 2T tandems and the spectral variation during the day, energy yield calculations have shown that 4T cells may slightly outperform the 2T cells in several locations (by less than 2% relative).[19,103] However, BOS-related expenses increase for the 4T tandem case due to the requirement to power separately both cells. Added to the fact that capital expenditure required to build from scratch a perovskite solar cell production line is likely larger than adding additional deposition tools to an existing c-Si production line, 2T designs may be more economically viable.
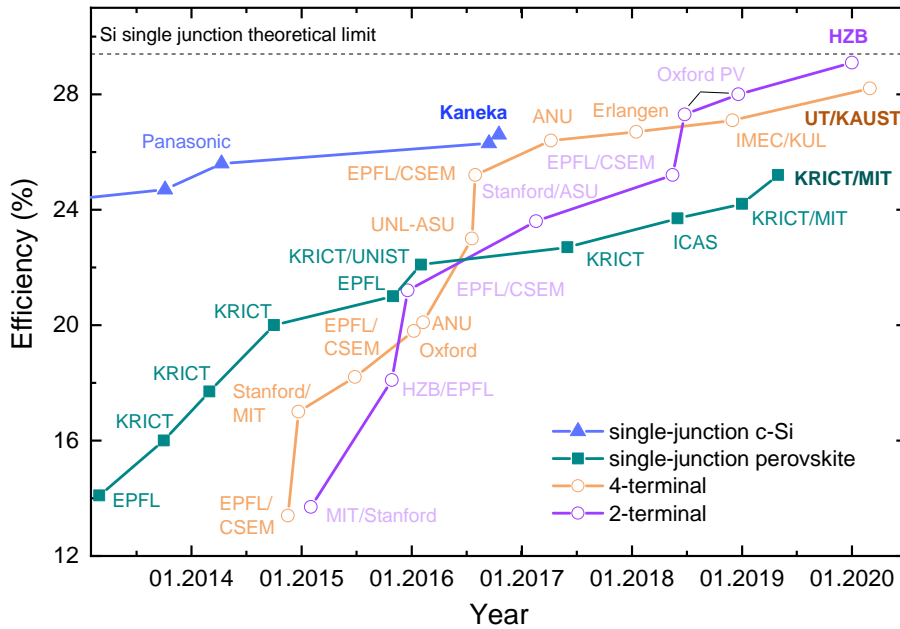
Figure 1.8 – **Evolution in PCE of record perovskite and c-Si single-junctions and perovskite/c-Si tandem solar cells.**

1.5.1 History of monolithic 2T perovskite/c-Si tandems

The first monolithic tandem was reported in 2015 and involved a homojunction c-Si solar cell and a silicon tunnel junction and achieved a performance of 13.8%.[104] The low efficiency was mainly attributed to a large parasitic absorption and lack of surface passivation in the c-Si bottom cell. The first monolithic tandem featuring a SHJ bottom cell was presented by Albrecht *et al.*, a device that reached an efficiency of over 18%.[105] The use of a SHJ bottom cell was made possible by the development of a low temperature (< 200°C) perovskite top cell fabrication process. An atomic layer deposition (ALD) deposition of SnO$_2$ replaced the high-temperature annealed mesoscopic TiO$_2$ electron

selective layer. As a consequence of the low-temperature top cell deposition, indium tin oxide (ITO) could be used as a recombination junction, enabling infrared transparency and low contact resistivity in between both sub-cells. Shortly after, Werner *et al.* presented a monolithic perovskite/SHJ tandem with an efficiency of 21.2% by introducing a sputtered indium zinc oxide (IZO) recombination layer and a sequential two-step physical vapour deposition/solution-processing (PVD/SP) fabrication route for the perovskite cell.[106] This was the status at the start of this thesis.

Soon after, Werner and co-workers promoted the IR response of the SHJ cell by introducing a pyramidal texture on the rear-side of the c-Si cell.[13] All reported perovskite/SHJ tandems presented earlier were based on double-side polished (DSP) c-Si bottom cells, which introduced a substantial amount of IR-light losses due to weak light trapping in the bottom cell. The introduction of single-side rear texture (SST) was realised by depositing a protecting mask on the front side of the c-Si wafer during texturisation. This led to a monolithic perovskite/c-Si tandem with an active area > 1 cm^2 with a PCE of 20.5%.

At that time, all the monolithic perovskite/c-Si tandems were developed in the n-i-p configuration (perovskite HTL facing sunwards), which led to significant parasitic absorption in the UV/blue part of the spectrum. The main reason was linked to the fact that a thick ($\approx$ 150 nm) doped spiro-OMeTAD layer was used. With p-i-n cells gaining momentum, several groups flipped the polarity of the perovskite cell. Fu *et al.* produced a p-i-n perovskite semitransparent cells with a 16.1% PCE with a transmittance of 80% to near-infrared wavelengths using spin-coated PTAA as the HTM and a fullerene-based PCBM as ETL. The semitransparent contact consisted in ZnO nanoparticles as buffer layer and a sputtered ZnO:Al layer.[107] A breakthrough came from Bush and co-workers when they presented the first monolithic perovskite/c-Si tandem featuring a perovskite/c-Si tandem in the p-i-n configuration, achieving a certified PCE of 23.6% on 1 cm^2.[108] The perovskite layer, sandwiched between inorganic layers NiO$_x$ as HTL and SnO$_2$ deposited by ALD as buffer layer, showed very promising thermal and environmental stability and withstood 1000 hours of operation at 35°C (unencapsulated) and 1000 hrs in 85% relative humidity with standard encapsulation (EVA/glass). These impressive stability results were achieved thanks to the i) compact ALD-SnO$_2$ layer used as a protective layer against TCO sputtering, ii) the composition of the perovskite layer with the introduction of FA$^+$ and Cs$^+$ as a replacement to the commonly used but thermally less stable MA$^+$ cation. Furthermore, the partial substitution of iodide by bromide halide was used to tailor the perovskite band gap in order to reach current matching in between both sub-cells and a higher V_{oc}.

The first contributions to the field discussed in this thesis involve a recombination junction based on a layer stack of highly doped nanocrystalline Si, which enabled to gain in optics and in electrical performance (discussed in chapter 3). Similarly, by introducing a high-index layer such as a nanocrystalline SiO$_x$:H layer on the front side of the c-Si bottom cell, Mazzarella and co-workers reduced the IR reflection at the polished front-side of the

c-Si bottom cell by 1.4 mA cm^{-2}. When combined with a perovskite top cell deposited in the p-i-n configuration using the layer stack as in ref,[108] a current density of 19 mA cm^{-2} could be reached (cumulative J_{sc} of 38.7 mA cm^{-2}), leading to a certified PCE of 25.2%

Further improvements in the optical performance of monolithic perovskite/c-Si tandem were achieved by replacing the single-side textured (SST) silicon bottom cell (polished at the front side) by a double-side textured (DST) silicon bottom cell. This was achieved by mastering the deposition of all the top cell layers directly on the silicon texture by means of vacuum-based depositions. These developments will be discussed in the chapter 4. An alternative involves downsizing the pyramids size to 500 nm - 1 μm and planarising the c-Si texture with the perovskite layer (thickness > 800 nm - 1 μm).[109,110] The benefits and downsides of this strategy will be discussed in chapter 5.

Another way of using a textured bottom cell without requiring a conformal perovskite coating could be achieved by mechanically stacking both sub-cells and connecting them with a conductive layer.[111,112] Lamanna and co-workers recently obtained a 26% 2T tandem using this approach.[112] This strategy is similar to the 4T design, where both sub-cells are fabricated separately (constraint-free from a processing point of view) and so costs are potentially higher and optics less favourable (parasitic absorption in the additional transparent electrodes, presence of metal fingers on the c-Si cell that may induce additional shadowing). In addition, the main benefit of 4T designs (no current matching required in between both sub-cells) does not apply in this case as the cells are connected in series. As a consequence, it is not likely that a strategy that combines disadvantages of the 2T (current matching) and 4T tandems (higher production cost, more parasitic absorption) designs will prevail in the future.

During the summer of 2018, Oxford PV, a British-based company focusing on the commercialisation of monolithic perovskite/c-Si tandems, announced a record PCE of 27.3% obtained on 1 cm^2 and independently certified by Fraunhofer Institute. Later that year, the same company further pushed the efficiency to 28%. The device structure has not been communicated. Early 2020, HZB and Kaunas University further pushed the efficiency to a certified value of 29.15% on $\approx$ 1cm^2. The device structure is yet to be reported. Figure 1.9 summarises the main milestones leading to improved optics. One can observe from the external quantum efficiency (EQE) spectra, that the optical performance of 2T cells is now on par with the most advanced c-Si technologies.

Table 1.1 is a list of few 2T perovskite/c-Si tandems reported at the time of the writing of this thesis (April 2020). Information such as perovskite composition, band gap, top cell polarity, recombination junction, bottom cell type and active area are displayed. Power output efficiencies (at the publication date) are displayed in Figure 1.10. One can see from the plot that the reduction in parasitic absorption in the Spiro-OMeTAD by depositing the perovskite in the p-i-n configuration (red data points) led to a big leap forward and is now widely adopted.[108] However, there is no fundamental aspect hindering

n-i-p designs from catching up with the p-i-n configuration. The lack of a highly efficient, highly transparent HTL that can be deposited on top of the perovskite is now the main reason behind this difference in performance. Nevertheless, promising alternatives are being investigated.[113]

One can also see that SHJ bottom cells gave the best PCEs so far, mainly due to their high V_{oc} and high efficiencies. Nevertheless, other silicon solar cell technologies (cells based on high-temperature passivating contacts, PERC) showed PCE in the 24-25% range.[11,114] For now the optical gain from the DST c-Si bottom cell is counterbalanced by the difficulty of depositing a good quality perovskite on textured silicon. This is yet not explicit which of DST or SST tandems will be included in the first commercial modules (if any). But from a performance and economic point of view, DST cells appear more promising due to their superior optical performance and their direct compatibility with industrial c-Si cell front sides. Indeed, simulations have shown that choosing a DST design should lead to an energy yield increase of 6-7% annually over SST (4-5% gain if an anti-reflection foil is used on the SST device, an approach difficult to implement industrially).[115,116] Moreover, only silicon cells that are textured on their front-side are used in the industry. In the prospect of upgrading existing silicon cell production lines for tandem production, c-Si process flows will need to be adapted, which will come at additional costs. This means that the potential efficiency gain (*e.g.* from a superior perovskite quality) or manufacturing cost reduction (*e.g.* when using solution-based deposition routes) induced by SST wafers should overcome all benefits brought by DST bottom cells.
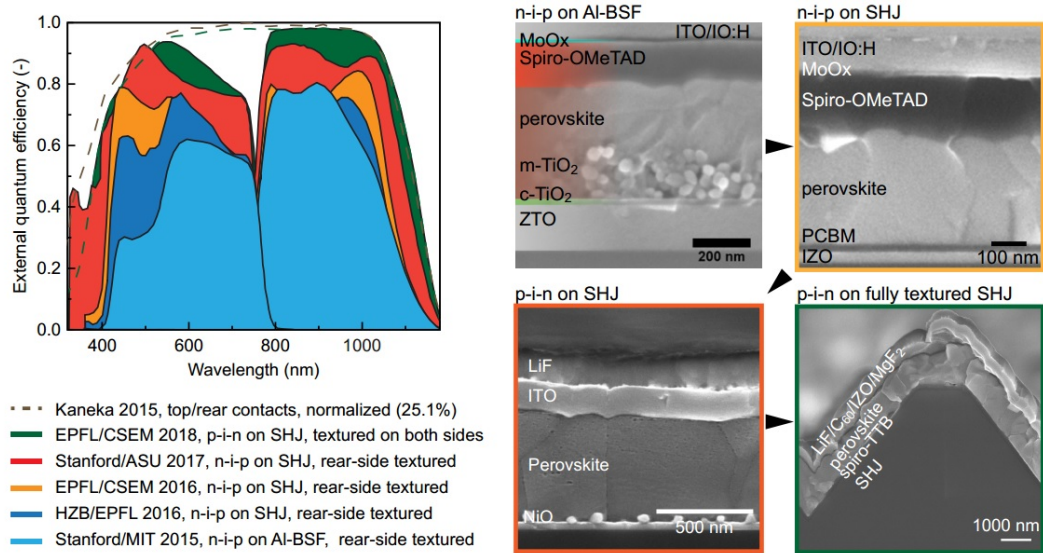

Figure 1.9 – Light management improvements in monolithic perovskite/c-Si tandems. External Quantum Efficiency (EQE) of the perovskite/c-Si tandems extracted from refs.[10,13,104,105,108] Scanning electron microscopy (SEM) cross-sections of the front side of different devices.

Table 1.1 – Efficiency table from 2T perovskite/c-Si tandems. This is a non-exhaustive list of the monolithic perovskite/c-Si tandem reported to date. The values in red represent the highest efficiencies reported at the time of the publication/certification. The values marked with an * are independently certified efficiency values. BC stands for blade-coating

date	Perovskite	Deposition	Eg	Polarity	Recomb. Junc.	Silicon	Wafer type	Texture	LM	Area	PCE	Institute	Paper
2015/02	MAPbI3	SP	1.55	n-i-p	n+/p+ Si	HoJ	n-type	DSP	ARC	1	13.7	MIT/Stanford	104
2015/10	FAMAPb(I−Br)3	SP	1.56	n-i-p	ITO	SHJ	n-type	DSP	ARC	0.12	18.1	HZB/EPFL	105
2015/12	MAPbI3	PVD/SP	1.55	n-i-p	IZO	SHJ	n-type	DSP	ARF	0.17	21.2	EPFL/CSEM	106
2016/06	MAPbI3	PVD/SP	1.55	n-i-p	IZO	SHJ	n-type	SST	ARF	1.43	20.5	EPFL/CSEM	13
2016/11	MAPbI3	PVD/SP	1.55	p-i-n	ZTO	HoJ	n-type	DSP	ARF	1.43	16	EPFL/CSEM	117
2017/01	CsFAPb(I−Br)3	SP	1.63	p-i-n	ITO	SHJ	n-type	SST	ARC	1	23.6*	Stanford/ASU	108
2017/10	CsMAPb(I−Br)3	PVD/SP	1.63	n-i-p	nc-Si	SHJ	n-type	SST	ARF	0.25	22.8	EPFL/CSEM	9
2017/10	CsFAPb(I−Br)3	PVD/SP	1.63	n-i-p	nc-Si	SHJ	n-type	SST	ARF	12.93	18	EPFL/CSEM	9
2017/10	CsRbFAMAPb(I−Br)3	SP	1.6	n-i-p	ITO/Cr/Pd/Ag	HoJ	n-type	SST	ARC	1	22.5	ANU	118
2017/10	CsRbFAMAPb(I−Br)3	SP	1.62	n-i-p	ITO	HoJ	n-type	SST	ARF	1	22.5	ANU	118
2017/10	CsFAMAPb(I−Br)3	SP	1.69	n-i-p	ITO	SHJ	n-type	DSP	N/A	0.03	20.5	PKU	119
2017/12	FAMAPb(I−Br)3	SP	N/A	n-i-p	ITO	SHJ	n-type	DSP	-	0.13	18.8	NKU	120
2018/06	CsFAPb(I−Br)3	PVD/SP	1.6	p-i-n	nc-Si	SHJ	n-type	DST	ARC	1.42	25.2*	EPFL/CSEM	10
2018/06	MAPbI3	SP	1.58	n-i-p	SnO2/p+ Si	HoJ	n-type	DSP	ARF	4	20.5	UNSW	121
2018/06	MAPbI3	SP	1.58	n-i-p	SnO2/p+ Si	HoJ	n-type	DSP	ARF	16	17.1	UNSW	121
2018/06	N/A	N/A	N/A	N/A	N/A	N/A	N/A	N/A	N/A	1	27.3*	OxfordPV	122
2018/07	CsFAPb(I−Br)3	SP	1.63	p-i-n	ITO	HoJ	p-type	SST	ARC	1	16.2	MIT	123
2018/08	CsFAPb(I−Br)3	SP	1.68	p-i-n	ITO	SHJ	n-type	SST	ARF	1	25	ANU/Stanford	124
2018/08	FAMAPb(I−Br)3	SP	1.59	n-i-p	SnO2/p+ Si	HoJ	n-type	SST	ARF	16	21.8	UNSW	125
2018/10	CsFAMAPb(I−Br)3	SP	1.6	p-i-n	ITO	SHJ	n-type	SST	ARF	0.81	25.5	HZB/U. Ljubljana	116
2018/12	CsRbFAMAPb(I−Br)3	SP	1.63	n-i-p	TiO2/p+ Si	PERC	n-type	SST	ARF	1	24.1	ANU	126
2018/12	CsRbFAMAPb(I−Br)3	SP	1.63	n-i-p	TiO2/p+ Si	HoJ	n-type	SST	ARF	1	22.9	ANU	126
2018/12	N/A	N/A	N/A	N/A	N/A	N/A	N/A	N/A	N/A	1	28*	OxfordPV	127
2019/01	CsFAMAPb(I−Br)3	SP	1.64	p-i-n	ITO	SHJ	n-type	SST	ARC	0.42	25.4	ASU/UNL	128
2019/02	CsFAPb(I−Br)3	PVD/SP	1.6	p-i-n	nc-Si	HTPC	p-type	DST	ARC	1.42	25.1	EPFL/CSEM	11
2019/04	CsFAMAPb(I−Br)3	SP	1.63	p-i-n	ITO	SHJ	n-type	SST	ARC	1.088	25.2*	HZB/U.Ox/OxPV	129
2019/04	CsFAPb(I−Br)3	SP	1.63	p-i-n	ITO	SHJ	n-type	SST	ARC	57.4	22.6	CSEM	130
2019/04	MAPb(I−Br)3	SP	1.6	p-i-n	ITO	SHJ	n-type	SST	ARF	0.19	23.4	SNU	131
2019/05	CsFAMAPb(I−Br)3	SP	1.6	p-i-n	ITO	SHJ	n-type	SST	ARC	0.77	26	HZB	132
2019/08	MAPbI3	SP	1.55	n-i-p	IZO	HoJ	p-type	DST	ARF	0.25	18.3	UNIST	111
2019/08	MAPbI3	SP	1.55	n-i-p	IZO	HoJ	p-type	SST	ARF	0.25	17.4	UNIST	111
2019/09	CsFAPb(I−Br)3	SP	1.7	n-i-p	ITO	SHJ	n-type	SST	ARC	0.25	21.6	ISE	133
2020/01	CsFAMAPb(I−Br)3	SP	1.64	n-i-p	ITO	IBC-SHJ	n-type	SST	ARC	0.78	17.1	HZB	134
2020/01	N/A	N/A	N/A	N/A	N/A	N/A	N/A	N/A	N/A	1	29.1*	HZB	135
2020/02	CsFAMAPb(I−Br)3	SP	1.68	p-i-n	InOx	SHJ	n-type	DST	ARC	0.83	25.7*	UT/KAUST	110
2020/03	CsFAMAPb(I−Br−Cl)3	SP	1.67	p-i-n	ITO	SHJ	n-type	SST	ARF	1	27	NREL/ASU	136
2020/04	CsMAPb(I−Br)3	BC	1.6	p-i-n	ITO	SHJ	n-type	DST	ARF	0.42	26.1	ASU/UNC	109

21
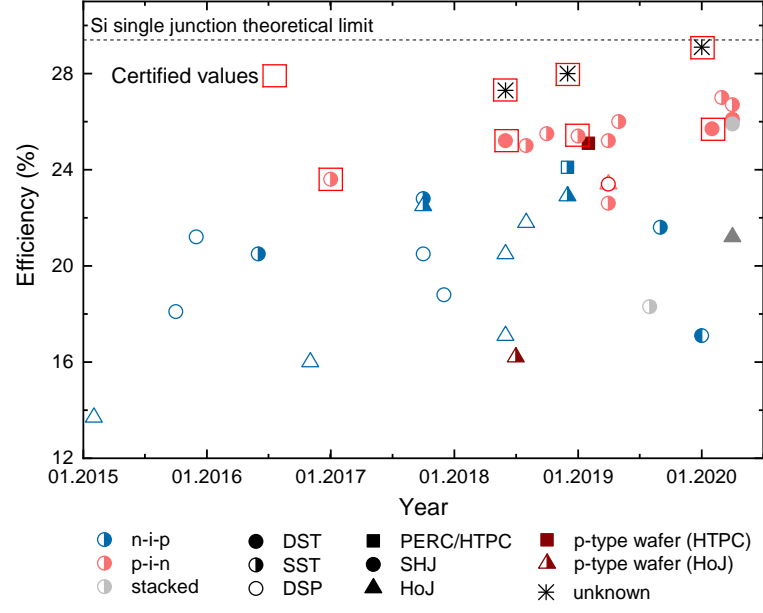
Figure 1.10 – Efficiency table for 2T perovskite/c-Si tandems. The values presented in this Figure are taken from table 1.1

1.5.2 Economical analysis: Do perovskite/c-Si tandems make sense?

It is quite an adventure to estimate the potential economic benefit of perovskite/c-Si tandems over c-Si single-junctions. Perovskite solar cells being an emerging technology, we have to deal with a lot of unknown parameters such as production costs, choice of the deposition methods (solution-processing vs. vacuum-based or hybrid ones), charge transport layers, c-Si bottom cell technology (SHJ vs. PERC, cells based on passivating contacts), SST vs. DST bottom cells (index matching interlayer required, additional anti-reflection coatings in the former case), PCE gain by switching from a single-junction to a tandem, module lifetime, etc. These uncertainties make any cost estimations far-fetched. As a result, rather than giving an answer to the question whether perovskite/c-Si tandems will produce cheaper electricity than c-Si single-junctions, we will try to define, based on literature data, what are the boundary conditions for their deployment in terms of efficiency, lifetime and additional process costs.

In order to be cost-effective, the benefits resulting from the efficiency gain of the tandem solar cell should overcome the additional costs required during its manufacturing. Most importantly, it should be more economically viable than either the top or bottom single-junction cell operating separately. In order to fulfill those requirements, it was found that tandems make economic sense only when four conditions are satisfied, i) the band gap and performance of the sub-cells should enable to reach high efficiencies, ii) the manufacturing costs ($/m^2) of each sub-cells should be in the same order of magnitude, iii) both technologies should exhibit long-term stability when deployed in the field, iv)

the single-junction PCE of both sub-cell should be comparable, as introduced by Peters *et al.* as a "marriage of equals".[137] In other words, if one sub-cell is significantly more efficient than the other, the PCE benefit of doing a tandem will not be able to compensate the manufacturing costs of the additional cell. On the other hand, if one sub-cell is significantly more expensive to produce than the other, manufacturing costs will increase drastically for a little gain in PCE and the cheaper sub-cell single-junction will prevail.

For perovskite/c-Si tandems the conditions i) and iv) are already satisfied (the band gap of the perovskite and c-Si are ideal for tandems and record PCE of perovskite and c-Si cells stand at 25.2% and 26.7%, respectively). Regarding manufacturing costs, here again, due to the emerging nature of perovskite solar cells, it is difficult to estimate the perovskite manufacturing costs. Perovskite solar cells are often regarded as compatible with low-cost manufacturing. It was estimated that the $/W of a perovskite production line could be below 1$/W for a > 3 MW/yr production line factory (and below 0.5$/W for a 1000 MW/year production line). Those values are relatively similar to the ones for c-Si (0.2-0.25 $/W in 2020).[138] In order to assess whether tandems may compete with single-junctions, BOS costs must be taken into account. It is generally accepted that the production costs of the tandem should be less than 50% of the BOS costs in order to be viable.[137]

Yu and co-workers calculated, taking into account c-Si solar cell production costs and BOS projections for 2020, that the production cost for the perovskite top cell should be below 46 $/m^2 for solar parks and 145 $/m^2 for residential PV (BOS costs are higher for residential PVs, Figure 1.2). This estimation was made with a c-Si bottom cell at 42 $/m^2 and the following considerations, PCE_{bottom} = 22.1%, PCE_{top} = 21.7%, PCE_{tandem} = 32.1% (1.7 eV), no coupling losses with tandem integration. Figure 1.11a-b displays the maximum cost tolerated for the perovskite top cell manufacturing as a function of band gap, coupling efficiency for utility and residential systems. One can clearly see that due to the higher BOS costs for residential installations, a higher cost for perovskite manufacturing can be accepted.[25, 139]

Several attempts to estimate the perovskite production costs have been reported. Chang and co-workers estimated a perovskite single-junction module cost in between 37 and 100 $/m^2 (depending on the materials used),[140] Li and co-workers estimated the perovskite single-junction manufacturing costs at 32.7 $/m^2 (p-i-n structure with inorganic charge transport layer) and at 121.18 $/m^2 for 2T tandems.[141] Similarly, Mathews *et al.* predicted perovskite single-junction costs of 31.6 $/m^2 (making predictions regarding the economy of scale for a > 100 MW/year production line).[142] Finally, the manufacturing costs of the perovskite module was estimated to be 31.7 $/m^2, with manufacturing costs as low as 6.8 $/m^2 for the perovskite solar cell alone.[143] A different approach was used by Werner and co-workers. They correlated the efficiency gain by switching from a c-Si single-junction to a tandem design with the number of additional processing steps required (assuming a 3000 wafers/hour factory, 1.5 $/m^2 of consumables per processing step). By assuming

BOS costs of 27 \$/m^2 for utility PV and 63 \$/m^2 for residential systems, the authors found that an absolute 4% efficiency gain translates into a saving of 2.1–2.7 cts \$/W and 6.4–7.6 cts \$/W for utility abd residential PV.[144] This gain is non-negligible considering the c-Si learning curve of a 0.25–0.3 \$/W within the next five to ten years.[145]

Probably the best figure of merit to determine the viability of an energy production system is the LCOE, which is the ratio of the cost of the system over its lifetime and the electricity produced (cts \$/kWh). Once again, LCOE predictions are difficult considering the fact that it requires assumptions on energy yield, manufacturing costs and module degradation rate over the years. However, estimates retrieved from literature for 2T perovskite/c-Si tandems are of 5.5 cts \$/kWh,[139] 5.22 cts \$/kWh,[141] for residential installations. Finally, performing similar calculations, Qian and co-workers estimated that to be viable in comparison to single-junction c-Si cell, the PCE of a 2T tandem should be higher than 28.7% (considering a perovskite degradation rate of 2% relative/year, 25 years lifetime and additional cost of manufacturing the tandem of 50% compared to a 405 W PERC module at 23.3% at STC, degradation rate of 0.4% relative/year, Figure 1.11c).[146]

All those results evidence the fact that perovskite/c-Si tandems could play a major role in the future of PV. In most reports, the tandem efficiency was considered to be in the range of 28-32%. It is quite clear nowadays that the efficiency of the perovskite/c-Si tandem will overpass the 30% barrier in the coming years (at least for small devices at STC) considering the actual record of 29.1% obtained after only 5 years of research. As a matter of fact, the PCE of tandems should not be a problem regarding commercialisation. The higher the PCE of the tandems, the more competitive it will be over single-junction devices. However, the path to a commercial product is still long and uncertain. The questions to be answered are i) whether the perovskite top cell can be deposited on 6 inch industrial c-Si cells and yield similar performance, ii) whether it can be done at a reasonable cost, using inexpensive charge transport layers and inexpensive deposition methods, iii) if the perovskite processing is compatible with industry standards and regulations (lead content, use of heavy solvents such as DMF, DMSO) iv) can perovskite/c-Si tandems be integrated in a high efficiency module at a high throughput and, most importantly, v) whether the perovskite cell can withstand > 25 years in real operational conditions, degrading < 1-2 relative%/year. This last point is likely the most challenging and will determine the industrial future of perovskite/c-Si tandems.
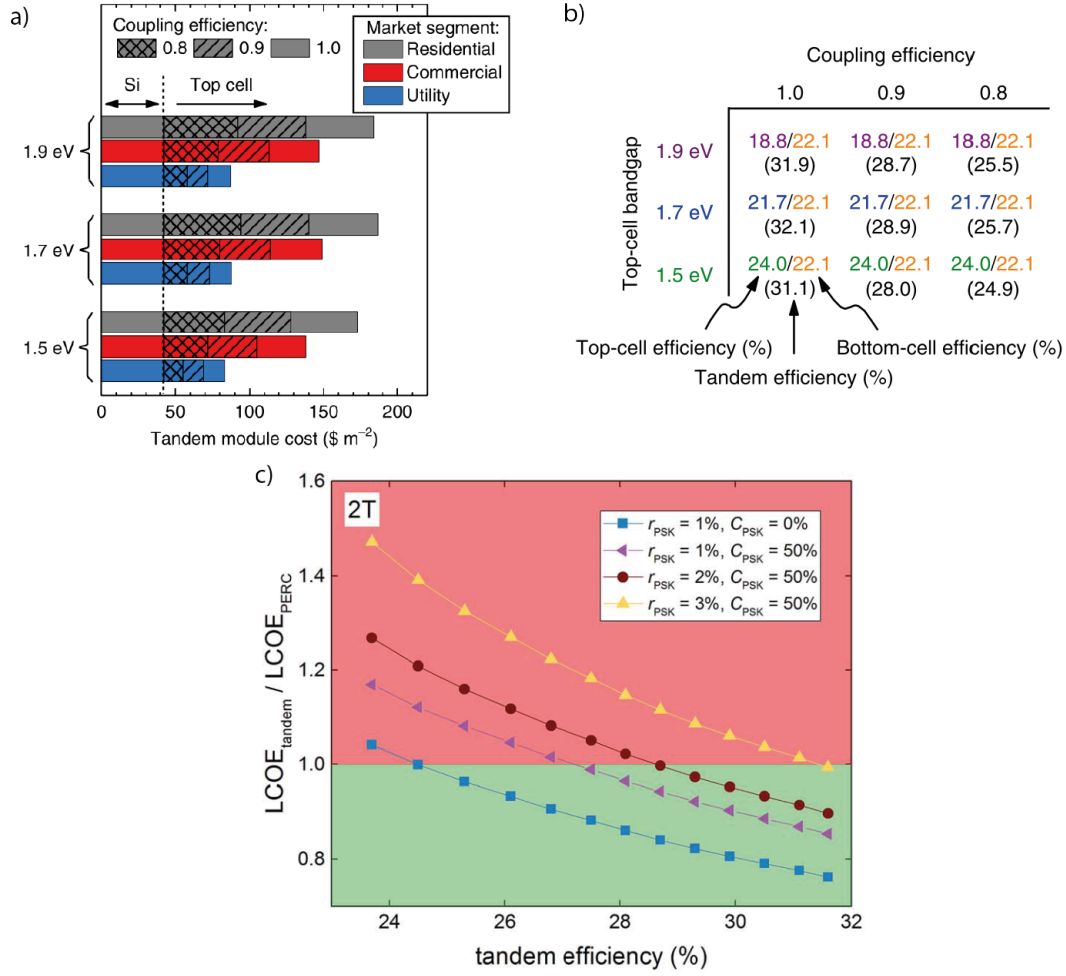
Figure 1.11 – Economic analysis of perovskite/c-Si tandems. a) Maximum tandem module cost to reach system capital cost parity with a c-Si system in 2020 for various US markets, coupling efficiencies, and top-cell band gaps. All cases assume that both sub-cells operate at 75% of their limiting efficiencies. Plot from ref.[25] b) The table showing the sub-cell and tandem absolute efficiencies associated with these variations in top-cell band gap and coupling efficiency. Plot from ref.[25] c) Simulated LCOE ratios between a perovskite/c-Si tandem module with variable PCEs and a 405 W PERC module in 2025 from ref.[146] C_{PSK} is the ratio of perovskite manufacturing cost/total tandem cost. r_{PSK} is the yearly perovskite degradation rate.

Tandem development with the sequential PVD/SP method

2 Perovskite top cell development for tandems

Abstract

In this chapter, we first briefly explain the requirements that must be satisfied by the perovskite top cell in view of a tandem integration (from a processing and operational point of view). Then, we introduce the perovskite deposition method used during the first part of this thesis, *i.e.* the hybrid sequential two-step physical vapour deposition/solution-processing (PVD/SP) method. This approach is preferred in comparison to standard wet-chemical routes due to its ability to coat textured c-Si substrates. Thanks to the introduction of caesium halides during the first evaporation step and bromine in the second solution step, the perovskite band gap can be tuned from 1.6 to 1.8 eV, optimal values for a perovskite top cell pairing with c-Si. Finally, we describe the different perovskite solar cell architectures produced during this thesis (p-i-n and n-i-p configurations), the different transparent electrodes and contacts employed and discuss their advantages in tandems.[1]

---

[1]This chapter is based on the work done during several years of perovskite development at PVlab and, as a result, is the product of a common effort. I especially want to thank Dr. Jérémie Werner, who did tremendous work to develop the different perovskite configurations (n-i-p and p-i-n) and the semitransparent electrodes. Dr. Brett Kamino and Dr. Davide Sacchetto for the p-i-n configuration development and semitransparent p-i-n electrode. Concerning the hybrid two-step sequential method, I want to acknowledge Dr. Jérémie Werner, Dr. Matthias Bräuninger, Dr. Björn Niesen, Dr. Quentin Jeangros, Arnaud Walter, Peter Fiala, Dr. Fan Fu and Dr. Terry Chien-Jen Yang. I acknowledge Dr. Quentin Jeangros for the STEM and TEM images. My contribution was to develop the wide band gap Cs/FA-based perovskite with the support of the whole group. Few of the results presented here were already published by Werner *et al.* and can be found in ref.[17]

2.1   Introduction

In opposition to 4T tandems, monolithic 2T tandems require that the perovskite top cell process is made compatible with the c-Si bottom cell. As already discussed in the literature review section, the fact the SHJ solar cells are preferred as bottom cells limits the perovskite deposition temperature to $< 200°C$, or passivation will be lost due to hydrogen effusion from the a-Si:H layers.[147] This low thermal budget prevents the use of inorganic ETLs based on nanoparticles such as TiO_2 or SnO_2 as these usually require a sintering step at 450-500°C. In addition, due to the series connection, 2T tandems are strongly affected by the current matching in between both sub-cells. In order to reach high efficiencies, perfect light management through the full layer stack is hence required. Considering a bottom cell band gap of 1.1 eV (c-Si), the top cell band gap should be as high as 1.7 eV in order to reach current matching. This value could be lowered in practice to 1.6-1.65 eV as parasitic absorption in the top electrode affects the current in the perovskite top cell. Such band gaps can be achieved by incorporating bromine (and caesium) into the lattice of $MAPbI_3$ or $FAPbI_3$ (see section 1.4).

Another requirement for tandems lies in the development of a transparent top electrode. While the perovskite single-junction features a full area electrode on top of the stack, long-wavelength photons must be transmitted to the bottom cell in a tandem. The requirements needed and development of such electrodes will be presented in the section 2.2.2.

One last requirement in view of direct compatibility with standard c-Si designs is to be capable of depositing the perovskite top cell directly on the texture of c-Si to reduce reflection losses. This implies that ideally each layer should be conformally coated on top of the c-Si texture. Our aim is to develop a process flow that is independent on the size of the pyramids (up to a few microns in height), hence ruling out process flows solely based on solution-processing. The first part of this thesis focuses on a hybrid route to make the absorber, which involves a thermally evaporated lead template and a spin-coating step of an organohalides solution. Burschka and co-workers first introduced the sequential fabrication method for the perovskite absorber.[80] Their two-step method consisted in first depositing the PbI_2 precursor (by spin-coating in this case) and then converting it to the perovskite by exposure to an organohalide solution by dipping the template in a MAI solution or directly spin-coating the solution onto the PbI_2 precursor. Shortly after, a hybrid PVD/SP sequential method was introduced, where the PbI_2 template is formed by thermal evaporation and then converted to the perovskite by spin-coating a MAI solution in isopropanol.[89,90] This innovative method has several advantages over the wet-chemical route, i) the evaporation of the lead template can tolerate rough and textured surfaces, *i.e.* a textured c-Si wafer, ii) no heavy solvent such as DMF and DMSO that might prevent commercialisation due to safety concerns are used, iii) it enables the use of organic charge transport layers beneath the perovskite that would otherwise be washed away by the wet-chemical approach. In addition, spin-coating the organohalide

is easier to control compared to their thermal evaporation (see the second part of this thesis). For those reasons, the hybrid PVD/SP was selected to deposit the perovskite layer during the first part of this thesis. Due to their superior thermal stability over $MAPbI_3$, $CsFAPb(I, Br)_3$ compositions were chosen as a starting point.

2.2 Results and discussion

2.2.1 Perovskite absorbers processed with the PVD/SP method

Figure 2.1 depicts the two-step PVD/SP process used here. First, the substrates are loaded into a high vacuum chamber ($\approx 10^{-6}$ Torr, Lesker Mini SPECTROS). Then the inorganic template, either lead iodide (PbI_2) or PbI_2 combined with caesium halides (CsBr, CsI or CsCl) is thermally evaporated. The PbI_2 is evaporated at 1 Å/s, while the rate of the Cs-halide is varied (defined below in % of the evaporation rate of PbI_2). The deposition rates are controlled by quartz crystal monitors. The organohalide solution (MAI, FAI, FABr in ethanol) is then spin-coated onto the rotating inorganic template (dynamic solution dispensing). The organohalide solution interdiffuses into the PbI_2 to form the perovskite layer upon annealing performed at temperatures between 100°C and 150°C. Additional experimental information concerning the perovskite layer formation is given in the appendix A.

PbI$_2$/(CsX) evaporation

Organohalide spin-coating (MAI/FAI/FABr)

Annealing 30 min 100-150°C 0-50% RH
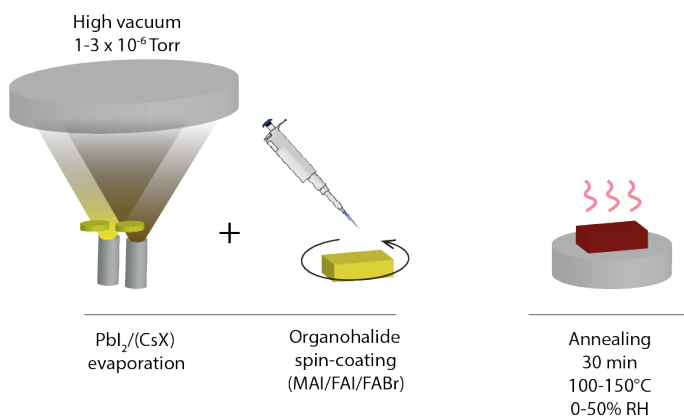
Figure 2.1 – **Sketch of the hybrid sequential two-step PVD/SP deposition method.** PVD evaporation is carried out in a Lesker Mini SPECTROS evaporation chamber. The deposition rate of the PbI_2 is 1 Å/s. The annealing is carried inside a N_2-filled glovebox for MALI cell, in air ($\approx$ 30% RH) for FA-based cells.

Most research groups directly add the caesium halide to the precursor solution by dissolving it. In our case, due to its low solubility in ethanol, the solvent used to spin-coat the organohalide solution, co-evaporation was preferred. Other solvents like DMSO, or water could not be used as they would compromise the PbI_2 film, which needs to remain conformal when using textured c-Si substrates.

Figure 2.2 displays results obtained by atomic force microscopy (AFM), UV/visible/near-infrared spectroscopy (UV/Vis/NIR) and X-ray diffraction, which characterise the morphology, optical and crystallographic properties of the perovskite films processed with this

method. Note that different absorber compositions (MAPbI$_3$, Cs$_x$FA$_{1-x}$Pb(I$_{1-y}$Br$_y$)$_3$) can be obtained by adjusting the template and solution chemistry. We observe that the CsFA-based perovskites are slightly rougher than MAPbI$_3$ perovskites (Figure 2.2a). This is especially true for perovskite layers made with only FAI as organohalide. However, by introducing a faction of FABr, smooth perovskite films can be obtained. The introduction of bromine into the film increases the band gap of the material (Figure 2.2b-c). Perovskite films produced with a molar ratio of FAI to FABr between one to two or pure FABr (denoted as 1:2 and 0:1) result in band gaps of $\approx$ 1.63 eV and $\approx$ 1.68 eV (from Tauc plots), which are well suited for tandems. Accordingly, the X-ray diffractograms of these layers show that the introduction of the smaller Br atom (in comparison to I) slightly shifts the perovskite (100) diffraction peak towards higher values, in accordance with the shrinkage of the unit cell.[148,149]
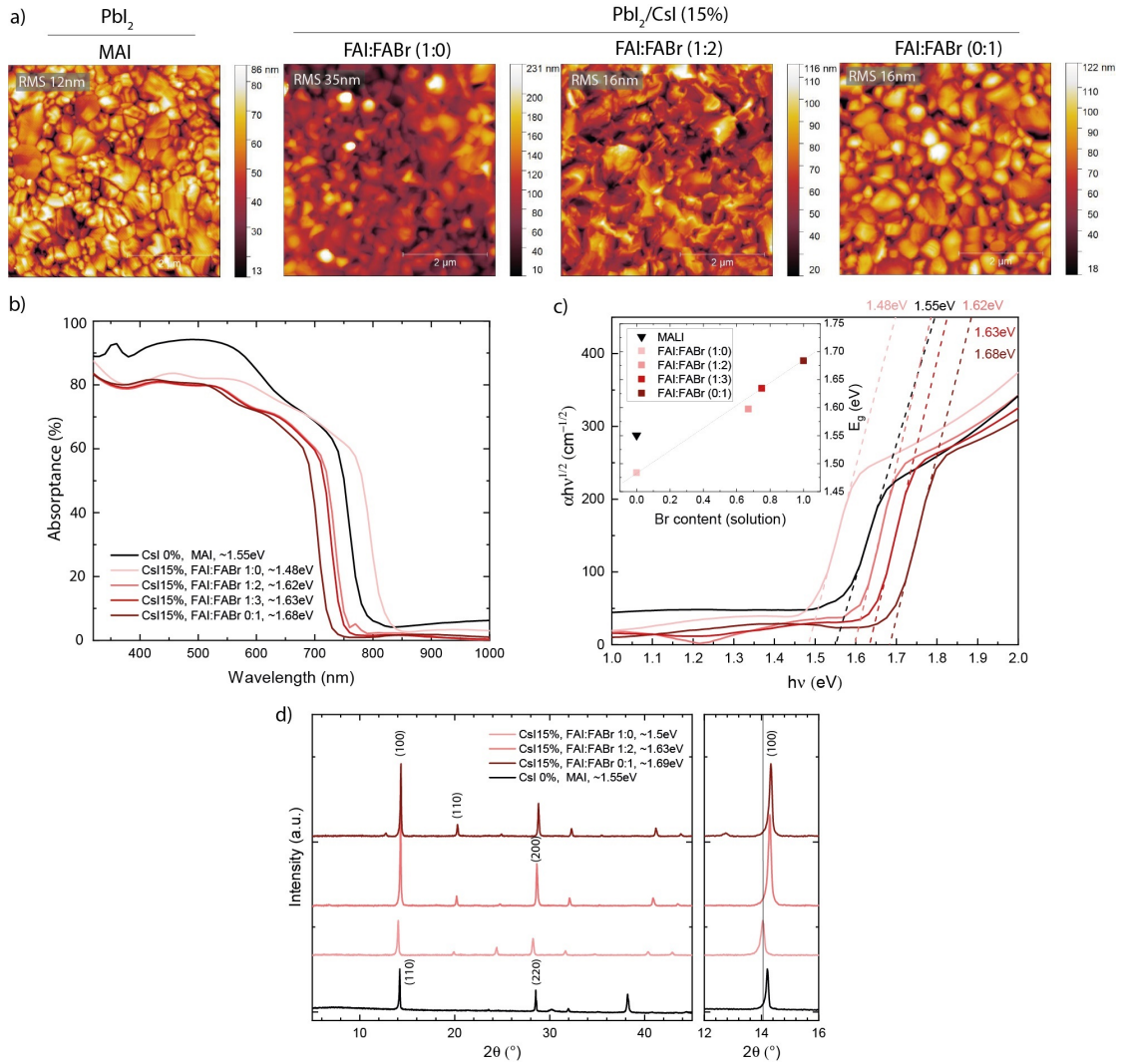

Figure 2.2 – **Film characterization of MALI and CsFA-based perovskites produced by the two-step PVD/SP method.** a) AFM top view maps, b) UV/Vis/NIR absorptance measurements, c) Tauc plot and band gap values, d) X-ray diffractograms of the different perovskite layers.

The organohalide spin-coating step plays a major role to achieve a full perovskite conversion. The concentration of the organohalide solution should be carefully chosen to avoid unconverted PbI_2 (concentration too low) from appearing or over-saturation of the film with organohalides (Figure 2.3a-b). It is worthwhile to mention that the concentration of the organohalide solution should be adapted to the Cs content introduced during the co-evaporation step (Figure 2.3c).

In addition to the organohalide concentration and Cs content, other process parameters are found to have an important impact on the interdiffusion process. The perovskite layer quality depends on process parameters such as spin-coating speed (here 3000 or 4000 rpm), relative humidity during the annealing process and the annealing duration (here 30 min vs 60 min). From the residual PbI_2 peak in the X-ray diffractograms (Figure 2.4), one can conclude that the interdiffusion process (organohalides into the lead template) is promoted by a humid environment (RH $> 50\%$[150]) and that high substrate rotation speeds (4000 rpm) leads to unconverted PbI_2 (as more solution is washed off the substrate). In addition, a prolonged annealing duration (> 60 min) may lead to the volatilisation of the organic cation, leaving behind residual PbI_2.[151]

The evaporated caesium halide precursor also plays a critical role in the resulting perovskite film (Figure 2.5a). As foreseen, increasing the Cs content (8% vs 12% CsCl) tends to blue-shift the perovskite absorption edge. This is further evidenced by the perovskite (100) diffraction peak shift towards higher angles (Figure 2.5b). In addition, it was found that replacing CsI by CsCl leads to a widening of the band gap as well. The main reason for this increase in band gap comes from the fact that higher Cs content in the layer can be achieved when using CsCl in comparison to CsI. And this Cs content remains higher even if the CsI deposition rate is superior to the one of CsCl (CsCl 8% vs CsI 15%). This comes from the fact that the amount of Cs-halide in the perovskite layer is determined by the evaporated thickness measured by the crystal quartz monitor (calibrated by profilometry). This method has the disadvantage to overlook the morphology (especially porosity) of the evaporated film. CsCl and CsBr are found to form more compact layers in comparison to CsI once evaporated (data not shown). This also means that the CsI evaporation rate is overestimated compared to the other Cs-halide precursors. Figure 2.6 displays a scanning transmission electron microscopy energy dispersive X-ray spectroscopy (STEM EDX) analysis of the cross-section of different perovskite layers produced with CsI, CsCl and CsBr precursors. Table 2.1 shows the composition of the films estimated by EDX using the Cliff Lorimer method.[152] Some I is missing due to the knock-on damage induced by the electron beam. For example, the perovskite film with 15% CsI has a Cs to Pb ratio of 0.16, while the perovskite film fabricated with 8% CsCl show a Cs to Pb ratio of 0.21. As previously reported in the literature, the presence of Cl is not observed within the perovskite fabricated with CsCl.[153] This suggests that the Cl probably escapes the film upon annealing. The broadening of the band gap is credited to the Cs increase rather than to the addition of Cl into the film.
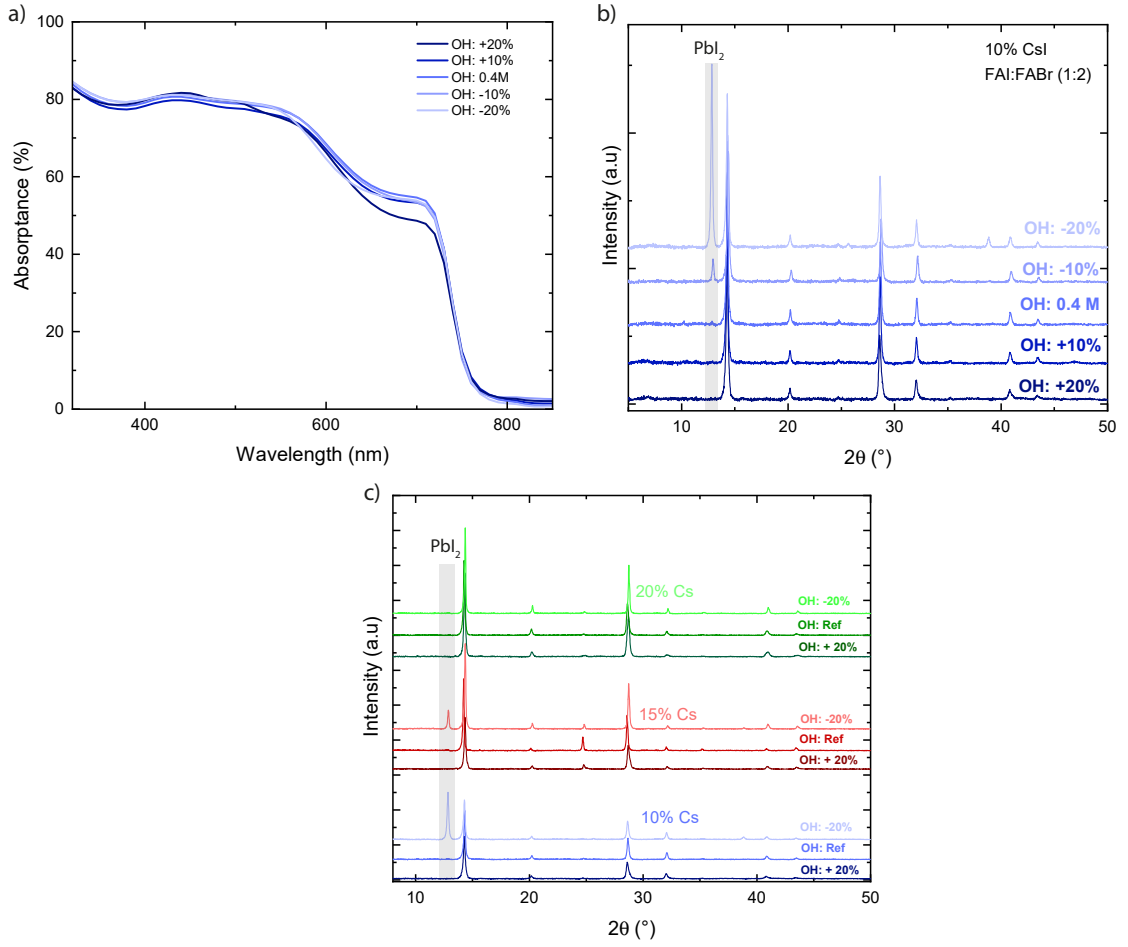
Figure 2.3 – Effects of the organohalide concentration and caesium content on the perovskite formation. a) UV/Vis/NIR absorptance of the perovskites film fabricated with different organohalide concentrations, b) corresponding X-ray diffractograms, c) X-ray diffractograms of the perovskite layer with an evaporation rate of CsI of 10, 15, 20% of that of PbI_2 and + or - 20% of organohalide in solution (reference at 0.4 M). The thickness of the PbI_2 layer is fixed to 160 nm. An organohalide FAI:FABr ratio of 1:2 is used in all cases.

Figure 2.4 – Impact of process parameters on the perovskite conversion. X-ray diffractograms of perovskite layers produced by the hybrid PVD/SP method where the spin-speed, relative humidity (RH) during annealing and annealing duration were varied. The thickness of the PbI_2 layer is fixed to 160 nm. An organohalide FAI:FABr ratio of 1:3 is used in all cases. A CsCl 8% deposition rate relative to that of PbI_2 was used in this case. The diffraction peak at 12.7° corresponds to the PbI_2 (001) diffraction.
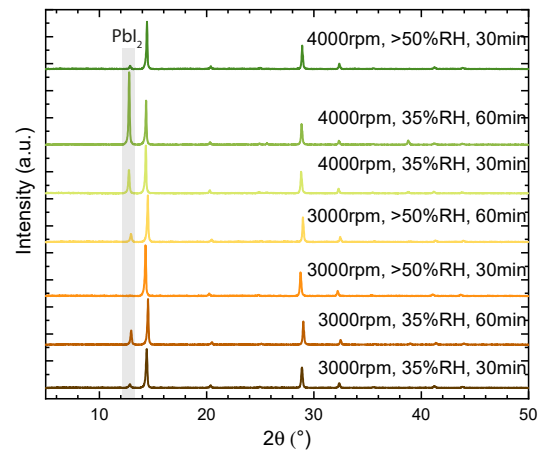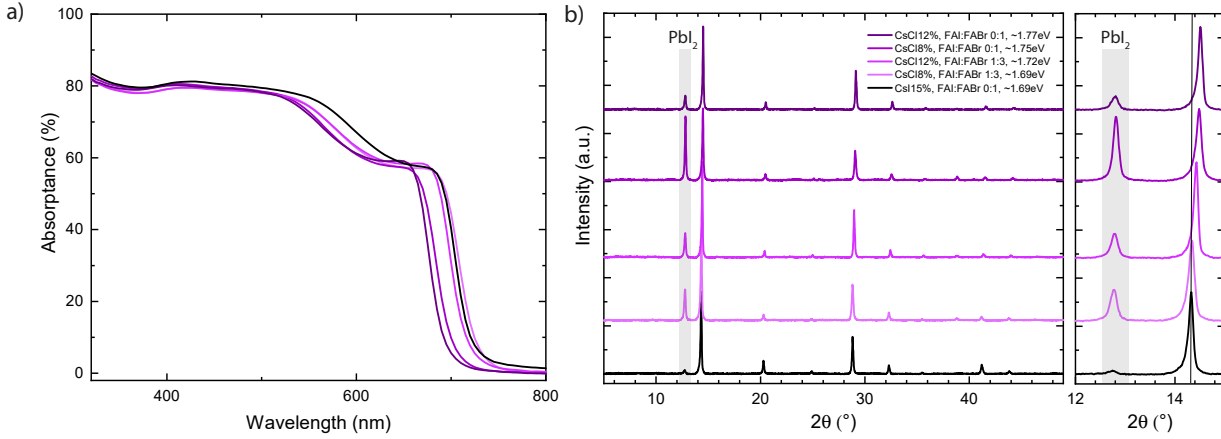
Figure 2.5 – Characterisation of perovskite layers with different Cs-halide precursors. a) UV/Vis/NIR absorptance of the perovskite films, b) corresponding X-ray diffractograms.

We can see that by varying the FABr to FAI ratio and the Cs-halide precursors, perovskite films with band gaps ranging from 1.5 eV to 1.77 eV can be obtained. Now that we have developed perovskite films with the hybrid sequential deposition method with a highly tunable band gap, we will now present the different perovskite solar cell architectures and layer stacks used during this thesis.
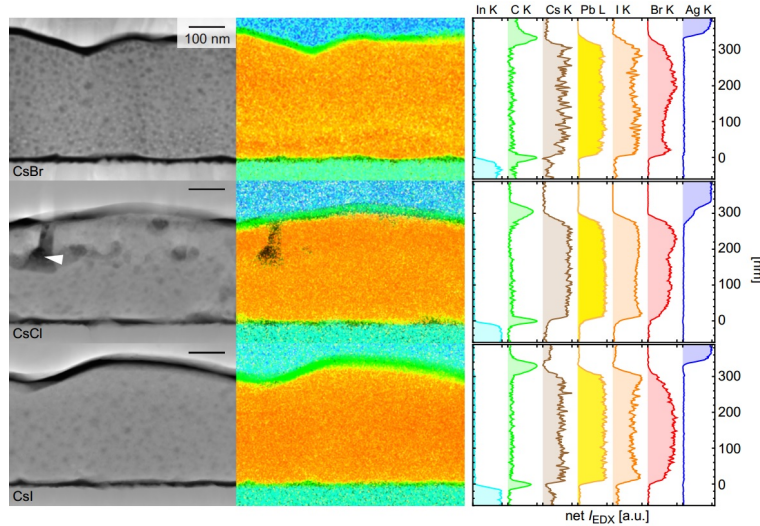
Figure 2.6 – STEM-EDX cross-section maps with different Cs-halide precursor. The different perovskite layers were fabricated using different organohalide ratios and Cs-halides evaporation rates. The cell with CsI (15%) was fabricated with a FAI:FABr ratio of 0:1. Similarly, the CsCl cell (8%) was fabricated with a FAI:FABr ratio of 0:1. An organohalide ratio of 1:2 was chosen for the CsBr cell (10%).

35

Table 2.1 – Elemental quantification (in atomic %) of the perovskite layers in Figure 2.6

Process	OH (FAI/FABr) caesium	0/1 CsI (15%)	0/1 CsCl (8%)	1/2 CsBr (10%)
at (%)	Bromine	22.8	18.3	23.8
	Iodine	36.3	38.8	36.9
	Lead	35.2	35.5	33.3
	caesium	5.7	7.4	6.1
ratio	Cs/Pb	0.16	0.21	0.18
	Br/I	0.63	0.47	0.64

2.2.2 Perovskite solar cell architectures

Perovskite solar cells in the n-i-p configuration

Historically, perovskite solar cells have been mostly deposited in the n-i-p configuration, also called the standard architecture. In that configuration, the electron transport layer (ETL) is first deposited onto the substrate (FTO, ITO, SHJ bottom cell). The perovskite is subsequently deposited, followed by the hole transport layer (HTL) and metal contact. In this case, the cell is illuminated from the ETL side. This architecture is still the most commonly used and dominates the perovskite single-junction efficiency race. The n-i-p configuration was initially adopted due to the benefit of using a TiO_2 mesoporous scaffold that allows perovskite infiltration within the scaffold and thus increases carrier collection due to the large contact area with the ETL. As already discussed in the previous section, the high temperature ($> 450°C$) required to sinter the mesoporous scaffold is not compatible with SHJ bottom cells. As a result, thermally evaporated C_{60}, which does not require any post-annealing treatments, is preferred in our case. Then the perovskite is deposited by the hybrid PVD/SP method. Spin-coated Spiro-OMeTAD is then used as HTL. For opaque devices (reference devices), gold is then thermally evaporated on top of the Spiro-OMeTAD layer.

Figure 2.7 shows a schematic view of the n-i-p perovskite solar cell fabrication process used during this thesis. For tandem applications, it is clear that the electrode needs to be as transparent as possible to prevent parasitic absorption. Various strategies have been employed as semitransparent electrodes for perovskite solar cells, such as silver nanowires,[154,155] transparent conductive oxides,[156–158] metal[159–161] or graphene-based[162] electrodes. Amongst them, transparent conductive oxides (TCOs) are the most promising as they combine high transparency over the entire spectrum, sufficient conductivity, do not introduce any shortcomings regarding stability and they are already used in the industry to make layers over large-areas at high-throughput.[47,163] Nevertheless, a direct TCO deposition by sputtering will induce some damage in the underlying perovskite/charge transport layers due to the presence of a plasma and ionic bombardment.[12,164] As a result, the presence of a buffer layer in between the charge selective layer and the TCO is usually required.[156–158,165–167] Recently, few attempts to deposit the TCO directly on

top of the charge transport layer have succeeded provided the latter is thick enough and the deposition of the TCO is made softer (conditions that may be incompatible with high throughput industrial requirements).[168,169]

Here, 10 nm of evaporated MoO_x is chosen as buffer layer to protect the spiro-OMeTAD from sputtering damage.[157,158,166] Indium zinc oxide (IZO) is preferred over conventional ITO as TCO. Indeed, IZO achieves good optoelectronic properties already in the as-deposited state, at least better than our ITO. In turn, it does not require any post-deposition annealing.[170] Further information about the development of the near-IR transparent front electrode can be found in ref.[158] STEM-EDX of the cross-section of a CsFA-based n-i-p perovskite solar cell is shown in Figure 2.8.
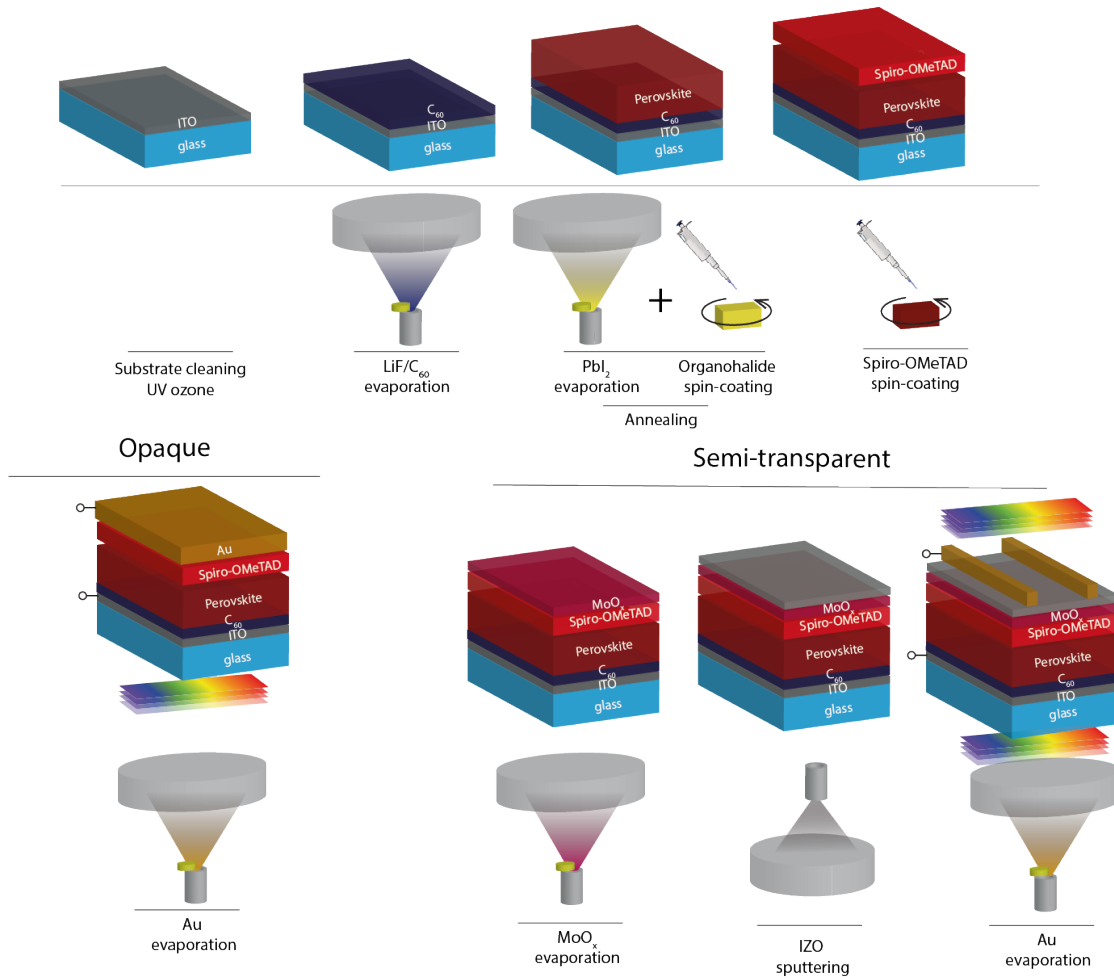
Figure 2.7 – **Schematic view of the fabrication methods used to make perovskite solar cells in the n-i-p configuration (opaque and semitransparent designs)** More information about the devices fabrication and process parameters are given in appendix A.

Figure 2.9a displays the *J-V* curves of opaque and semitransparent perovskite solar cells in the n-i-p configuration. The perovskite absorber was deposited according to the methodology explained in section 2.2.1 with the following parameters: CsI: 15%,
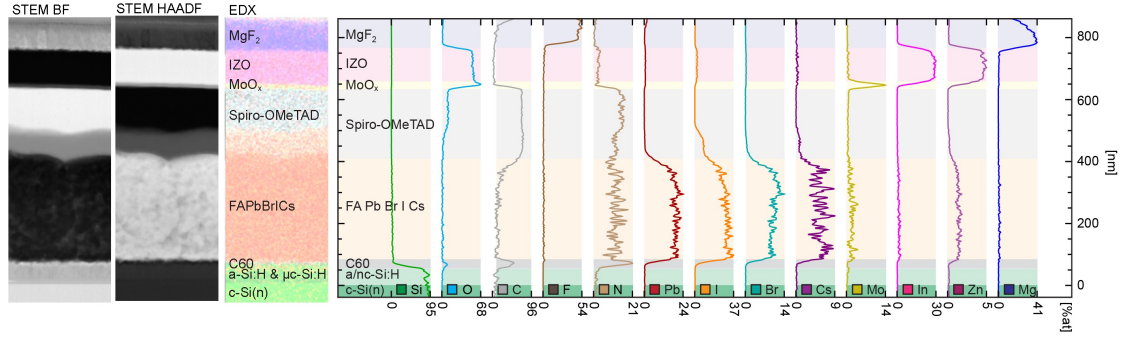
Figure 2.8 – **Cross-section EDX map of a CsFA-based cell.** STEM bright-field (BF) and high-angle angular dark-field (HAADF) images, EDX map of the CsFA-based perovskite solar cell. Corresponding EDX line profiles of the Si, C, Cs, Pb, I, F, O, Mo, In, Zn, Mg edges, shown individually after background subtraction and quantification using the Cliff Lorimer method.

FAI:FABr 1:2, $E_g \approx 1.63$ eV for a total perovskite thickness of 300 nm. In Figure 2.9a, both perovskite solar cells are measured from the glass/ETL side. One can note that similar efficiencies are reached for both the opaque and semitransparent case (PCE > 15%). The opaque design reaches a higher current density, thanks to the reflection of light on the gold electrode at the rear side of the device. One the other hand, the V_{oc} of the opaque device is often lower than the semitransparent one, likely due to the beneficial role of the MoO_x layer.[158,166] The *FF* is slightly lower in the case of the semitransparent cell, which was expected due to the resistive nature of the MoO_x layer. 8-10 nm MoO_x is found to be the best trade-off in between limiting V_{oc} losses due to sputtering damage and increased series resistance.[158,166]

Figure 2.9b shows the external quantum efficiency (EQE) of the opaque and semitransparent perovskite solar cells. One can see that, in comparison to the opaque case, the semitransparent cell (illuminated from the glass/ETL side) performs poorly (loss of ≈ 1 mA cm^{-2}) in the 650-800 nm region due to the finite thickness of the perovskite layer. For opaque devices light reaching the back of the device is reflected back to the perovskite layer, thus increasing the absorption probability. The EQE curve of the semitransparent perovskite solar cell illuminated from the TCO/HTL side (equivalent to the top illumination in a tandem in n-i-p configuration) is also displayed in Figure 2.9b. One can note that a limited current density of ≈ 14.5 mA cm^{-2} is obtained. The main reason is that significant amount of parasitic absorption (accounting for 2-2.5 mA cm^{-2}) occurs in the UV/blue (320-450 nm) region of the spectrum due to the thick spiro-OMeTAD layer.[158] To increase current density, it is absolutely essential to replace the spiro-OMeTAD layer with a more transparent HTL. However, few viable options exist at this stage. The layer must exhibit suitable optoelectronic properties at the required thickness, has to be deposited at low temperature with deposition techniques compatible with textured substrates and must be thin enough to prevent parasitic absorption. Recently progress has been made in that regard when Raiford and co-workers developed a n-i-p semitransparent perovskite solar cell by replacing the spiro-OMeTAD by a thin evaporated

2,2',7,7'-tetra(N,N-di-tolyl)amino-9,9-spiro-bifluorene (Spiro-TTB) layer and a vanadium oxide buffer layer.[113] But the option taken by most research groups, including us, to lower parasitic absorption was to invert the polarity of the perovskite cell to the p-i-n configuration. This switch provides more flexibility in terms of HTL choice.
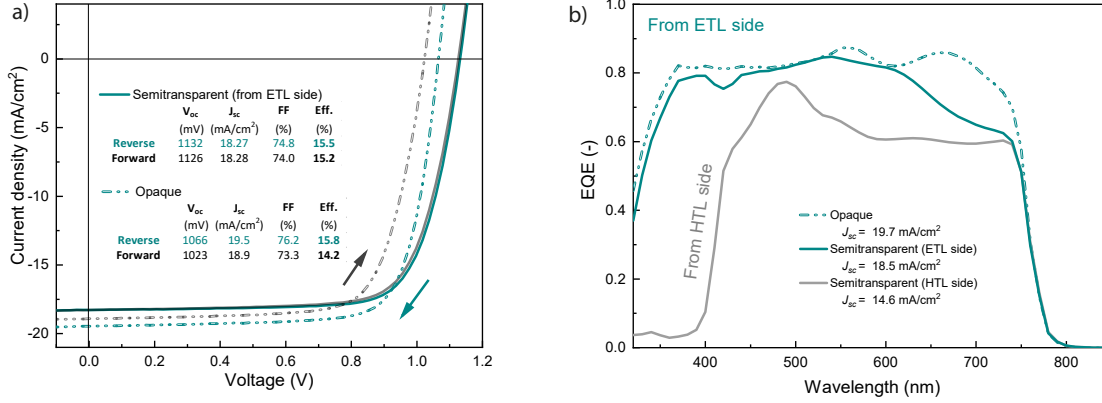

Figure 2.9 – **Electrical characteristics of n-i-p perovskite single-junctions.** a) *J-V* curves of opaque and semitransparent perovskite solar cells. The cells are illuminated from the glass/ETL side, b) corresponding EQE spectra. The semitransparent cell is illuminated from both the ETL and HTL sides. All perovskites solar cells presented here were produced with the hybrid sequential deposition method reported in the section 2.2.1 (CsI: 15%, FAI:FABr 1:2, $E_g \approx 1.63$ eV for a perovskite thickness of 300 nm).

Perovskite solar cells in the p-i-n configuration

Perovskite solar cells fabricated in the p-i-n configuration have recently gained interest, especially in the field of perovskite/c-Si tandems due to the possibility of using thin evaporated ETLs such as C_{60}.[10,108,116,124,132] Here we use thermally evaporated Spiro-TTB (17 nm) as HTL below the perovskite. This layer was chosen due to its suitable band alignment with the perovskite valence band onset and for its ability to be evaporated. The perovskite is then deposited on top of that layer using the two-step PVD/SP method (section 2.2.1). 1 nm LiF and 20 nm C_{60} are thermally evaporated on top of the perovskite layer. The thin layer of LiF is found to reduce the surface recombination rate compared to the perovskite/C_{60} interface.[124,171] For opaque p-i-n cells, 120 nm of silver is then subsequently evaporated on top of the C_{60} layer. For the semitransparent perovskite solar cells, we use a similar transparent electrode to that developed by Bush *et al.* which consists in a C_{60}/SnO_2/TCO stack. Here, SnO_2 deposited by ALD acts as a n-type buffer layer to protect the perovskite cell against sputtering damage. Similarly as in the n-i-p configuration, sputtered IZO is used as TCO for both semitransparent single-junction cells and perovskite/c-Si 2T tandems. Figure 2.10 presents a schematic representation of the fabrication procedure for p-i-n opaque and semitransparent perovskite cells. Additional information regarding p-i-n devices fabrication is provided in the appendix A.

Figure 2.11a displays the *J-V* curves of the opaque and semitransparent perovskite solar cells in the p-i-n configuration. Here again, the perovskite was deposited according to
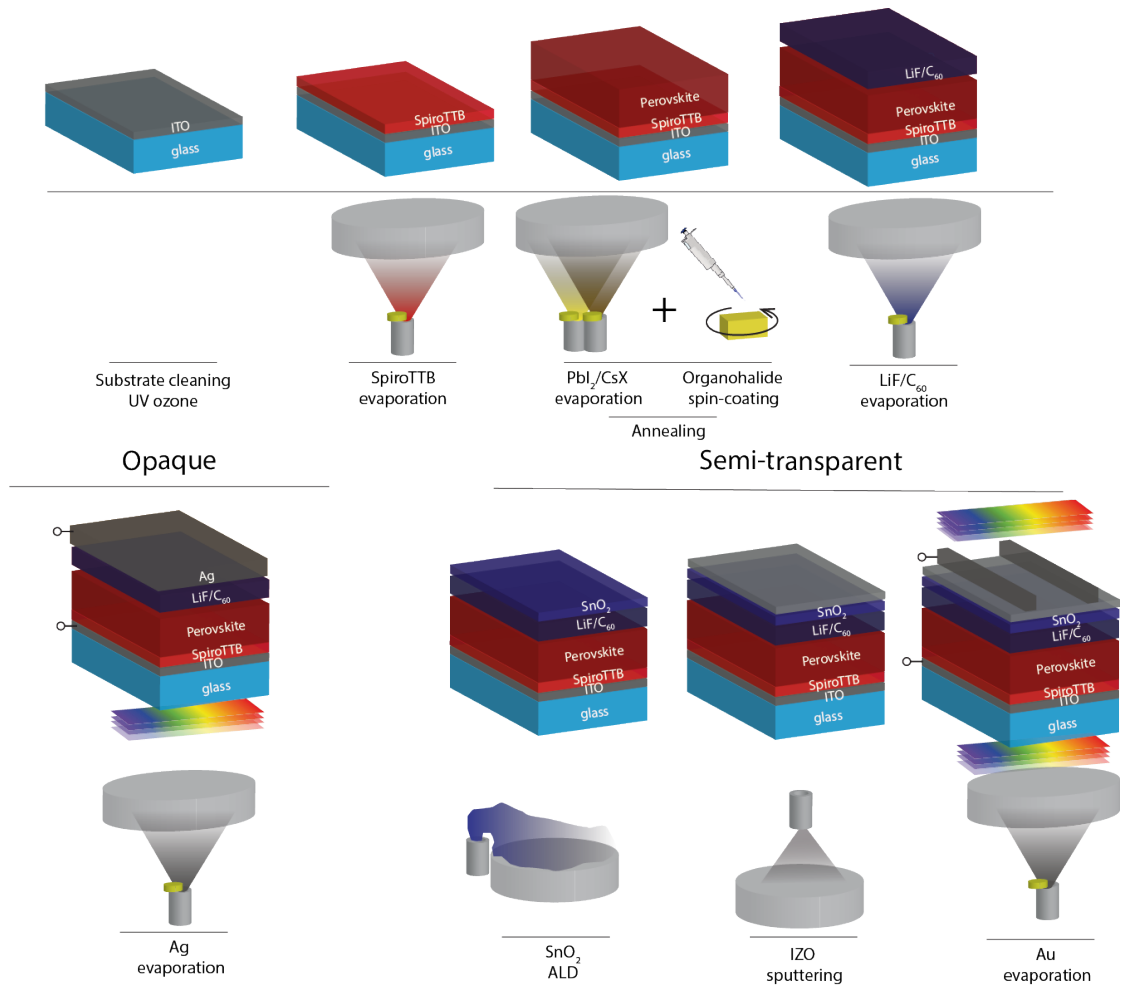
Figure 2.10 – **Schematic view of the fabrication route of perovskite solar cells made in the p-i-n configuration.** More information about device fabrication and process parameters are given in appendix A.

the methodology explained in section 2.2.1 (CsI: 15%, FAI:FABr 1:2, $E_g \approx 1.63$ eV for a total perovskite thickness of 300 nm). As before, the semitransparent cell has a lower current density due to the un-absorbed red part of the spectrum. These losses could be regained by increasing the thickness of the perovskite layer. This will be discussed in the chapter 4. In addition to losses in J_{sc}, few losses are observed in FF and V_{oc} between semitransparent and opaque designs. This is attributed to the increased resistivity due to the introduction of the SnO_2 and IZO layers. In addition, a thin evaporated layer of TmPyPb was found to be beneficial once introduced in between the C_{60} and Ag electrode for the opaque case.[172] This layer creates a permanent dipole moment that improves the interfacial energy level alignment with the perovskite layer and facilitates electron extraction. The presence of this layer (used only in opaque cells) slightly improved the FF and V_{oc} of the perovskite solar cells. Figure 2.6 shows cross-section of such devices.

Figure 2.11b represents the EQE of the cells. The semitransparent perovskite cell is illuminated from either directions (from the glass/HTL or TCO/ETL side). One can see that, this p-i-n cell design, even if the integrated current density is still lower if measured from the ETL side, is less prone to parasitic absorption compared to n-i-p cells (Figure 2.9). While ≈ 3 mA cm^{-2} is lost by switching from superstrate to substrate illuminations in the n-i-p cells, p-i-n cells lose ≈ 2 mA cm^{-2}. Figure 2.12 displays the J-V measurements of a p-i-n semitransparent perovskite solar cell measured with superstrate and substrate illuminations. One can see that the electrical characteristics of the cell do not depend on the illumination direction (except for the J_{sc} due to differences in parasitic absorption).
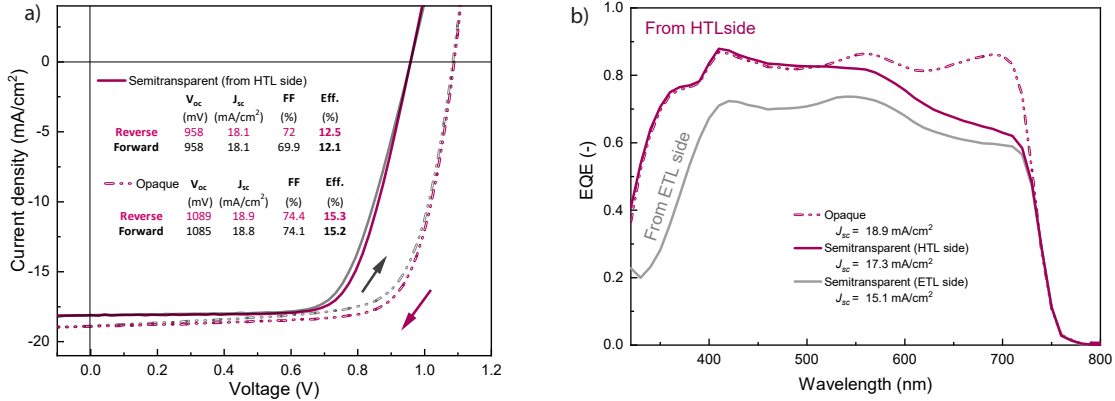
Figure 2.11 – **Electrical characteristics of the p-i-n perovskite single-junctions.** a) J-V curves of opaque and semitransparent perovskite solar cells. The cells are illuminated from the glass/ETL side, b) corresponding EQE spectra. The semitransparent cell is illuminated from either the HTL or ETL side. All perovskites solar cells presented here were produced with the hybrid sequential deposition methods reported in the section 2.2.1 (CsI: 15%, FAI:FABr 1:2, $E_g \approx 1.63$ eV for a perovskite thickness of 300 nm).

2.3   Conclusion

In this chapter, the different perovskite top cell requirements for their implementation in a tandem with a c-Si bottom cell are discussed. In the perspective of growing the perovskite

Figure 2.12 – **Substrate vs superstrate _J-V_ curves of a p-i-n perovskite solar cell.** The perovskites solar cell was produced with the hybrid sequential deposition methods reported in the section 2.2.1 (CsBr: 10%, FAI:FABr 2:1, $E_g \approx 1.6$ eV for a perovskite thickness of 300 nm).
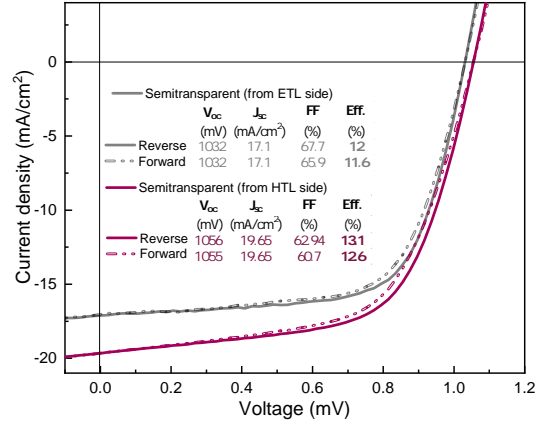
on top of a textured c-Si bottom cell, processes based solely on solution-processing should be avoided. As a result, both the perovskite and charge transport layers were deposited here (in part) by vapour-based techniques. A hybrid two-step PVD/SP method is used to deposit the perovskite layer. First, a lead-halide (with or without Cs halide) template is thermally evaporated in a high vacuum system. Subsequently, a solution of organohalide dissolved in ethanol is spin-coated on this template, before an annealing step crystallises the perovskite absorber. By introducing Cs halides by co-evaporation with lead halide and spin-coating a mixture of FABr and FAI, perovskite layers with band gaps from 1.5 to 1.77 eV are produced, optimal values for a top cell in a tandem with c-Si. Perovskite solar cells were fabricated first with the n-i-p polarity and then the p-i-n one. For n-i-p cells, thermally evaporated C_{60} is used as the ETL, whereas spin-coated spiro-OMeTAD is used as HTL. Semitransparent n-i-p perovskite solar cell using MoO_x as a buffer layer to protect the underlying layer from sputtering damages are also described. This architecture will be used as the top cell of a tandem in the chapter 3. Spiro-OMeTAD layer is the main bottleneck of this architecture as 2-3 mA cm^{-2} are lost due to the parasitic absorption once measured in substrate configuration (HTL sunwards). In addition, this layer is deposited by spin-coating, which prevents the use of a textured c-Si bottom cell in tandems. As a result, an inverted p-i-n architecture is developed to mitigate these issues. Thermally evaporated spiro-TTB replaces spiro-OMeTAD, whereas $LiF/C_{60}/SnO_2/IZO$ is used as the ETL contact and top electrode. This cell design exhibits less optical losses at its front electrode, paving the way towards the deposition of conformal perovskite top cells on textured c-Si cells (chapter 4).

3 Nanocrystalline recombination junction for tandems

Abstract

The recombination junction that connects the sub-cells of a tandem plays a major role in its performance. This layer enables the carriers of opposite charge from each sub-cell to recombine with each other. This layer should have i) a high carrier selectivity for both types of carriers, ii) a suitable conductivity to prevent increased series resistance while still mitigating the impact of shunts that may be present in the perovskite top cell, iii) a high transparency in the near-infrared region to prevent parasitic absorption of photons that should be absorbed in the c-Si cell. Current monolithic perovskite/c-Si tandem designs rely mostly on TCOs as recombination layer, which lead to optical losses in the infrared part of the spectrum and reduced shunt resistance. We develop a recombination junction based on nanocrystalline silicon layers to mitigate these losses. When employed in monolithic perovskite/SHJ tandem cells with a planar front side, this junction is found to increase the bottom cell photocurrent by more than 1 mA cm^{-2}. In combination with a caesium-based perovskite top cell, this leads to tandem cell power-conversion efficiencies of up to 22.7% obtained from J-V measurements and steady-state efficiencies of up to 22.0% during maximum power-point tracking. These values were, to the best of our knowledge, the second-highest PCE reported for such tandems at the time of fabrication (2017) and the highest using a perovskite in the n-i-p configuration. In addition, thanks to its low conductivity mitigating the impact of shunts, the nanocrystalline silicon recombination junction enables up-scaling the tandem active area, resulting in a 12.96 cm^2 cell with a steady-state efficiency of 18%. This was the first demonstration of a perovskite/c-Si tandem cell with an area significantly larger than 1 cm^2.[1]

3.1   Introduction

A crucial element of any 2T tandem cell is the intermediate recombination connecting both sub-cells in series. This junction should enable carriers collected in one sub-cell to recombine with carriers of opposite charge collected in the other sub-cell without introducing electrical or optical losses. So far, mainly TCOs have been used as recombination layer in the fabrication of perovskite-based 2T tandems.[93,105,106,108,117] While in principle effective, this approach suffers from several drawbacks: parasitic absorption of wavelengths above 800 nm due to free-carrier absorption in the TCO,[163] poor refractive index matching with silicon causing enhanced reflection losses at the TCO/silicon interface,[173] and usually high lateral conductivity promoting shunt paths through the top cell.[174,175]

A strategy to effectively mitigate TCO-related optical losses is to integrate a p+/n+ recombination junction, as widely used in III-IV semiconductor and thin-film silicon tandem solar cells.[176–178] A first demonstration of a silicon-based recombination junction for perovskite/silicon tandem cells was made by Mailoa *et al.*, who used a diffused-junction c-Si solar cell, although with a limited efficiency of 13.7%.[104] A particularly interesting low-temperature ($< 200°$C) approach lies in using hydrogenated nanocrystalline silicon (nc-Si:H) deposited by plasma-enhanced chemical vapour deposition (PECVD) employing silane gas with high hydrogen dilution.[178] By adding either trimethylboron or phosphine to the silane/hydrogen mixture in the reactor, highly doped nc-Si:H can be obtained,[179] a requirement for recombination junctions exhibiting low resistance and narrow energy barrier widths to enable tunnelling of charges. Such nc-Si:H layers have recently been used as charge carrier selective contact in high-efficiency SHJ solar cells in both sides-contacted and back-contacted configurations.[180–182] Building on this knowledge, this chapter presents a nc-Si:H recombination junction for monolithic perovskite/SHJ tandem cells, which reduces reflection and parasitic absorption losses in comparison to commonly used TCO recombination layers.

3.2   Results and discussion

3.2.1   Device fabrication

Monolithic perovskite/SHJ tandem cells with nc-Si:H recombination junctions were fabricated with a layer stack as shown in Figure 3.1a. A rear-side textured SHJ bottom cell in the front-emitter configuration (*i.e.*, with the hole-collecting side facing sunwards) was used.[117] More information regarding device fabrication is given in the appendix A. On top of the polished front side of the bottom cell, the p+/n+ nc-Si:H recombination layer stack with a crystallinity of 17.7%, as obtained from Raman spectroscopy (Figure 3.2), was deposited by PECVD. High-resolution transmission electron microscopy (HRTEM) micrographs of the recombination junction shown in Figure 3.1b confirm the presence of

crystal grains in the nc-Si:H layers. Furthermore, coloured inverse fast Fourier transforms (iFFT) generated from several Si (111) and (022) crystalline orientations demonstrate the presence of epitaxial growth between the p- and n-doped regions of the recombination junction, evidenced by crystals spanning across the nc-Si:H(p+)/nc-Si:H(n+) interface (marked by arrowheads in Figure 3.1b). The position of this interface is inferred from the EDX map (Figure 3.1b), which is presented alongside the corresponding STEM high-angle annular dark-field (HAADF) micrograph. These STEM and TEM images of Figure 3.1c indicate a recombination layer thickness of $\approx$ 50 nm (nc-Si:H(p+) $\approx$ 25 nm, nc-Si:H(n+) $\approx$ 25 nm).

The n-i-p perovskite top cell was deposited directly onto the nc-Si:H recombination junction and featured a C_{60} electron transport layer, a perovskite absorber layer fabricated with the hybrid PVD/SP method introduced in chapter 2, and a Li-doped spiro-OMeTAD hole transport layer. In this case, the perovskite absorber layer was produced by co-evaporating PbI_2 and CsI with deposition rates of 1 Å/s and 0.1 Å/s, respectively. Then, the organohalide solution was spin-coated on top of the CsI/PbI_2 template and contained either pure MAI or a mixture of FAI and FABr to obtain either $Cs_xMA_{1-x}PbI_3$ or $Cs_xFA_{1-x}PbI(_{1-y}Br_y)_3$ perovskites. The tandem cells were completed by a $MoOx$/indium zinc oxide (IZO) transparent front electrode, Au fingers to contact the cells, and a MgF_2 anti-reflective layer.

To gain more information on the incorporation of caesium into the perovskite layer, EDX of a $Cs_xMA_{1-x}PbI_3$ layer was performed in combination with STEM (Figure 3.1c). The background-subtracted maps of the Cs K, Pb L and I K edges suggest a uniform distribution of these elements within the perovskite layer (Figure 3.1c) and a Cs:Pb atomic concentration ratio of 0.18 is obtained (in line with table 2.1). It should be mentioned that some iodide diffused into the hole transport layer during the processing as marked by an arrowhead in Figure 3.1b.[183] Iodine diffusion is thought to occur already during processing, where excess iodine present on the surface may redissolve during spiro-OMeTAD spin-coating (dissolved in chlorobenzene). The X-ray diffraction (XRD) pattern confirms the formation of a perovskite phase for both perovskite compositions, $Cs_xMA_{1-x}PbI_3$ or $Cs_xFA_{1-x}PbI(_{1-y}Br_y)_3$ (Figure B.1).

The monolithic tandem solar cells with the nc-Si:H recombination junction and a $Cs_{0.19}MA_{0.81}PbI_3$ perovskite top cell reached an efficiency of up to 22.7% on an area of 0.25 cm^2 and 21.7% on a larger scale of 1.43 cm^2, as obtained from J-V measurements. Steady-state efficiencies of 22.0% and 21.2%, were achieved during maximum power-point tracking for 1000 s, respectively (Figure 3.3a,b). Moreover, the J-V curves exhibited negligible hysteresis. These tandem cells showed a high V_{oc} of > 1750 mV, which demonstrates the capability of the nc-Si:H junction to efficiently recombine electrons from the top cell with holes from the bottom cell. FF values are comparable to the ones obtained with a TCO recombination layer reported earlier.[106] This suggests that the presence of the nc-Si:H stack does not introduce significant electrical losses.[181] A rear-side textured
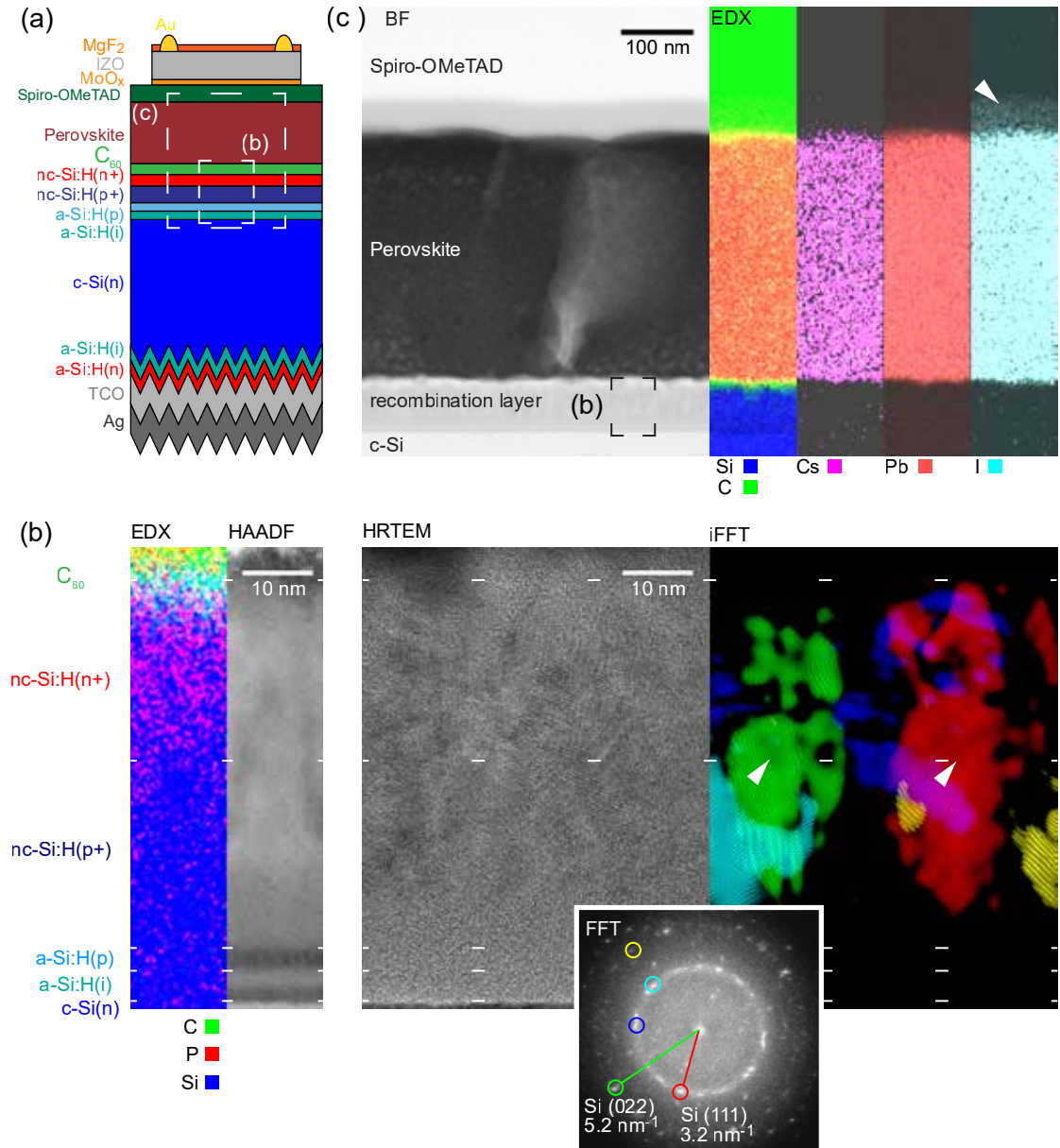
Figure 3.1 – Perovskite/c-Si tandem with a nc-Si:H recombination junction a) Schematic view of the perovskite/SHJ monolithic tandem cell with a nc-Si:H recombination junction, b) EDX map and corresponding STEM HAADF image of the recombination junction, which show the position of the different interfaces, HRTEM micrograph of the recombination junction, corresponding FFT and superposition of coloured inverse FFTs computed from selected Si (111) and (022) reflections (pseudo dark-field image), c) STEM BF image of a cross-section of the perovskite cell and corresponding EDX maps of Si K, C K, Cs K, Pb L, I K edges, either combined in the same image or, for the inorganic perovskite elements, shown individually after background subtraction.
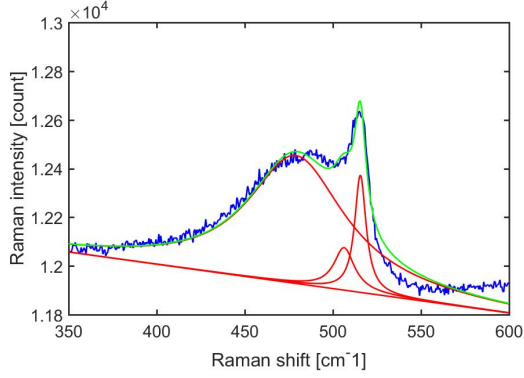
Figure 3.2 – **Raman spectrum of the nc-Si:H p-n recombination junction deposited on a glass substrate**. The layer stack is glass/a-Si:H(i)/a-Si:H(p)/nc-Si:H(p+)/nc-Si:H(n+). The crystalline fraction of the full amorphous/nanocrystalline stack was extracted by deconvoluting the Raman shift by three Lorentzian curves centred at 480 cm^{-1} for the amorphous peak, at 519 cm^{-1} and at 510 cm^{-1} for the crystalline peak. The crystallinity fraction is defined as the ratio between the area below the curve of the crystalline peaks (at 510 cm^{-1} and 519 cm^{-1}) over the total area below the crystalline and amorphous peaks.

single-junction SHJ solar cell reference for the bottom cell, comprising the nc-Si:H layer stack at the front, shows an efficiency of 16.45% with a (V_{oc}) of 693 mV for an aperture area of 0.25 cm^2 (Figure B.2). The EQEs of these tandem cells demonstrate a current mismatch of more than 1 mA cm^{-2} between the sub-cells (Figure 3.3c), with the tandem cell photocurrent being limited by the top cell.

In an ideal monolithic tandem device with a c-Si bottom cell, the top cell band gap should be $\approx$ 1.75 eV to reach current matching.[184, 185] Here, the Cs$_{0.19}$MA$_{0.81}$PbI$_3$ perovskite band gap is 1.58 eV, well below that optimal value. As already discussed in chapter 2, one main limitation of the top cell current is linked to parasitic absorption in the spiro-OMeTAD layer (Figures B.3b and B.4b). This loss can be avoided by adopting an inverted p-i-n perovskite configuration or by using a thinner HTL as it will be shown in the next chapter.[108, 113] As demonstrated for the case of interdigitated back-contacted SHJ cells,[181] the nc-Si:H recombination layer polarity can be inverted to form an a-Si:H(i)/a-Si:H(n)/nc-Si:H(n+)/nc-Si:H(p+) stack without losing its functionality, hence making this concept compatible with either polarity (see chapter 4).

To demonstrate the versatility of the nc-Si:H junction, tandem devices with a top cell based on a Cs$_{0.19}$FA$_{0.81}$PbI($_{0.78}$Br$_{0.22}$)$_3$ perovskite material were fabricated using the sequential deposition protocol described in chapter 2. XRD measurements confirm the presence of the perovskite phase (Figure B.1). This absorber has the advantage of being more moisture- and temperature-stable compared to MA-based perovskite materials.[186, 187] This Cs$_{0.19}$FA$_{0.81}$PbI($_{0.78}$Br$_{0.22}$)$_3$ composition (confirmed by Rutherford backscattering spectrometry (RBS)) has a band gap of 1.63 eV, which can be readily tuned to higher values by increasing the Br content.[188] With this absorber and the nc-Si:H recombination layer, a monolithic tandem efficiency of 20.5% is obtained with an aperture area of 0.25 cm^2 (Figure 3.4). Semitransparent perovskite single-junction J-V curves and EQE measurement from the glass and spiro-OMeTAD side are displayed in Figure B.4.

47
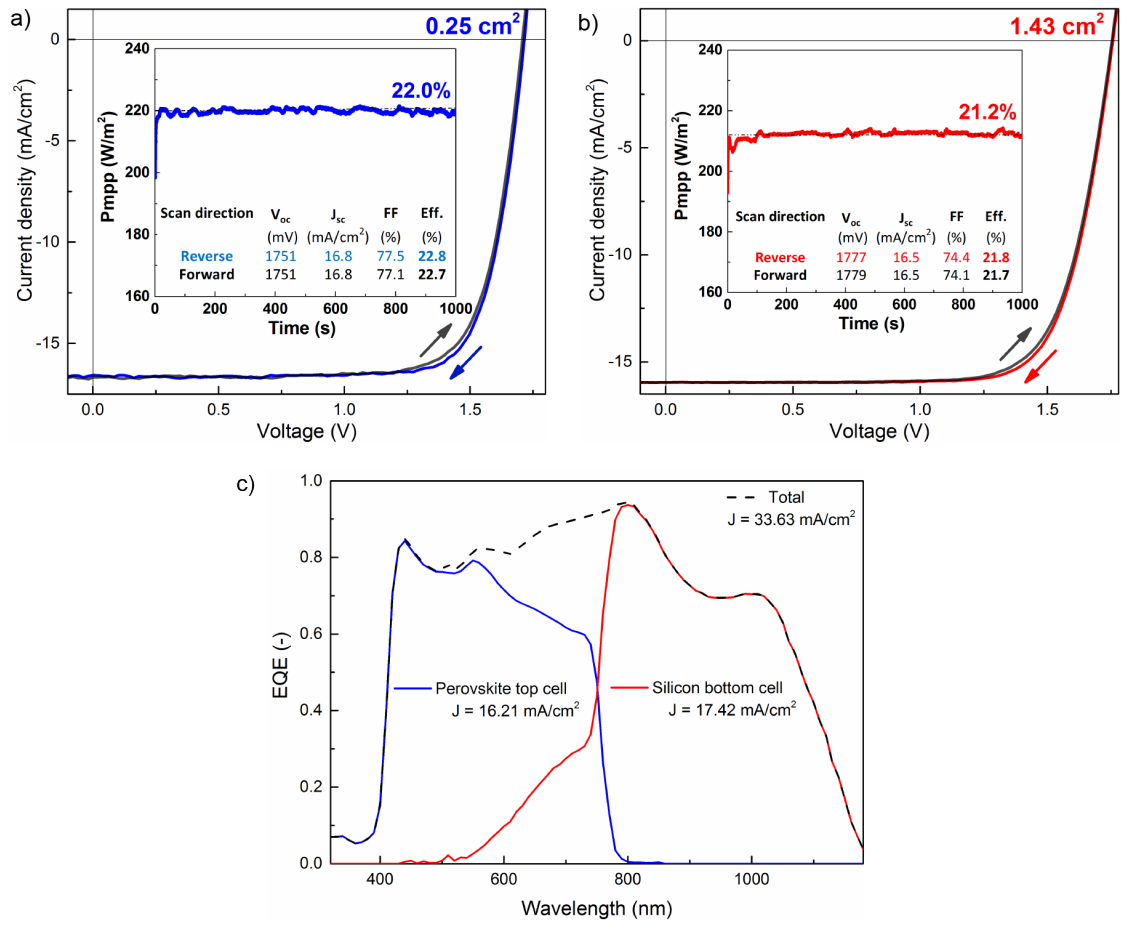
Figure 3.3 – **Solar cell characterisation of monolithic perovskite/SHJ tandem cells with a nc-Si:H recombination junction.** *J-V* curves of perovskite/SHJ monolithic tandem cells (perovskite composition: $Cs_{0.19}MA_{0.81}PbI_3$ with a) 0.25 cm^2 and b) 1.43 cm^2 aperture area. c) EQE of the 0.25 cm^2 tandem cell.
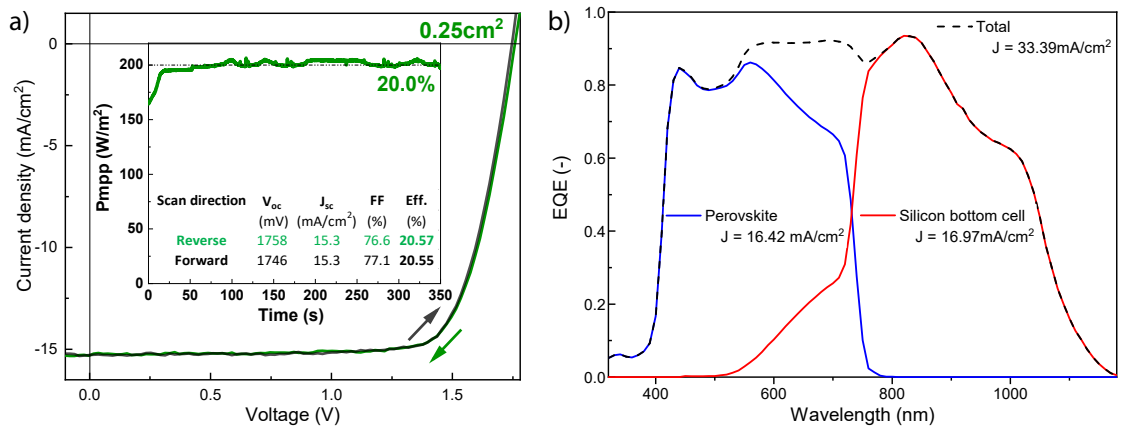
Figure 3.4 – **$Cs_{0.19}FA_{0.81}PbI(_{0.78}Br_{0.22})_3$/SHJ tandem cell with a nc-Si:H recombination junction.** a) *J-V* curve with an aperture area of 0.25 cm^2. b) Corresponding external quantum efficiency (EQE) spectra.

3.2.2 Optical benefits of using the nc-Si:H recombination junction

Next, we compare the optical performance of the nc-Si:H junction to an ITO recombination layer. The band gap of nc-Si:H is considerably smaller than that of ITO, leading to absorption in the blue part of the spectrum (Figure 3.5a). This absorption has, however, only a very limited effect on the tandem cell performance as the top perovskite cell absorbs all the light up to wavelengths of ≈ 550 nm. In the near-infrared region (> 800 nm), the silicon recombination junction absorbs less light than its ITO counterpart, which is prone to free carrier absorption, making more photons available to the bottom cell.

To assess the effect of the presence of a TCO between both sub-cells, tandem cells with the $Cs_{0.19}FA_{0.81}PbI_{(0.78}Br_{0.22})_3$ perovskite top cell and the nc-Si:H recombination junction were fabricated, either with or without an additional 40 nm-thick ITO layer sputtered onto the nc-Si:H junction. The reflectance spectra of these tandem cells, presented in Figure 3.5b, show that the reflectance peak at wavelengths of 700-900 nm is almost completely suppressed when the TCO is absent (leading to a reflectance $< 2.5\%$ without ITO). In addition, without the intermediate TCO layer, the reflectance is also strongly reduced at wavelengths > 1000 nm. These results can be explained by the fact that nc-Si:H and c-Si have nearly identical refractive indices ($n_{c-Si} = 3.6$–3.7 at 800 nm), as compared to the considerably lower value of ITO ($n_{ITO} = 1.6$–2 at 800 nm, depending on its doping).[49,189] As a result of the better index matching, the nc-Si:H recombination junction mitigates reflection at the sub-cell interface and thus increases light transmittance to the SHJ bottom cell.
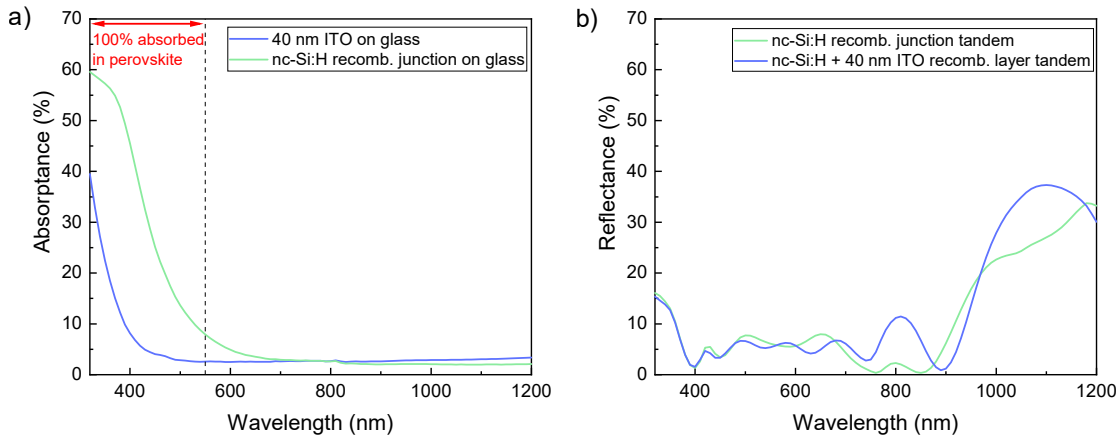
Figure 3.5 – **Optical properties of the nc-Si:H and ITO recombination junctions.** a) Absorptance of a 40 nm-thick ITO layer and the nc-Si:H recombination junction deposited on glass, b) Reflectance of monolithic $Cs_{0.19}FA_{0.81}PbI_{(0.78}Br_{0.22})_3$/SHJ tandem cells with the nc-Si:H junction, either with or without an additional 40 nm-thick ITO layer deposited on the nc-Si:H stack.

EQE spectra shown in Figure 3.6a confirm these observations and demonstrate the impact of the TCO interlayer on the current distribution between the sub-cells. The EQE of the SHJ bottom cell is considerably higher at wavelengths of 750-950 nm without the ITO layer, resulting in an increase in current density by more than 1 mA cm^{-2}. In contrast,

the current generated in the perovskite top cell is virtually unaffected by the presence of the ITO layer. It is noteworthy to mention that the shape of the bottom cell EQE spectrum strongly depends on the exact thickness of all layers present in the tandem device, hence the exact current gain in the bottom cell varies.[106] Nevertheless, the current gain of > 1 mA cm^{-2} was reproducible, also with other TCOs (Figure 3.6b). These results confirm that using a nc-Si:H recombination junction can significantly improve the optical performance of monolithic tandems using front-side-polished c-Si bottom cells.

Figure 3.6 – **Comparison between perovskite/SHJ tandems with and without ITO on the nc-Si:H junction.** a) EQE spectra of Cs$_{0.19}$FA$_{0.81}$PbI$_{(0.78}$Br$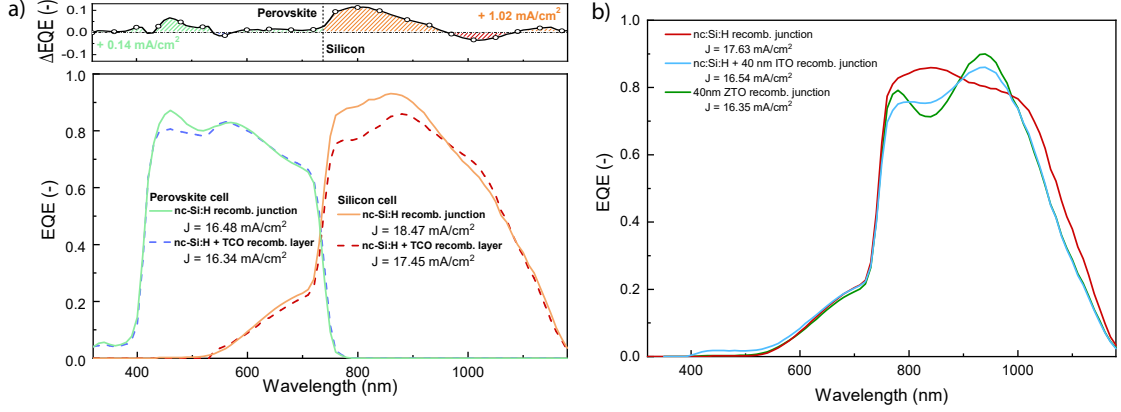_{0.22})_3$/SHJ solar cells with a nc-Si:H recombination junction, either with or without an additional 40 nm-thick ITO layer deposited on it, b) EQE spectra of SHJ bottom cells made with double-side-polished wafers and with a layer stack of either nc-Si:H, nc-Si:H + 40 nm ITO, or 40 nm of zin tin oxide (ZTO) deposited at their front.

3.2.3   Electrical benefits of using the nc-Si:H recombination junction

In addition to optical advantages, the nc-Si:H recombination junction features a lower conductivity compared to TCOs.[181] In monolithic tandem cells, this lower conductivity is beneficial as it reduces possible shunt paths through pinholes or defects present in the perovskite top cell.[14,174] J-V measurements at several light intensities of the perovskite/SHJ tandems with and without a TCO intermediate layer support this hypothesis (Figure 3.7). At one sun, both cells show a high V_{oc}. However, under reduced light intensity, the presence of the ITO layer with a high lateral conductivity leads to strong losses in V_{oc}, indicating an increased contribution of shunts. The tandem cell without ITO retains a high V_{oc} even at low illumination.

The high shunt resistance induced by the nc-Si:H recombination junction is an essential ingredient to enable efficient large-area perovskite/SHJ monolithic tandems. To demonstrate the up-scalability of the tandem cells presented here, a Cs$_{0.19}$FA$_{0.81}$PbI$_{(0.78}$Br$_{0.22})_3$ perovskite top cell was deposited on a 5 x 5 cm^2 SHJ bottom cell with the nc-Si:H junction. With an aperture area of 12.96 cm^2, an efficiency of 18% during maximum power-point tracking is obtained (Figure 3.8). Figure 3.9 shows a picture of the large-area monolithic perovskite/SHJ tandem. The discrepancy in efficiency between the large-area
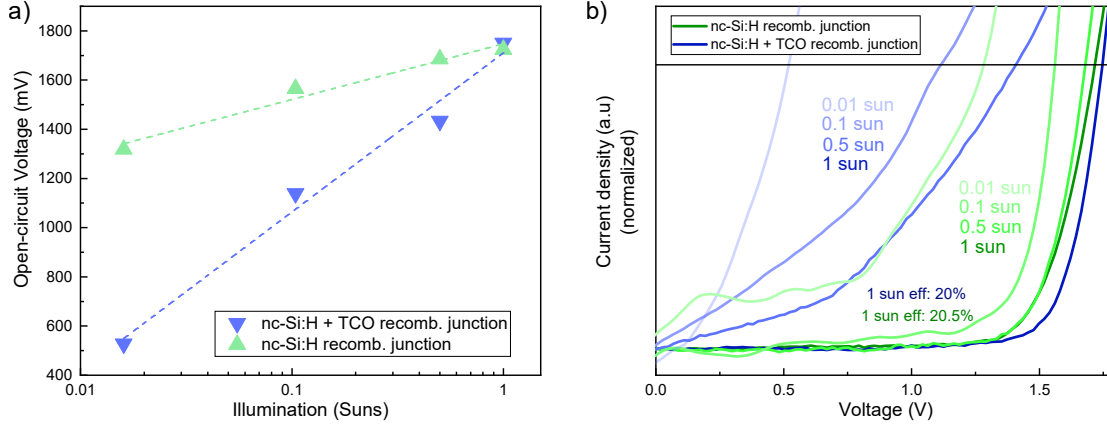
Figure 3.7 – **Low illumination behaviour of perovskite/SHJ tandems with and without ITO on the nc-Si:H recombination junction.** a) V_{oc} of the $Cs_{0.19}FA_{0.81}PbI_{(0.78}Br_{0.22})_3$/SHJ monolithic tandem cells with nc-Si:H and nc-Si:H/ITO recombination junctions, measured at several illumination intensities (1, 0.5, 0.104 and 0.016 sun), b) corresponding normalized J-V curves.

devices (12.96 cm^2) and the smaller ones is significant. However, closer inspection shows that most of the loss in efficiency stems from the lower fill factor. A large part of this loss is caused by the increased series resistance from the top electrode metallisation, which consists of 130 nm-thick evaporated Ag fingers. The development of screen-printed Ag metallisation, as used for commercial silicon solar cells, is expected to reduce significantly this efficiency gap between small and large cells.[130]
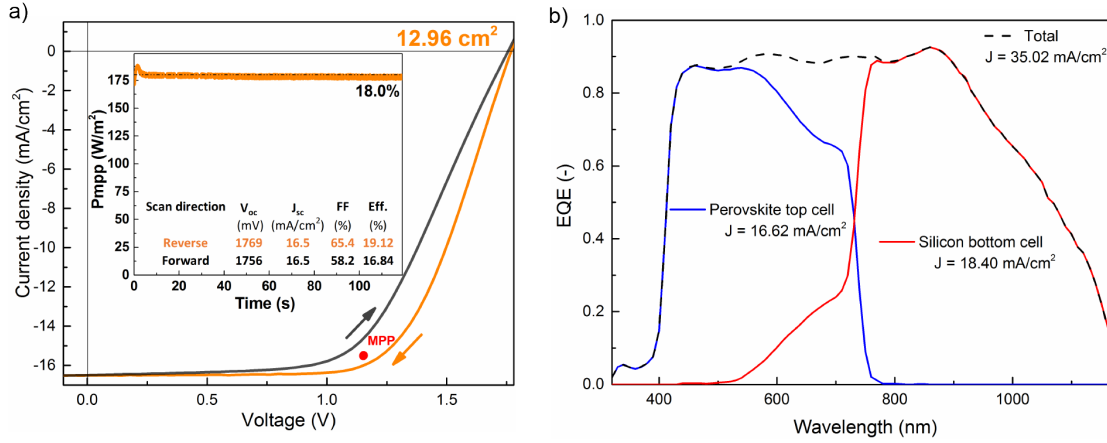
Figure 3.8 – **12.96 cm^2 large $Cs_{0.19}FA_{0.81}PbI_{(0.78}Br_{0.22})_3$/SHJ monolithic tandem** a) J–V curves and b) corresponding EQE spectra.

3.3 Conclusion

In this chapter, we developed monolithic perovskite/SHJ tandem cells with a nc-Si:H recombination junction deposited by PECVD at low temperatures (< 200°C), reaching steady-state efficiencies of up to 22.0% and 21.2% for aperture areas of 0.25 cm^2 and

Figure 3.9 – Picture of the 12.96 cm^2 perovskite/SHJ. The SHJ bottom cell is 5 x 5 cm^2. 120 nm of evaporated Ag is used as front-side metallisation.
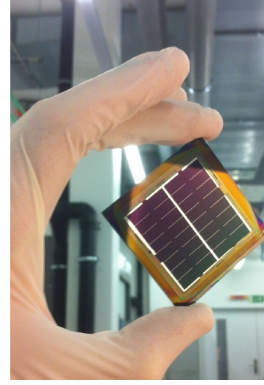
1.43 cm^2, respectively. Those results were amongst the highest PCEs for perovskite/c-Si tandems at the date of report (2017). The nc-Si:H junction is fully compatible with SHJ bottom cell fabrication processes since it can be deposited in the same PECVD reactor as the passivating amorphous layers. Parasitic absorption and reflection losses at the interface between the sub-cells are reduced thanks to the use of this nc-Si:H junction and the bottom cell current density is increased by more than 1 mA cm^{-2} in comparison to a tandem cell containing a TCO recombination layer. In addition, this nc-Si:H junctions does not compromise the electrical properties of the device. Furthermore, the low conductivity of the nc-Si:H recombination junction mitigates shunt paths through the perovskite top cell, enabling the demonstration of a 12.96 cm^2 monolithic perovskite/SHJ tandem cell with 18% steady-state efficiency, which was the largest perovskite/c-Si tandem solar cell reported at the date of fabrication (2017).

From the work presented here, it is quite clear that further improvement in PCE will come from an increase in the current densities. In this study, current densities of 16 mA cm^{-2} are obtained. Simulations have shown that current densities over 20 mA cm^{-2} can be reached for such devices. The main reason for the low current densities are explained by i) the strong parasitic absorption in the Spiro-OMeTAD layer (> 2 mA cm^{-2} when facing sunwards), ii) high reflection losses at the front of the silicon due to mirror-like effect of the polished silicon wafer (reflection losses > 1-1.5 mA cm^{-2}). These limitations will be tackled in the next chapter.

4 Perovskite/c-Si tandems with c-Si wafers textured on both sides

Abstract

State-of-the-art monolithic 2T perovskite/c-Si tandem devices often feature c-Si bottom cells that are polished on their front side to be compatible with the perovskite fabrication process. This concession leads to higher potential production costs, higher reflection losses and non-ideal light trapping. To tackle this issue, we developed a top cell deposition process that achieves the conformal growth of multiple compounds with controlled optoelectronic properties directly on the micrometre-sized pyramids of textured monocrystalline Si. Tandem devices featuring a SHJ cell and a nanocrystalline silicon recombination junction demonstrate a certified steady-state efficiency of 25.2%, which was at the time of publication, the highest reported perovskite/c-Si tandem solar cell efficiency. The optical design yields a current-density of 19.5 mA cm^{-2} thanks to the c-Si pyramidal texture and a cumulative current density (perovskite and SHJ) over 40 mA cm^{-2}, approaching that of record SHJ single-junctions. Similar efficiencies were achieved with a bottom cell based on a p-type wafer contacted at high temperature with full-area passivating contacts. To the best of our knowledge, these devices were the first functional cells reported that featured a bottom cell textured on its front and also the first reported to surpass the 25% mark. [1]

4.1 Introduction

As already discussed in previous chapters, light management in perovskite/c-Si tandem is highly important to reach a PCE over 30%.[19,92,190,191] We have seen how the introduction of c-Si texture at the back of the c-Si cell can improve the near-infrared response of the device by light trapping.[13] However, up to now, most state-of-the-art monolithic 2T perovskite/c-Si tandems featured bottom cells that are textured at the rear but polished on their front side. Such mirror-like flat surfaces significantly simplify the perovskite fabrication process but introduce high reflection losses. By introducing a texture at the front of the device, primary reflections can be strongly reduced due to the double bounce effect (transforming *e.g.* a 10% reflection on a flat surface to 1% on a textured surface as incident light reflected by a pyramid will likely reach an adjacent pyramid and be absorbed). To illustrate the potential optical gain, Figure 4.1 displays the simulated reflectance of a simple perovskite/c-Si tandem architecture (TCO/perovskite/c-Si wafer/TCO/Metal) using a single-side textured wafer (SST, texture at the back) and a double-side textured wafer (DST, texture on both sides). One can observe that both the external (primary reflection at the surface) and escape (light escaping from the wafer) reflectance contributions are mitigated for the DST case. Overall, a gain of > 2 mA cm^{-2} is observed, mainly attributed to the primary reflection reduction. This gain in current density could translate in a $> 1.5\%$ absolute efficiency gain (considering a well-optimized tandem cell (*FF* of 83%, V_{oc} of 1.9 V, J_{sc} increasing from 19 mA cm^{-2} to 20 mA cm^{-2}, 1 mA cm^{-2} in both sub-cells).[190,192]

Figure 4.1 – **PV lighthouse simulation of single- and double-side textured tandems.** Simulation of a single-side textured (textured at the rear, SST) perovskite/c-Si tandem solar cell (top), a double-side textured (textured on both sides, DST) perovskite/c-Si tandem solar cell (bottom). The simulation stack is from top to bottom, 100 nm MgF$_2$, 80 nm ITO, 500 nm Perovskite (1.62 eV from ref[17]), 280 μm Si, 150 nm ITO, 200 nm Ag. The size of the pyramids is 3.5 μm in height and 5 μm in width (angle of 54.7°). The wavelength interval is 20 nm, 50000 rays with 10000 bounces per ray were simulated.
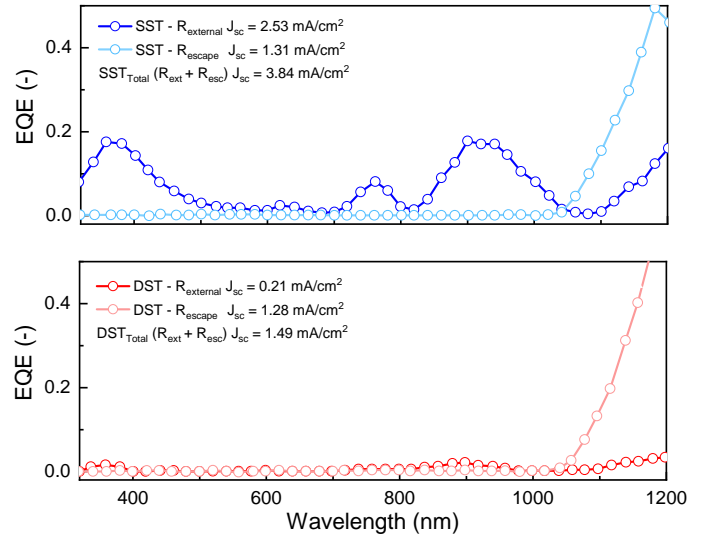
Several alternatives exist to circumvent or mitigate the reflection losses of the SST design, such as the introduction of an anti-reflective foil,[95,117,193] or textured glass,[19] perovskite nano-texturing[194] or advanced optics techniques (introduction of an intermediate reflector, *e.g.* index-tunable material) in between both sub-cells.[129,174,195,196] However such

---

Ingenito for the development of the high-temperature passivating contact c-Si bottom cell.

strategies might lead to increased fabrication costs, reliability concern (polymeric anti-reflection foil degradation, increased soling for nano-textured strategies), and provide less efficient light management capability as simple KOH c-Si texturing. Developing a top cell process flow compatible with such KOH textures would also allow the use of conventional c-Si bottom cells used in the industry without any additional polishing step.

The use of textured c-Si bottom cells prevents conventional solution-processing techniques to deposit the perovskite top cell unless the size of the pyramids is precisely controlled. Indeed, solution-processing does not produce conformal layers on fully textured c-Si bottom cells as shown in Figure 4.2. This might create shunts between the front side transparent conductive oxide and the SHJ bottom cell if the pyramids are higher than the perovskite thickness. Planarisation of the c-Si textured bottom cell (where the c-Si pyramids have been downsized) by blade coated or spin-coated perovskites have been reported recently (after the completion of the study presented in this chapter).[109,110] These approaches may enable large-area perovskite deposition via solution-processing on textured c-Si wafer.[109] Nevertheless, planarisation methods still require additional light-trapping scheme (*i.e.* an anti-reflection foils) in order to optically compete with a conformal perovskite coating on micron-sized pyramids. In addition, these methods require precise control of the pyramids size to avoid shunting.
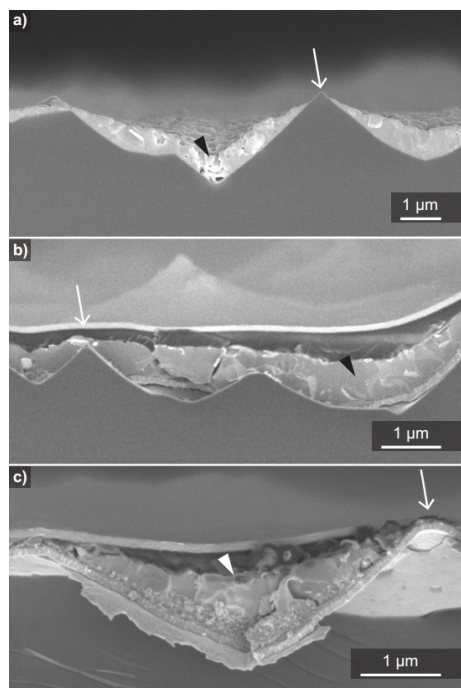
Figure 4.2 – **Solution-processed top cells on textured c-Si wafers.** Secondary electron SEM images of the cross-section of solution-processed a) perovskite layer, b) planar and c) mesoporous perovskite cells on textured c-Si. The perovskite layer was deposited using the one-step method.[197] The solution-processed layers and contacts, for example, TiO_2 in panel c) accumulate within the valleys (arrowheads). Shunts are likely to form at the summits of pyramids since the perovskite absorber is absent in these regions (arrows).

Combining the developments of chapter 2 and chapter 3, we demonstrate here perovskite/c-Si tandem cells that feature a c-Si wafer textured on both sides that is conformally coated with a perovskite top cell for optimal light management.

4.2   Results and discussion

4.2.1   Perovskite growth on different c-Si textures

A first step towards the fabrication of textured perovskite/c-Si tandems involves controlling the growth of the perovskite layer on textured c-Si wafers. Various texturing methods have been developed over the years for mono- and multi-crystalline silicon wafers, yielding various pyramid sizes and shapes.[198–203] Here we focus on alkaline texturing as it is the industrial method employed to texture monocrystalline c-Si. Monocrystalline (100) silicon texturing is performed by anisotropic etching with an alkaline solution (NaOH or KOH), revealing the (111) facets of c-Si.[201] Texturing parameters, such as duration, etchant concentration, additive(s) and temperature all play a crucial role in the resulting pyramid size.[202,203] In this section, we produced different silicon textures by i) changing the etching duration and ii) smoothening the pyramids by a nitric acid/acetic acid/HF solution.[204] More information concerning the texturisation and etching experimental parameters are given in the appendix (section A.2.1). The aim is to assess the impact of the texture morphology on the perovskite quality and optical performance.

As the presence of pyramids results in the decrease of incident light reflection in comparison to the flat scenario, one can expect that changing their size and morphology impacts the reflectance. Figure 4.3a-b represents the simulated EQE of perovskite/c-Si tandems featuring different pyramid sizes simulated with the software Setfos from Fluxim. The results suggest that the tandem EQE is not affected by the size of the pyramids (from 1 μm to 20 μm), which may help in view of growing a higher quality perovskite layer. On the other hand, smoothening the pyramidal texture leads to increased reflectance. As a consequence, while the pyramid size can be adapted to processing constraints, a light smoothening of the pyramidal morphology may still be considered if it improves the elelectronic properties of the top cell. To test this interplay between texture, optical performance and perovskite quality, various c-Si textures were prepared.

Figure 4.4 illustrates the c-Si pyramid morphologies (confocal and electron microscopy images and AFM mapping) as a function of the alkaline (KOH) etching time (20 min, 40 min, 60 min). A large number of small pyramids (1-2 μm) are obtained for 20 min of texturing (Figure 4.4). Pyramids considerably increase in size at longer etching duration, yielding fewer but bigger (4-6 μm) pyramids for 40 min of etching. Etching up to 60 min does not lead to bigger pyramids. A slight decrease in height is even observed (Figure 4.4a,f). As a result, changing the etching duration yields pyramids from 1-2 to 5-6 μm in height.

In addition to the texturing duration, post-etching for 5 s to 60 s by immersion in a nitric acid/acetic acid/HF solution leads to a smoothening of the pyramids (Figure 4.5). With smoothening time, one can observe that the average size of the pyramids shrinks (Figure 4.5b-d). The maximum height shifts from > 5 μm to 2.5 μm. Despite this shrinkage, the
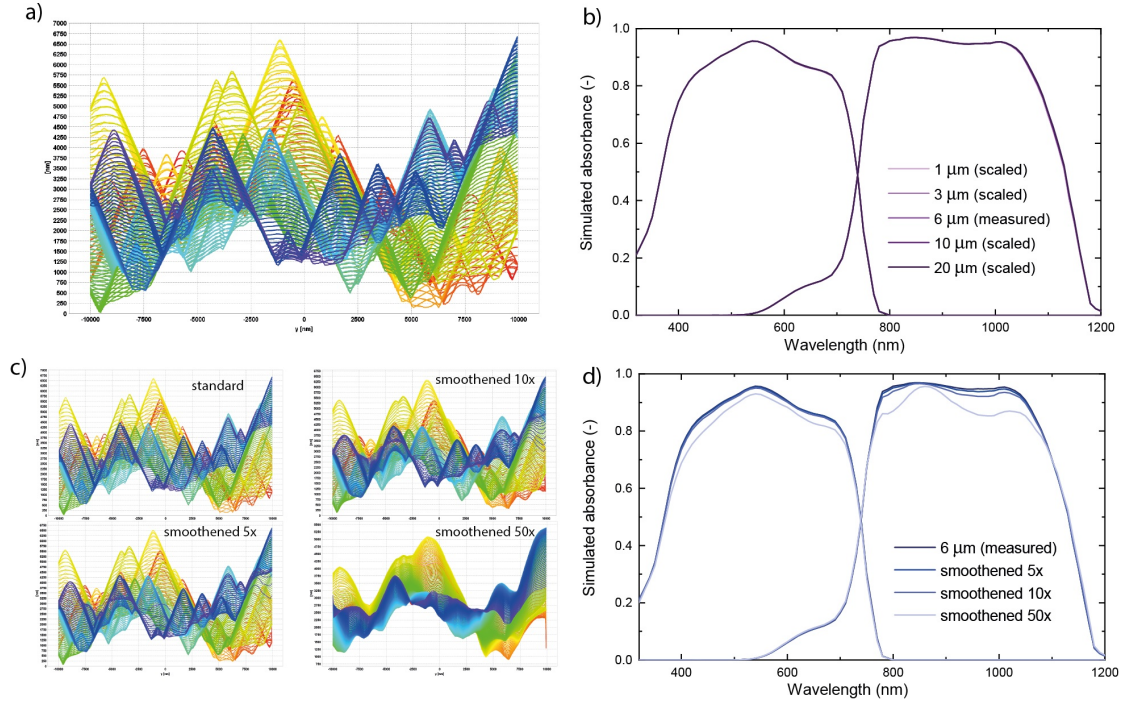
Figure 4.3 – Simulation of impact of the different c-Si textures on the perovskite/c-Si EQE performed with Setfos from Fluxim. a) textures with different pyramids sizes used as simulation inputs based on AFM measurements of a standard c-Si texture (pyramids of 5-6 μm in height), b) Corresponding EQE simulations for the different textures. The simulated stack is the one of Figure 4.9g, c) Simulated c-Si pyramids with standard non-smoothened pyramids (top left), r = 5 smoothened (bottom left), r = 10 smoothened (top right), r = 50 smoothened (bottom right). The different smoothening were obtained by convolving the initial data with a Gaussian Kernel of radius r (in pixel), d) Corresponding EQE simulations for the different smoothenings.
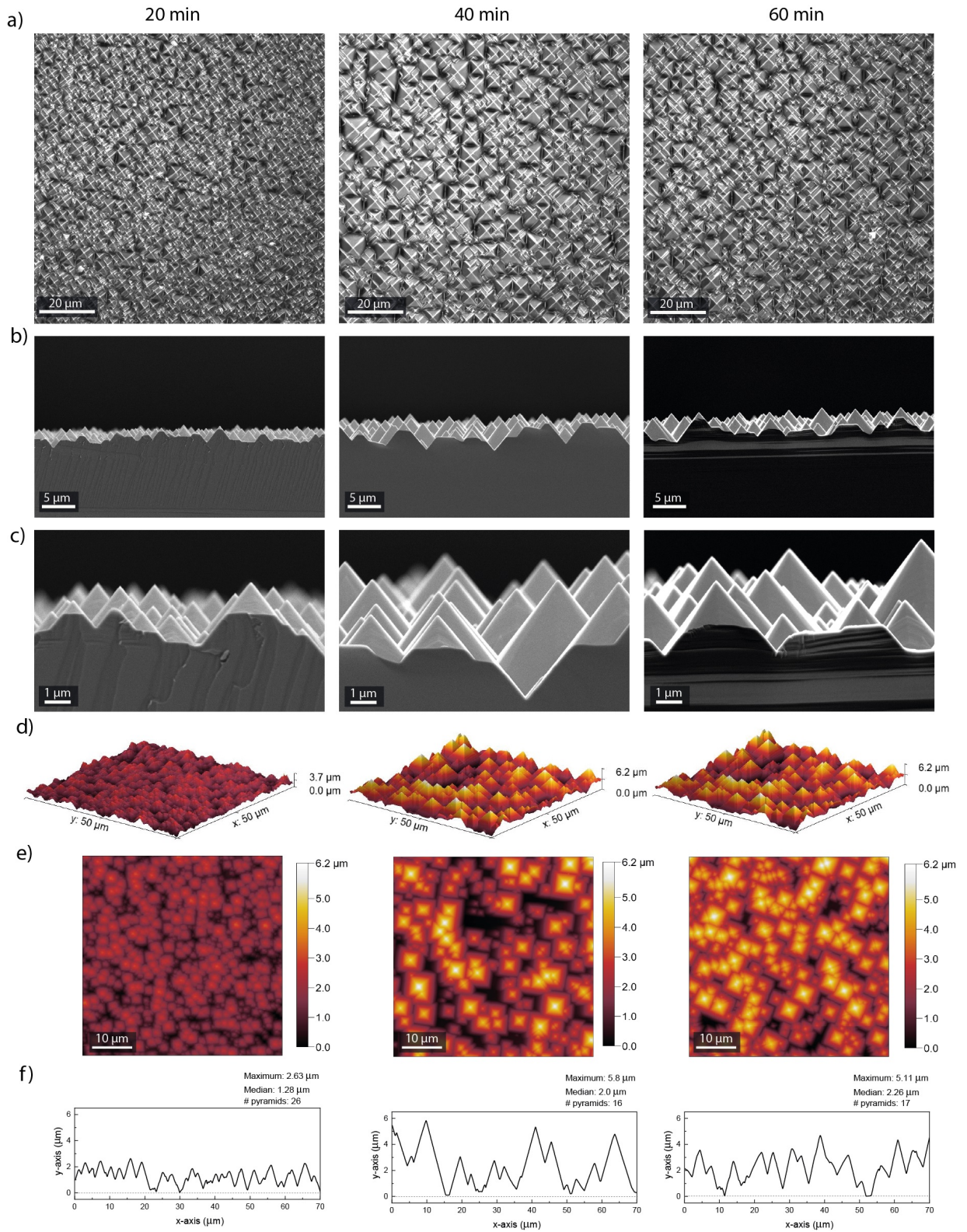
Figure 4.4 – Pyramids morphology with different etching time. a) Top view confocal microscopy images of the different textures, b) SEM cross-sections, c) SEM cross-sections at higher magnifications, d) 3D AFM maps (50 μm x 50 μm), e) corresponding 2D AFM maps, the color scale has been scaled to a maximum of 6.2 μm, f) AFM profile of the diagonal from of e), taken from bottom left to top right.

shape of the pyramids is not drastically altered by the rapid smoothening (5-10 s). On the other hand, prolonged etching (30-60 s) leads to a severe flattening of the pyramids. This has the consequence of decreasing the sharpness of the pyramids and leads to the formation of flat regions between the pyramids (Figure 4.5a). The simulation results of Figure 4.3 are confirmed by reflectance measurements of bare c-Si wafers featuring the different textures (Figure 4.6). If wafers of different pyramid sizes show no or few differences in reflectance, a smoothening of the pyramids leads to higher optical losses.
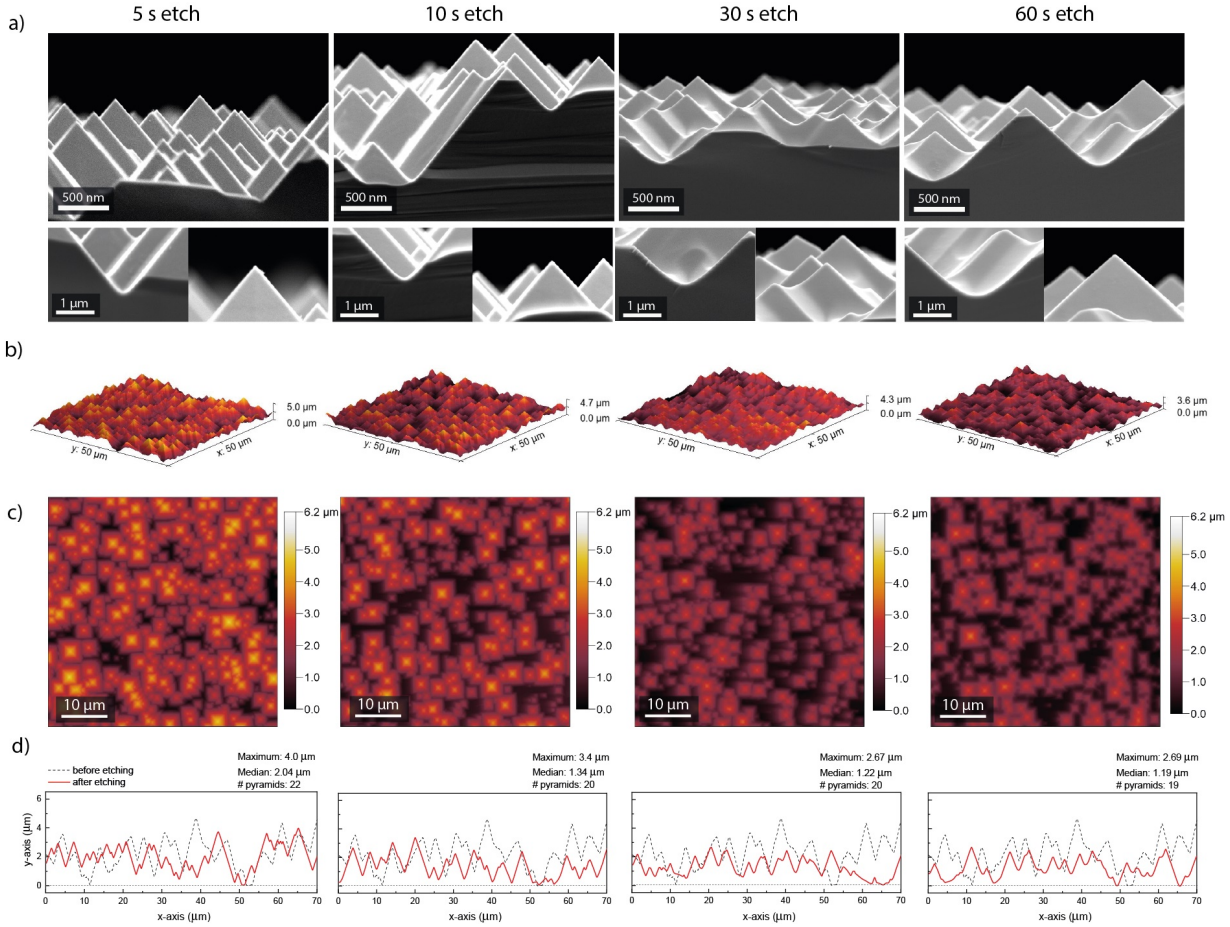
Figure 4.5 – Pyramids morphology after different smoothening duration. a) SEM cross-sections, b) 3D AFM maps (50 μm x 50 μm), c) corresponding 2D AFM maps, the color scale has been scaled to a maximum of 6.2 μm, d) AFM profile of the diagonal of c), taken from bottom left to top right. The dashed black line in the profile represents the initial condition before the smoothening (taken from Figure 4.4).

We will now focus on the growth of the perovskite layer on these different textures. The perovskite is deposited using the sequential PVD/SP method, described in chapter 2. The first step is the evaporation of the lead halide template on the c-Si wafer. Here, we evaporate 400 nm of PbI_2 with a Cs to Pb ratio of 0.19 (evaporation rate of CsBr been fixed as 10% of the one of PbI_2). One can see from the SEM cross-section images (Figure 4.7) that the lead template is conformally deposited on top of the c-Si texture, filling the valley as well as the tip of the pyramids with some porosity. It is worthwhile to mention
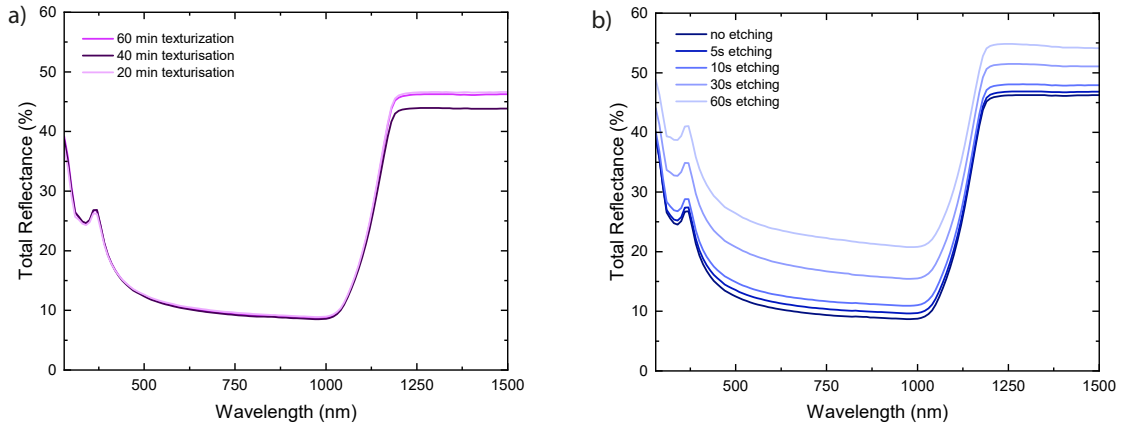
Figure 4.6 – **Reflectance measurements of the bare c-Si wafer with different textures.** a) Reflectance measurements of c-Si wafers with different pyramid sizes from Figure 4.4, b) Reflectance measurements the c-Si wafers with different smoothening from Figure 4.5. The wafers featured the same texture on both sides. No rear reflector was placed on the rear side of the wafer.

that 235 nm of PbI_2/CsBr is measured at the edge of pyramids, which corresponds to a vertically measured thickness of 400 nm (pyramid tilt angle of 54°). Here, no major difference is observed between the different textures. Spin-coating of a mixture of FAI and FABr (1:2) and annealing leads to uniform perovskite formation in all cases, resulting in a 450 nm-thick conformal perovskite coating. X-ray diffractograms reveal full PbI_2 to perovskite formation in each case (Figure 4.7b).

The wafers featuring different smoothening were also co-processed and the results are displayed in Figure 4.8. Here, a SST (single-side textured) wafer has been added to extend the analysis to the flat scenario (absence of pyramids). For the flat reference, the lead template morphology appears more compact in comparison to the porous PbI_2 layer obtained in the textured case (Figure 4.7). It is likely that the porosity results from shadowing effect induced by neighbouring pyramids and oblique surfaces.[205] Similar trends are observed for the different smoothening; dense PbI_2 layers are formed at the valleys of the pyramids for strong smoothening (30-60 s), whereas porous PbI_2 layers are observed at the edges of the pyramids. Although this effect is less pronounced for short smoothening times (5-10 s), the deposited layers still seem more compact within the valleys compared to unsmoothened cases (Figure 4.7). This difference in porosity has a direct impact on the perovskite formation. Indeed, unconverted PbI_2 clusters appear on the flat substrate and at the valleys of heavily smoothened features (bright residues marked by arrowheads on the SEM images in Figure 4.8a, right panels). This is confirmed by X-ray diffractograms (Figure 4.8b). Unconverted PbI_2 is observed in all samples (except for the 5 s smoothening) and the intensity of the PbI_2 (100) peak scales with the smoothening duration. This effect is attributed to the liquid-solid interaction during spin-coating. The organohalide solution may infiltrate the voids of the porous PbI_2 layers during spin-coating, ensuring that enough organohalides are available to react with the PbI_2 template. The presence of a dense template at the valleys will hinder this
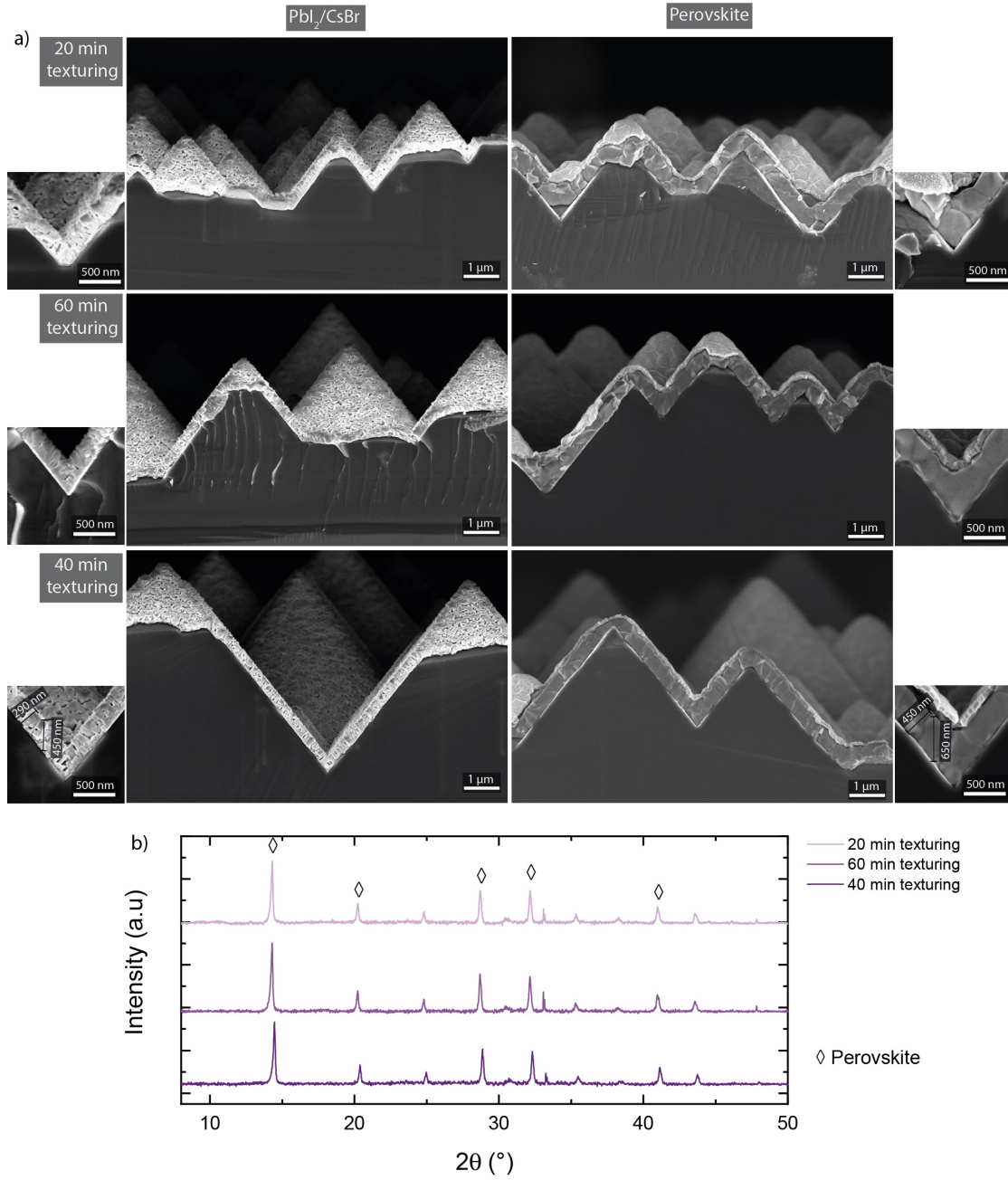
Figure 4.7 – **Perovskite growth on c-Si textures with different pyramid sizes.** a) PVD deposition of the PbI$_2$/CsBr template (left), zoom on one valley (inset), perovskite layers produced by the sequential PVD/SP method (right), zoom on one valley (inset), b) Corresponding X-ray diffractograms of the perovskite layers shown in a).

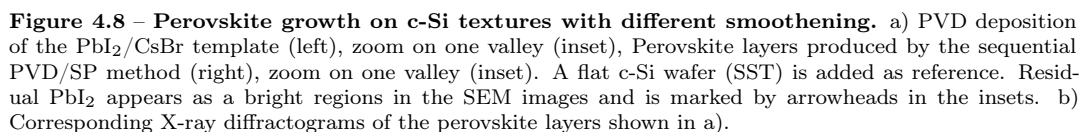infiltration, resulting in PbI$_2$ clusters at these locations.[206–210]

To illustrate this effect of template infiltration, the perovskite conversion process is presented step by step in Figure 4.9a-c. The image, directly taken after the organohalide spin-coating (Figure 4.9b), reveals that the pores of the template are now filled with the organohalide solution. The porosity seems essential to achieve full perovskite formation 4.9c-f. A STEM EDX map of the perovskite top cell indicates that the inorganic elements of the perovskite, namely Cs, Pb, Br and I, interdiffuse completely during the annealing step when this porosity is present. Even though smoothening the pyramids may have been beneficial for the perovskite quality (by making the texture easier to coat conformally), valleys are incompletely converted. As a result, sharp textures (*i.e.* as obtained after KOH etching) should be favoured with our process flow (Figure 4.9e-h).

After investigating the impact of the texture on the perovskite growth, we now switch focus to full solar cells. The perovskite solar cell is deposited into the p-i-n configuration and contacts are made by evaporation, sputtering and ALD (see chapter 2). First, the spiro-TTB HTL is deposited by thermal evaporation. Once the perovskite formed by the sequential PVD/SP method, the ETL, here a stack of LiF and C$_{60}$, is subsequently deposited by thermal evaporation. A buffer layer of SnO$_2$ is then deposited by ALD and indium zinc oxide (IZO) sputtered onto the stack, serving as the transparent front electrode. The front metal grid is made of evaporated Ag, while MgF$_2$ acts as anti-reflective coating. More detail concerning the device fabrication is given in the appendix A. The device structure is presented in Figure 4.9g. STEM-EDX maps of the different elements (C, Sn, In, Zn, O) shown in Figure 4.9h indicate that layers are conformally coating the c-Si wafer.

Next, the electrical properties (*J-V* curves) of the perovskite single-junction cells on the different c-Si wafers are measured. To be able to judge the effect of the different textures on the perovskite solar cell properties, the c-Si wafer is purely used as rear electrode. To do so, the charge carrier selective contact polarity at the rear of the SHJ is changed from p-type to n-type (a-Si:H (p) to a-Si:H (n)). As a result, due to the absence of a p-n junction in the c-Si cell (n-type contact at the front, n-type wafer, n-type contact at the rear), the wafer acts as an electrode (Figure 4.9g).

Figure 4.10a shows electrical parameters (V_{oc}, FF, J_{sc} and efficiency) extracted from *J-V* curves (4 cells per condition, reverse and forwards scans) for each pyramid sizes (20, 40, 60 min KOH etching). No significant difference is observed for the 3 different pyramid sizes, as expected as the perovskite growth seems unaffected by the pyramid size (Figure 4.7). In addition, the EQE spectra yield similar results, confirming that the optical performance does not depend on pyramids size, at least in this range (Figure 4.10b).

Similarly, perovskite solar cells were also co-processed on the smoothened pyramids. Here

Figure 4.8 – **Perovskite growth on c-Si textures with different smoothening.** a) PVD deposition of the PbI$_2$/CsBr template (left), zoom on one valley (inset), Perovskite layers produced by the sequential PVD/SP method (right), zoom on one valley (inset). A flat c-Si wafer (SST) is added as reference. Residual PbI$_2$ appears as a bright regions in the SEM images and is marked by arrowheads in the insets. b) Corresponding X-ray diffractograms of the perovskite layers shown in a).

Figure 4.9 – Cell design and microstructure of the perovskite top cell on textured c-Si. a) SEM images of the conformal PbI$_2$/CsBr template evaporated on the c-Si pyramids and b) the organohalide solution spin-coated on this PbI$_2$/CsBr template (before annealing). The left and right insets show magnified views of the bottom of a pyramid valley before and after spin-coating the organohalide solution, respectively, c) a cross-section of the full perovskite top cell deposited on the SHJ bottom cell, which was prepared by focused ion beam (FIB) (sample tilted to 54°, dimensions along the y-axis to be multiplied by a factor 1.2 when compared to h), d) the summit of a pyramid (left) and the bottom of a valley (right), e) Top-view SEM and f) Side-view SEM images of the perovskite layer, g) Schematic view of a fully textured monolithic perovskite/c-Si stack (with the c-Si stack acting as rear electrode), h) Cross-section STEM EDX map and corresponding line profiles of the relevant elements after background subtraction (K ionisation edges for all elements, with the exception of Pb, for which the L edge is used). The noise in the F signal within the perovskite layer is an artefact of the background subtraction step.

Figure 4.10 – **Perovskite single-junction solar cells with different pyramid sizes defined by the KOH etching time (20, 40, 60 min)** a) *J-V* parameters (4 cells per condition, reverse and froward scans displayed), b) Corresponding EQE spectra.

the results show that smoothening of the pyramids lowers all electrical parameters (V_{oc}, FF, J_{sc} and efficiency). If 5 s of etching gives similar results as non-etched devices, no benefit from the slight smoothening is observed. The presence of unconverted PbI$_2$ layer as observed 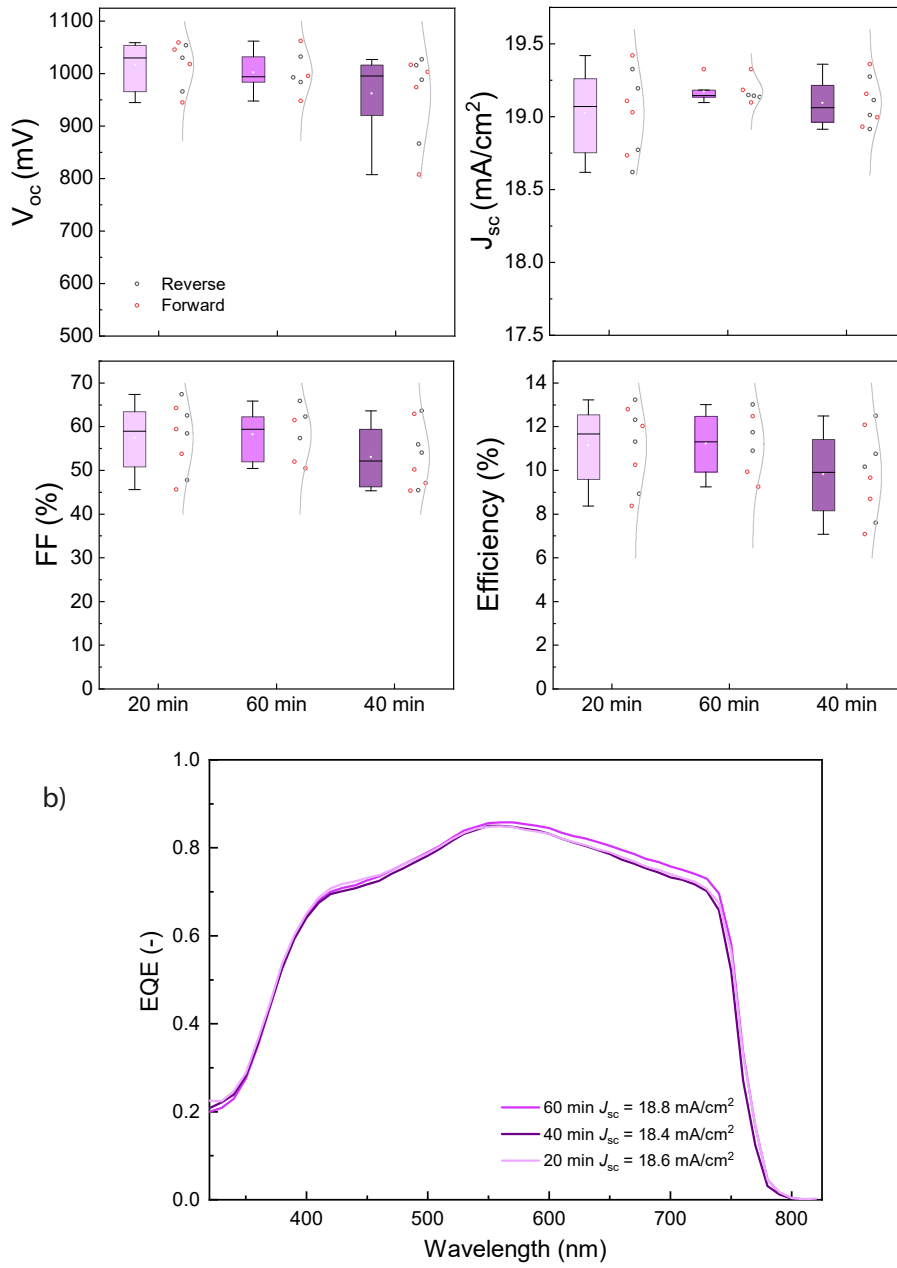in Figure 4.8a results in lower FF and V_{oc} as it may locally prevent charge extraction. The lower J_{sc} is induced by the stronger reflectance of smoothened wafers (10-60 s etching), which is confirmed by the integrated current densities obtained from the EQE spectra (Figure 4.8b).

To conclude this section, we have seen that the c-Si texture modifies the perovskite growth. The PbI$_2$ template morphology plays an essential role, it should be made porous to ensure organohalides infiltration during spin-coating to achieve full conversion with the process parameters used here. Any electrical benefit that may be induced by the smoothening of the c-Si pyramids is counterbalanced by the fact that a dense PbI$_2$ layer template forms within smoothened valleys (due to an absence of shadowing effects). These dense PbI$_2$ regions are difficult to convert, leading to unreacted PbI$_2$ clusters in the final perovskite layer, which are detrimental to the cell properties. We also have seen that changing the size of the pyramids (from 1-2 μm to 5-6 μm) does not modify the perovskite morphology and solar cell PCE. This attests the fact that the method developed here is compatible with a large range of c-Si textures, as long as they remain sharp. Now that we have identified the optimal texture for our perovskite fabrication process, we will focus on 2T tandems.

4.2.2   Benefits of the nanocrystalline hydrogenated silicon recombination junction

Perovskite/SHJ tandems were processed according to the device architecture shown in Figure 4.12a (the SHJ bottom cell features now a p-n junction on its rear side thanks to the introduction of p-type a-Si:H layer). The current density-voltage (J-V) characteristics of the best tandem devices that combine the layers detailed above and either an ITO or a nc-Si:H recombination junction are reported in Figure 4.12b. The J-V curve of the ITO-based cell is comparable to that of a filtered single-junction SHJ with an open-circuit voltage (V_{oc}) < 700 mV. This indicates that the top cell is shorted. On the other hand, the cell that employs a nc-Si:H layer stack as a recombination junction yields a V_{oc}> 1780 mV with a high efficiency (25.2% at MPP, as discussed below).

This significant difference in cell performance arises from a suboptimal ITO/spiro-TTB interface. While spiro-TTB is conformal after its evaporation on ITO (Figure 4.12c), it detaches from the pyramid summits and ridges during the 150°C annealing step required to crystallise the perovskite (Figure 4.12d). This locally uncovers the ITO, which appears as bright regions in the secondary electron SEM images shown in Figure 4.12d (indicated by arrowheads). The STEM EDX analysis shown in Figure 4.12e confirms the significant accumulation of spiro-TTB at the bottom of the Si valleys and its absence from some of
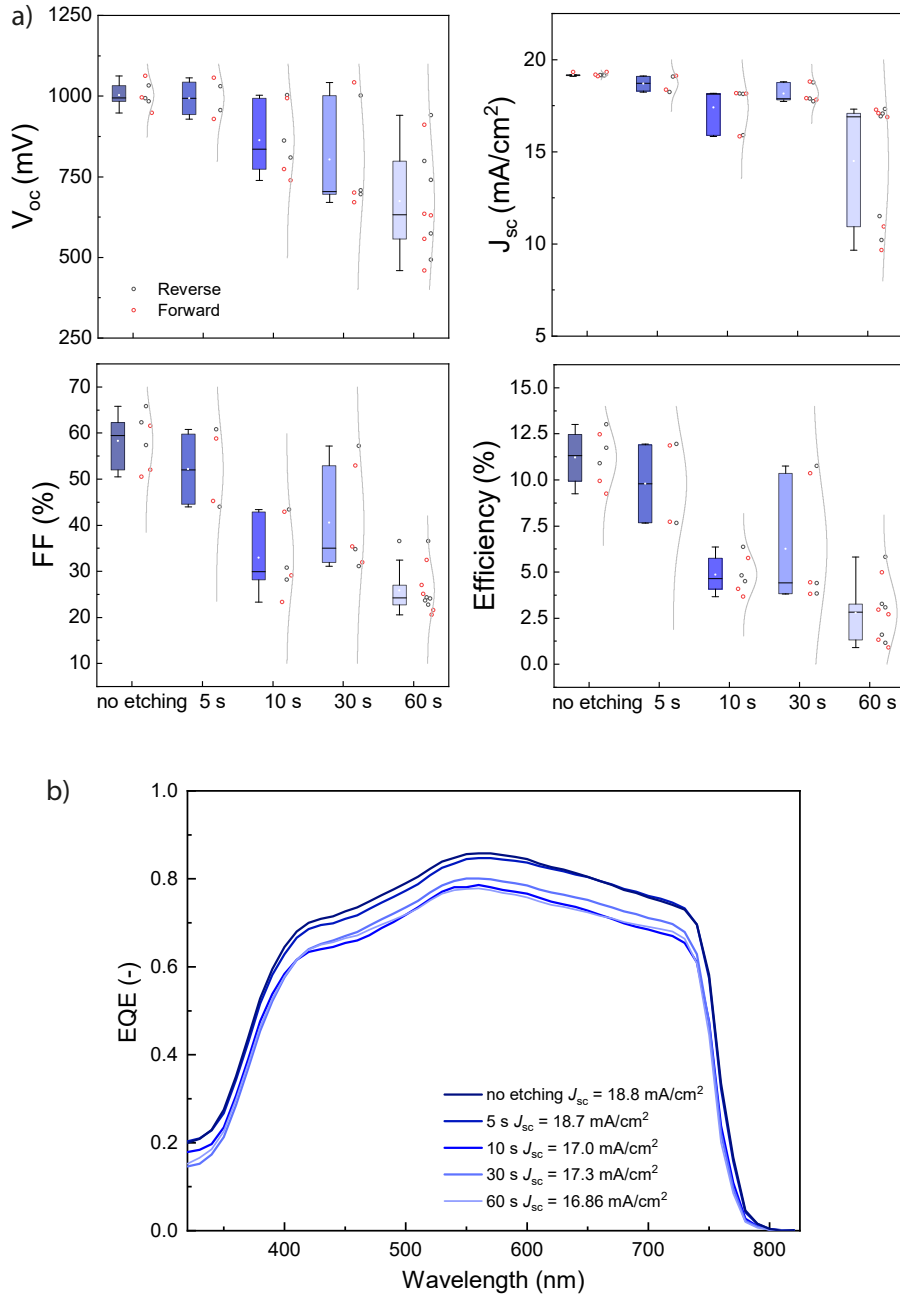
Figure 4.11 – **Perovskite single-junction solar cells deposited on different c-Si textures (pyramids smoothening).** a) *J-V* parameters (4 cells per condition, reverse and forward scans displayed), b) Corresponding EQE spectra.

the pyramid edges after annealing. These regions with a direct ITO/perovskite contact may act as recombination centers due to poor carrier selectivity. In comparison, when evaporated on nc-Si:H, spiro-TTB remains conformal, as confirmed by Figure 4.12f-h. Its thickness slightly increases at the bottom of the pyramid valleys after annealing (arrow in Figure 4.12h) but it still fully covers their edges. We assume that this effect is caused by a difference in surface tension between spiro-TTB and ITO when compared to nc-Si:H. Another reason that contributes to these differences in properties between ITO- and nc-Si:H-based tandem cells is the low conductivity of nc-Si:H.[9, 174, 181] This low conductivity may mitigate the impact of shunts induced *e.g.* by a direct perovskite/recombination junction contact due to a loss of conformality of spiro-TTB.

4.2.3   Improved optical system leading to a high efficiency

After identifying the adequate c-Si texture and combination of recombination junction and top cell materials, we assess now the optoelectronic properties of the tandem. EQE measurements highlight the advantage of switching from a SST to a DST architecture (Figure 4.13). While reflections occurring in the former design induce a current loss of 3.14 mA cm^{-2} in the wavelength the 360-1200 nm range, the introduction of a front texture reduces the overall reflectance, which drops to an equivalent integrated photocurrent value of 1.64 mA cm^{-2}. This optical gain stems directly from the presence of the c-Si front pyramidal texture, which i) suppresses the strong reflectance peak at 850 nm (reflection at the front of the c-Si wafer), ii) lowers primary reflections at the front of the tandem cell (double bounce effect) and iii) increases light trapping of infrared light in the c-Si cell. Overall, the reflection losses in fully textured perovskite/c-Si tandems are below 2% in the 360–1000 nm range, excluding metallisation.

In addition, the angular reflection loss of incident light is expected to be less dramatic in the case of DST vs SST bottom cells.[211] To attest the hypothesis, angular dependant EQE measurements were carried on DST and SST tandem (Figures B.5a-b and B.6). One can see that when the incident light angle is $> 50°$, the current density drastically decreases in SST tandems, with losses up to ≈ 3 mA cm^{-2} in both sub-cells with an incidence angle of 75°. As a comparison, at the same angle, less than 1 mA cm^{-2} and 1.5 mA cm^{-2} are respectively lost in the perovskite and SHJ cells for the DST case. It is noteworthy to mention that these experiments are not representative of the reality in the field. The EQEs are measured here in air without any encapsulation, which changes the spectral response of both designs, compared to modules installed in the field. Nevertheless, simulations of energy yields taking into account diffuse light contribution confirm that DST tandems are less prone to optical losses at high light incidence angles compared to SST tandems (with and without encapsulation, Figure B.6).[115, 116, 212]

A thickness/band gap optimisation to achieve current-matching conditions is shown in Figure 4.14. Overall, an optimum is reached for a 440 nm-thick perovskite absorber with
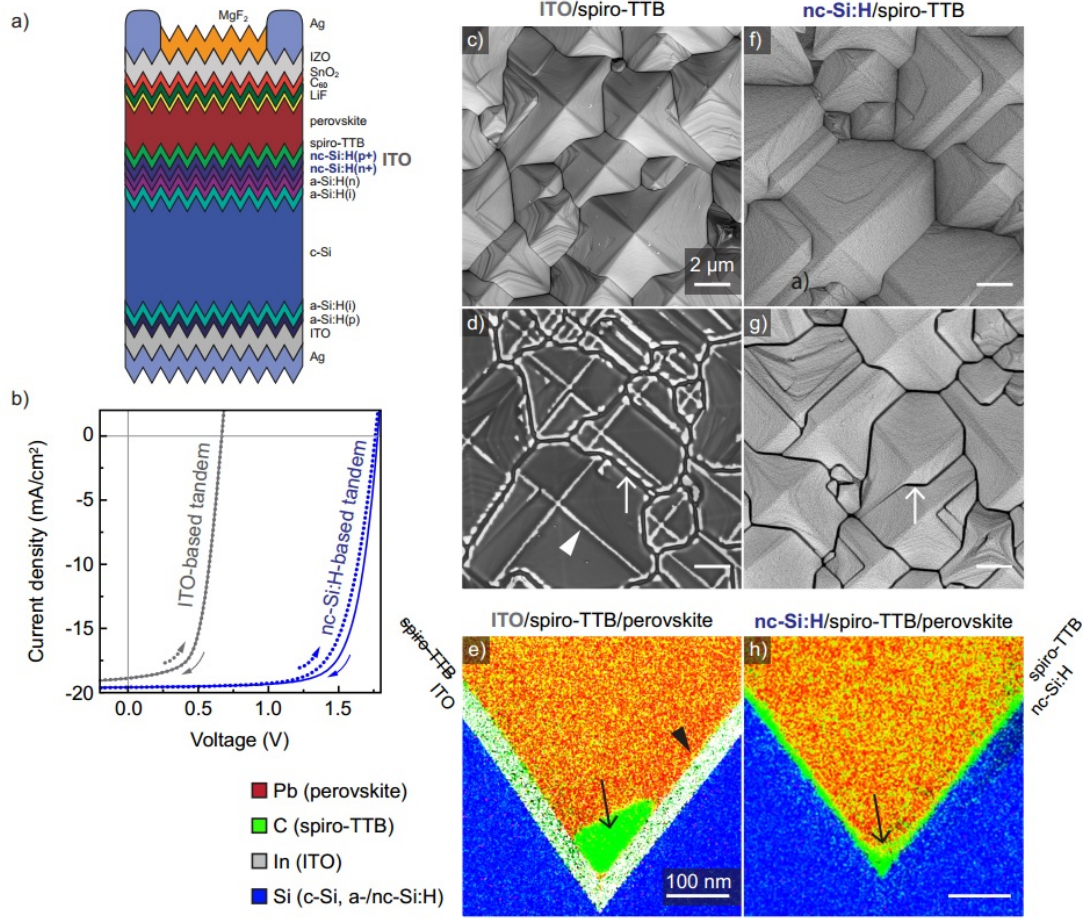
Figure 4.12 – **Comparison between different recombination junctions.** a) Schematic view of the fully textured monolithic perovskite/SHJ tandem developed here, b) *J-V* characteristics of fully textured perovskite/SHJ tandems that feature either an ITO or a nc-Si:H recombination junction according to the architecture in a). Top-view secondary electron SEM images of spiro-TTB c) as deposited on the ITO recombination layer, without any perovskite layer on top, and d) after annealing at 150°C to simulate the effect of the temperature applied during the perovskite crystallisation process. e) STEM EDX map of a cross-section of the ITO/spiro-TTB/perovskite stack at the bottom of a valley. SEM images of spiro-TTB f) as deposited on the nc-Si:H recombination junction without any perovskite layer on top and g) after annealing at 150°C, h) STEM EDX map of the nc-Si:H/spiro-TTB/perovskite stack at the bottom of a valley. Spiro-TTB slightly accumulates within the valleys during annealing when deposited on the nc-Si:H junction, while the effect is more severe with ITO (arrows, regions of dark contrast in the SEM images). This eventually leads to a local exposure of ITO (arrowheads, bright regions in the SEM images).

Figure 4.13 – **Optical comparison of DST and SST tandems.** EQE of perovskite/SHJ monolithic tandem cells with DST or SST bottom cells, alongside corresponding total absorptance curves, 1-R, where R is the reflectance of the device. These EQE and 1-R spectra do not include losses due to the front-side metal grid.
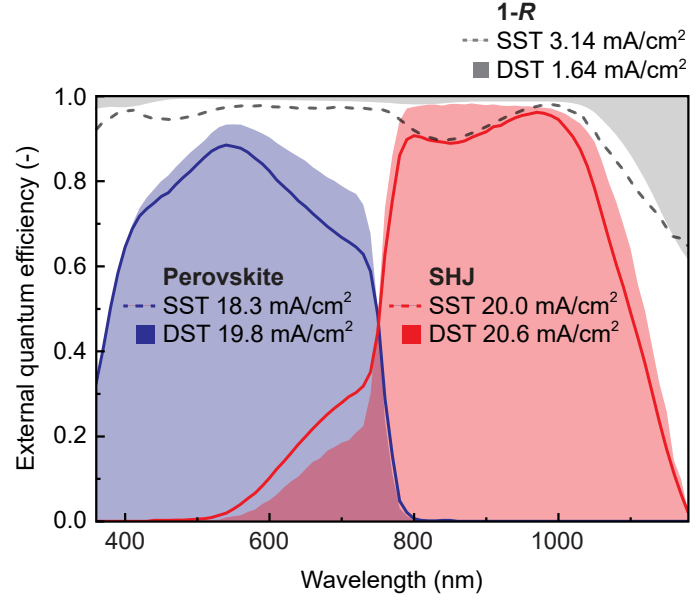
a band gap of 1.6 eV, with 20.1 mA cm^{-2} generated in the perovskite and 20.3 mA cm^{-2} in the SHJ (Figure 4.15a). The simple optical system presented here, which does not contain any light trapping feature other than the c-Si pyramids, exhibits a cumulative current of 40.4 mA cm^{-2} a value that approaches that of record IBC-SHJ devices (42.65 mA cm^{-2})[5] and surpasses what can realistically be achieved with front side polished devices without any complex light-trapping scheme.[173, 190] This high EQE photocurrent translates to an improved device performance. Fully textured monolithic perovskite/SHJ tandems featuring a nc-Si:H recombination layer yield a $V_{oc} > 1.78$ V (over an aperture area of 1.42 cm^2, Figure 4.15b). This is comparable to the sum of the standalone sub-cells (V_{oc} SHJ at 0.5 sun = 700 mV; V_{oc} perovskite = 1050 mV, as shown in Figure B.7). Thanks to the pyramidal Si texture, a J_{sc} of 19.5 mA cm^{-2} is obtained, a value this time including shadow losses induced by the front metal grid (covering 2.3% of the aperture area). The highest efficiency, certified by Fraunhofer ISE CalLab, is 25.52% obtained from the reverse scan and 24.09% from the forward scan (unencapsulated cell, Figure 4.15b). Other parameters retrieved from the J-V reverse scan include a V_{oc} of 1788 mV, a J_{sc} of 19.53 mA cm^{-2} and a fill factor of 73.0%. Maximum power point tracking yields a certified steady-state value of 25.24% during 700 s (Figure B.8). In-house measurement gave similar results (Figure B.9). The J-V hysteresis stems likely from the presence of mobile halide ions, as demonstrated in literature.[183, 213–215] For the same J-V scan rate, this behaviour is reduced when the temperature is increased (Figure 4.16) in accordance with literature data.[216] Finally, the sequential perovskite deposition method presented here yields reproducible results (Figure B.10).

The perovskite composition employed in high efficiency tandem devices yields a lower performance at the single-junction level on flat glass/ITO substrates when compared to
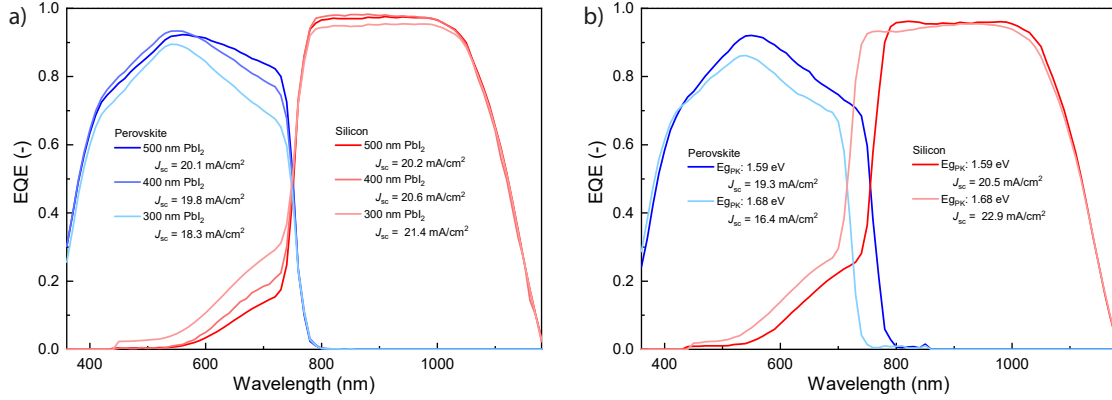
Figure 4.14 – Tandem current matching optimisation. a) EQE of fully textured monolithic perovskite/SHJ tandem solar cells with different thicknesses of thermally evaporated PbI$_2$/CsBr (value measured for a flat substrate) with a perovskite band gap of 1.6 eV. Corresponding thicknesses on the textured SHJ bottom cell are divided by $\approx$ 1.7 due to the geometry of the c-Si pyramids. The record device was fabricated using 400 nm of thermally evaporated PbI$_2$/CsBr, corresponding to $\approx$ 235 nm on the side of c-Si pyramids and leading to a final perovskite thickness of $\approx$ 440 nm, b) EQE of monolithic perovskite/SHJ tandem solar cells featuring two different band gaps for the perovskite top cell. The respective values are 1.59 eV (dark blue/red) and 1.68 eV (light blue/red).

Figure 4.15 – Certified performance of the fully textured perovskite/SHJ tandem. a) EQE spectra of a current-matched fully textured perovskite/SHJ tandem cell featuring a 1.6 eV perovskite absorber with a thickness of 440 nm alongside the 1-R curve, both excluding losses due to the front side metal grid, b) Corresponding certified *J-V* data (1.42 cm^2 aperture area, device shown in the inset).

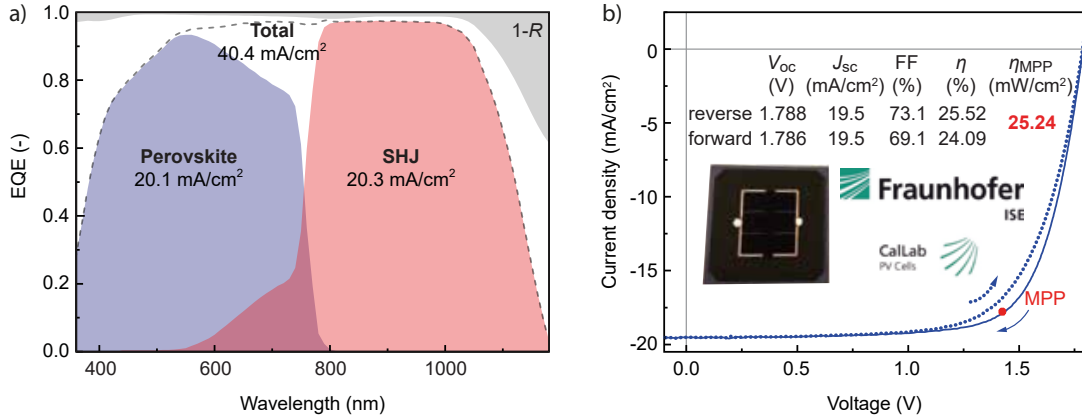that inferred from tandem results due to several factors (Figure B.7). Perovskite single-junctions feature an ITO/spiro-TTB interface, which is not optimal as demonstrated in Figure 4.12. Even if TEM indicates that spiro-TTB remains conformal on a flat ITO substrate (Figure B.11), some de-wetting might occur at the position of surface irregularities. In addition, the lateral conductivity of ITO reduces the shunt resistance of the device. These effects impact the FF and V_{oc} of perovskite single-junctions when compared to their top cell counterparts. Furthermore, with the deposition process used here, perovskite compositions that achieve current-matched conditions in tandems exhibit an increased surface roughness on flat surfaces (see chapter 2). Opening the band gap to 1.65 eV yields a smoother film morphology and enables single-junction efficiencies of 15% at MPP.[17] These differences between tandems and single-junctions highlight the necessity to optimise each configuration individually.
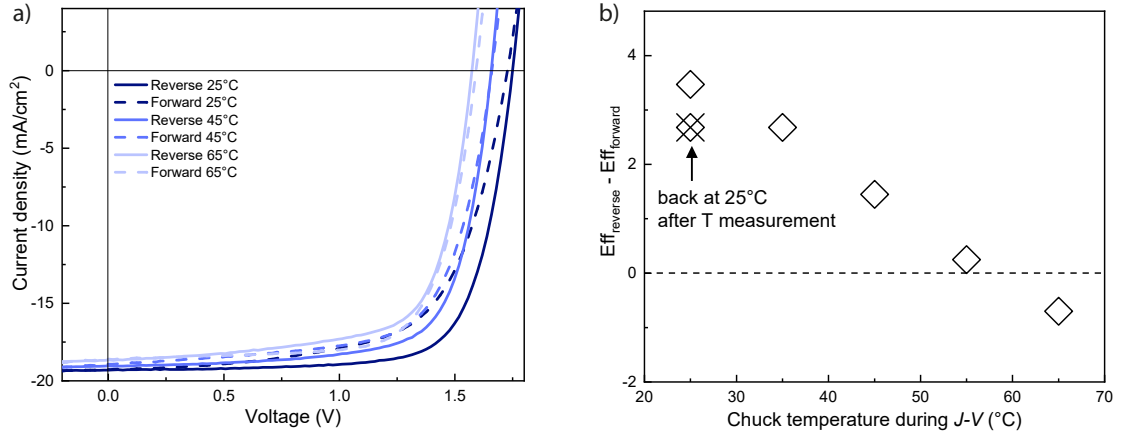

Figure 4.16 – **Thermal behaviour of the electrical properties of a perovskite/SHJ tandem.** a) Temperature-dependent J-V measurements of a monolithic textured perovskite/SHJ tandem solar cell, scanned in reverse (solid line) and forward (dashed line) conditions, b) Difference in efficiency between reverse and forward directions, ($\mathrm{Eff_{reverse}} - \mathrm{Eff_{forward}}$) as a function of the cell temperature.

4.2.4 Tandems based on p-type wafer contacted at high temperature using passivating contacts

The c-Si PV industry is dominated by p-type Si wafers, encouraging us to test our top cell deposition protocol with such c-Si wafer polarity. Prior to the demonstration shown below, only one perovskite/c-Si tandem device based on such bottom cells, in that case an Al-BSF cell, had been reported, achieving a low V_{oc} of 1.42 V (on 1 cm^2) due to strong recombination at the metal contacts. These issues limited the tandem efficiency to 16% during maximum power-point tracking. Switching to a PERC bottom cell reduces these recombination losses, but only tandems featuring n-type wafers have been reported so far, achieving V_{oc} of ≈ 1.7 V and efficiencies of ≈ 22-23%.[114,118] Another design, known under the acronyms TOPCON, poly-Si or POLO cell, which employs a more advanced passivating contact scheme, offers the advantage of combining high efficiency, temperature stability, and compatibility with industrial processes. The high

efficiencies are the consequence of a low charge carrier recombination at the contacts, resulting from the combination of a thin oxide (SiO_x) layer, a heavily doped Si-based layer and an annealing step at temperatures above 800°C. We combined here a simple c-Si bottom-cell process flow featuring full-area passivation at high temperatures with our PVD/SP deposition process. Details concerning the fabrication of the bottom cells are provided in the appendix A.2.3.

The tandem structure depicted in Figure 4.17a-b yields a steady-state efficiency of 25.1% during maximum power point tracking for 600 s (Figure 4.17c). Forward and reverse scans yield efficiencies of 24.9% and 25.4%, respectively. The current density is 19.5 mA cm^{-2} (19.7 mA cm^{-2} excluding shadowing induced by the metallisation as shown by the external quantum efficiency (EQE) spectra in Figure 4.17d). In comparison to monolithic perovskite/SHJ tandems presented above, a sightly lower infrared response is obtained due to the absence of texturing at the rear side of the bottom cell (Figure 4.17d). To the best of our knowledge, this was the first demonstration of a monolithic perovskite/c-Si tandem solar cell based on a p-type wafer that achieved an efficiency greater than 20%. These results demonstrate the wide adaptability of the perovskite top cell process flow developed here to various bottom cell architectures, including p-type c-Si wafers.

4.2.5 Device stability

The devices developed above exhibit high efficiencies thanks to improved optics, a prerequisite before any commercialisation of the technology can be envisaged. A second key requirement for commercialisation concerns device reliability. Planar single-junction produced with the hybrid method presented here pass 1000 hours damp heat degradation tests at 85°C and a relative humidity of 85% (Figure B.12) with a glass/glass and an edge sealant encapsulation. The stability of perovskite-based devices was then investigated further by exposing fully textured perovskite/c-Si monolithic tandem cells to continuous light irradiation. Figure 4.18a shows the electrical characterisation of a fully textured perovskite/SHJ tandem cell at MPP conditions under a continuous AM1.5G illumination without any UV-blocking filter. This measurement was carried out in ambient air (with a relative humidity level of 20-30%) without encapsulation for 60 hours. *J-V* scans were recorded regularly to monitor the evolution of the electrical parameters. After an initial light soaking period, the performance increases before remaining stable at 24% at MPP for 6 hours. The efficiency then starts to decrease linearly to $\approx$ 22% after 61 hours (linear rate of -0.15%rel/hour). The corresponding *J-V* data indicates that hysteresis increases during aging (Figure 4.18a-b). This behaviour suggests that more ions become available for migration with time. This effect might be triggered by halide migration into the carrier-selective layers under bias,[183,217] which leaves additional vacancies in the perovskite layer, or increased ionic conductivity from the diffusion of water into the hybrid perovskite material.[218]

a)

Ag
MgF₂
IZO
SnO₂
C₆₀
LiF
Perovskite
Spiro-TTB
nc-Si:H(p+)
a-SiCₓ(n)
SiOₓ

c-Si(p)

SiOₓ
SiCₓ:F(p)
ITO
Ag

b)

c)

	Voc (mV)	Jsc (mA/cm²)	FF (%)	PCE (%)
Forward	1735	19.5	73.5	24.92
Reverse	1741	19.5	74.7	25.41

d)

Perovskite
20.0 mA/cm²
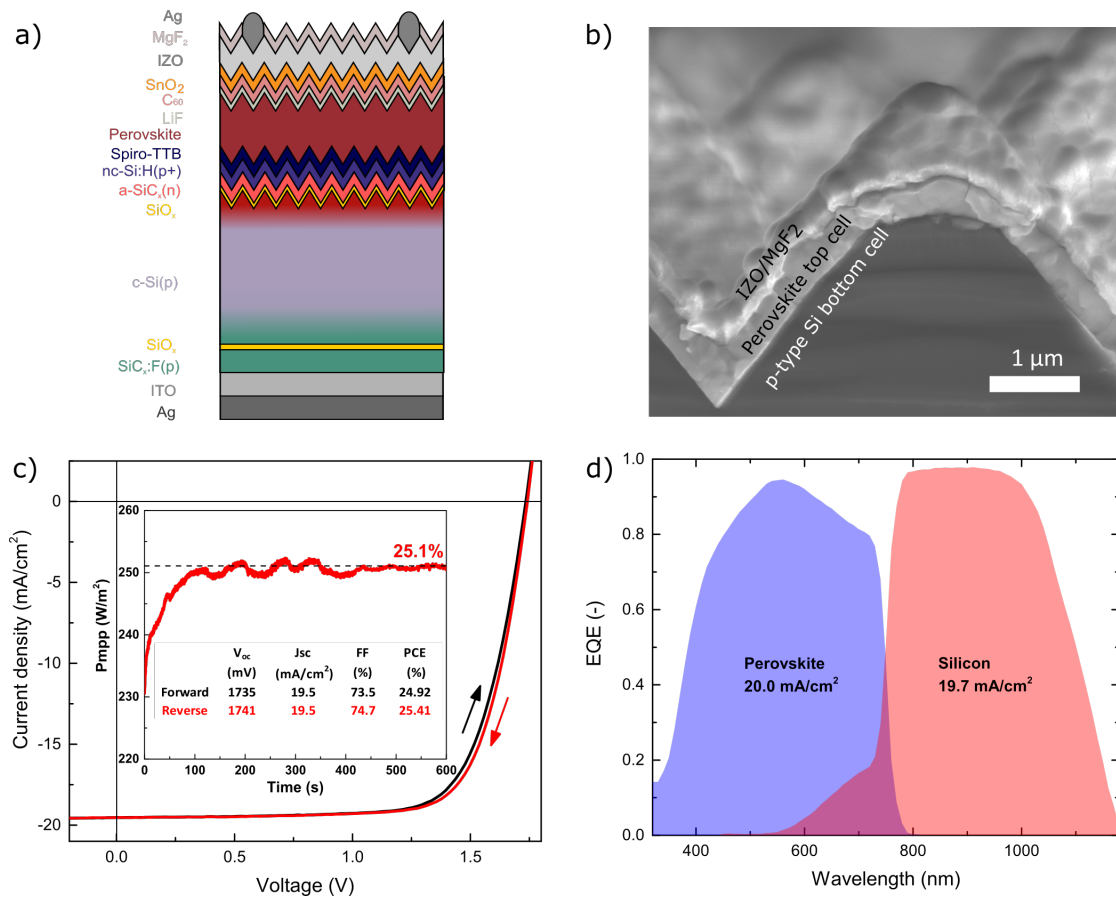
Silicon
19.7 mA/cm²

Figure 4.17 – **DST tandem using a p-type c-Si wafer** a) Schematic device structure of the perovskite/p-type c-Si tandem solar cell, b) Cross-sectional SEM image of the front side of the perovskite/c-Si tandem solar cell, c) J-V properties and maximum power-point tracking of the tandem cell, d) corresponding EQE spectra of the monolithic perovskite/SHJ tandem.

Similar degradation tests were carried out using tandem cells that were encapsulated using cover glass sheets and a butyl-edge sealant (without any laminated encapsulant, Figure 4.18c). This simple encapsulation scheme reduces the degradation rate such that the cell retained 90% of its initial power conversion output after 270 hours under constant illumination at MPP. Similar to previously reported degradation data for single-junction perovskite cells,[219] an exponential decay was also observed during the first 20 hours of illumination, followed by a linear regime for the next 250 hours (linear rate of -0.03 %rel/hour). Both J_{sc} and V_{oc} decrease accordingly after an initial increase in V_{oc} during the first few hours of operation (Figure 4.18d).

Overall, the tandems presented here exhibit an encouraging light soaking stability with tandems retaining most of their electrical properties for tens (unencapsulated) to hundreds (encapsulated) of hours without any sudden failure. But further stability improvements are required to yield fully reliable devices. These will likely arise from the optimisation of the device architecture, *e.g.* by replacing organic carrier-selective layers by inorganic materials and by introducing buffer layers to prevent the iodine migration and its reaction with the Ag electrode.[219,220] Ag oxidation was found to occur at the front and back Ag metallisation, the latter indicating that some iodide transport may occur in the form of volatile species[221,222] (Figure B.13). This halide vapour transport could be mitigated further by introducing a polymer encapsulant, a material that may also act as a UV light filter.[219]
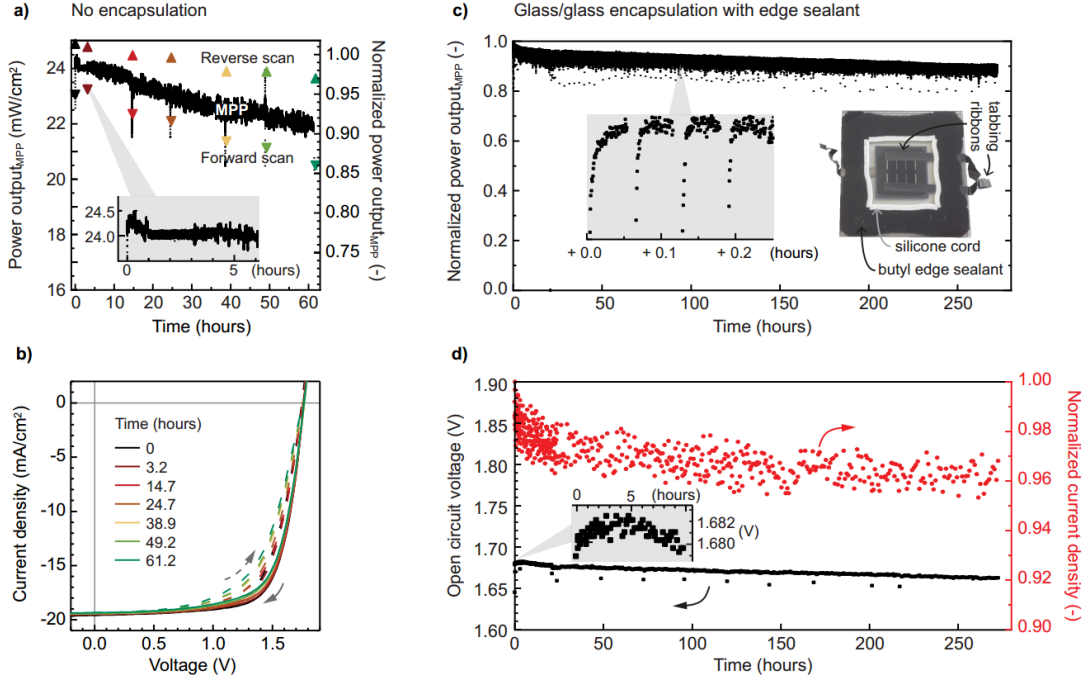
Figure 4.18 – **DST tandem stability during operation.** a) MPP tracking of an unencapsulated perovskite/SHJ tandem solar cell measured at 25°C in air (relative humidity of 20-30%), b) *J-V* scans were recorded every 10 hours during the experiment shown in a). Power output values extracted from these reverse and forward *J-V* scans are indicated in a) by triangles pointing upwards and downwards, respectively. c) MPP tracking of a glass/glass butyl-edge sealed perovskite/SHJ tandem solar cell in air (20-30% relative humidity). This device had an initial efficiency of 23.8% before encapsulation (measured at MPP for 1000 s) and 20.7% after encapsulation. This drop was mainly due to a decrease in J_{sc} as no index-matching encapsulant was present between the cell and the glass cover sheet. The spread in data points results from the recovery to MPP values after each *J-V* scan (recorded every 5 min). The left inset illustrates this recovery behaviour. The right inset is a picture of the encapsulated device; d) V_{oc} and J_{sc} values obtained from reverse *J-V* scans. The inset shows the V_{oc} during the first 10 hours of operation. Normalised power output efficiencies and currents are shown in c) and d) as the spectrum was not calibrated to 1 sun and no illumination mask was used on the encapsulated tandem cell.

4.3 Conclusion

In this chapter, we demonstrate perovskite/c-Si tandems that feature DST wafers for optimal light management. We investigate the growth of the perovskite absorber on different c-Si textures produced by KOH etching, in some cases followed by an isotropic smoothening (pyramid size from 1-2 μm to 5-6 μm with different smoothening). We notice that the morphology of the evaporated PbI$_2$ template strongly depends on whether the deposition is made on a flat or textured c-Si substrate. On flat c-Si or within flattened valleys of a smoothened texture, PbI$_2$ forms a compact layer that inhibits the organohalide solution infiltration in the layer, resulting in unconverted PbI$_2$. On the other hand, a porous lead template forms on KOH-etched wafers (not smoothened) and a full perovskite conversion is obtained, making such textures preferable for tandems. In a second step, we demonstrate monolithic perovskite/SHJ tandem solar cells based on DST wafers that achieve a certified MPP efficiency of 25.2%. Similar results were achieved

with tandems featuring a p-type wafer (25.1% at MPP). The key aspect enabling these advances is the top cell fabrication process that does not require any modification of the textured c-Si bottom cell, therefore allowing the use of existing industrial textured c-Si wafers. The process yields conformal perovskite, charge carrier selective and contact layers directly on the micron-sized c-Si pyramids, irrespectively of their size. Electrical and microstructural characterisation highlights the advantages of a nc-Si:H recombination junction over a conventional TCO, especially when featuring a thermally evaporated organic hole selective layer. This design exploits the high photocurrent potential of monolithic tandems to achieve values of 19.5 mA cm^{-2}. The pyramidal texture of the c-Si bottom cell directly reduces primary reflection losses and enhances light trapping in the infrared. In addition, the stability of tandem devices to light soaking and electrical bias was monitored up to 270 hours. Overall, the developed tandem fabrication procedure simplifies the overall process flow (as this design does not require any complex light-trapping scheme), yields high efficiencies thanks to improved optics and paves the way towards monolithic perovskite/c-Si tandem cells with efficiencies > 30%.

5 Textured perovskite/c-Si tandems: general conclusions and perspectives

5.1 Conclusions

In the first part of this thesis, we focused on the development of monolithic perovskite/c-Si tandems by depositing the perovskite solar cell directly on top of textured c-Si wafers. To do so, we first developed a wide band gap perovskite layer using a sequential PVD/SP process flow (chapter 2). The PbI_2/CsBr PVD step conformally coats the textured c-Si wafer (chapter 4). The porosity of the PbI_2/CsBr template is crucial to ensure its infiltration by the organohalide solution and a full conversion to the perovskite phase. A nanocrystalline silicon recombination junction, which consists of a highly-doped p-n junction, was identified as a versatile recombination junction that can accommodate the perovskite top cell either in the p-i-n or n-i-p cell configurations. The low conductivity of that layer compared to standard TCO-based recombination junction mitigates the impact of shunts that might be present within the perovskite top cell (chapter 3). Charge selective layers and transparent top electrodes (chapter 2) deposition by vacuum methods (PVD, ALD) enable monolithic tandems with efficiencies over 25% using textured c-Si bottom cells.

If the achievements presented here are encouraging in view of perovskite/c-Si tandems development and industrialisation, numerous research efforts are still needed. In the next section, we discuss the next steps and challenges required in view of commercial applications of perovskite/c-Si tandems.

5.2 Perspectives

5.2.1 Bringing fully textured tandems above 30%

It has already been discussed why the efficiency of perovskite/c-Si tandem is crucial in view of commercialisation. Taking into account the additional costs related to the

Evaporation	V_{oc} (mV)	J_{sc} (mA/cm²)	FF (%)	Eff. (%)
Reverse	1685	19.4	70.8	23.15
Forward	1663	19.4	68.0	21.95

Screen-printing	V_{oc} (mV)	J_{sc} (mA/cm²)	FF (%)	Eff. (%)
Reverse	1681	19.8	69.7	23.16
Forward	1663	19.8	68.0	22.36

Evaporated Ag
- - Forward
- - Reverse
Screen-printed Ag
- - Forward
- - Reverse

Figure 5.1 – **Comparison between evaporated and screen-printed metallisation.** *J-V* curves of textured perovskite/SHJ tandems featuring evaporated and screen printed metallisation.   The current density gain induced by using screen-printed Ag (line width of 85 μm) is 0.4 mA cm^{-2} compared to the 200 μm evaporated silver line.[130]
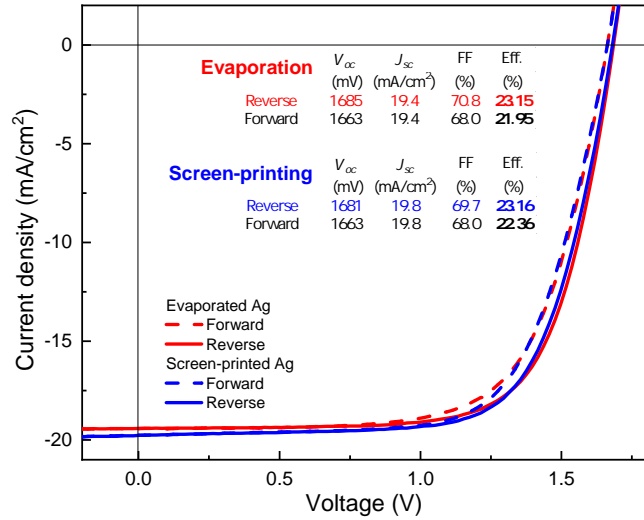
perovskite fabrication, a targeted PCE of 28-30% should be reached. Earlier this year, researchers from the Helmholtz-Zentrum Berlin reported an impressive certified efficiency of 29.15% for a perovskite/c-Si tandem of 1 cm^2 using a SST bottom cell. This is now clear that the 30% threshold is reachable, at least for small-scale devices. We briefly discuss here how the efficiency of our DST tandems can be further enhanced.

The devices presented here (chapter 4) show a high optical performance, with little margin to further improve J_{sc}. However, by reducing parasitic absorption in the front ETL/electrode stack and by reducing metallisation shadowing losses by introducing screen-printed Ag lines that have a more favourable aspect ratio when compared to thermally evaporated Ag (Figure 5.1), a current density over 20 mA cm^{-2} can be achieved at the device level. For example, considering the cell size of $\approx$ 1 cm^2 presented here, the 200 μm-wide evaporated Ag fingers lead to shadow losses of 2.3%, a value that could be decreased to 0.6% by replacing them with 50 μm wide screen-printed fingers. For similar design, switching from an evaporated to a screen-printed metallisation (width of 85 μm) increases the current density by 0.4 mA cm^{-2}. In addition, thinning down the C$_{60}$ and SnO$_2$ to reasonable values may lead to a gain of 0.6 mA cm^{-2} (Figure 5.2). Furthermore, the introduction of a TCO with a higher band gap such as IO:H can further push the current density gain to 1.4 mA cm^{-2}.[223] When distributed in both sub-cells, this may lead to a J_{sc} of 20.7 mA cm^{-2} (meaning an efficiency gain of $\approx$ 1% using the *J-V* characteristic of our best DST tandem presented in chapter 4).

With further realistic improvements in V_{oc} by increasing the perovskite band gap from 1.6 eV to $\approx$ 1.7 eV and improving the absorber quality, the tandem V_{oc} can be as high as 1900 mV.[224] In order to keep current-matching condition in between both sub-cells, the thickness of the perovskite top cell will have to be increased. Another way to increase both the V_{oc} and FF might involve doping the charge carrier transport layers. Doping those layers was found to increase the built-in voltage within the perovskite and reduce
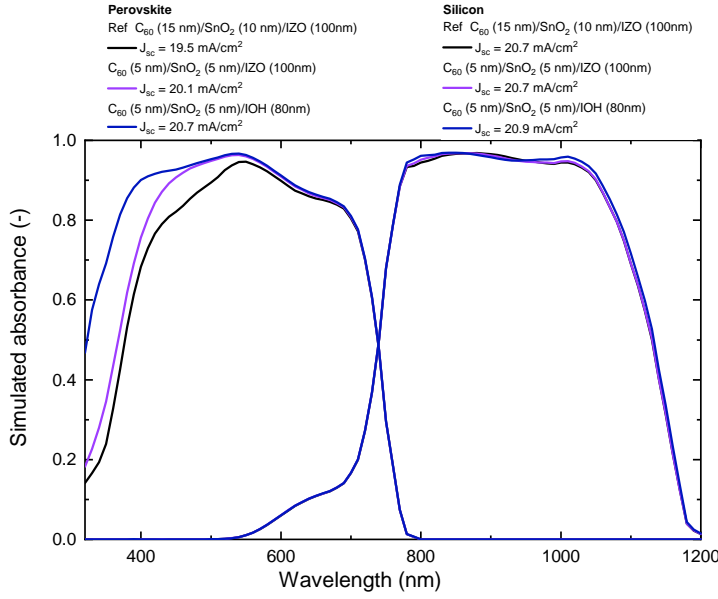
Figure 5.2 – **Simulation of parasitic absorption in the front contact.** Simulation of the EQE of perovskite/SHJ tandems with different front electrode stacks. n and k values from the ref[17] simulated stack adapted from ref.[10] The simulation was made by Dr. J. Werner using the SETFOS software developed by Fluxim.

recombination at the interfaces.[225] Finally, *FF* values of 80% have been already reported for the state-of-the-art perovskite/SHJ tandem with SST wafers.[108] Here the challenge is to thin down the charge carrier transport layers and increase their carrier mobility, which might also be achieved by doping.

5.2.2 Triple junctions perovskite/perovskite/c-Si tandems[1]

Another way to further increase the device efficiency is to form a triple junction. An efficiency of 35.9% has been reached using a 4T III-V/III-V/c-Si triple junctions, about 3% higher than the corresponding tandems.[7,8] Simulations have shown that perovskite/perovskite/c-Si triple-junction can also reach similar efficiencies.[226] The fabrication method reported in chapter 4 is compatible with the processing of perovskite/perovskite/c-Si triple junctions, as it involves a gentle solvent that does not dissolve the perovskite and temperatures within the thermal budget of an underlying perovskite absorber. The main challenge is to deposit the middle cell and top cells with suitable band gaps and thicknesses to reach current-matching in between all sub-cells. Proof-of-concept devices were made by adjusting the CsBr evaporation rate and the FAI to FABr ratio to achieve a perovskite band gap of ≈ 1.77 eV for the top cell and of ≈ 1.55 eV for the middle cell, values that diverge from the optimal ones of 1.4 eV and 1.8 eV. More information concerning the experimental details can be found in ref.[18] By using the cell structure depicted in Figure 5.3a, a perovskite/perovskite/c-Si triple-junction with a PCE efficiency of 13% was fabricated (Figure 5.3c). The current density of the device is still sub-optimal, as shown in Figure 5.3d. Simulations have shown that a current density of > 13 mA cm^{-2}

---

[1]This work has been published in ref,[18] the device fabrication and characterisation were carried out by Dr. Jérémie Werner.

could be obtained by adjusting perovskite band gaps towards more optimal values.[18] This would require the introduction of Sn into the perovskite lattice in order to reach band gap values < 1.5 eV. While several reports published have reported efficient Sn-Pb based perovskites.[100,101,227,228] Sn-based mixed-cation, mixed-halide perovskites deposited by PVD to coat conformally a textured bottom cell is still a nascent field.[229] The hybrid PVD/SP method presented here can be made compatible with these compositions by incorporating Sn in the template.
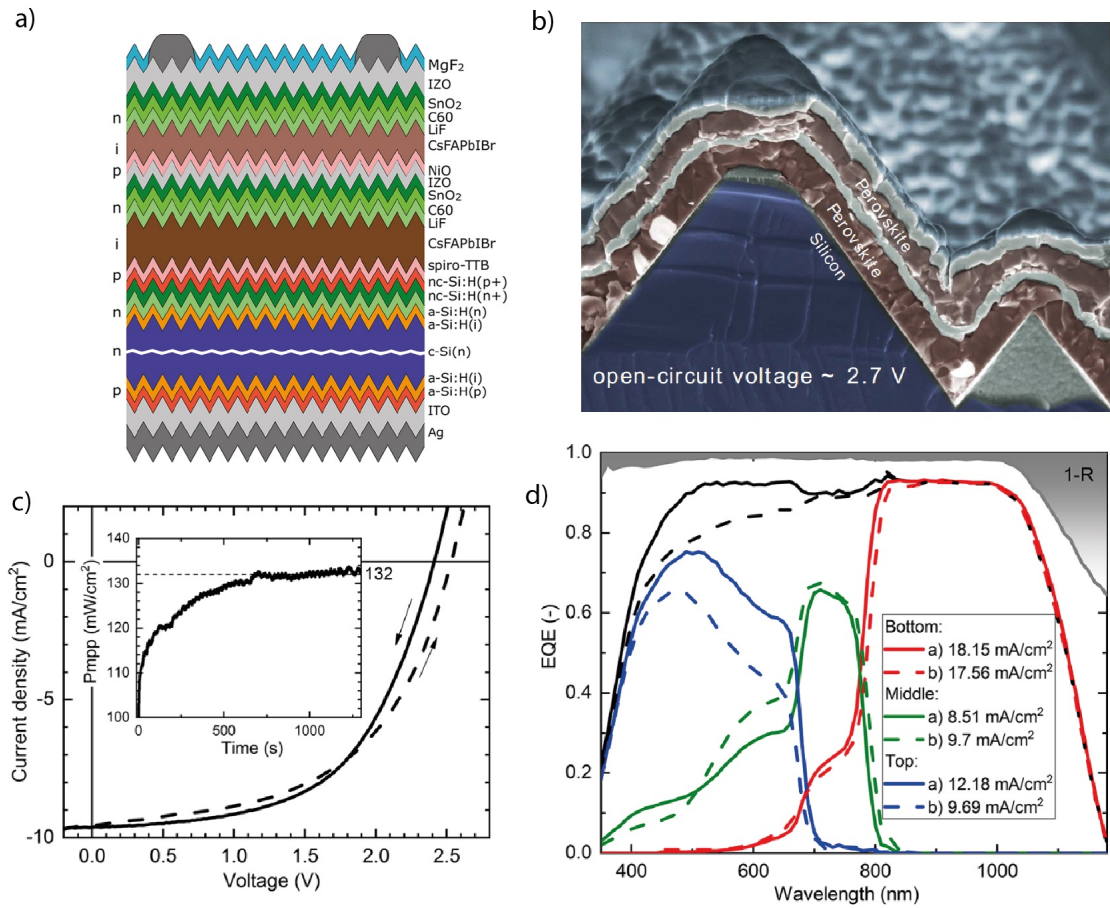

Figure 5.3 – Perovskite/perovskite/c-Si triple-junction. a) Schematic view of the triple junction solar cell, b) SEM cross-section image, c) *J-V* parameters, d) corresponding EQE.

5.2.3 Monolithic perovskite/c-Si tandem for efficient water-splitting [2]

Due to the intermittent nature of the solar irradiation, developing storage for the produced solar electricity is of major importance. Hydrogen production through water splitting driven by solar energy is an attractive solution for such purpose.[230, 231] From the different approaches available to generate hydrogen fuel from solar energy, water electrolysis catalysed by a solar cell has led to the highest efficiency so far.[232–235] Cheng and co-workers used a III/V tandem solar cell and reached over 19% solar-to-hydrogen efficiency at 1 sun with a Rh-based catalyst for water splitting.[233] But here again, the use of expensive III/V solar cells drastically increase the overall cost of the full system. Similarly, Luo and co-workers connected 2 perovskites single-junction solar cells in series and reached over > 12% efficiency as a lower-cost alternative. Perovskite/c-Si tandem cells developed in the chapter 4 achieve a V_{oc} of 1.7-1.8 V, a value above the 1.23 V required for water-splitting. By combining a carbon cloth (CC)/TiC/Pt and NiFe-layered double hydroxide (LDH) catalyst and a DST perovskite/c-Si tandem solar cell, a solar to hydrogen (STH) efficiency of 18.7% was achieved. This value comes close to the best results achieved with III/V solar cells. More details about the catalyst synthesis and water-splitting experiment are given in ref.[20]
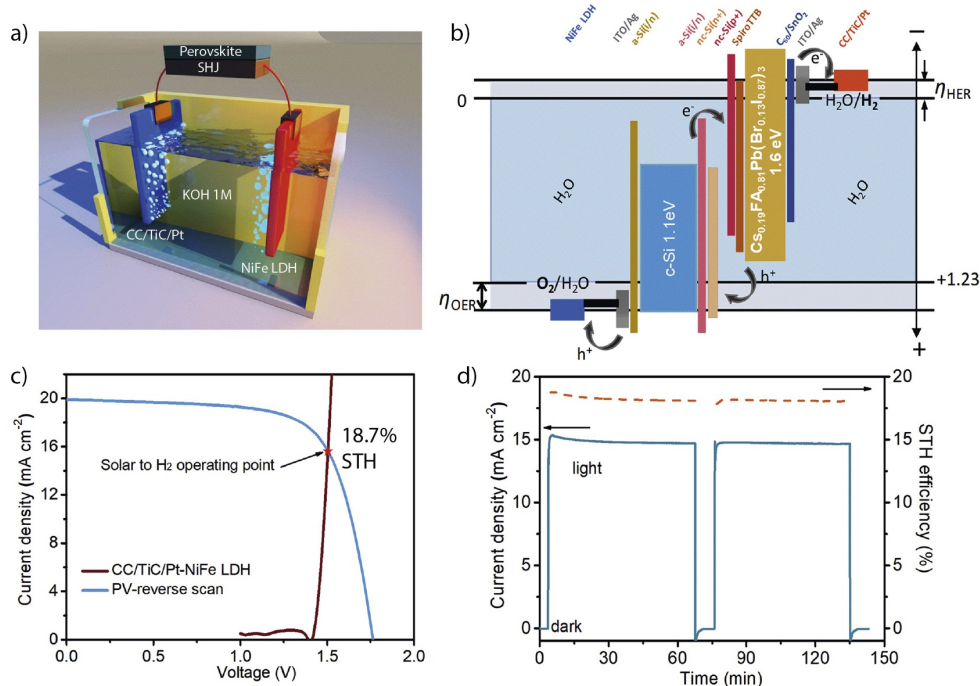
Figure 5.4 – **Water-splitting driven by a DST perovskite/SHJ tandem.** a) Schematic diagram of the solar-driven water-splitting system. b) Simplified schematic energy diagram of the perovskite/SHJ tandem solar cell and water-splitting setup, c) *J-V* curve of the perovskite/SHJ tandem solar cell from reverse scan under simulated AM 1.5G 100 mW cm^{-2} illumination and linear sweep voltammetry curve of CC/TiC/Pt and NiFe-LDH electrodes based two-electrodes configuration. The illuminated surface area of the tandem cell and the electrode was 1.42 cm^2, d) Current density-time curve of the solar-driven water splitting device without external bias under chopped simulated AM 1.5G 100 mW cm^{-2} illumination and the calculated STH conversion efficiency. From ref.[20]

5.2.4 Towards industrial 6 inch textured tandems

For now, most of the high-efficiency results for perovskite single-junctions and perovskite/c-Si tandems have been achieved using small devices (≈ 1 cm^2).[10,95,108,124,132,171,236–238] For the case of perovskite/c-Si tandems, the perovskite top cell should be deposited at high throughput over the full area of 6 inch wafers (≈ 225 cm^2), which is the industrial standard for c-Si. Spin-coating, the main method used in the perovskite research community, is unlikely to achieve this throughput and to yield the desired uniformity over these dimensions (even if, spin-coating has been demonstrated up to a size of a 4 inch wafer[9,121,130]). Solution processing via slot-die coating, blade coating and inkjet printing are viable solution-based options for large-scale perovskite deposition.[238–241] Nevertheless, while those methods could be suited for perovskite deposition onto SST c-Si cells, their adaptation to DST bottom cells is challenging. Recently, Chen and co-workers produced perovskite/c-Si tandems on textured wafers using blade coating with an efficiency of 26%.[109] This method planarises the c-Si wafer texture and requires a precise control over the pyramid size, which may be difficult to achieve over a large area and in an industrial environment. This planarisation also has the disadvantage of mitigating the optical

benefit of the silicon texture by introducing a flat surface on the front side of the device. This optical concession may be mitigated by introducing additional light management items, as done with SST devices.[95] On the other hand, vapour-based deposition methods such as physical vapour deposition (PVD) and chemical vapour deposition (CVD) should be able to coat conformally the silicon texture over a large area, enabling to fully benefit from the c-Si front side texture.[242–244] We aim to tackle this issue in the second part of the thesis, where we replace the remaining spin-coating step of our hybrid PVD/SP method with a vapour transport deposition step.

Perovskite solar cell by the sequential PVD/VTD method

Part II

6 The vapour transport deposition setup

Abstract

Vapour deposition has been identified as one of the most suited fabrication process for perovskite solar cells commercialisation due to its ability to deposit uniform layers over a large area with high reproducibility. In addition, the method is compatible with flat and complex substrates such as textured crystalline silicon wafers for tandem applications. In this chapter, a novel vapour transport chamber (VTD) is presented. This system dissociates the organic vapour evaporation zone from the reaction chamber. Once evaporated, the organic vapour is transported to the chamber by a carrier gas. This enables to deposit perovskite layers at different temperatures (ranging from 80°C to 140°C). This chapter serves as an introduction to this part of the thesis and describes the home-made VTD system and defines characterisation methodologies for organohalides identification which will be used in the next chapters.[1]

6.1 Introduction

Most of the high-efficiency perovskite solar cells reported so far still feature a small active area (1 cm^2 or less) as they are usually processed using spin-coating, a method difficult to upscale and industrialise at low costs.[245] In addition, perovskite wet chemistry processes usually involve toxic heavy solvents such as dimethylformamide (DMF) and dimethylsulfoxide (DMSO), an issue for large-scale manufacturing. Furthermore, in view of designing high-efficiency perovskite/c-Si tandem solar cells, solution-processing makes it difficult to deposit a conformal perovskite top cell on top of a textured bottom c-Si cell (chapter 4). In view of these limitations, vapour-based deposition techniques offer several advantages. They have the potential to yield cells with the same efficiency as solution-processing and should enable to coat conformally rough substrates on larger areas than spin-coating.[246–248] In addition, these methods are already adopted by the PV industry to produce cadmium telluride (CdTe), copper indium gallium selenide (CIGS) absorbers or the front side emitter of c-Si cells for example.[249,250] Overall, various vapour-based deposition techniques have been used to fabricate perovskite cells with different compositions.[251,252] Figure 6.1 presents different vapour deposition methods for perovskite fabrication. The methods can be divided into two main categories, one-step methods and sequential two-step methods, where the inorganic template is first deposited (by PVD or VTD) and in a second step, the template is converted to the perovskite phase by an organic PVD or VTD step. In addition, single-source evaporation has been developed by evaporating pre-synthesized perovskite crystals.[253,254]
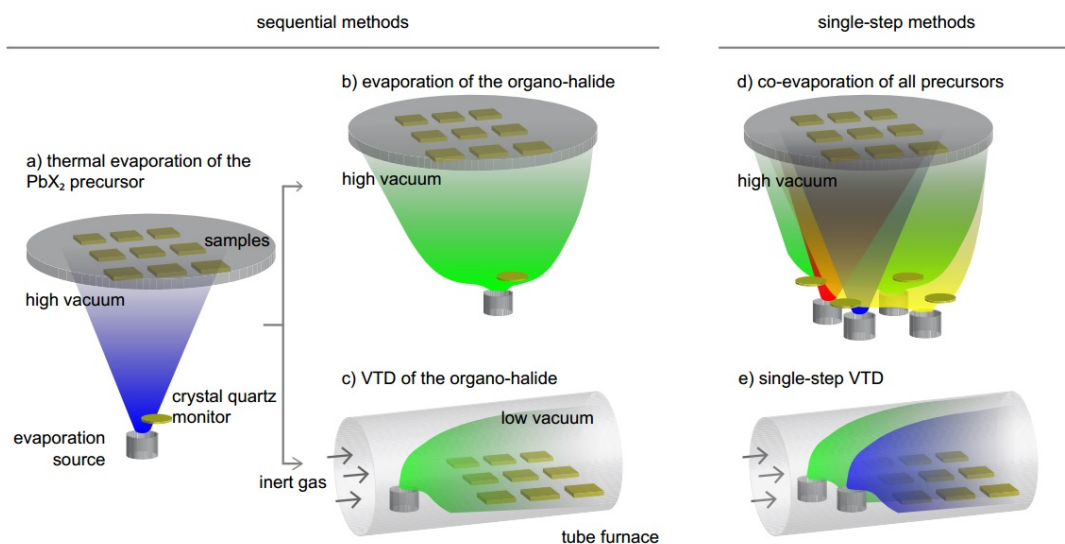

Figure 6.1 – **Various perovskite vapour-based deposition processes reported in the literature.** a) and b) PVD by sequential evaporation of the inorganic and organic precursors, a) and c) hybrid sequential thermal evaporation and VTD, d) co-evaporation and e) single-step VTD.

One-step and two-step PVD, where both the inorganic and organic precursors are sublimed in high vacuum (usually 10^{-6} mbar), have been used to make perovskite single-junction

devices achieving efficiencies up to 20%.[255] However, the usual way of controlling the evaporation rate by a quartz crystal microbalance has been challenging for organohalides.[256,257] The high vapour pressure of these materials leads to their deposition outside of the usual ballistic deposition cone, hence introducing cross-talking between the different crystal microbalances when co-depositing from several sources at the same time. In addition, the presence of impurities in the organohalide material often prevents the stabilisation of the sublimation rate, making the whole process complicated to control.[258] Alternatively, controlling the organohalide deposition rate through the chamber pressure has been shown to yield valuable results.[248,257] Nevertheless, the chamber pressure also depends on several parameters, such as the presence of water molecules or the outgassing of organohalides from the chamber wall due to their low sticking coefficient.[258,259]

Alternatively, organohalides have also been deposited by VTD, and more specifically by chemical vapour deposition (CVD), as the vapours reacted directly with the lead halide template.[206,260–263] The first cells produced by CVD achieved an efficiency of 12.1%. These were produced by converting a solution-processed PbI_2 template to the perovskite phase by exposing it at high temperature to a MAI vapour in a petri dish.[260] A PVD-CVD sequential approach was later introduced. The inorganic lead iodide precursor was thermally evaporated in high vacuum, before crystallising the perovskite by a CVD of the organohalide in a multi-zone tube furnace (in a low vacuum).[261] The organic material was sublimed in the higher temperature zone of the tube furnace and its vapours were carried by N_2 to the PbI_2 template. Adding a hot air flow and tuning the relative humidity level in the tube furnace was shown to be beneficial to the cell properties, overall improving the efficiency to 18.9%.[206] Using a similar approach, and switching to a FAI precursor, efficiencies of 14.2% and 7.7% were achieved on active areas of 0.13 cm^2 and 1 cm^2, respectively.[264] Values reaching 9% and 5.8% were then achieved with mini-modules of 12 cm^2 and 15.4 cm^2.[252] By introducing caesium into the perovskite layer, 5 x 5 cm^2 mini-modules with an active area of 12 cm^2 delivered an efficiency of 14.6%, while 12.2% was achieved for 8 x 8 cm^2 mini-modules (with an active area of 41.25 cm^2).[265,266] Finally, a 10%-efficient $CsFAPbI_3$ perovskite cell deposited on an active area of 91.8 cm^2 was recently reported.[267] More recently, attempt to develop perovskite layer from a single- or two-step CVD deposition has gained interest. However, the efficiency of the perovskite cells using those methods are still limited.[268–270] Table 6.1 summarises the main reports of perovskite deposited by CVD.

While two-step hybrid PVD/CVD methods produce large-scale perovskite cells with ever-improving efficiencies, the use of a tube furnace comes with several drawbacks. The main issue is that the temperatures at the source(s) and substrate(s) are not fully independent due to their proximity, even when using a multi-zone furnace. This issue becomes especially severe when co-depositing from several sources at the same time (e.g. in the case of mixed FA/MA perovskite absorbers). This temperature interdependence prevents a precise control of each evaporation rate and hence of the film stoichiometry. In addition, the furnace at the substrate position must be maintained at a sufficiently

high temperature (typically 150-160°C) to avoid any condensation of organohalides on the furnace walls, which would otherwise lower the precursor usage. Overall, this interdependence between the conditions at the chamber walls, source(s) and substrate(s) hence narrows down the processing window that can be achieved. Finally, another issue that may occur in tube furnaces is a gradient of organic vapour concentration along the tube length, leading to poor reproducibility and spatial inhomogeneities in the deposition rate.[264]

In view of these difficulties to deposit organohalides reliably via standard PVD or CVD routes, we report here a vapour transport deposition system, where the organohalide evaporation is carried out in a separate chamber and subsequently transported, through a showerhead, into the reaction chamber. This design enables independent control of the temperature of the sources, gas lines, reactor walls, and substrates.

Table 6.1 – Table summarising different CVD-based perovskite deposition techniques in literature and a selection of their deposition parameters.

Date	Method	Substrate	System	Substrate (°C)	Source (°C)	Carrier gas	Pressure	Organohalide	Area (cm²)	Efficiency (%)	Paper
2013	2 step SC-CVD	PbI2 (PVD)	Petri dish	150°C	150°C	-	760 torr	MAI	0.12	12.10%	260
2014	2 step PVD-CVD	PbCl2 (PVD)	2 zone tube furnace	130°C	180°C	N2	0.75 torr	MAI	0.1	11.80%	261
2015	2 step SC-CVD	PbI2 (SC)	flipped cell on crucible	155°C	155°C	-	760 torr	MAI	NA	8.10%	271
2015	2 step SC-CVD	PbI2 (SC)	2 zone tube furnace	140°C	180°C	-	NA	MAI	0.12	12.73%	262
2015	2 step SC-CVD	PbI2 (SC)	1 zone tube furnace	70-110°C	70-110°C	N2	0.095 torr	MAI	0.09	14.70%	263
2015	2 step SC-CVD	PbI2 (SC)	1 zone tube furnace	145°C	145°C	-	760 torr	MAI	0.12	12%	272
2015	2 step SC-CVD	PbCl2 or PbI2 (SC)	2 zone tube furnace	160°C	180°C	N2	NA	FAI	0.135	14.20%	264
2015	2 step SC-PVD-CVD	PbI2-PbBr2-PbCl2 (PVD-SC)	closed space vapor transport (CSVT)	150°C	160°C	-	158 torr	MAI-MABr	0.01	16.20%	273
2015	1 step CVD	PbI2 and PbCl2 (CVD)	2 zone tube furnace	80°C	120°C (MAI) 300°C (PbI2) 360°C (PbCl2)	Ar	0.001 torr	MAI	NA	11.10%	274
2015	2 step SC-APCVD	PbI2 (SC)	1 zone tube furnace	145°C	145°C	-	760 torr	MAI-MACl	0.12	13.76%	275
2015	2 step SC-CVD	PbI2 (SC)	1 zone tube furnace	100°C	100°C	-	0.002 torr	MAI	NA	12%	276
2015	2 step SC-CVD	PbBr2 (SC)	closed petri dish	150°C	150°C	-	760 torr	MABr	NA	8%	277
2016	2 step SC-LPCVD	PbI2 (SC)	1 zone tube furnace	110°C	110°C	N2	0.045-100 torr	MAI	0.24	15.37%	278
2016	2 step SC-CVD	PbI2 (SC)	Tube furnace	150°	140-150°C	-	760 torr	MAI	0.11	18.90%	206
2016	2 step PVD-CVD	PbI2 or PbCl1 (PVD)	1 zone tube furnace	160°C	180-210°C	-	0.75 torr	FAI	0.09	15.80%	252
								FAI	0.09	10.80%	
2016	2 step PVD-CVD	PbI2 (PVD)	Closed chamber	120°C	120°C	-	1.5-7.5 torr	MAI	0.09	5.80%	279
								MAI	25	11.60%	
2016	2 step SC-CVD	PbI2 (SC)	1 zone tube furnace	150-175°C	150-175°C	-	760 torr	MAI	NA	17.60%	280
2017	2 step PVD-CVD	CsBr-PbI2 (PVD)	1 zone tube furnace	160°C	160°C	-	0.75 torr	FAI-FACl	0.09	17.20%	266
								FAI-FACl	64	12.22%	266
2018	2 step CVD	Sn-Pb (CVD)	1 zone tube furnace	145°C	185°C	Ar	760 torr	MAI	0.1	14.04%	281
2018	2 step PVD-CVD	CsBr-PbBr2 (PVD)	1 zone tube furnace	140°C	140°C	-	NA	FAI	0.09	18.20%	282
2018	3 step SC-CVD-dip coating	PbI2 (SC)	2 zone tube furnace	155°C	190°C	-	1 torr	FAI	12	15%	265
2019	2 step PVD-CVD	PbI2-CsBr (PVD)	2 zone tube furnace	190°C	150°C	Air	1 torr	FAI	91.8	10.40%	267
2019	2 step VTD	PbI2 (VTD)	VTD system	100°C	210°C (MAI) 450°C (PbI2)	N2	10 torr	MAI	NA	6.80%	268
2020	2 step (PVD-CVD)	PbO (sputtering)	2 zone tube furnace	140°C	220°C	Ar	1.72 torr	MAI	NA	10.20%	244

6.2 Results and discussion

6.2.1 Vapour transport system development

Figure 6.2a describes the vapour transport deposition (VTD) setup schematically. In brief, it consists in a reaction chamber and a remote evaporation unit connected by a gas transport line. The heated carrier gas (N_2) is fed into the evaporator to drive the evaporated organohalides into the reaction chamber. To prevent organohalides condensation in the evaporator and gas transport lines, the N_2 carrier gas flow is heated prior to the evaporator by heating blankets, as are the gas lines and reaction chamber. A showerhead is placed at the inlet of the chamber to ensure a uniform deposition over the deposition table (which can accommodate up to one 6 inch wafer at this stage). The temperature of the substrates can be varied from 25°C to 180°C (depending on the temperature of the chamber walls). A primary pump is attached to the bottom of the chamber and the overall pressure is controlled by a butterfly valve.
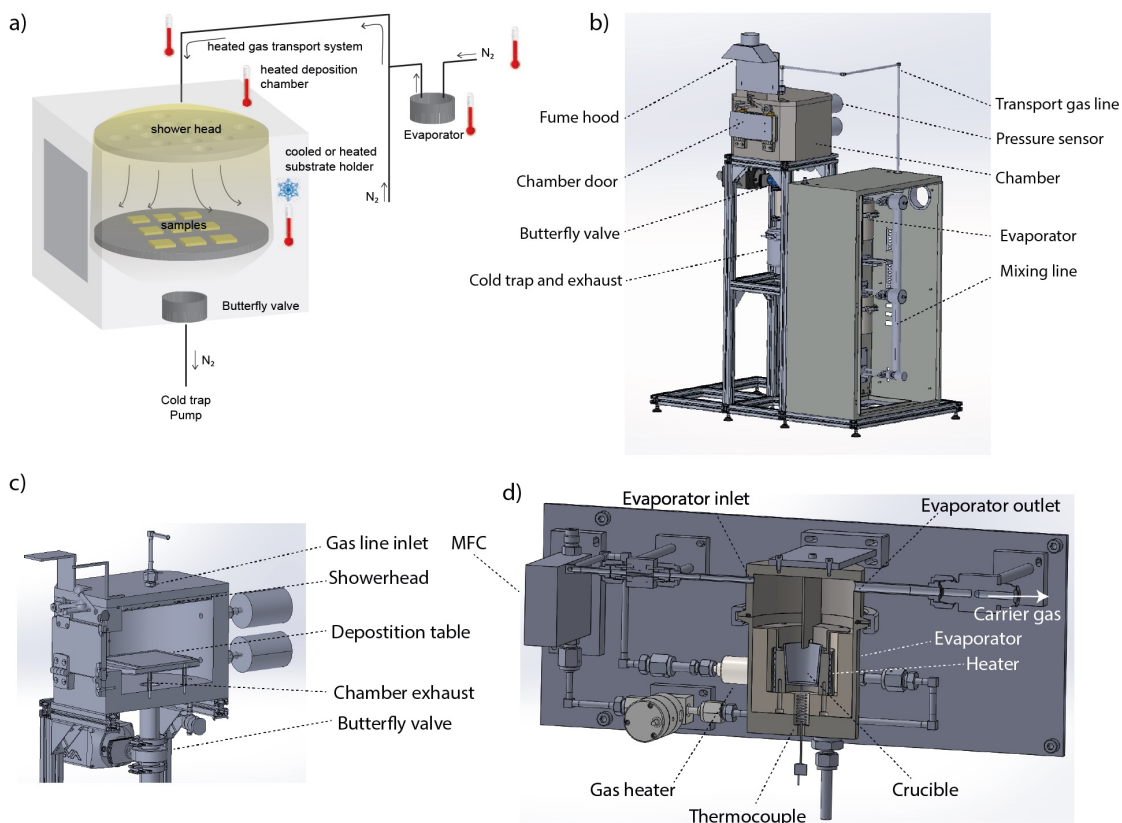

Figure 6.2 – **Schematic views of the custom-made VTD setup.** a) simplified description of working principle of the VTD setup b) view of the overall setup, c) cross-section of the deposition chamber, d) cross-section of the evaporation unit, including the carrier gas arrival, preheating gas unit and the evaporator.

The different components of the system are briefly described below.

Carrier gas inlet N_2 is used as a carrier gas to drive the evaporated organic vapours

from the evaporator into the deposition chamber. A mass flow controller (MFC, range 200-1500 sccm) regulates the carrier gas flow. A carrier gas preheating unit consisting in a commercial tubular heating coil (gas heater, Figure 6.2d) and thermal heating blankets (heating of the gas line up to 150°C is possible) enables to modify the temperature of the carrier gas upstream of the evaporator (Figure 6.3). In the absence of heating blankets, the carrier gas entering the evaporator was found to be < 30°C whether the commercial gas heater was on (at 250°C) or off (Figure 6.3a). The main reason being that the carrier gas cools down passing through the unheated tubes on its way to the evaporator. In addition, the measured gas heater outlet temperature was found to be drastically beneath the targeted temperature (250°C) due to the relatively low pressure reached within the tube. For those reasons, external heating blankets (25-150°C) were added in between the gas heater and evaporator (Figure 6.3b and B.14a). At equivalent temperature setpoint, the carrier gas temperature measured at the heater outlet, evaporator and chamber inlets scales linearly with flow rate, which is mainly due to the improved thermal conductance at higher pressures. For example, at a flow rate of 800 sccm and a preheating gas line temperature setpoint of 150°C, the carrier gas reaches a temperature of 60°C at the evaporator inlet, whereas the temperature of the gas at the inlet of the chamber reaches 100°C (Figure 6.3).
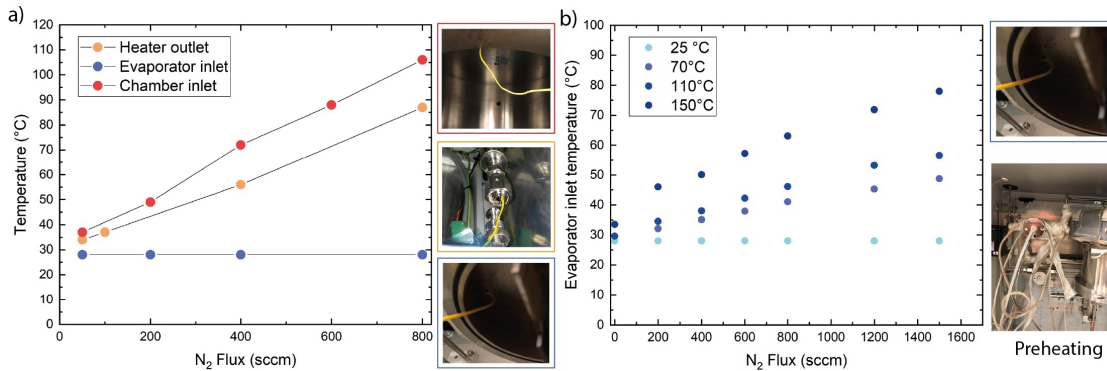

Figure 6.3 – Temperature of the carrier gas at different locations. a) Initial temperature measured at the outlet of the heater (orange), at the evaporator inlet (blue) and at the inlet of the chamber (red) as a function of different carrier gas mass flow, without any additional heating unit. The temperature of the transport line to the chamber is set to 200°C, pictures of the different parts of the setup (inset), b) Temperature measurements at the evaporator inlet as a function of the flow rate and temperature of the heating blanket in between the MFC and the evaporator, pictures of the different parts of the setup and the additional heating blankets (inset). The commercial gas heater setpoint was kept at 250°C for the whole experiment.

Evaporator The upper part of the evaporator is enveloped in heating blanket to prevent organohalide condensation (Figures 6.2d and B.14b). The evaporation of MAI (≈ 1 g) is performed in a graphite crucible, whose temperature is directly monitored by a thermocouple in direct contact with the bottom of the crucible. Figure 6.4 displays a temperature profile of the crucible during evaporation. First, the crucible temperature is increased to the targeted temperature at a rate of 10°C/min, before reaching a steady-state regime with a temperature accuracy $+/- 2\%$. Finally, once the deposition is performed, the temperature of the crucible decreases at a rate of 2°C/min.

Figure 6.4 – Crucible temperature profile during an evaporation. The crucible temperature is increased at a rate of 10°C/min for the first 10 min. After that, a steady-state temperature control within 2% from the setpoint is obtained. The samples are taken out of the chamber when the temperature control of the crucible stops. The system is constantly flushed by N_2 during the ramp-down phase to prevent organohalide condensation in the evaporator and the gas transport line.
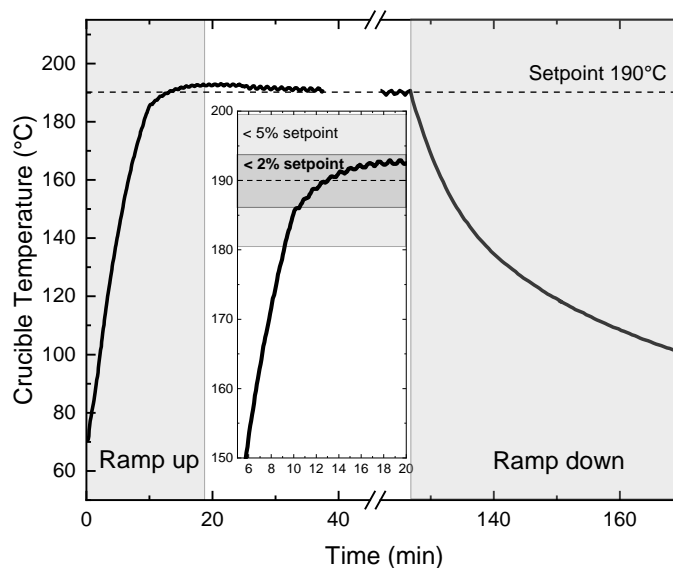
Gas transport line The pipes connecting the evaporator to the chamber can be heated up to 200°C thanks to a heating blanket (Figures 6.2b and B.14d)

Chamber Organohalide vapours carried by N_2 are forced through a showerhead to improve the homogeneity of the deposition (Figures 6.2c and B.14e, inset i). The temperature of the deposition table can be modulated via an oil circuit (from 25°C to 180°C, controlled by a thermocouple). The deposition chamber walls can be heated thanks to the heating blankets (from 25°C to 200°C). For blankets set to 200°C, the temperature measured on the inner side of the chamber reaches $\approx$ 150°C. The temperature of the heating blankets is set to 200°C throughout this chapter unless stated otherwise.

Exhaust The exhaust of the chamber is directly located beneath the deposition table (Figure B.14e, inset ii) and a trap cooled by a water circuit is placed after the chamber to condense the residual organohalides (Figures 6.2b and B.14f). Finally, a butterfly valve is placed after the cold trap to regulate the pressure of the system (at 800 sccm of N_2, a working pressure of 12 mbar is obtained when the value is closed (0% of opening), at 100% of opening, a working pressure of 3.7 mbar is obtained). Finally, a dry pump with a pumping capability of 25'000 L/min is attached to the system.

6.2.2   Characterisation methodology

Sublimation of organic molecules is a complex mechanism. The high temperature ($>$ 200°C) needed to evaporate the organohalides leads to molecule degradation into fragments, creating new chemical species through bonds rearrangement or di-trimerisation.[151, 283, 284] We use here liquid nuclear magnetic resonance (NMR) spectroscopy and Fourier transform infrared (FTIR) spectroscopy to characterise the molecular species resulting from the thermal evaporation of organohalides.

In this work, we are mainly interested in the evaporation of MAI and FAI molecules. As a first step, we characterise both MAI and FAI fresh powders (as purchased). In addition, we will see that the presence of ammonium iodide (NH_4I) is related to the degradation of both MAI and FAI, which will be discussed in detail in the next chapters. As a result, the characterisation of fresh NH_4I powder is also presented in this section.

Characterisation by nuclear magnetic resonance

Liquid ^{1}H, ^{13}C, 2D ^{1}H-^{1}H correlation spectroscopy (COSY) NMR are used to characterise the fresh organohalide (MAI, FAI, NH_4I) samples. Even though liquid ^{1}H NMR spectroscopy is on its own sufficient to identify which chemical species are present, we performed here additional ^{13}C, ^{1}H-^{1}H COSY NMR to confirm the ^{1}H NMR spectroscopy results. We use deuterated dimethyl sulfoxide (DMSO-d6) as a solvent for all the NMR analysis, as it is widely used as solvent for perovskite preparation and thus not harmful to the organic molecule (Figure B.15). For the NMR characterisation, either the organohalide powder, condensate (by organic vapour deposition, OVPD) or perovskite layers are dissolved in DMSO-d6 and introduced in a NMR tube. 1 μl of hydrogen iodide (HI) is added inside the NMR tube to acidify the solution to prevent proton exchange in between the organohalide and the water traces in DMSO.[285] Proton exchange during analysis leads to unresolved and broader amine peaks, making the interpretation more difficult. Adding 1 μl helps resolving the peaks (Figure B.16).

Figure 6.5 shows the NMR characterisation of the fresh MAI molecule. Resonances from the amine NH_3 (7.5ppm) and methyl groups (2.3-2.4 ppm) are easily identified from the ^{1}H NMR spectra (Figure 6.5a, top). Integrating the peaks yields a ratio of $\approx$ 1:1 between the functional groups, as expected for MAI.[285,286] From ^{13}C NMR (Figure 6.5a, bottom), only one peak at 25 ppm is observed which is consistent with the carbon from a methyl group (CH_3). In 2D ^{1}H-^{1}H COSY, cross-peaks (peaks that appear off the diagonal) represent couplings between pairs of nuclei by magnetisation transfer. This means that the peaks appearing off the diagonal represent atoms with two different chemical shifts connected (coupled) by few chemical bonds. For example, the cross-peak appearing at (2.34 ppm, 7.49 ppm) in the 2D ^{1}H-^{1}H NMR tells us that the methyl group (2.34 ppm) is directly connected (as a result of the magnetic coupling) to the amine group within the same molecule, which confirms that the 2 functional groups are part of the same molecule (Figure 6.5b).

Concerning FAI ^{1}H NMR spectra, Figure 6.6a highlights the protons from the amine group (8.65 and 9 ppm). However, these appear at a slightly higher chemical shift due to the presence of the double bond (the double bond is partially delocalised due to resonance). The difference in the chemical shift in between both amines is attributed to the diamagnetic anisotropy of the double bond.[285] The peaks observed at 7.85 ppm correspond to the proton on the carbon atom. The multiplicity arises from the coupling
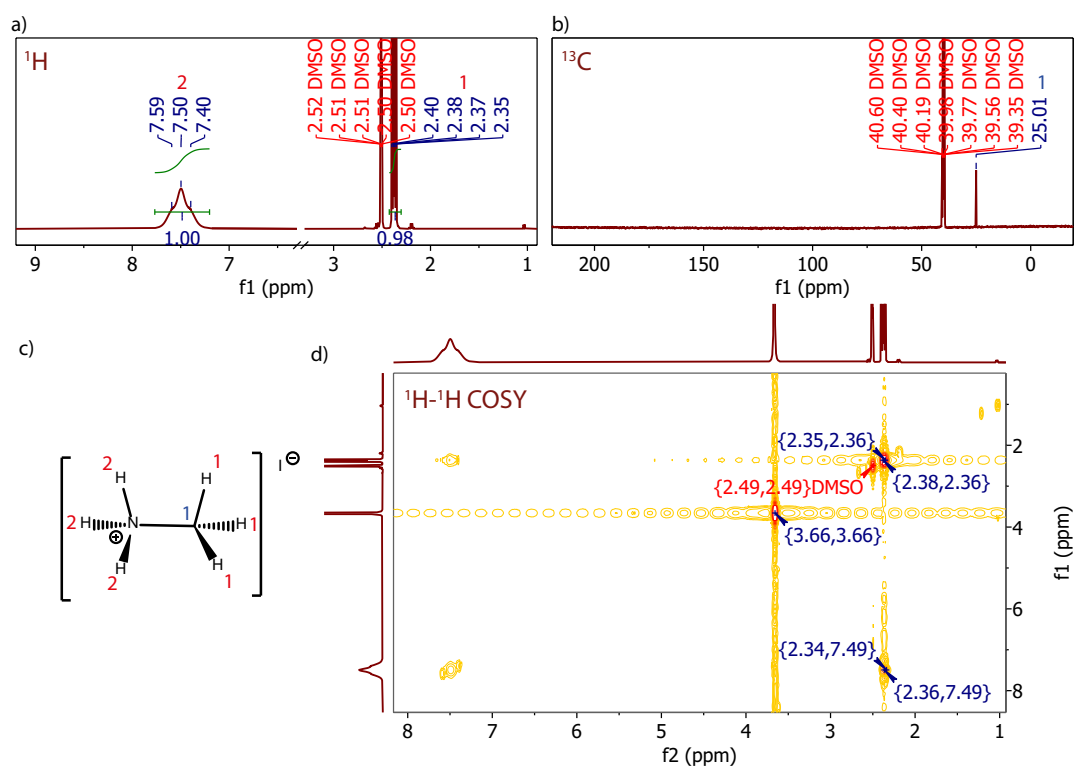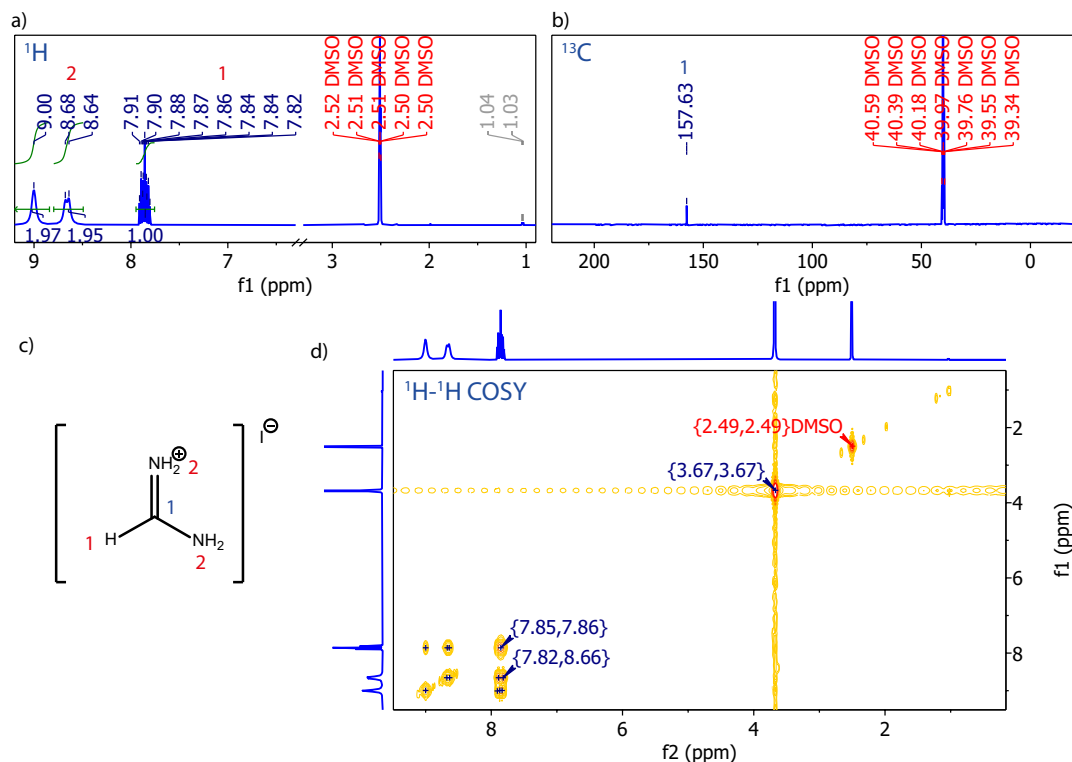
Figure 6.5 – **NMR characterisation of MAI.** a) ^{1}H-proton NMR of MAI in DMSO-d6, b) ^{13}C-carbon NMR, c) MAI molecule, d) 2D [1]H-^{1}H correlation spectroscopy (COSY).

with the 2 amine groups. Integration of the different peaks reveals the ratio of $\approx$ 2:2:1 (amine:amine:carbon in alpha position) as expected for FAI. ^{13}C NMR spectrum indicates the presence of the deshielded carbon peak typical from an alkene (157 ppm). Cross-peak in the 2D ^{1}H-^{1}H COSY NMR again indicates the coupling of the amine groups with the proton on the carbon atom (Figure 6.6b).

Figure 6.6 – NMR characterisation of FAI. a) ^{1}H-proton NMR of FAI in DMSO-d6, b) ^{13}C-carbon NMR, c) FAI molecule, d) 2D ^{1}H-^{1}H correlation spectroscopy (COSY).

As mentioned earlier, the presence of the ammonium cation NH_4^+ highlights the thermal degradation of both MAI and FAI upon sublimation. The presence of the cation arises from the release of ammonia (NH_3) (common product of the degradation of MAI and FAI) which is in acid/base equilibrium with NH_4^+. The presence of NH_4^+ cations and halides lead to the formation of the stable ammonium halide NH_4X compound. The latter could be observed by condensing organohalides on the deposition table of the VTD setup (boiling point, bp = 235°C). In opposition, ammonia (bp = -35°C) is volatile in ambient condition and is thus not detectable. Figure 6.7 shows the NMR characterisation of NH_4I. The presence in the ^{1}H NMR spectra (Figure 6.7a, top) of the three equidistant peaks starting at $\approx$ 7 ppm corresponding to ^{1}H-^{14}N J-coupling is a signature of the NH_4^+ cation.[285] ^{13}C NMR spectra (Figure 6.7a, bottom) shows no peak associated with carbon atoms due to their absence in the molecule. The 2D ^{1}H-^{1}H COSY (Figure 6.7b) shows only the presence of diagonal peaks that indicates the absence of neighbouring nuclei coupling.
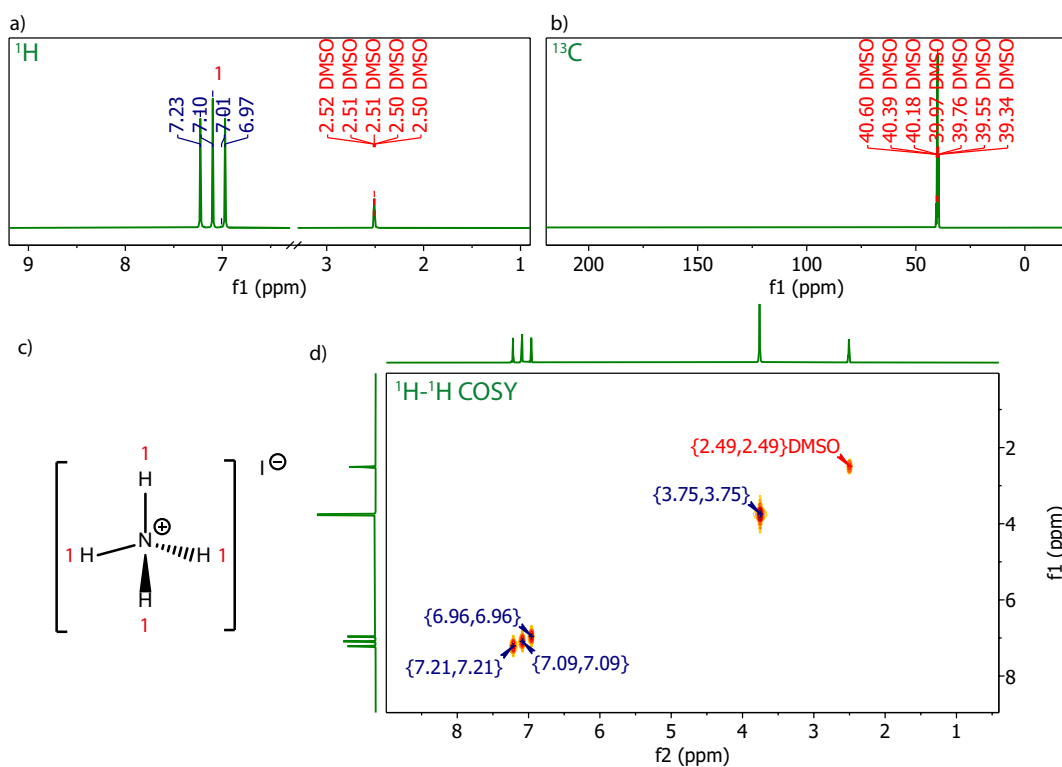
Figure 6.7 – NMR characterisation of ammonium iodide. a) ^{1}H-proton NMR of ammonium iodide in DMSO-d6, b) ^{13}C-carbon NMR, c) ammonium iodide, d) 2D ^{1}H-^{1}H correlation spectroscopy (COSY).

Characterisation by Fourier transform infrared spectroscopy

Fourier transform infrared spectroscopy (FTIR) is also used to identify the different organic molecules present in a sample. FTIR spectroscopy relies on the identification of the different bonds within a molecule based on the infrared absorptance resulting in their vibrational mode (stretching, bending, rocking). As a result, organic molecules exhibit a distinct FTIR signature depending on their chemical bonds. Here, we analysis the IR-transmittance of samples deposited on a silicon wafer (the c-Si is transparent to energies where the vibrations of the organic bond occur). The deposition is either done by condensation in the VTD setup or by spin-coating the organics in isopropanol. Figure 6.8a presents the FTIR spectra of the three different organohalides mentioned above (MAI, FAI, NH_4I). The black curve represents the background of the measurement, *i.e.* the H_2O and CO_2 traces within the measurement chamber. Water molecule presents various vibrational modes in the 1200-1800 (H_2O bending) and 3400-4000 cm^{-1} (H_2O stretching) range, whereas CO_2 mainly posses two vibrational modes at 620 cm^{-1} (O=C=O bending) and 2350 cm^{-1} (O=C=O stretching).[287] The FTIR setup is purged with N_2 to prevent the presence of those parasitic peaks, however the absorption from those molecules can still be observed in the spectra.

We can clearly see from Figure 6.8a that each molecule has its own signature. MAI is mainly identified due to the sharp $C-H_3$ rocking peak at 915 cm^{-1} and the broad N-H stretching peak from the NH_3 group at 3090 cm^{-1}. Due to the two amine ($-NH_2$) groups, FAI exhibits N-H symmetric and asymmetric stretching vibrational modes at 3150 and 3350 cm^{-1}. In addition, FAI can be recognised by the sharp C=N stretching vibration at 1705 cm^{-1}. Similarly as MAI, NH_4I presents a broad N-H stretching peak from the NH_4 group at 3090 cm^{-1}. Furthermore, NH_4^+ deformation is identified at 1388 cm^{-1}. Table 6.2 summarises the different bond vibrational modes found in literature for MAI, FAI, NH_4I and compares them to the ones found in our experiments.

Few changes can occur whether the organic material is analysed alone or in the perovskite lattice as evidenced in Figure 6.8b (N-H stretching shifts to 3188 cm^{-1} and CH_3 rocking contribution vanishes in MALI layer). In addition to the identification of the different organic bonds present, FTIR enables a quantitative analysis of mixed-cation perovskite compositions using these changes in vibrational modes (Figure 6.8c). The intensity of the peak from a given bond scales directly with the number of bonds (or molecules) present in the sample. This analysis is used later on to quantify organohalide depositions made in our VTD system.
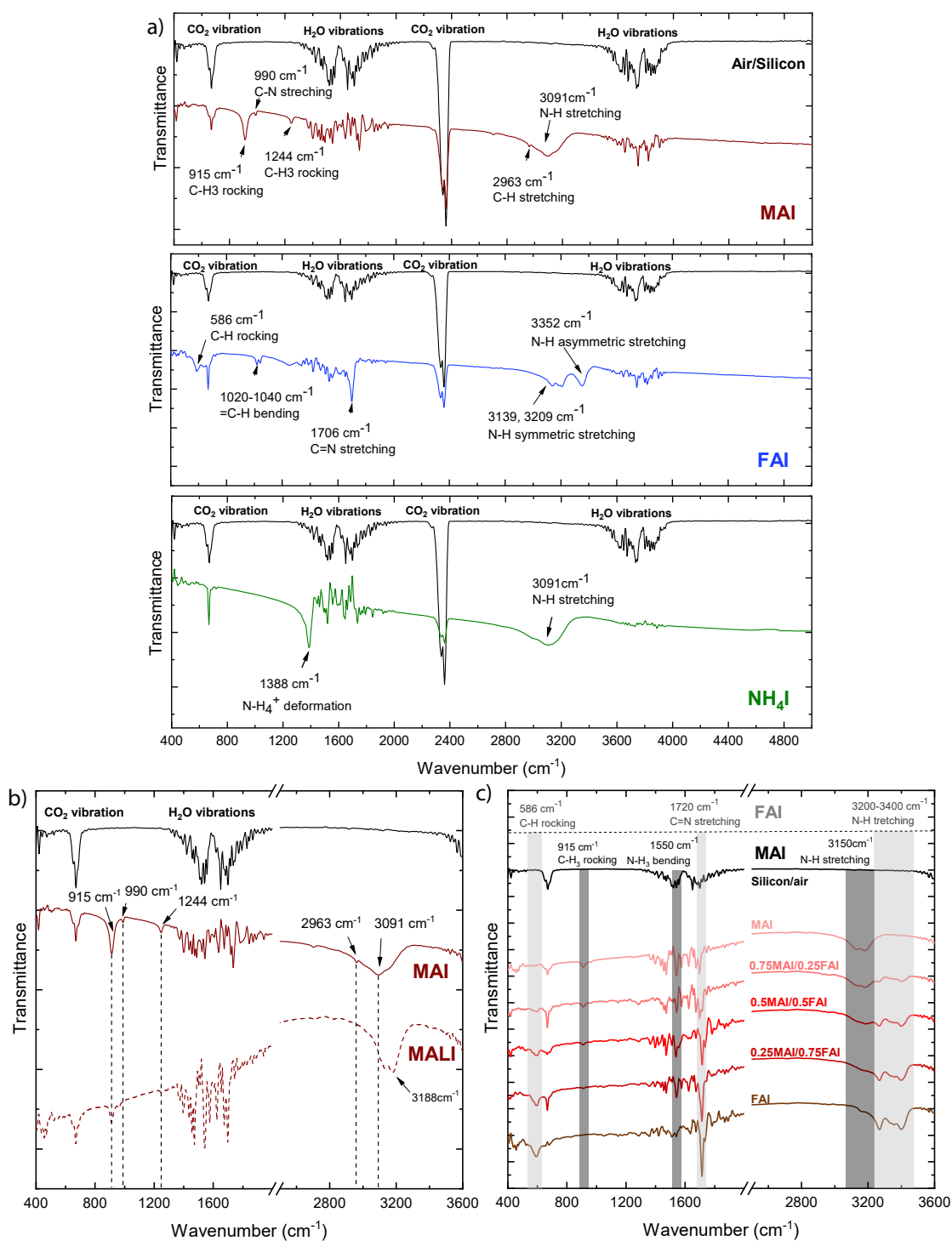
Figure 6.8 – FTIR of spin-coated organohalides. a) FTIR of organohalides spin-coated onto a silicon wafer, b) MAI and MALI IR-transmittance, c) Different perovskites compositions (different MAI and FAI ratios) measured by FTIR.

Table 6.2 – **FTIR vibrational modes in organohalides from literature.**[287–290] C-H and N-H bending contributions appearing in the 1400-1500 cm^{-1} cannot be identified due to the presence of the H$_2$O vibration peaks.

Bond	Vibrational mode	From literature	This work
		Wavenumber (cm^{-1})	Wavenumber (cm^{-1})
N-H$_4$	deformation	1400	1390
N-H$_3$	stretching	3080(as)-2993(sym)	3091
	bending	1486(sym)-1563(as)	H$_2$O peaks
N-H	Strechting	3354(sym)-3399(as)	3200-3300
	bending	1616	H$_2$O peaks
C=N	stretching	1711	1706
C-H$_3$/N-H$_3$	rocking	1252	1244
C-H	stretching	2963(as)-2912(sym)	2963(as)
	bending	1427(sym)-1463 (as)	H$_2$O peaks
=C-H	bending	1049	1040
C-H$_3$/N-H$_3$	rocking	912	915
C-N	stretching	990	990
-C-H rock	rocking	587	580

6.3 Conclusion

In this chapter, we first reviewed the different vacuum-based techniques for perovskite deposition, mainly emphasising sequential two-step methods including a VTD step for the organohalides deposition. Secondly, the home-built VTD system used during this thesis is described. The organohalide evaporation is carried out in an evaporator unit and the vapours are then flushed through the chamber for the reaction with the lead template. This enables to control both the evaporation of the organics and reaction kinetics for the perovskite formation. Finally, the different methods for organohalide identification are presented. ^{1}H NMR and FTIR spectroscopy techniques are used to characterise the as-purchased precursors that will be used later in the VTD system (MAI, FAI, NH$_4$I).

7 MAI deposition by vapour transport deposition

Abstract

To test our VTD reactor, we first focus on MAI evaporation. This chapter investigates organohalides transport to the chamber, substrate temperature effects on deposition kinetics and perovskite formation using the two-step sequential PVD/CVD method. We will see that MAI can be deposited in a wide temperature range (80-150°C) which strongly impacts the perovskite morphology. Proof-of-concept perovskite solar cells that achieve a PCE of 12% on an active area of 0.25 cm^2 are presented. Thanks to the presence of the showerhead and the large size of the chamber, a homogeneous organohalide deposition on textured 6 inch c-Si wafers is demonstrated, a first step towards industrial-scale perovskite/c-Si tandems.[1]

7.1 Introduction

When it comes to evaporated perovskite solar cells, most of the results are based on MALI cells with only few reports dealing with FA-based perovskites. The reason being that MAI evaporation is less challenging than FAI. First, MAI has a higher vapour pressure, which eases its evaporation and reaction with PbI_2. In addition, as already discussed, the atomic size of the MA cation leads to a suitable tolerance factor as opposed to the bigger FA cation that might yield non-photoactive phases (see chapter 1). As a consequence, MAI is used during this chapter to gain further insights regarding organohalide evaporation and transport in our VTD chamber.

7.2 Results and discussion

7.2.1 MAI evaporation investigated by thermogravimetry-mass spectrometry

The first step toward understanding the evaporation of MAI is to identify how the molecule evaporates and what temperature is the most suitable to carry out the evaporation. In that regard, we performed thermogravimetry-differential scanning calorimetry (TGA-DSC) coupled with a mass spectrometer (MS).

Here, we perform TGA-MS analysis on a MAI powder in the temperature range 40-400°C with a temperature increase of 5°C/min (Figure 7.1a). Table 7.1 presents the list of m/z ratios (fragments and molecules) that were included during the TGA-MS experiment. Those m/z ratios are a collection what was reported in the literature. One can see that for temperatures below 170°C, no product is detected (note that the y-axis is displayed in log scale and ion currents below 170°C are principally noise from the background). CH_3I and HI are the first molecules to be observed, followed by NH_3 and CH_3NH_2. MA molecules appear at 225-250°C. These results are in good agreement with what was observed previously by other groups, *i.e.* the parent MAI molecule is not observed directly and CH_3I, HI, NH_3 and CH_3NH_2 molecules are observed instead.[259,283,284] However, it is, based on that experiment, not possible to determine precisely at which temperature each product starts to evaporate.

Table 7.1 – Thermal degradation fragments of methylammonium iodide from literature.[291] m/z values for species marked with an (*) are not included in our TGA-MS experiments.

m/z	Ion	Molecule/Fragment
15	CH_3^+	CH_3I fragment, CH_3NH_2 fragment
16	NH_2^+, CH_4^+, O^+	NH_3 fragment, o_2 fragment, CH_3NH_2 fragment
17	NH_3^+, OH^+	NH_3 parent peak, H_2O fragment
18	NH_4^+	$NH_3 + H^+$ (proton transfer H_2O parent peak)
18	H_2O^+	H_2O parent peak
28	N_2^+	N_2 parent peak
29	CH_3N^+	CH_3NH_2 fragment
30	CH_3NH^+	CH_3NH_2 fragment
30	CH_4N^+	$(CH_3)_3N$ and CH_3NH_2 fragment
31	$CH_3NH_2^+$	$(CH_3)_3N$ and CH_3NH_2 fragment
32	O_2^+, $CH_3NH_3I^+$	O_2 parent peak, CH_3NH_2 fragment
42	$C_2H_4N^+$	$(CH_3)_3N$ fragment
44	$C_2H_6N^+$	$(CH_3)_3N$ Hydrogen dissociation
45	$C_2H_7N^+$	$(CH_3)_3N$ Hydrogen dissociation*
58	$C_3H_8N^+$	$(CH_3)_3N$ parent peak
59	$(CH_3)_3N^+$	$(CH_3)_3N$ parent peak
63	I^{++}	HI fragment*
64	HI^{++}	HI parent*
127	I^+	HI fragment
128	HI^+	HI parent
141	CH_2I^+	CH_3I Hydrogen dissociation*
142	CH_3I^+	CH_3I parent peak
159	$CH_3NH_3I^+$	CH_3NH_3I Methylammonium parent
254	I_2^+	I_2 parent*
317	$(CH_3NH_3I)_2^+$	MAI dimer*

To identify the evaporation temperature of each product, we carried out TGA-MS at constant temperatures. Temperatures selected were relevant ones used in our home-built setup (160-240°C). First, the temperature was increased to 160°C at $\approx 5°C/min$ and stabilised for 30 min to reach steady-state evaporation conditions. The temperature was then further increased by 20°C and stabilised for 30 min at each 20°C interval until 240°C. Figure 7.1b shows the ionic currents of each molecule detected during the analysis. Results are similar to what was observed during the non-isothermal TGA-MS, *i.e.* CH_3I and HI are the dominant species at each temperature. Note that CH_3 and I observed during the experiment are probably fragments of CH_3I and HI appearing due to their ionisation during the MS measurement rather than real products of the evaporation. Interestingly, the MA molecule is only observed at high temperature in both cases ($> 220°C$), whereas it is generally observed at lower temperatures in literature. This discrepancy is likely linked to the loss of the MA and MAI during transport from the TGA to the MS unit. In most MS experiments carried out in the literature, either the connection from the TGA to the MS is continuously heated to prevent condensation of the organohalides or the evaporation and MS analysis are directly performed in a high vacuum chamber, thus preventing material loss during transport. In our particular case, the connection in

between the TGA and the MS is not heated, potentially leading to organohalide (MAI, MA) condensation, hence affecting the analysis.

The NH_3 molecule is hardly observed at temperatures below 240°C. However, it should be in principle detected whenever CH_3I is detected. It is possible that NH_3 reacts with HI and I to form ammonium iodide (NH_4I), which could also condense on the tube in between the TGA and MS unit, preventing its quantification. A second reason might be that NH_3 is harder to distinguish from the O_2 (m/z = 16), H_2O (m/z = 18) backgrounds. Figure 7.1c shows an isotherm measurement at 200°C (where the background was recorded only at 200°C), NH_3 is then clearly detected in this case.

To summarise, we observe by TGA-MS the presence of CH_3I, HI, MA and NH_3 as the main products of the evaporation of MAI, as expected from literature. MA is observed at high temperatures (220-240°C) despite the fact that MA is also probably present at a lower temperatures. Those results suggest that MAI evaporation can be performed up to a temperature of 220-240°C.

7.2.2 Methylammonium iodide transport to the chamber

A high concentration of MAI molecules should reach the chamber to drive efficiently the perovskite formation reaction, which implies that i) a sufficient amount of MAI is sublimed in the evaporator and few MAI molecules either ii) condense during transport to the chamber or iii) degrade during evaporation or transport. To assess evaporation and transport conditions, the substrate holder was maintained at a temperature below the sticking coefficient of MAI (< 80°C) to condense MAI on c-Si or glass/indium tin oxide (ITO) substrates. Condensation on the chamber walls was avoided by maintaining their temperature > 150°C. From the SEM images of Figure 7.2a, evaporating MAI at a crucible temperature ($T_{crucible}$) of 200°C for 150 min yields ≈ 500 nm-thick layers on c-Si (deposition rate of ≈ 0.5Å/s in these conditions). Based on these cross-section images, MAI appears to grow via the Stranski-Krastanov mode on c-Si, complicating a precise thickness assessment.[292]

FTIR transmittance data indicate that the fresh precursor and evaporated MAI are chemically similar, with both featuring the N-H stretching vibration at 3000-3300 cm^{-1} and C$-$H$_3$ rocking at 915 and 1244 cm^{-1} (Figure 7.2b, see Table 6.2 for the different FTIR vibration modes for MAI[288]). Figure 7.3 shows the full series of FTIR spectra of MAI deposited on c-Si with $T_{crucible}$ set to temperatures ranging from 180 to 220°C. Higher evaporation temperatures lead to higher deposition rates, as highlighted by the decrease in FTIR transmittance, higher MAI mass loss from the crucible and increased deposited layer thickness.

The chemical structure of the deposited layers is investigated by ^{1}H nuclear magnetic resonance spectroscopy (^{1}H NMR) (Figure 7.2c). Resonance from the amine NH_3 (7.5
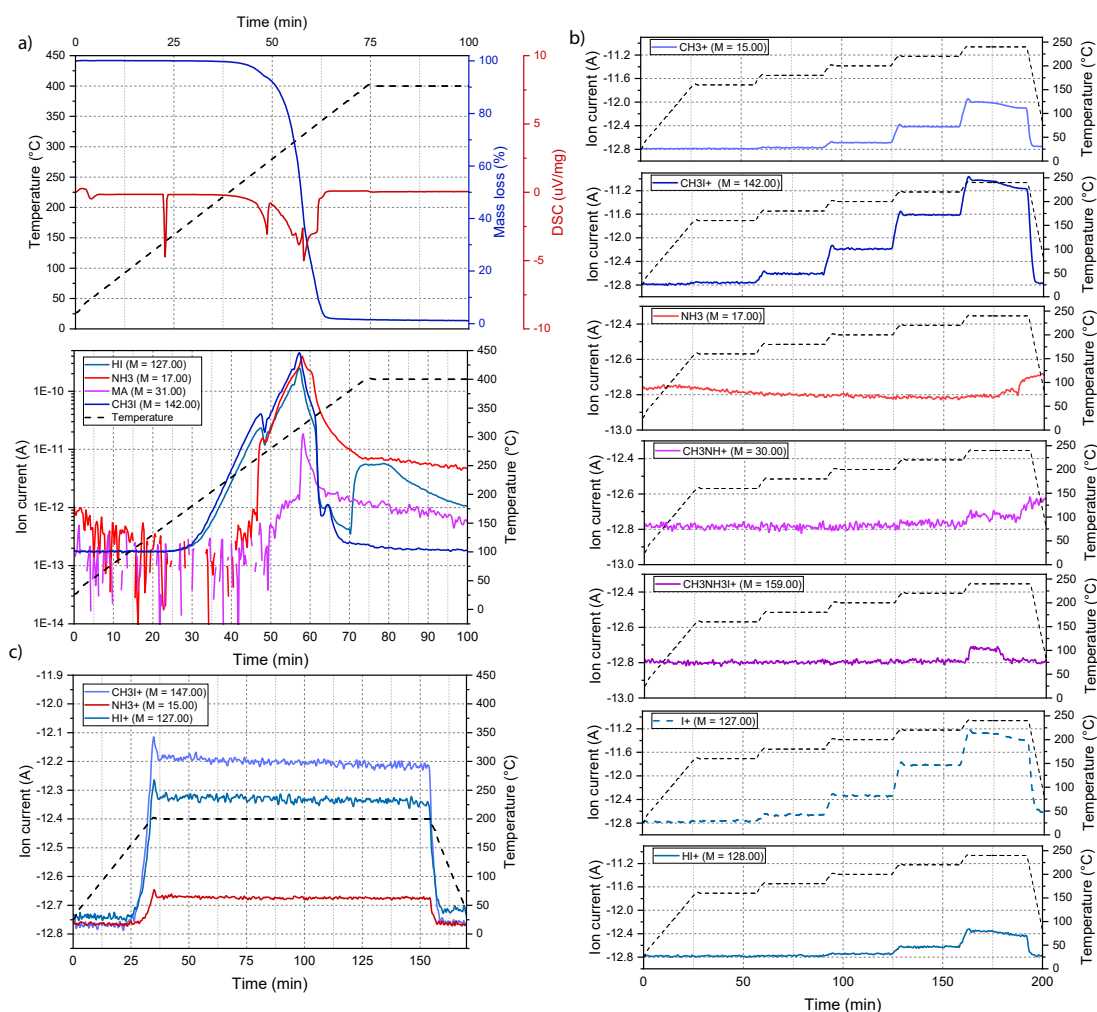
Figure 7.1 – **Isothermal thermogravimetric-mass spectrometry (TGA-MS) analysis of methy-lammonium iodide.** a) Total TGA-MS analysis of MAI (20-400°C), b) TGA-MS isotherms (30 min) of MAI (160-240°C), c) isotherm at 200°C.
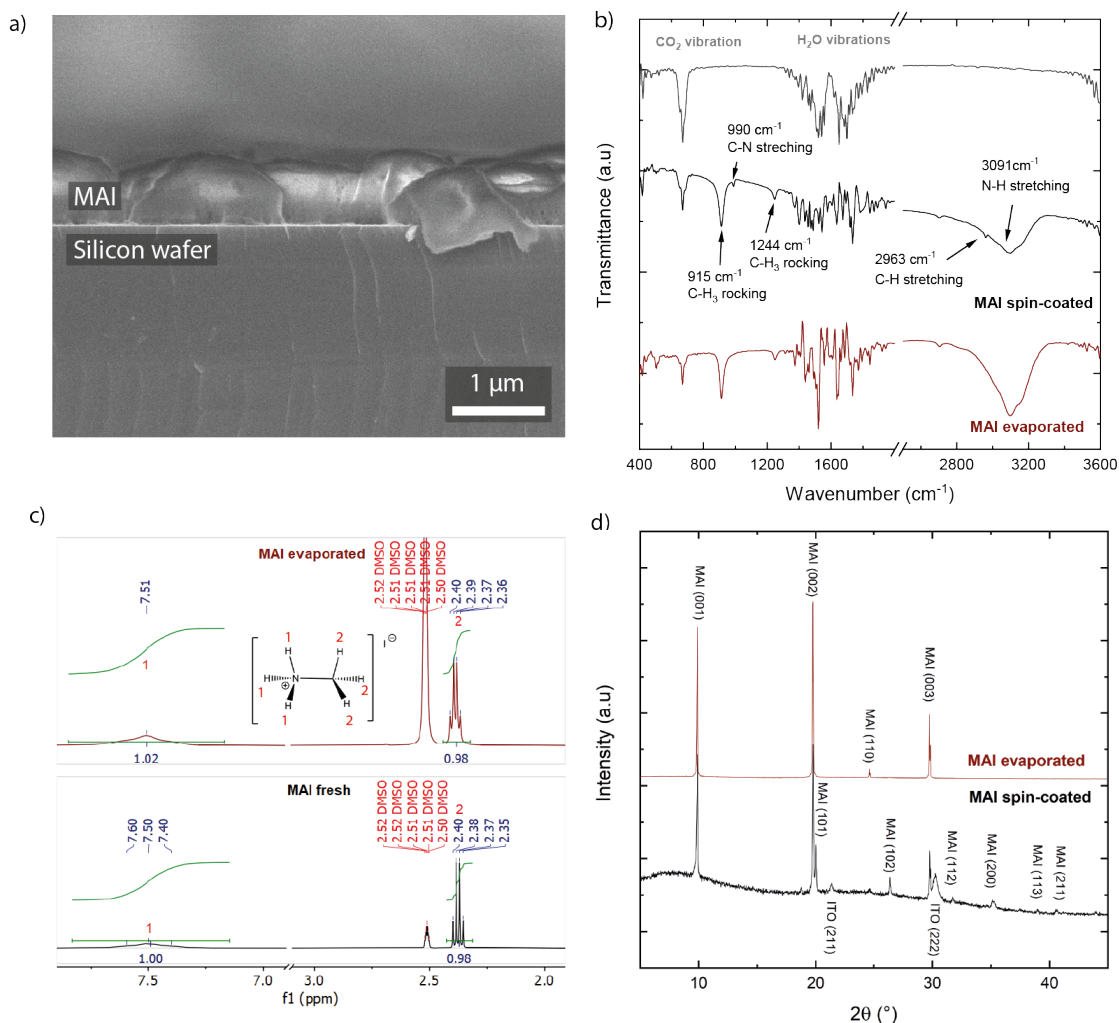
Figure 7.2 – **Characterisation of MAI deposited in the VTD chamber.** a) SEM cross-section image of MAI deposited on top of a c-Si wafer at 70°C for 150 min, b) FTIR spectra of the spin-coated (black) and evaporated (brown) MAI on top of a silicon wafer, c) Liquid ^{1}H NMR of as purchased (black) and evaporated (brown) MAI (left), scheme of the MAI molecule (right), d) X-ray diffractograms of as purchased (black) and evaporated (brown) MAI on top of a glass/ITO substrate.
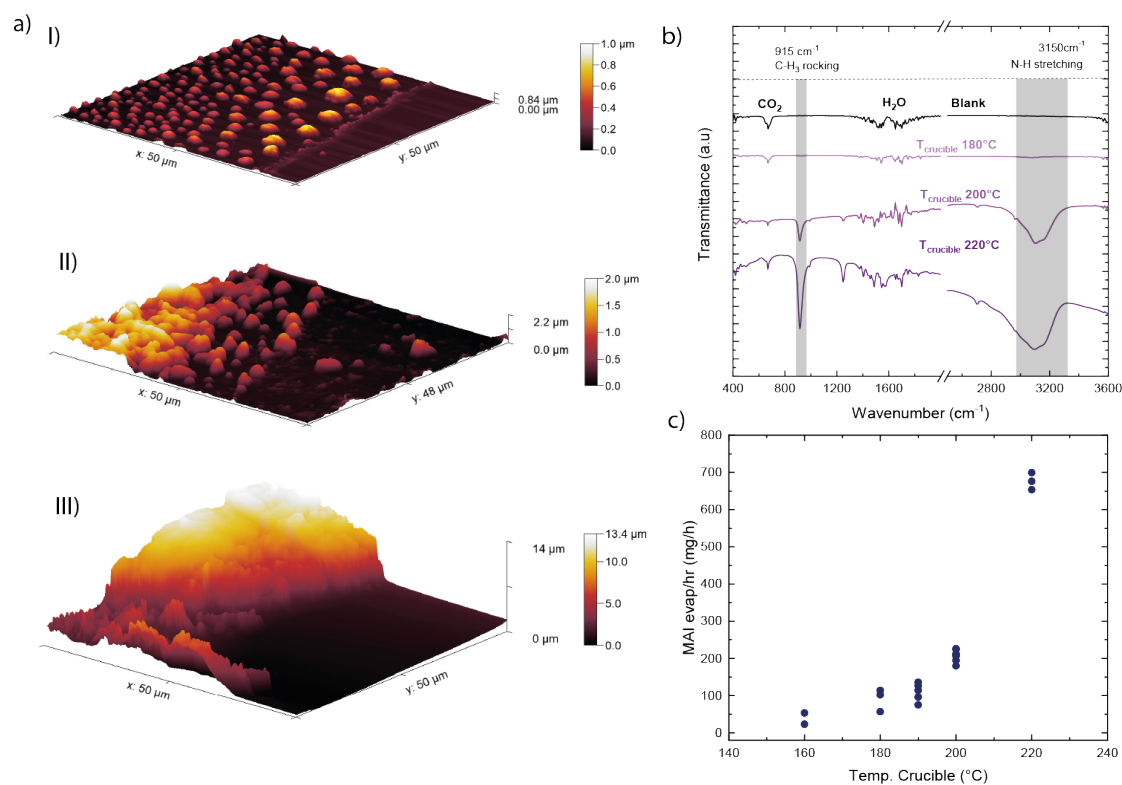
Figure 7.3 – **MAI deposited at different crucible temperatures.** a) 3D AFM images of the MAI on a silicon wafer (deposition table at 70°C) for 2 h with the crucible held at 180°C I), 200°C II) and 220°C III). To determine the thicknesses of the depositions, the right part of the scan was covered by a Kapton tape and removed before measuring the AFM maps, b) FTIR transmittance spectra of the corresponding MAI deposition, c) mass loss (in mg/h) measured in the crucible during evaporation as a function of the crucible temperature setpoint.

ppm) and methyl groups (2.3-2.4 ppm) is similar to that obtained for spin-coated MAI layers, confirming the presence of pure MAI when $T_{crucible}$ is set to 200°C. Integrating the peaks yields a ratio of $\approx$ 1:1 in between both functional groups, as expected for MAI.[285, 286] The ^{1}H NMR spectra of Figure 7.4 indicate that pure MAI is deposited when evaporating at a $T_{crucible}$ of up to 200°C, while some degradation occurs at 220°C. The presence of the three equidistant peaks starting at $\approx$ 7 ppm indicates that NH_4^+ cations are also present in the film.[285] The presence of the NH_4^+ cation, even though it is not directly detected in the TGA-MS measurement (Figure 7.1), comes from the degradation of MAI into NH_3 and CH_3I. NH_4^+ is the result of the reversible protonation of ammonia. The powder inside the crucible remains chemically pristine, even after heating at 220°C for 2 hours (Figure 7.5).
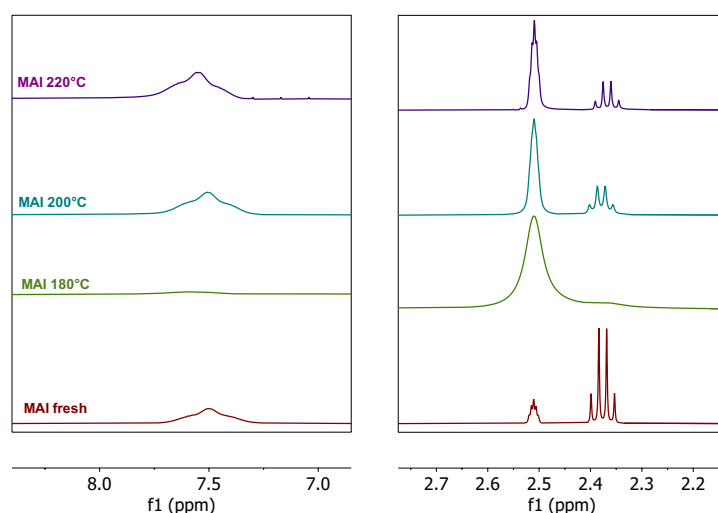
Figure 7.4 – **Liquid ^{1}H NMR of MAI depositions (carrier gas = 800 sccm, Working pressure = 4 mbar, duration = 2 h) at different evaporation temperature.** Fresh MAI powder (brown), $T_{crucible}$ = 180°C (green), $T_{crucible}$ = 200°C (light blue), $T_{crucible}$ = 220°C (purple).

A small amount of impurities is identified in the powder left in the crucible after 5 evaporations ($>$ 10 h of evaporation at 200°C), as indicated by the presence of small peaks (2.8-3.2 ppm and 8.0-8.5 ppm) in the ^{1}H liquid NMR (Figure 7.6). Furthermore, these impurities are not observed in the MAI deposited on the table for the fifth evaporation, leading to the conclusion that the same MAI powder can be used for several evaporations. MAI is deposited in its tetragonal phase (space group P4/nmm) based on X-ray diffractograms (Figure 7.2d).[293]

The gas line that connects the evaporator to the chamber must remain at high temperature to prevent any MAI condensation within the tubes. MAI does not reach the chamber when setting the gas line temperature ($T_{gas\,line}$) to 100°C (Figure 7.7). Increasing this temperature to 150°C and 200°C ensures MAI transport to the chamber, in larger quantity for the latter case (Figure 7.7).
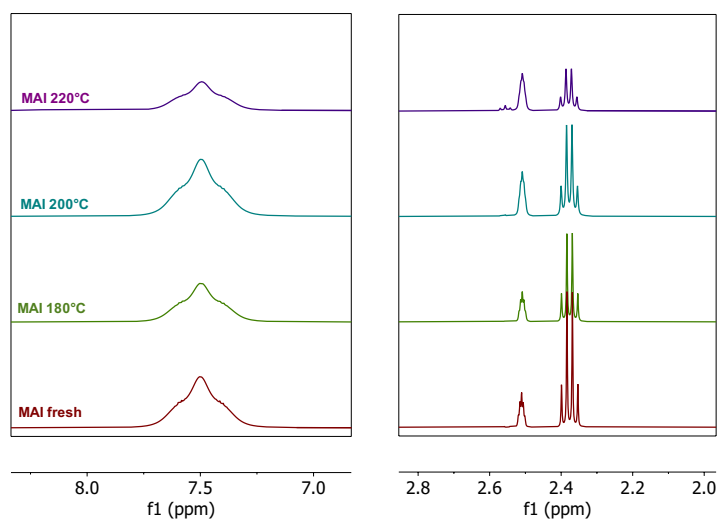
Figure 7.5 – Liquid ^{1}H NMR of the MAI powder left in the crucible after different evaporation temperatures. Fresh MAI powder (brown), $T_{crucible} = 180°$C (green), $T_{crucible} = 200°$C (light blue), $T_{crucible} = 220°$C (purple).
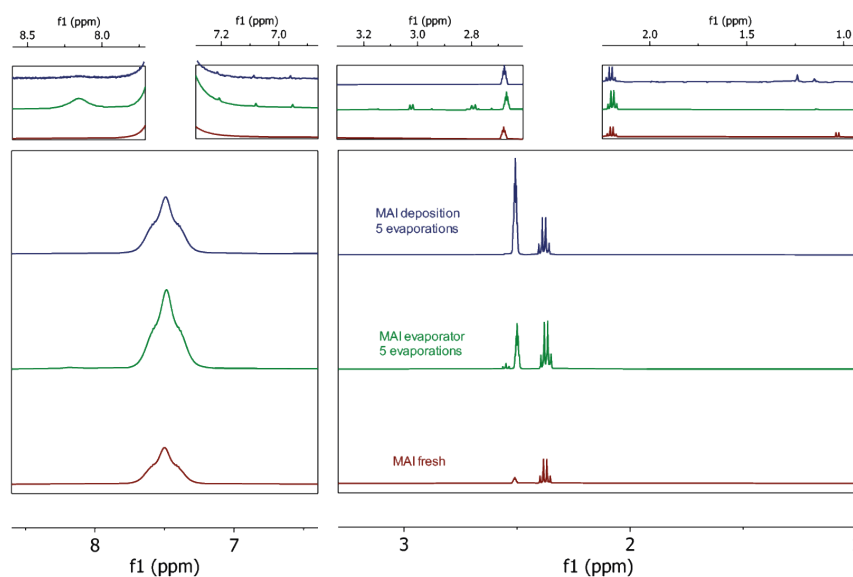

Figure 7.6 – Liquid ^{1}H NMR of the MAI deposited on the table and the MAI powder left in the crucible after 5 depositions (> 10 h of deposition). Liquid ^{1}H NMR of the fresh MAI powder, MAI left in the crucible after 5 depositions (carrier gas = 800 sccm, working pressure = 4 mbar, duration > 10 h) and MAI deposited after 5 deposition onto the deposition table without changing the MAI powder in the crucible (carrier gas = 800 sccm, working pressure = 4 mbar, duration > 10 h).
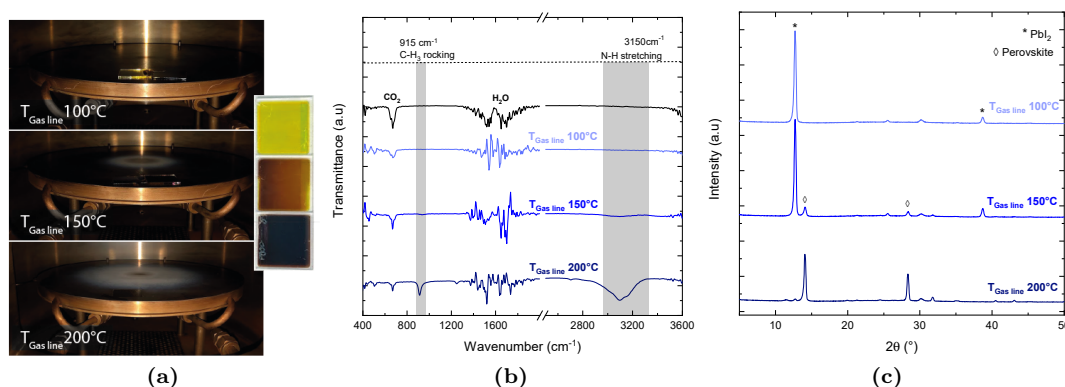
Figure 7.7 – **Impact of the gas line temperature.** a) Pictures of the table after deposition (table at > 50°C, $T_{crucible}$ = 200°C, carrier gas = 800 sccm, working pressure = 4 mbar for 2 h) with the gas line (in between the evaporation and chamber) at 100°C (top), 150°C (centre) and 200°C (bottom), corresponding picture of the perovskite layers deposited(inset), b) FTIR spectroscopy of the MAI deposition deposited on a silicon wafer with the gas line at 100°C (light blue), 150°C (blue), 200°C (dark blue), c) X-ray diffractograms of the perovskite layer deposited with the gas line at 100°C (light blue), 150°C (blue), 200°C (dark blue). The showerhead was removed for this experiment.

Preheating of the carrier gas prior to the evaporator is also essential to avoid any MAI condensation before the chamber. We can see that, in the absence of the carrier gas preheating ($T_{Preheating}$ = 25°C), almost no MAI molecules reach the chamber, preventing the conversion of the PbI_2 layer to perovskite (Figure 7.8). Similar results are obtained by preheating the tube at 80°C. A preheating setpoint of 150°C leads to a large MAI amount within the chamber and a full perovskite conversion.

In the absence of *in-situ* monitoring of the deposition rate, the evolution of the mass loss in the crucible can be taken as a figure-of-merit for the evaporation rate as already demonstrated for the crucible temperature measurements. In Figure 7.9, the mass loss as a function of different evaporation parameters such as working pressure, flow rate, deposition time and gas preheating is analysed. As discussed above, the crucible temperature setpoint has the most significant impact on the evaporation rate, although it was found that the process working pressure and preheating of the carrier gas also play a role. The effects of those processing parameters onto the mass losses are discussed briefly here.

Carrier gas (sccm) (Figure 7.9a). The influence of the carrier gas flow rate on the sublimed MAI loss is complex as the temperature of the incoming N_2 flux depends strongly on the flow rate itself. This effect will also affect the mass loss experiment. In addition, in order to keep the working pressure in the range of 12-13 mbar for the different experiments, the butterfly valve was opened at 13% for 1500 sccm experiment, 0% for 800 sccm and 0% for 200 sccm with an additional mixing gas flow rate of 600 sccm to stay in the same pressure range. We can clearly see that more material sublime at 200 sccm. Even though the effect is not fully understood yet, we think this is due to the fact that the relatively cold temperature of the carrier gas cools the powder and thus diminishes the evaporation rate. A higher flux means stronger cooling capacity of the
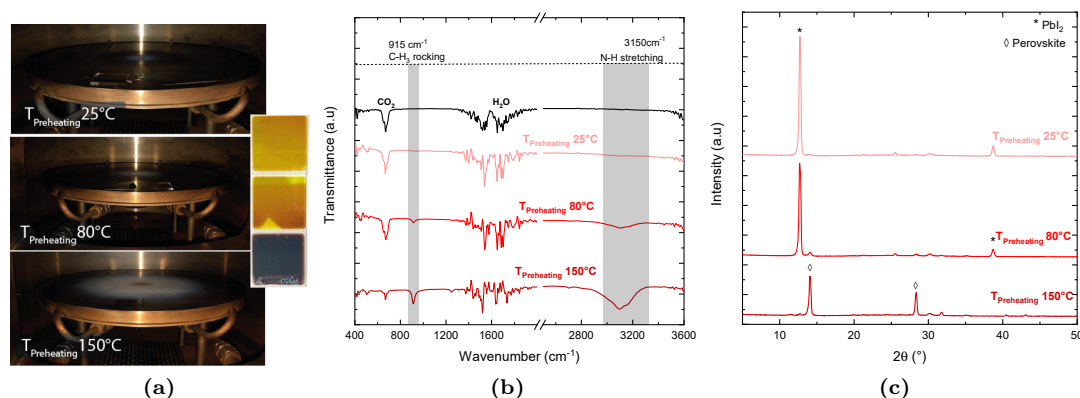
Figure 7.8 – **Impact of the carrier gas preheating temperature.** a) Pictures of the table after the deposition (table at $< 50°C$, $T_{crucible}=200°C$, carrier gas = 800 sccm, working pressure = 4 mbar for 2 h) with different temperature of the preaheating gas lines (before the evaporator), no preheating (top), 80°C (centre) and 150°C (bottom), corresponding perovskite layers formation (inset), b) FTIR spectroscopy of the MAI deposition on a silicon wafer with preheating the gas line at room temperature (25°C) (light blue), 80°C (blue), 150°C (dark blue), c) X-ray diffractograms of the perovskite layer deposited with the gas line at 100°C (light blue), 150°C (blue), 200°C (dark blue). Note that the temperature of the carrier gas at the inlet of the evaporator is dependant on the gas flow and is lower than the tube temperature. The corresponding gas temperature is 29°C without preheating, 40°C for gas line preheating of 80°C and 60°C for a gas line preheating of 150°C (see Figure 6.3). The showerhead was removed for this experiment.

powder. Nevertheless, a higher flow rate is also correlated with an increase in carrier gas temperature, which also increases the sublimation rate (Figure 7.9b) and explains why at 1500 sccm the sublimation rate is enhanced in comparison to 800 sccm.

Preheating of the pipes (°C) (Figure 7.9b). A preheating of the pipes increases the carrier temperature from 25°C to 65°C at 800 sccm. The increased temperature of the carrier gas at the inlet of the evaporator positively impacts the sublimation rate. This observation is coherent with the effect of the temperature of the crucible.

Evaporation duration (min) (Figure 7.9c). Several depositions from $t = 0$ min (crucible ramped up to setpoint and cooled down) and t = 320 min were performed. One can observe that MAI sublimation follows a linear trend, which suggests a good reproducibility. t = 0 min corresponds to the ramp-up to the temperature setpoint and cooling down to $< 100°C$ without any dwell time. ≈ 40 mg of MAI was evaporated during the process.

Working pressure (mbar) (Figure 7.9d). Increasing the working pressure lowers the sublimation rate, as expected.

Crucible temperature (°C) (Figure 7.9e). As the temperature increases, the vapor pressure of the organic material should increase exponentially according to the Clausius-Clapeyron relation. We confirm that the mass loss of the MAI molecule follows a similar trend. This implies that by increasing the temperature by 10°C, the vapour pressure of the organohalide is measured to increases by a factor of ≈ 1.64.

115

Initial MAI mass (g) (Figure 7.9f). The effect of the initial mass of MAI in the crucible is more complex to analyse. While it seems that there is indeed a correlation between the initial mass and the mass evaporated, the correlation is neither linear nor reproducible (saturation after 2.5 grams). We suspect that the powder/crucible contact area changes from one experiment to the other, which may affect the sublimation rate.
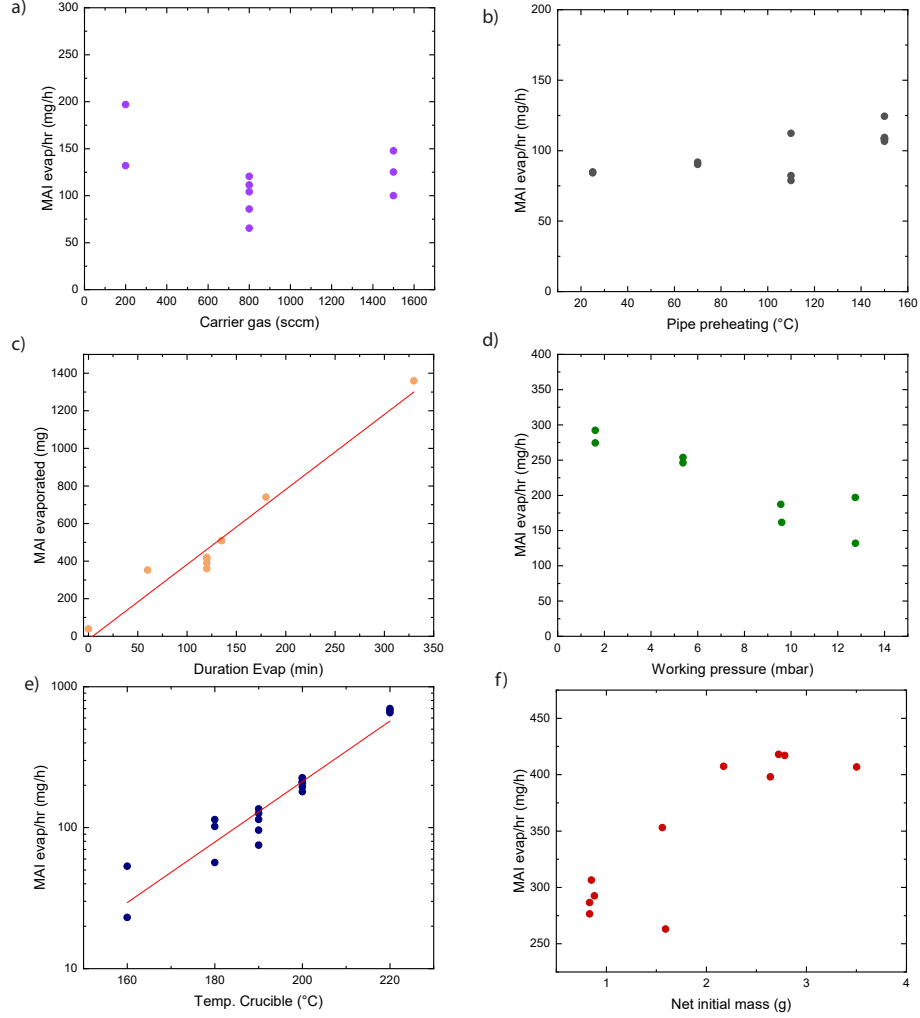

Figure 7.9 – Mass loss analysis as a function of evaporation parameters. Mass loss (in mg/h) measured in the crucible during evaporation as a function of a) the carrier gas flow rate, b) preheating gas temperature, c) duration of the evaporation (total mass evaporated given in mg on y-axis), d) working pressure, e) crucible temperature setpoint (y-axis is displayed in log scale), f) initial MAI mass. During all evaporations, for the sake for reproducibility and if not stated otherwise, deposition parameters are: $\approx$ 1 g of MAI, $T_{crucible} = 200°C$, carrier gas = 800 sccm, working pressure = 12 mbar, duration $\approx$ 2 h, $T_{preheating} = 150°C$.

7.2.3 Vapour phase interaction and perovskite formation

In CVD conditions, the growth conditions of the perovskite layer, and hence its morphology, strongly depends on the substrate temperature $(T_{substrate})$.[261,263] Furthermore, the

sorption/desorption of the organic molecule also depends on $T_{substrate}$.[259] Figure 7.10 investigates the effects of a $T_{substrate}$ varying from 80°C to 160°C. In that regard, a glass/PbI_2 (150 nm) template, previously deposited by thermal evaporation, is placed on the deposition table. Three different perovskite formation regimes are observed. First, when the temperature of the deposition table is kept at relatively low temperature ($<$ 100°C), a significant amount of MAI directly condenses on the surface (Figure 7.10b), first reacts with PbI_2 to form $MAPbI_3$, before further accumulating on the surface when PbI_2 has been fully consumed (Figure 7.10c). Oversaturation of MAI on the perovskite layer leads to the formation of a hydrated $(CH_3NH_4)_2PbI_6{\cdot}2\,H_2O$ phase (when the layer is in a humid environment at room temperature).[288] Annealing this hydrated phase at 100°C for 10 min reverses the crystal structure to a mixture between the photoactive perovskite α-phase and MAI (Figure 7.11).
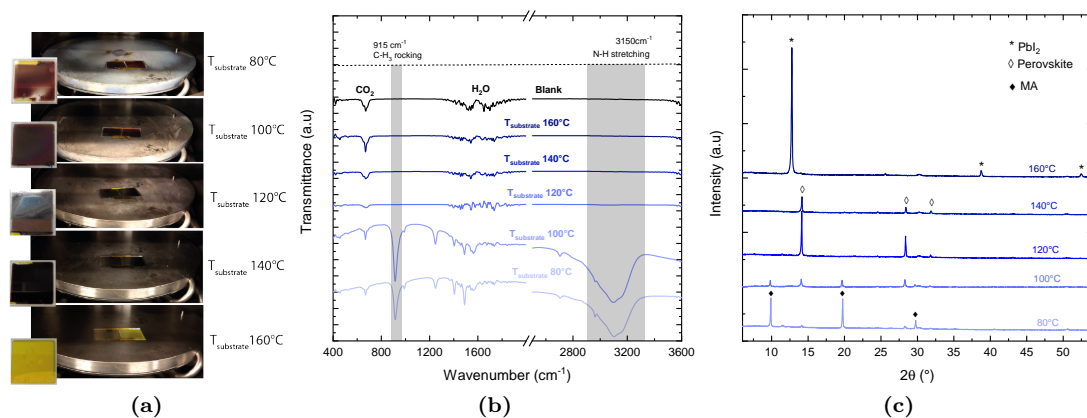
Figure 7.10 – **Effect of the table temperature on the deposition of MAI.** a) Picture of the deposition table and perovskite layers (inset) as a function of the table temperature, b) corresponding FTIR characterisation of the deposited MAI layer, c) X-ray diffractograms of the corresponding perovskite layers.

For a $T_{substrate}$ between 120°C and 140°C, few or no organics are observed to condense on the deposition table and a pure perovskite α-phase is found to form via XRD, indicating that an equilibrium between MAI adsorption, desorption, and its reaction with PbI_2 has
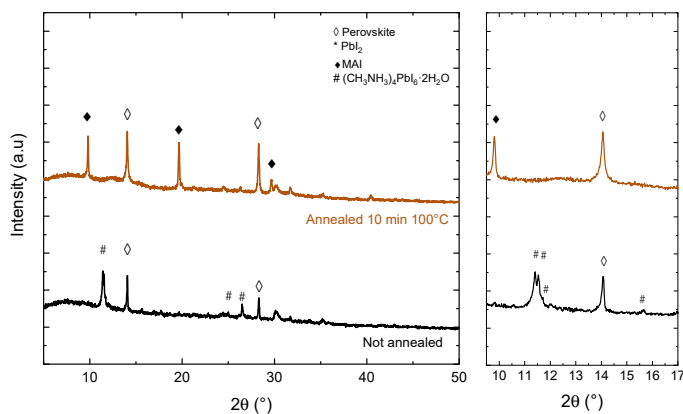

Figure 7.11 – **X-ray diffractograms of overstaturated PbI_2 layer and dihydrate formation.** X-ray diffractograms of overstaturated PbI_2 layer with MAI forming the dihydrate $(CH_3NH_3)_4PbI_6$ $2\,H_2O$ phase, and the same film annealed for 10 min at 100°C showing the perovskite and MAI tetragonal phases.

been reached.[259] Finally, at a temperature of 160°C, no reaction occurs between PbI_2 and MAI after 2 hours of deposition, likely due to the temperature being too high for MAI to absorb on PbI_2.

To gain further insights on the mechanisms of MAI desorption, MAI films deposited on a c-Si wafer were annealed at 100°C, 120°C and 140°C in atmospheric and low vacuum (0.15 mbar) conditions (Figures 7.12 and 7.13). While MAI desorbs for each condition tested, irrespective of the vacuum level, the process is slow at 100 and 120°C. When increasing the temperature to 140°C, MAI films are fully desorbed within 2 hours (in atmospheric conditions) and 15 min (in low vacuum conditions), indicating that the deposition rate of MAI should be sufficiently high to counterbalance desorption.
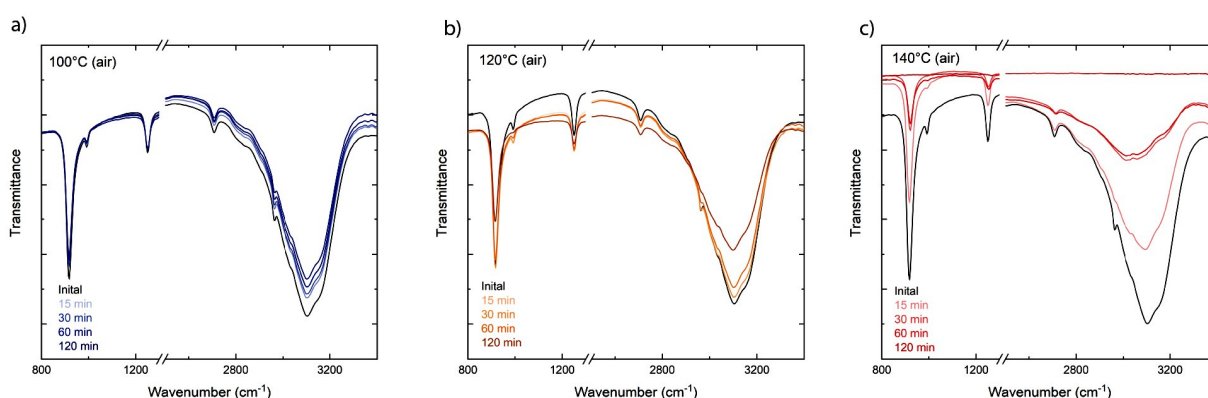
Figure 7.12 – **FTIR transmittance spectra of MAI films annealed at different temperature in air.** ($T_{crucible}$ = 200°C, carrier gas = 800 sccm, working pressure = 12 mbar, duration ≈ 4 h). Films are heated at 100°C a), 120°C b) and 140°C c) in air for 2 h. The FTIR transmittance is measured after 15 min, 30 min 60 min and 120 min. Only few MAI molecules desorb from the film at 100°C, at 120°C only significant desorption occurs after 120 min. At 140°C, a significant amount of the MAI molecule already desorbs after 15 min, and total desorption is observed after 120 min.
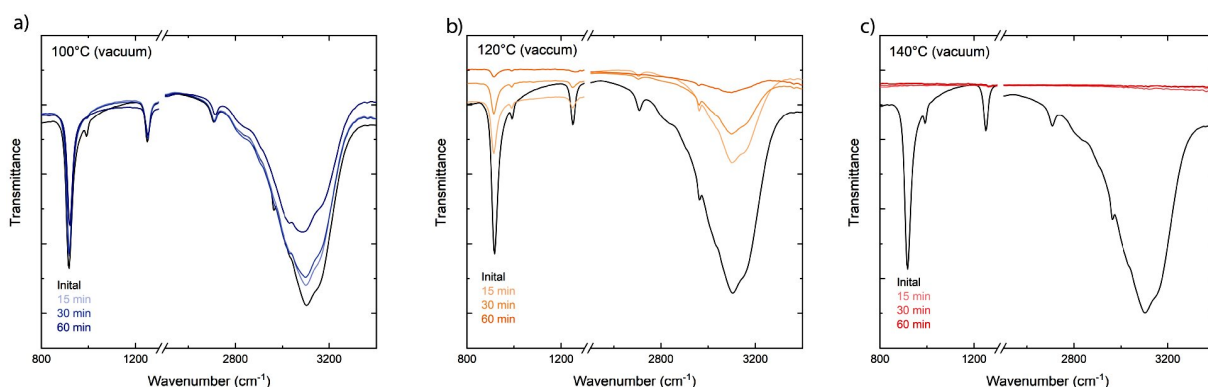

Figure 7.13 – **FTIR transmittance spectra of MAI films annealed at different temperatures in vacuum.** ($T_{crucible}$ = 200°C, carrier gas = 800 sccm, working pressure = 12 mbar, duration ≈ 4 h). Films are heated at 100°C a), 120°C b), and 140°C c) under vacuum (0.15 mbar) for 60 min. The FTIR transmittance is measured after 15 min, 30 min 60 min and 120 min. Few MAI molecules desorb from the film at 100°C but desorption happens already after 15 min, at 120°C most of the MAI molecules have desorbed after 15 min, however desorption is not complete after 60 min. At 140°C, total MAI desorption is observed after 15 min already.

Figure 7.14 further investigates the influence of $T_{substrate}$ on the perovskite conversion process. The perovskite formation reaction occurs faster as $T_{substrate}$ is kept low (for the same evaporation parameters), leading to a full perovskite conversion in less than 1 hour at 80°C. On the other hand, the full conversion is observed after 2 hours at 120°C, with the difference resulting from the differences in adsorption and desorption rates.
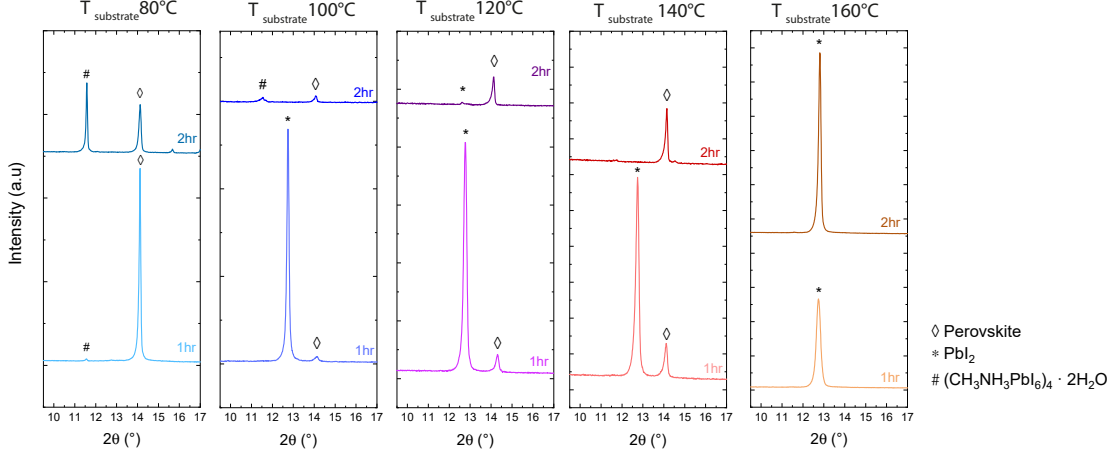

Figure 7.14 – **Perovskite layer formation at different table temperatures as a function of the deposition time.** X-ray diffractograms of the perovskite layer at different table temperature (80°C, 100°C, 120°C, 140°C) and time (1 h, 2 h), deposition parameter are $T_{crucible} = 200$°C, carrier gas = 800 sccm, working pressure = 12 mbar.

Figure 7.15 displays the morphology evolution from the PbI_2 template to the perovskite formation during a CVD deposition with $T_{substrate} = 120$°C. First, we observe that for the first 2 hours of deposition the perovskite phase forms and exhibits large grains and a full lead iodide to perovskite conversion (Figure 7.14). During prolonged deposition duration (> 3 h), as no more PbI_2 is available for reaction, organic material will start to accumulate at the surface of the film, creating clusters. In addition to the formation of those clusters, perovskite grains start to dewet from the substrate, creating pinholes through the layer. EDX top view mapping (Figure 7.15b) acquired at 3 different locations support that hypothesis. These clusters are mainly composed of carbon and iodine and are probably MAI. EDX spectra acquired in between dewetted grains reveal a large amount of indium and oxygen, corresponding to the presence of bare ITO. Note that according to simulations (Casino simulation software), for a 10 keV acceleration voltage and assuming a perovskite density of (3.7 g/cm^3), the electron interaction volume is deeper than the perovskite layer thickness (> 600 nm). As a result, the elemental analysis by EDX provides only a convoluted view of the different morphological features (Figure B.17).

Similar trends are observed for depositions performed at $T_{substrate} = 140$°C (even though organohalides accumulation seems to be less pronounced), suggesting that pinholes formation and organohalide saturation is hard to avoid at these deposition temperatures. These observations indicate that the duration of the evaporation is of significant importance.

119

A too-short deposition time leads to the presence of residual PbI_2, whereas prolonged deposition might lead to MAI accumulation and grains dewetting. In both cases, the efficiency of the perovskite solar cell will be affected.
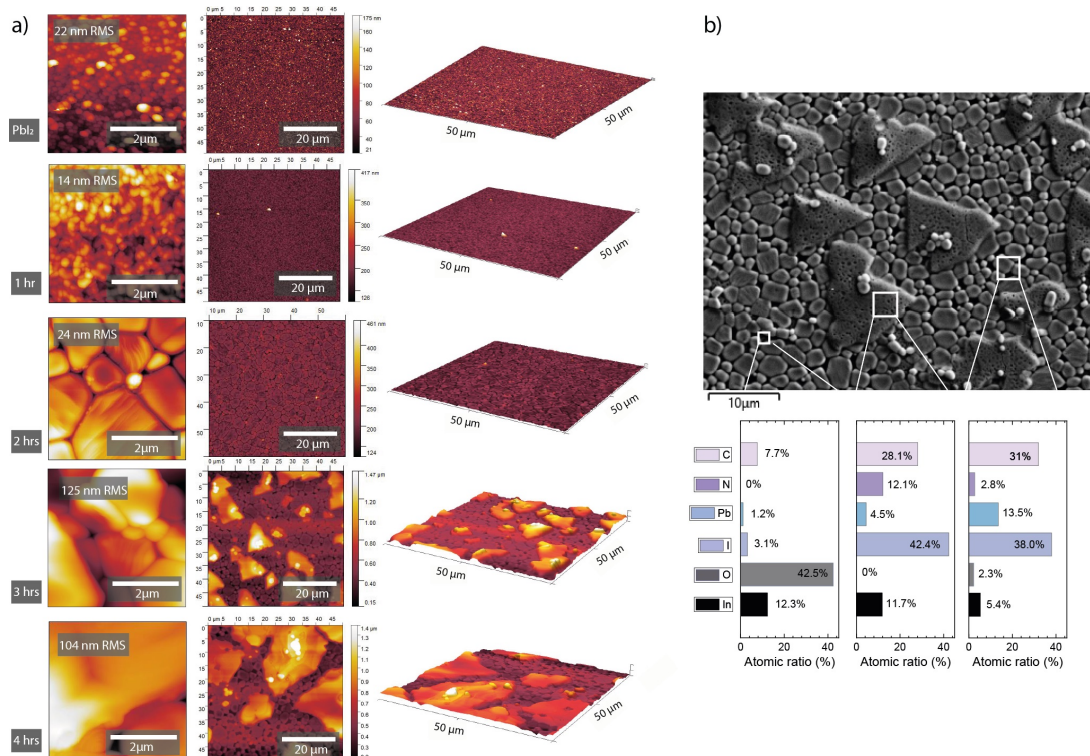

Figure 7.15 – Perovskite layer morphology as a function of the CVD deposition time. a) AFM maps, 2D 5 x 5 μm^2 scale (left), 2D 50 x 50 μm^2 scale (middle), 3D 50 x 50 μm^2 scale projection, b) Top-view SEM image of the perovskite layer after 4 h of CVD deposition (top), EDX acquired at 10 keV at several locations (bottom).

In addition to its influence on the perovskite formation kinetics, $T_{substrate}$ also impacts the perovskite morphology (Figure 7.17). Higher temperatures lead to a larger perovskite grain size, with some grains reaching lateral dimensions exceeding 800 nm at 140°C. At a $T_{substrate}$ of 120°C, similar grain sizes and morphologies are obtained for layers processed by the PVD/SP and PVD/CVD methods. Similarly, by maintaining $T_{substrate}$ constant and by varying $T_{crucible}$ from 180°C to 220°C, the perovskite conversion rate can be controlled (Figure 7.18).

a)

b)

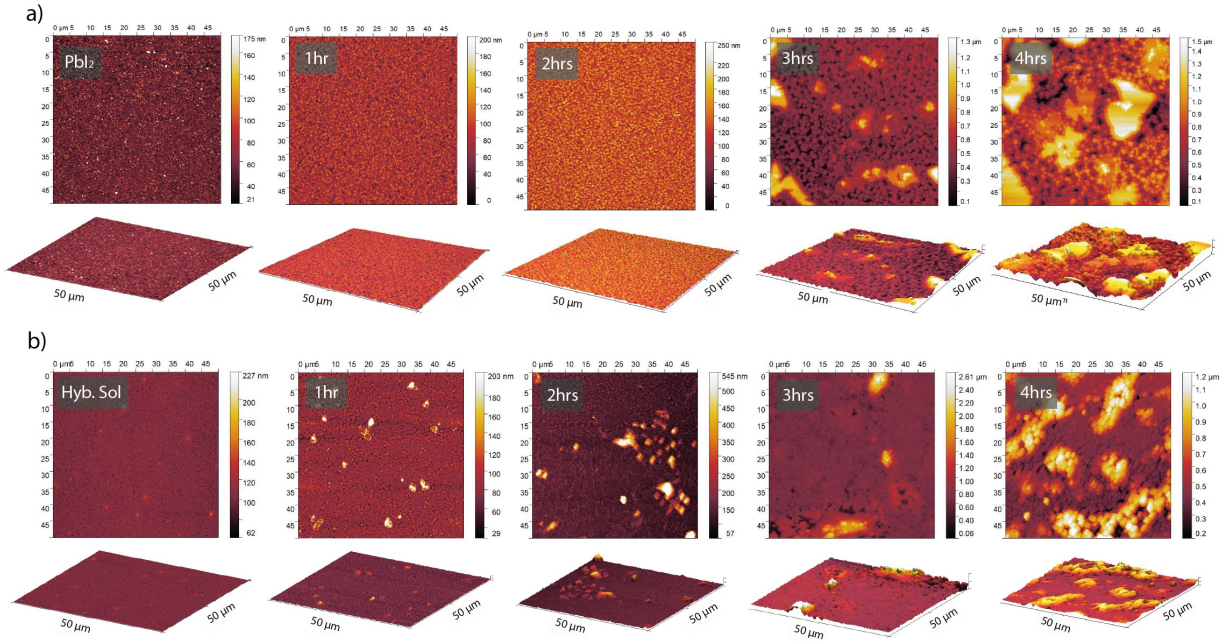**Figure 7.16** – **Atomic Force microscopy (AFM) of the perovskite layer morphology as a function of the CVD deposition time.** a) 2D 50 x 50 μm^2 view AFM maps of the evolution (0-4 h) of a PbI$_2$ layer during CVD at 140°C, b) 2D 50 x 50 μm^2 view AFM maps of the evolution (0-4 h) of a MALI layer fabricated by the hybrid PVD/SP method during a MAI CVD at 140°C.
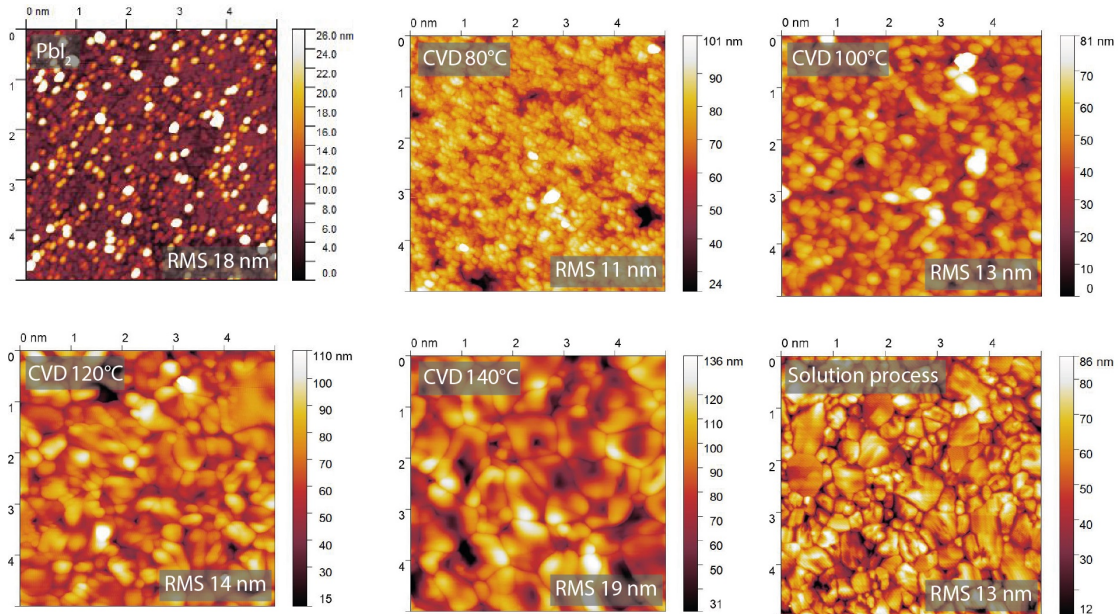

Figure 7.17 – **Perovskite grain size as a function of the table temperature.** 2D AFM images of the PbI$_2$ and perovskite layers deposited at 80°C, 100°C, 120°C, 140°C. A perovskite fabricated by the PVD/SP method is shown for comparison (30 min annealing at 120°C after the spin coating step).
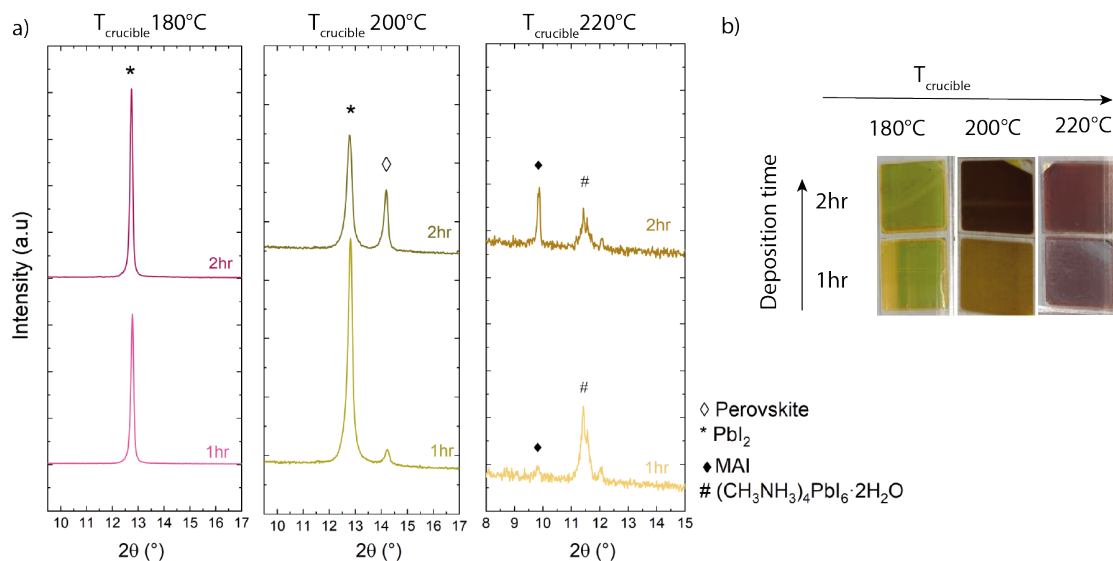
Figure 7.18 – Perovskite layer formation at different crucible temperatures. a) X-ray diffractograms of the perovskite layer at different crucible temperatures (180°C, 200°C, 220°C) with time (1 h, 2 h), b) Picture of the perovskite layers.

7.2.4   Proof-of-concept devices

Based on the results presented earlier, $T_{substrate}$ and $T_{crucible}$ were set to 120-140°C and 200-210°C, respectively. In these conditions, a full conversion of the PbI_2 template to the perovskite is achieved after 2-3 h of evaporation based XRD and UV/Vis/NIR absorptance data (Figure 7.19). Figure 7.20 compares the morphology of cells featuring layers processed by two hybrid processes: PVD (PbI_2)/SP (MAI) and PVD (PbI_2)/CVD (MAI). From cross-sectional and top-view SEM images, morphologies resulting from these two methods appear similar (Figure 7.20).
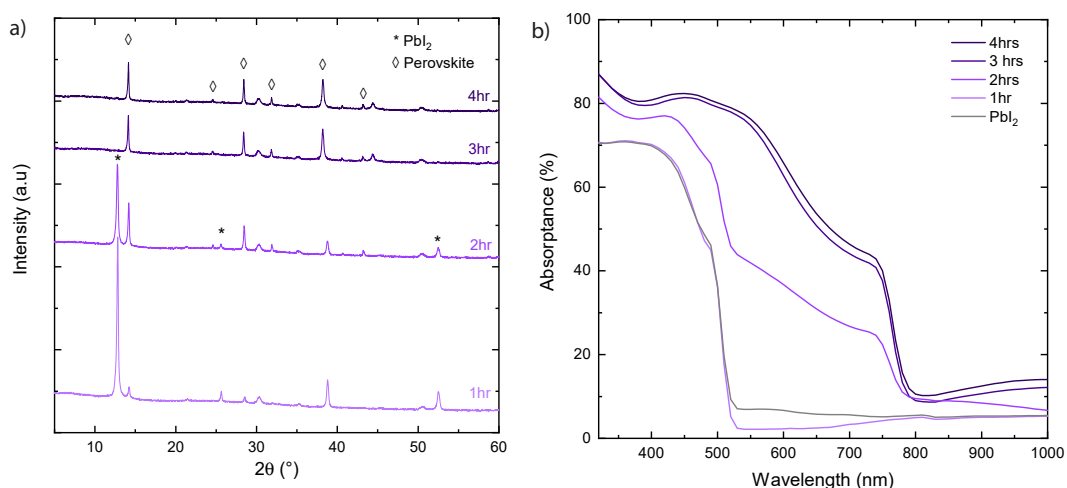

Figure 7.19 – X-ray diffraction and spectrometry perovskite formation with time. a) X-ray diffractograms of the perovskite formation over time, b) UV-Vis-NIR absorbance of the same layers.
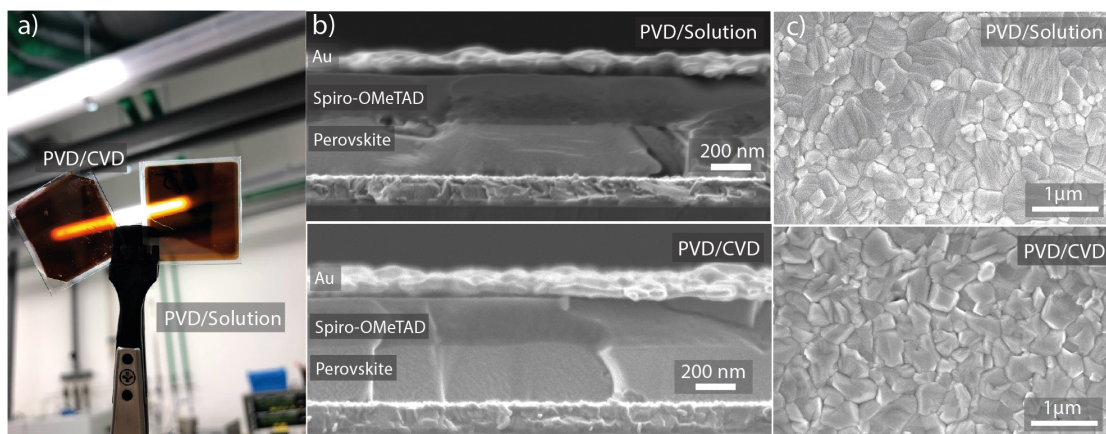
Figure 7.20 – **Morphology comparison of perovskite layers deposited by sequential hybrid PVD/SP and PVD/CVD.** a) Picture of the perovskite layer produced by the sequential hybrid solution (right) and CVD (left) methods, b) cross-section, c) top-view SEM images of the perovskite layers.

Perovskite solar cells are fabricated in the n-i-p configuration using ITO as a substrate. First, 1 nm of LiF and 6 nm of C_{60} is thermally evaporated on top of a glass/ITO substrate. Then, 150 nm of PbI_2 is thermally evaporated in a high vacuum chamber at 1 Å/s. The PbI_2 template is converted to the perovskite phase by CVD of MAI as described above ($T_{crucible}$ = 200°C or 210°C, 800 sccm, $T_{substrate}$ = 120°C or 140°C, $T_{preheating}$ = 150°C, $T_{gas\,line}$ = 200°C, working pressure = 12 mbar, Duration = 1-3 h). The samples are transferred to a nitrogen-filled glovebox and washed by IPA to remove any MAI excess. The samples are then annealed for 5 min at 120°C on a temperature-controlled hotplate to remove the IPA excess. A solution of spiro-OMeTAD dissolved in chlorobenzene is then spin-coated at 4000 rpm for 30 s. Finally, 100 nm of gold is evaporated at a rate of 1 Å/s as the electrode. PVD/SP cells are fabricated following the same procedure with the exception that the organohalide (0.5M MAI in ethanol) are spin-coated on top of the lead template and annealed for 30 min at 120°C. A sketch of the device structure is presented in Figure 7.21a. More information regarding device fabrication is given in the appendix (subsection A.1.3).

J-V parameters of perovskite solar cells fabricated with the PVD/CVD method with $T_{substrate}$ = 120°C and 140°C indicate that 2 h of deposition leads to the best results in both cases (Figure B.18 and B.19). This is in good agreement with the previous results obtained, where we concluded that short deposition duration leads to unreacted PbI_2 and prolonged deposition duration to organohalide accumulation on the layer (Figure 7.14). Furthermore, it is found that $T_{substrate}$ = 140°C gives more reproducible results than $T_{substrate}$ = 120°C, regardless of the deposition duration (Figure B.18 and B.19). This is mainly attributed to the fact that a lower $T_{substrate}$ leads to an oversaturation of the film in organohalides, thus preventing carrier collection.[294] J-V and EQE measurements of the best perovskite solar cell are presented in Figure 7.21b-c, showing a reverse scan efficiency of 12.3%, value which is on par with the cells produced with the hybrid PVD/SP methods.

External quantum efficiency (EQE) data of the perovskite cells in figure 7.21c, indicate that the main difference in efficiency for the different deposition methods comes from the reduced current density. The discrepancies in current-densities seem to come from a collection issue rather than an optical loss (broadband EQE reduction). Even though the precise reason for that collection loss is still not well understood, we suppose that the principal causes could be related to i) the delamination of the perovskite grains observed in Figure 7.15 leading to higher grain boundary recombination ii) the presence of organic materials (MAI, hydrated phases) at grain boundaries and surfaces that prevent charge collection,[294] iii) smaller carrier diffusion length in the PVD/CVD perovskite.
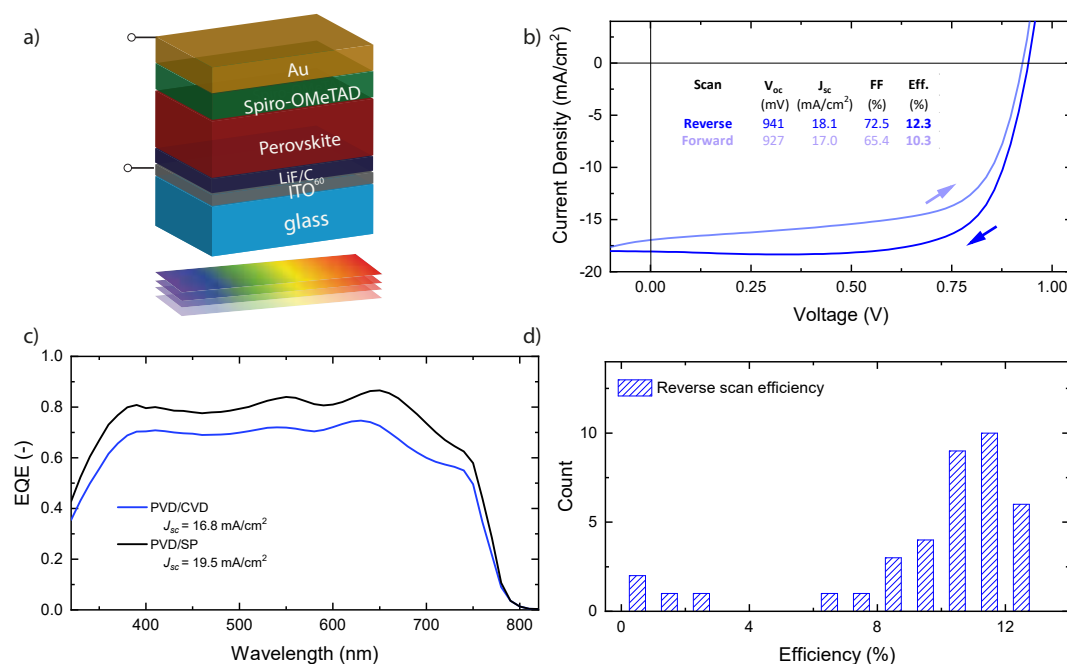

Figure 7.21 – **Perovskite solar cells by sequential hybridPVD/CVD and PVD/SP methods.** a) Device schematic image of the perovskite cell, b) Best forward and reverse *J-V* curves, c) External quantum efficiency (EQE), d) Statistical efficiency distribution (reverse scan) for perovskite solar cells fabricated by the PVD/CVD processes.

Another reason explaining the difference in efficiency between the PVD/SP and PVD/CVD methods comes from the ITO layer underneath the perovskite and of the ETL. Indeed, ITO degrades in acidic conditions.[295,296] As discussed previously, the evaporation of MAI involves the formation of acidic hydrogen iodide as a by-product. Such strong acid can deteriorate the ITO properties during the evaporation. Figure 7.22 displays the evolution of the optical and electrical properties of the underlying ITO layer during evaporation in our VTD setup. To characterise the ITO layer, the perovskite layer was dissolved by a DMSO solution (note that the same treatment was done on the fresh ITO substrate to rule out the effect of the solvent on the ITO properties). We can conclude that the optical and electrical properties of the ITO are not changing drastically during the first 2 hours of evaporation, even though the ITO morphology already starts to change. However, after 2 h of deposition, the ITO resistivity increases drastically, its roughness increases

and pinholes start to form (Figure 7.22c). EDX maps taken after 4 hours of evaporation indicate that indium and tin start to cluster, whereas oxygen accumulates at the grain boundaries. In consequence, these results indicate that ITO is not suitable for prolonged exposure to MAI by-products. Fluorinated tin oxide (FTO) that features better acidic stability was also tested. This, however, did not lead to an overall efficiency increase (Figure B.20). Nevertheless, this effect might be directly linked to sub-optimal interfaces between the C_{60} and FTO, judging by the poor performances obtained for the reference PVD/SP cells (Figure B.21). In addition, other ETLs (spin-coated PCBM, and compact TiO_2 layers) were used. Overall, current-density losses are observed in most cases (Figure B.21), indicating that this loss comes from the perovskite absorber itself.

Even though the PVD/CVD approach is still coming short efficiency-wise compared to the best PVD/SP cells, one can notice that the statistical distribution of devices from several batches suggests higher yield for perovskite solar cells fabricated with the PVD/CVD approach (Figure 7.21d). These results are encouraging regarding manufacturing over large areas with a high yield.

7.2.5 Large scale conformal coating of perovskite layers

Vapour phase deposition method should enable to coat homogeneously larger areas compared to spin-coating,[243, 246] as hinted by several CVD studies.[252, 265] Currently, perovskite layers grown by CVD have been deposited over an area of up to 100 cm^2 (in a tube furnace).[244, 267] The vapour transport deposition system presented here enables depositions over larger areas, as highlighted by the SEM cross-sectional images of MAI deposited at low $T_{substrate}$ (Figure B.22). While some local roughness resulting from the growth mechanism of MAI is noticed, a similar thickness is measured across the full wafer.

Homogeneous perovskite layers are deposited over 15 x 15 cm^2 glass substrates by exposing a 150 nm-thick PbI_2 template to MAI ($T_{substrate}$ and $T_{crucible}$ of 120°C and 200°C, respectively). As shown in Figure 7.23, a thickness difference of 8% relative is measured across this area, a difference that mainly comes from the inhomogeneity of the PVD step. X-ray diffraction patterns acquired at the centre, middle and edge of the substrate confirm the presence of a pure $MAPbI_3$ layer across the substrate (Figure 7.23).

In addition to large-area deposition, such vapour-based deposition system enables conformal coatings on various substrate textures,[10, 243, 244] a promising feature in view of designing perovskite/c-Si tandems featuring bottom cells textured on both sides for optimal light management. Figure 7.24a shows a picture of a perovskite layer grown on a KOH-textured 6 inch c-Si wafer. SEM cross-section images confirm the conformal deposition of the perovskite layer. Figure 7.24b shows cross-section SEM images of the perovskite layer on textured c-Si at various locations. The XRD patterns indicate a full conversion of the PbI_2 template to $MAPbI_3$ across the wafer area. These results

emphasise the suitability of the vapour transport deposition system presented here to deposit perovskite layers over large areas and various surface textures.

7.3   Conclusion

This chapter detailed a versatile showerhead-based vapour transport deposition system that enables the deposition of MAI. The system is able, over large areas and various substrate textures, to convert a PbI_2 template to a photoactive $MAPbI_3$ perovskite phase through an exposure to MAI vapours. Advantageously, this system decorrelates the precursor evaporation conditions from the deposition ones, providing a wider processing window compared to conventional tube furnaces. A wide range of optical, microstructural, crystallographic and chemical characterisation techniques were combined to identify the optimum evaporation, gas transport and deposition conditions. Absorbers processed by converting a thermally evaporated PbI_2 template to the perovskite phase by a CVD of the MAI were included in small area solar cells (0.25 cm^2), achieving an efficiency of 12% at the proof-of-concept stage. More importantly, homogeneous perovskite layers are obtained over large areas: 225 cm^2 glass/ITO substrates and 239 cm^2 (6 inch) c-Si wafer textured by KOH-etching, an important step towards the fabrication of perovskite cells with industry-relevant active areas.
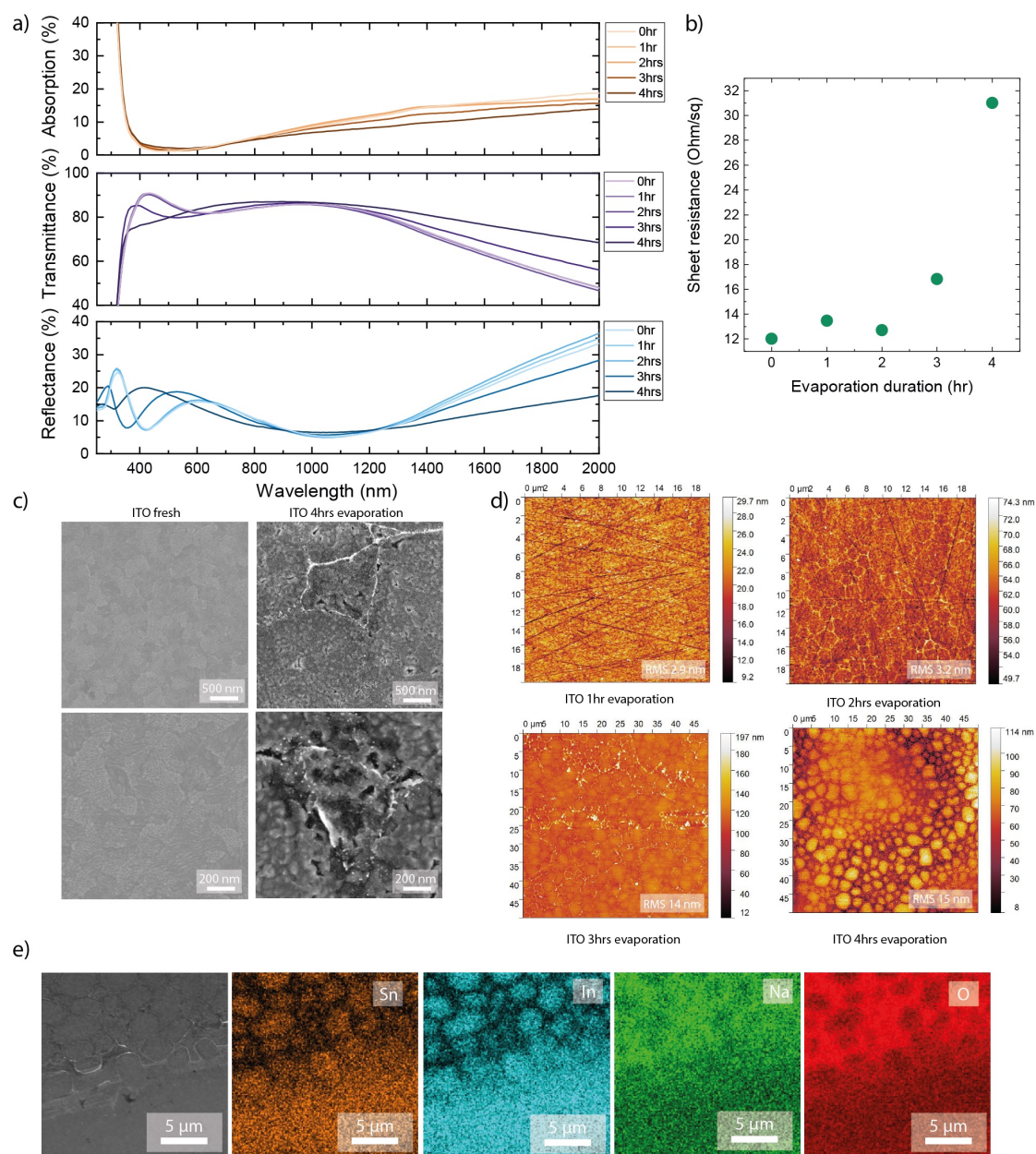
Figure 7.22 – **Optical, electrical properties and morphology of the ITO during CVD deposition.** a) Absorptance, tansmittance and reflectance, b) Electrical properties, c) SEM top-view images of the inital ITO (left) and after 4 h of CVD of MAI (right), d) AFM maps, e) SEM top-view of an ITO substrate after 4 h of CVD of MAI (left), along the EDX chemical map of the different elements (from left to right: Sn, In, Na, O).
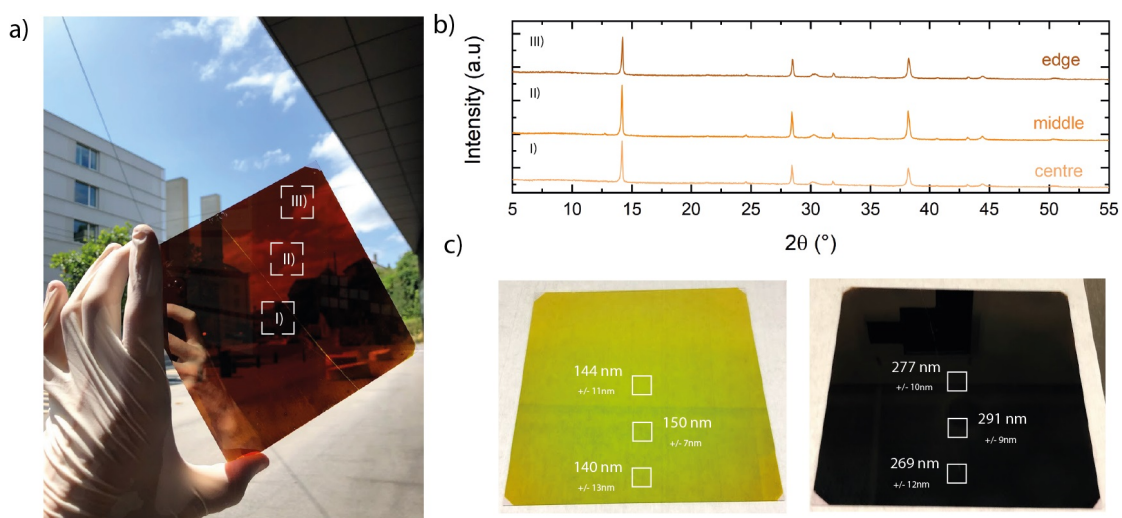
Figure 7.23 – **Large-scale perovskite layer deposition by CVD.** a) Picture of a perovskite layer deposited on a 15 x 15 cm^2 glass/ITO substrate, the total area of the deposition is 225 cm^2, b) X-ray diffractograms of the perovskite film measured at the centre I), middle II) and edge III) of the 15 x 15 cm^2 perovskite layer in picture a), c) pictures of the PbI$_2$ layer deposited by PVD in a high vacuum chamber (left), perovskite layer converted by the sequential hybrid PVD/CVD method (right), alongside thickness measurements.
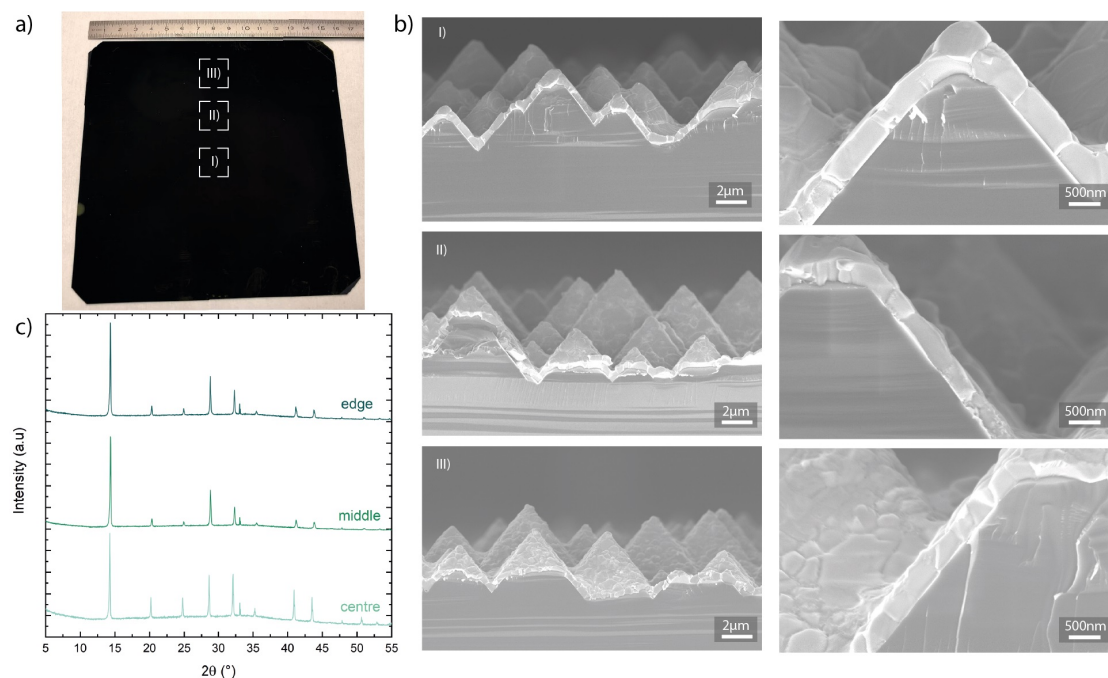
Figure 7.24 – **Large-scale CVD deposition on a 6 inch textured c-Si wafer.** a) Picture of a perovskite layer deposited by the PVD/CVD method on top of a textured 6 inch c-Si wafer, b) cross-section SEM of the perovskite layer acquired at different locations (low magnification, left, high magnification, right), c) corresponding X-ray diffractograms of the perovskite layer taken at different locations of that textured c-Si wafer.

8 FAI deposition by vapour transport deposition

Abstract

In this chapter, we focus on the deposition of FAI using the VTD setup described previously. First, FAI evaporation performed using the same parameters as for MAI results in the presence of mostly ammonium iodide within the chamber. Optimising process and system parameters (carrier gas flow rate, temperature of evaporation, gas line temperature) did not enable to introduce FAI in the chamber. Thanks to TGA-MS measurements, sym-triazine is identified as the main evaporation product of FAI. Due to its low boiling point, sym-triazine does not react with the lead iodide template and does not stick to the deposition table when depositing with the table at low temperature. The mechanisms of sym-triazine formation and ways to prevent it are discussed and investigated.[1]

8.1 Introduction

As already discussed in chapter 1, due to the lower thermal, moisture stability and power conversion efficiency of MALI cells, research efforts are currently shifting towards mixed-cation mixed-halide compositions. Besides the eventual gain in stability enabled by switching from MA- to FA-based perovskites, in our particular case, the MA-based perovskite has been found to degrade to PbI_2 during the deposition of the SnO_2 buffer layer (100°C for 60 min in vacuum, Figure B.23), making MA incompatible with our current tandem process.

In this section, FA-based evaporations using the home-built VTD system described in the previous pages are described. First, sublimation parameters used in the previous chapter for MAI evaporations are transposed to FAI. The limitations and differences in the evaporation of FAI are discussed and potential improvements are proposed.

8.2 Results and discussion

Only a few publications relate the fabrication of FA-based cell by CVD or PVD. From literature, FAI is usually sublimed at a slightly higher temperature than MAI, and a Cs precursor is incorporated into the PbI_2 template to prevent the formation of the undesired perovskite delta-phase.[264,266,267] Despite those slight changes, FAI sublimations are carried out similarly as MAI. As a start, we use the same deposition parameters for FAI as for MAI. In comparison to the previous chapter, caesium is introduced the Pb template by co-evaporating CsBr with PbI_2 or $PbBr_2$ (0.1 Å/s and 1 Å/s, respectively).

Figure 8.1a shows X-ray diffractograms of the $CsBr/PbI_2$ or $PbBr_2$ layers before and after FAI sublimation in the VTD system. Deposition parameters are the same as the ones used for optimised MAI depositions ($T_{crucible} = 200$°C, 800 sccm, $T_{substrate} = 140$°C , $T_{preheating} = 150$°C, $T_{gas\,line} = 200$°C, working pressure = 12 mbar, Duration = 2 h). For those evaporation parameters, no reaction was found to occur in between the $CsBr/PbI_2$ template and FAI, as evidenced by the absence of perovskite diffraction peaks. However, an exchange of halides is observed for the $CsBr/PbBr_2$ template, as highlighted by the shift of the $PbBr_2$ diffraction peaks to those of PbI_2. These observations imply that no FA cation reacts with the perovskite film. But the halide exchange from $PbBr_2$ to PbI_2 confirms the presence of iodine (such as HI, I^-, I_2), as observed in the MAI case (Figure 7.1). Similarly, depositions performed with a low substrate temperature ($T_{substrate} = 80$°C), analysed by liquid ^1H NMR indicate mainly the presence of the ammonium cation (Figure 8.1). The FA cation is also detected but in a small amount. Integration of the protons from the 2 amines group of the FA molecule (8.5-9 ppm) suggests that for each molecule of FA evaporated > 230 molecules of ammonium cation are observed (4 protons from the 2 FA amine groups vs. 4 protons for NH_4I). This observation indicates that the FA cation degrades during sublimation of the molecule or during transport to the
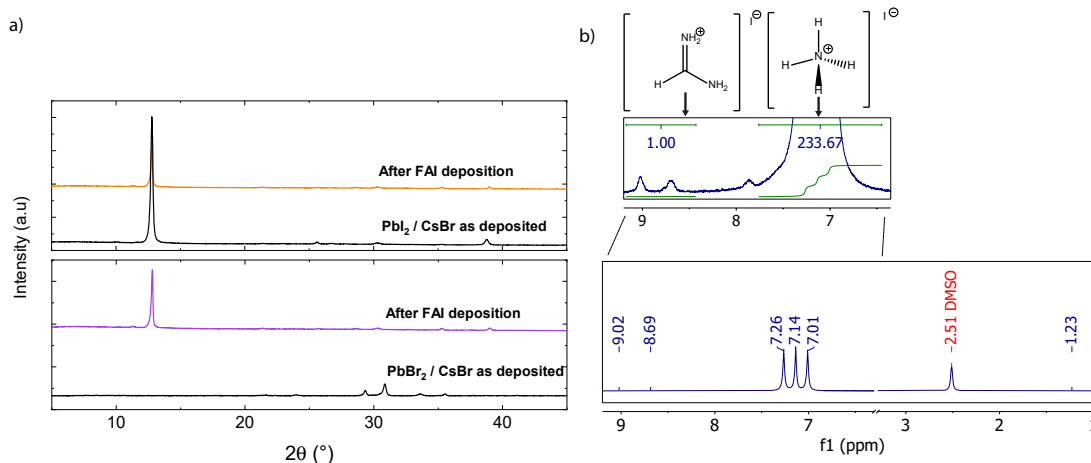
chamber.

Figure 8.1 – FAI evaporation. a) X-ray diffractograms of CsBr/PbI$_2$ and CsBr/PbBr$_2$ layers before and after the evaporation, b) Liquid ^{1}H NMR of the condensed organohalide ($T_{substrate} = 80°$C).

In order to assess which of the previous scenarios is the most likely, with the same deposition conditions, the CsBr/PbI$_2$ substrate was placed directly into the evaporator. The substrate was tapped onto the metallic plate that forces the carrier gas to pass through the crucible, facing the evaporator exhaust (Figure 8.2a). The temperature of the heating blanket surrounding the evaporator was maintained at 160°C (instead of 200°C) to enable FAI deposition and perovskite formation. In this case, the perovskite was observed to form in 2 h of deposition, as indicated by X-ray diffraction (Figure 8.2b). In addition, a liquid ^{1}H NMR analysis of the perovskite film dissolved in DMSO-d6 confirms the presence of the FA cation, without any trace of the ammonium cation (Figure 8.2c). This result indicates that FAI evaporation is occurring within the evaporator and that the transport or reaction within the chamber is the cause of the problem.

Few potential causes for the absence of FAI within the chamber can be listed. First, the transport to the chamber could cause the degradation of the FA cation (temperature of the gas line may be too high, the path to the chamber too long, kinetic energy from collisions with the wall may break the molecules). Second, FA cations may condense on the wall during transport, preventing organics from reaching the chamber. Third, the residence time and concentration of the FA cations within the chamber may be too low to initiate the perovskite formation. In the next section, we investigate the effects of FA transport to the chamber.

8.2.1 FAI evaporation and transport to the chamber

One of the crucial parameters for organohalide transport to the chamber is the carrier gas flow rate. As already discussed, the carrier gas flow rate has an impact on its temperature at the entry of the evaporator, the residence time of the organics within the gas line and
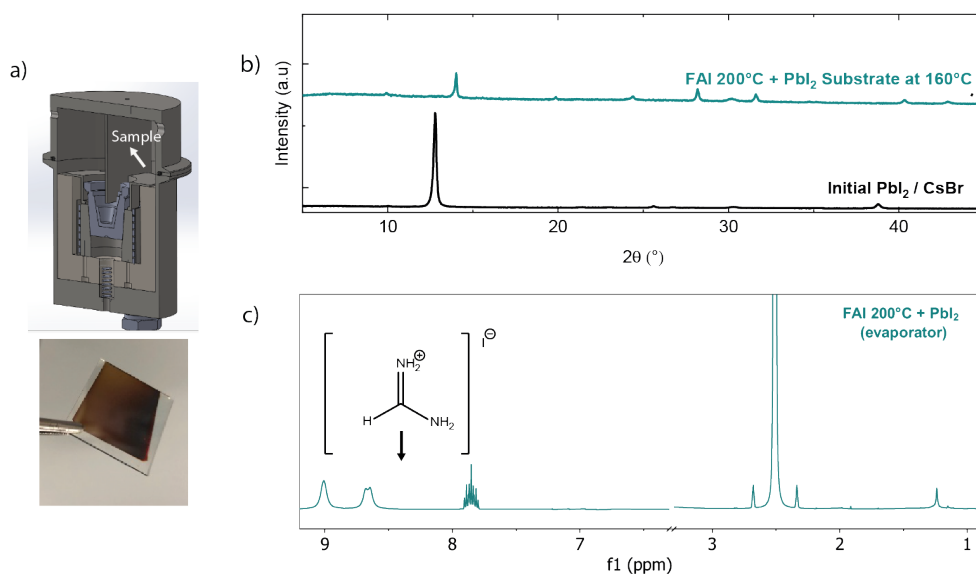
Figure 8.2 – **FAI sublimation and deposition in the evaporator unit.** a) Scheme of the evaporator and the position of the PbI$_2$ substrate (top), picture of the converted perovskite layer (bottom), b) X-ray diffractograms of CsBr/PbI$_2$ template before and after the evaporation of FAI, c) Liquid ^{1}H NMR of the perovskite film (dissolved in DMSO-d6).

pressure in the evaporator. The evaporation parameters from the previous experiment are kept constant. Only the carrier gas flow rate is varied from 0 sccm (no carrier gas) to 1500 sccm. The results show that with no flux, only NH$_4^+$ is condensing on substrates placed in the evaporator, whereas once a carried gas is introduced (200-1500 sccm) only the FA cation can be identified by both the FTIR and NMR (Figure 8.3). Three reasons may explain this observation. 1) The carrier gas flow, which is colder than $T_{crucible}$, cools down the powder and prevents FA degradation. The effective temperature of the powder is higher in the absence of the carrier gas and only FA degradation product such as NH$_4$ and HI/I$-$/I$_2$ are observed. This scenario is not likely as the absence of FAI without carrier gas is observed at each crucible temperature from 160-220°C (Figure B.24). 2) In the absence of the carrier gas to transport the molecules, FA accumulates within the bottom of the crucible and only the lighter NH$_4^+$ cation might reach the substrate. 3) Without any carrier gas, a mixture of gases (FA/HI/NH$_4$) in steady-state leads to the decomposition of the FA molecule. Even though the reasons of the FA absence in the evaporator if no carrier gas is used could not be established, this effect shouldn't be a problem as the system is meant to work with the presence of the carrier gas.

A similar analysis (variation of the carrier gas flux 200-1500 sccm) was carried out within the chamber by placing the substrate on top of the cold deposition table. Figure 8.4 displays the FTIR and liquid ^{1}H NMR measurements of the deposition. No organohalide is identified by FTIR due to the relatively low sensitivity of the method. However, NMR spectra indicate the presence of the ammonium cation for the 800 sccm and 1500 sccm cases (no deposition occurred in the case of 200 sccm). Here we think that the low flow
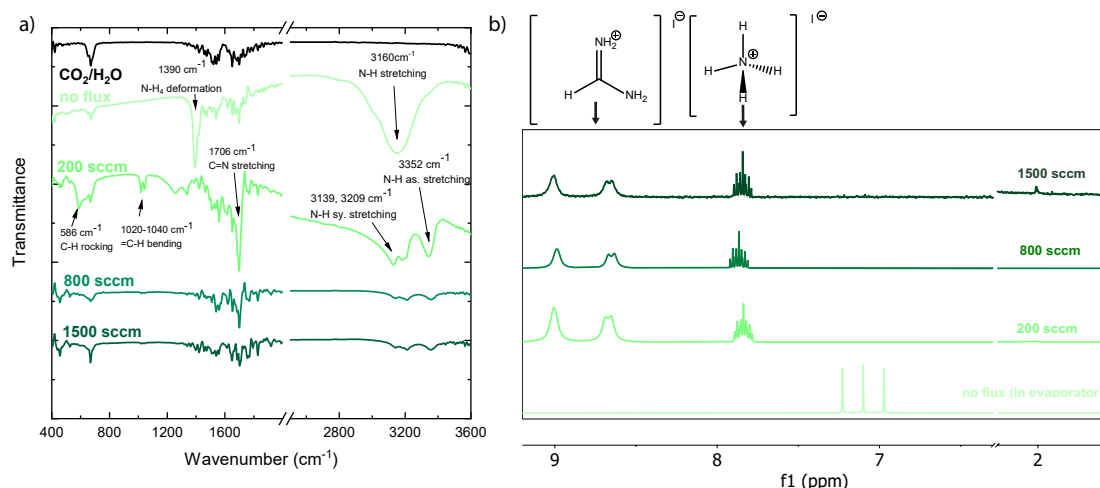
Figure 8.3 – **Organohalides deposition in the evaporator depending on the carrier gas flow rate.** a) FTIR of organohalides deposited on a silicon wafer placed in the evaporator. It is noteworthy to mention that more FA are present with a flow rate of 200 sccm, which could be mainly attributed to the fact that, at higher carrier gas flows, the FA molecule has more chance to exit the evaporator without sticking to the silicon wafer, b) Corresponding liquid ^{1}H NMR spectra. The intensities of the peak from the FA molecule are normalised. The crucible temperature was set to 200°C for 2 h.

rate of the carrier gas (and thus reduced temperature) leads to the condensation of NH_4I within the gas line. The fact that the FA cation is observed in the evaporator for those conditions but only the ammonium cation is detected in the chamber seems to indicate a degradation during the transport to the chamber.

Similarly to what was done for MAI, the effect of the gas line temperature (in between the chamber and the evaporator) is investigated. One might suspect the temperature used so far (200°C) and optimised from the MAI depositions to be too high and thus to lead to FA degradation during transport. Depositions with the substrate table maintained cold were performed with a gas line temperature ranging from 100°C to 200°C. A FTIR and NMR analysis of the corresponding evaporations is displayed in Figure 8.5. As for MAI, lowering the temperature of the gas line below 150°C leads to the condensation of the organohalides within the gas line (as no organohalide is detected). Unfortunately, as shown in Figure 8.5b, lowering the temperature of the gas line (*e.g.* to 150°C) does not prevent the formation of the ammonium cation. In short, reducing the temperature of the gas line to prevent FA degradation on the way to the chamber did not help. But similarly to MAI, it should be kept at a temperature higher than 150°C to prevent the condensation of the organic material in the transport line.

The temperature of sublimation is the main parameter that dictates the evaporation rate of the organohalides. Figure 8.6 presents a series where the temperature of the crucible was varied from 130°C to 260°C. For that experiment, ≈ 10 g of FAI powder was loaded in the crucible (usually 1 g). Only the ammonium cation is observed in the chamber, independently of the evaporation temperature. From literature, FAI is not expected to
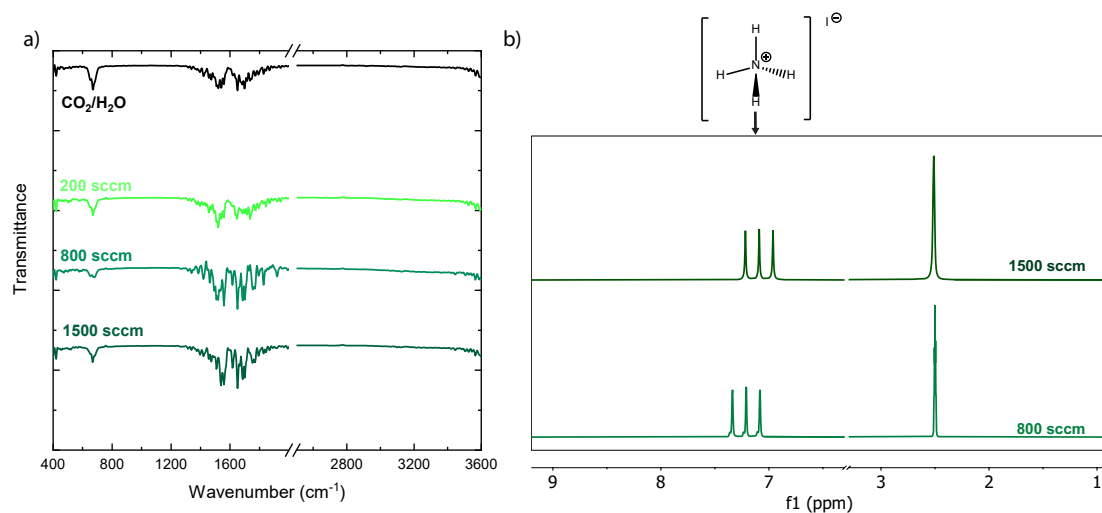
Figure 8.4 – **Characterisation of the organohalides deposited in the chamber depending on flow rate.** a) FTIR of organohalides deposited on a silicon wafer placed in the chamber, b) Corresponding liquid ^{1}H NMR spectra. The crucible temperature was set to 200°C for 2 h.
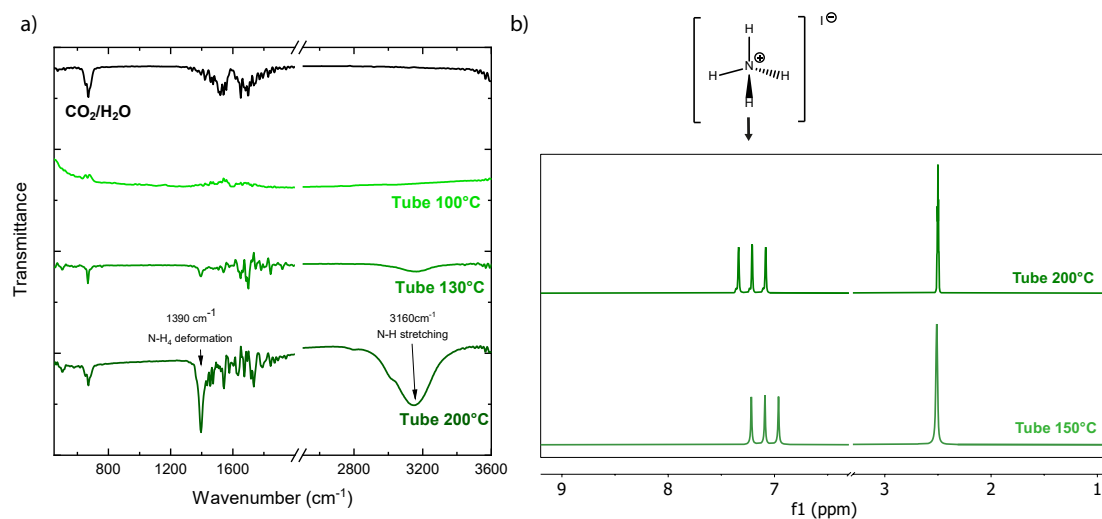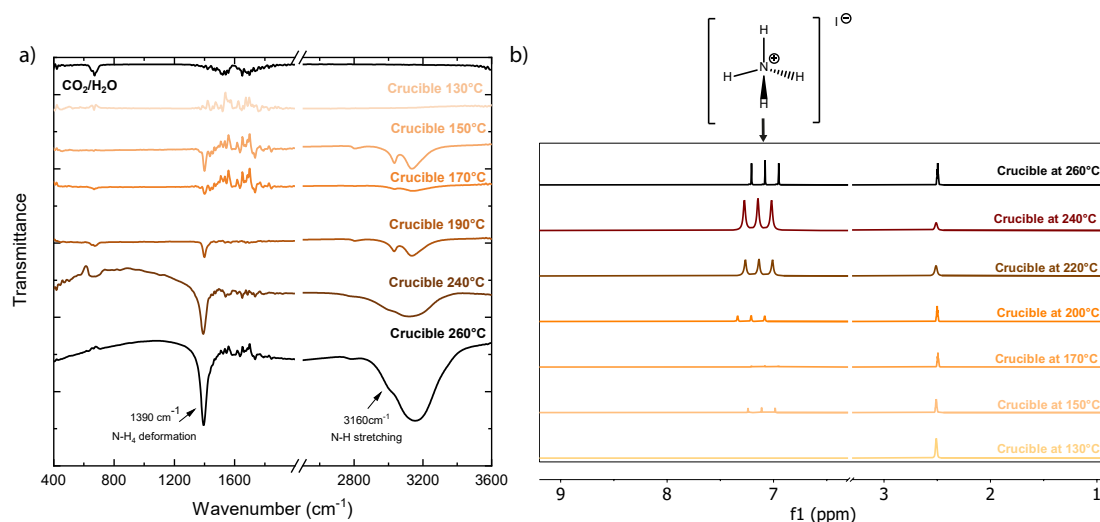

Figure 8.5 – **Characterisation of the organohalides deposited in the chamber depending on the gas line temperature.** a) FTIR of organohalides deposited on a silicon wafer placed in the chamber, b) Corresponding liquid ^{1}H NMR spectra. The flow rate was set to 800 sccm and the crucible temperature to 200°C, deposition duration was 2 h.

degrade at a temperature lower than 190°C, which is a temperature widely used for the CVD of FAI.[265, 267] Here again, rather than the degradation during the sublimation of the organic molecules, the results suggest either degradation or material loss during transport.

Figure 8.6 – **Characterisation of the organohalides deposited in the chamber depending on the crucible temperature (130-260°C).** a) FTIR of organohalides deposited on a silicon wafer placed in the chamber, b) Corresponding liquid ^{1}H NMR spectra. The flow rate was set to 800 sccm, the deposition duration was 2 h.

Different formamidinium salts (FABr and FACl) were also tested to rule out any effect that could be associated only with FAI (less volatile, reaction with HI, different evaporation products). Figure 8.7a presents the mass loss/h of the different FA salts as a function of the evaporation temperature. One can see that FABr and FACl are more volatile than FAI. As a result, the crucible temperature was set to 150°C (already more than 500 mg evaporated in 1 h) instead of 200°C for FAI. For both FABr and FACl, the condensate was analysed inside the evaporator and on the deposition table. In both cases, the results were similar (Figure 8.7). Fresh FABr and FACl powder show a similar pattern as FAI in ^{1}H NMR spectra (the chemical shift of the amine group increases with the electronegativity of the halide, Figure B.25).

In the evaporator, mostly the ammonium cation is observed with FABr and FACl with some residual FA cation. In the FAI case, only FA was observed. However, in the chamber, irrespective of the type of salt employed, only the corresponding ammonium salt is observed. In conclusion, the evaporation of different formamidinium salts leads to the same results within the chamber, excluding the possibility of a different evaporation behaviour of FAI. In addition, evaporating FABr and FACl leads to a change in the composition of the $CsBr/PbI_2$ templates due to an exchange of halides (Figure 8.7d). Diffraction peaks from $CsBr/PbI_2$ vanish after evaporating FABr or FACl, $PbBr_2$ or $PbCl_2$ appears (the other peaks can be assigned to NH_4PbI_3).
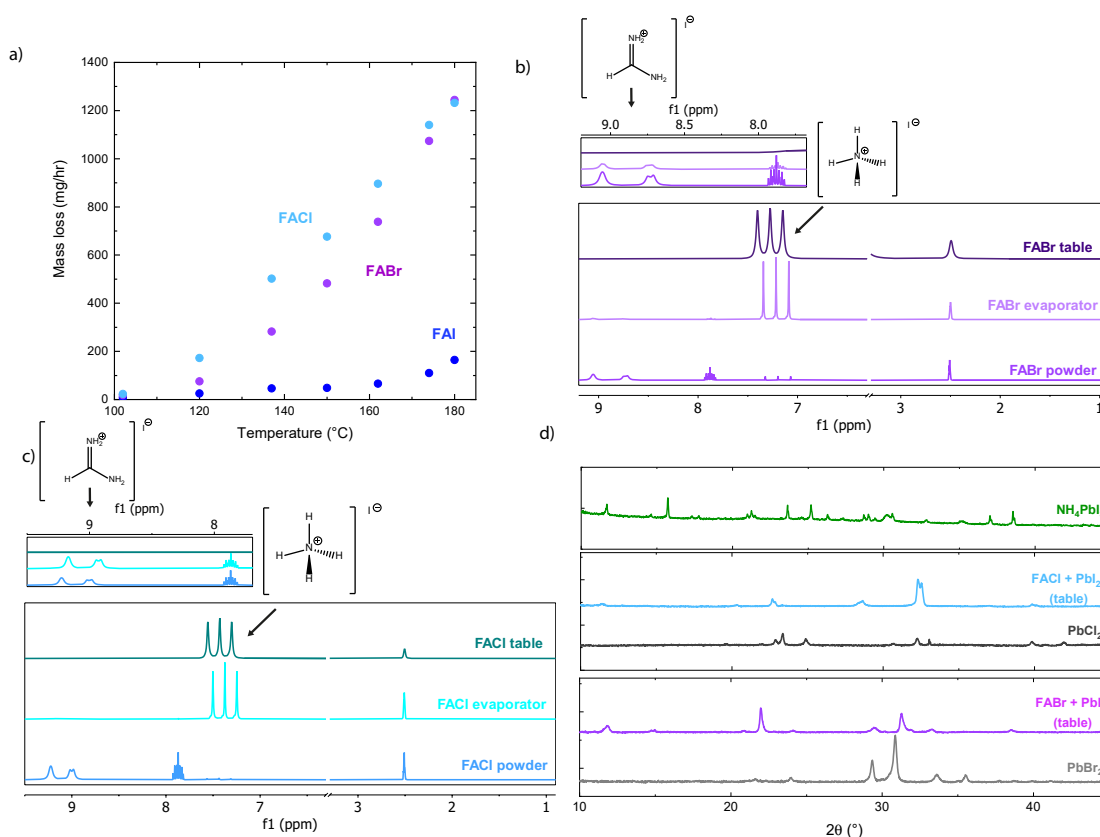
Figure 8.7 – Evaporation of FABr and FACl. a) Mass loss as a function of the crucible temperature for FAI, FABr and FACl, b) Liquid ^{1}H NMR of the FABr powder and analysis of the sublimed organics in the evaporator and on the deposition table, c) Liquid ^{1}H NMR of the FACl powder and analysis of the sublimed organics in the evaporator and on the deposition table, f) X-ray diffractograms of the PbI$_2$ after FABr and FACl exposure. PbBr$_2$, PbCl$_2$ and NH$_4$PbI$_3$ diffractograms are displayed as references.

8.2.2 Evaporation of FAI: is sym-triazine the culprit?

We performed TGA-MS on the FAI powder to determine the possible by-products forming during its sublimation.[2] To the best of our knowledge, only one report conducted TGA-MS on FAI powder and CsFAPbI$_3$ perovskite layers.[151] The authors found out that CsFAPbI$_3$ perovskite cells, upon thermal stress at low temperature ($< 95°$C), releases formamidine (FA+) as a result of the acid/base reaction (FAX $->$ FA$^+$ + HX$^-$), hydrogen cyanide (CHN) and ammonia (NH$_3$). Interestingly, sym-triazine (C$_3$H$_3$N$_3$), which is an heterocycle formed by the condensation of 3 FA molecules when releasing ammonia, was observed as a degradation product at a higher temperature ($> 95°$C). The FAI powder was found to sublime in a similar way. However, sym-triazine and FA seem to appear at a higher temperature ($> 250°$C). Here, we performed a TGA-MS analysis at different temperatures similar to those used in our VTD setup. Figure 8.8a shows the temperature profile used during the experiment, starting from $50°$C and up to $240°$C. First, the temperature was increased until $160°$C at $\approx 5°$C/min and then the temperature was

---

[2]The author wants to acknowledge Léo Duchêne who carried out the TGA-MS measurement.

stabilised for 30 min to reach a steady-state evaporation condition. The temperature was then increased stepwise by 20°C and stabilised for 30 min at each temperature until 240°C, as it was done with MAI. For that experiment, all the m/z ratios already used for the MS experiment of the MAI molecule are included (see table 7.1). In addition, several additional m/z ratios displayed in the table 8.1 were added.[151] Only the m/z ratios for which an intensity was observed are displayed in Figure 8.8b-h. One can clearly conclude that up to 200°C, apart from the sym-triazine parent peak and fragment, no other chemical species are detected with sufficient signal. FA (m/z = 44), MA (m/z = 30) and NH_3^+ or NH_3^+ (m/z = 17-18) appear at 220°C in very small concentrations. For the isotherm at 240°C, all the chemical species mentioned above increase in concentration. In addition, degradation products such as CH_3^+ (m/z = 15), CH_3I^+ (m/z = 142), I^+ (m/z = 127) and CHN (m/z = 27) appeared. It is noteworthy to mention that the decrease of all species at the end of the isotherm at 240°C emanates from the fact that most of the powder loaded in the crucible at the beginning of the experiment had already sublimed. Sym-triazine is the only molecule that appears for each isotherm (starting even at 160°C). And even if the quantification is not straightforward due to potential material losses during transport to the MS unit, sym-triazine is by far the main chemical species forming during FAI evaporation. In addition, it is interesting to note that the parent FAI molecule never appears in the MS scans. This absence suggests, as for MAI, that the evaporation of FAI occurs by the evaporation of FA cations and the halides separately. The reaction with PbI_2 to form the perovskite involves a reversible acid/base reaction in between FA and hydrogen halide, as for MAI.[283] The non-isothermal TGA-MS data (25-400°C) indicates that at temperatures > 260°C the molecule seems into dissociate to CH_4^+ and NH_3^+ rather than to evaporate as FAI or FA (Figure B.26). As a result, evaporation temperatures lower than 240-260°C should be used.

Among all the molecules identified with TGA-MS, except the NH_4^+ cation (that forms from the reaction between NH_3 and HI) and traces of FAI, none of the other molecules were detected by FTIR or NMR inside the deposition chamber of the VTD system (Figure 8.6). This discrepancy can be explained by the fact that all the molecules sublimed are either gases in ambient conditions (NH_3, NH_4^+, I_2, HI), not stable (CH_3^+ reacts to form CH_3I or CH_4), or too volatile to stick to a surface at 80°C (CH_3I bp = 42°C, CHN bp = 26°C, sym-triazine bp = 114°C).
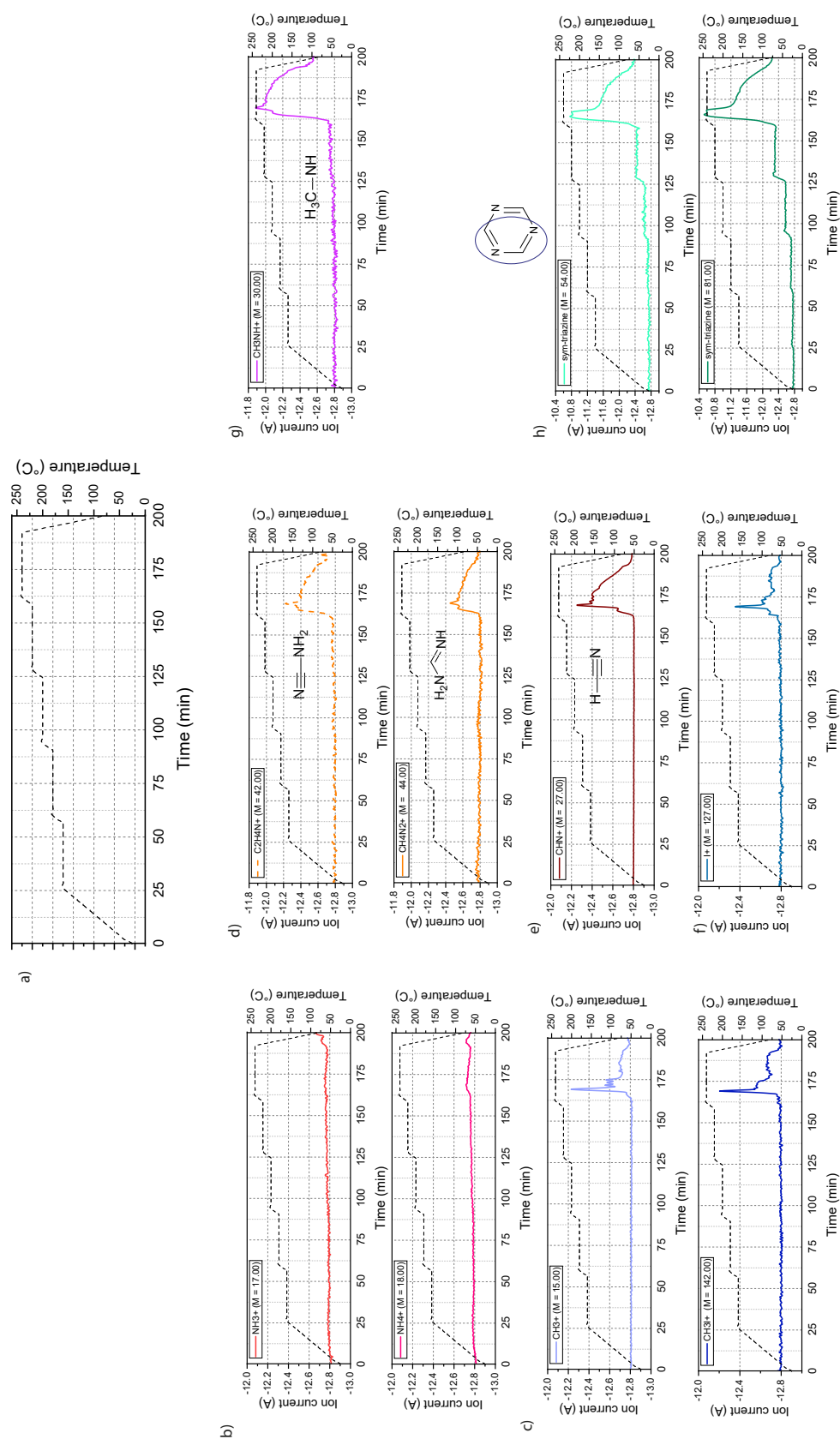
Figure 8.8 – **Isothermal TGA-MS analysis of FAI.** a) Temperature profile of the TGA-MS isotherm experiments (160-240°C), b) Ammonia (NH_3) and ammonium cation (NH_4^+) at 17-18 m/z, c) methyl group (CH_3) and iodomethane (CH_3I) at 15 and 142 m/z, d) cyanamide (CHN_2) and formamidine (HCN_2H_3) at 42 and 44 m/z. Fragments from (CH_3)$_3$N also present masses at 42 and 44 m/z (see table 7.1) from MAI evaporation. However, due to the absence of the parent peak at 58-59 m/z, we can suppose that the contribution here is indeed from FA, e) hydrogen cyanide (CHN) at 27 m/z, f) Iodine (I) 127 m/z, h) methylammonium (CH_3NH) at 30 m/z, g) sym-triazine fragment ($HCN-(H)CN$) and sym-triazine ($C_3H_3N_3$) at 54 and 81 m/z.
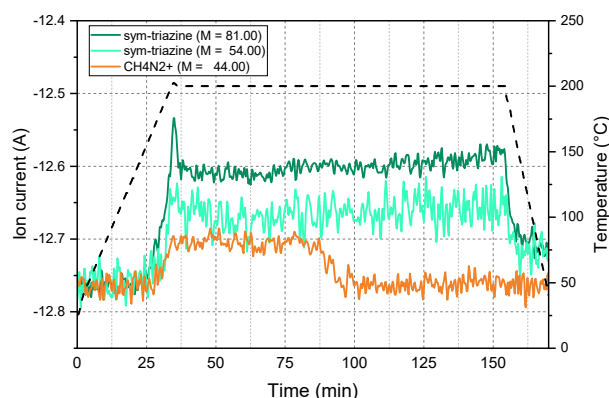
Figure 8.9 – **TGA-MS analysis of FAI at (200°C).** Only FA and sym-triazine (plus fragment) are identified for this isotherm. FA signal is constant for the first 75 min before decreasing.

m/z	Ion	Molecule/Fragment
17	NH_3^+	NH_3 parent peak
18	NH_4^+	$NH_3 + H^+$ proton transfer H_2O parent peak
27	CHN^+	CH_3NH_2 fragment
28	N_2^+	N_2 parent peak
44	HCN_2H_3	Formamidine parent peak
54	$HCN-(H)CN$	Sym-triazine fragment
80	$C_3H_2N_3$	Sym-triazine
81	$C_3H_3N_3$	Sym-triazine
172	$CH_5N_2I^+$	Formamidinium iodide parent peak

Table 8.1 – Thermal degradation fragment of formamidinium iodide in the literature[151]

It is not clear for now whether sym-triazine is a direct product of the evaporation of FAI or if it forms shortly after evaporation due to the condensation of the FA molecules in the vapour phase. FA molecules are not detected anymore in the vapour after few tens of minutes at 200°C (Figure 8.9). On the other hand, sym-triazine is detected over the entire duration of the experiment. This difference indicates that FA may evaporate first but then quickly reacts to form sym-triazine.

The FA cation is known to react through a condensation reaction to produce sym-triazine and ammonia according to the reaction presented in Figure 8.10. The reaction occurs due to the nucleophilic attack of the carbon by the amine group of two FA molecules (Figure 8.10b), leading to a linear dimer, which releases ammonia as a by-product. The presence of a third FA molecule enables the reaction to occur one more time, resulting in the closure of the heterocycle ring (sym-triazine). Sym-triazine is produced in high yield by condensation of FACl molecules in a basic solution and in the vapour phase. Increasing the temperature and reducing pressure pushes the reaction in favour of the sym-triazine production.[297,298] As a result, VTD/CVD conditions, where the powder is brought to a high temperature at a reduced pressure (1-12 mbar), tend to strongly shift the equilibrium towards the sym-triazine formation, probably in a more drastic way than during the TGA-MS measurement.
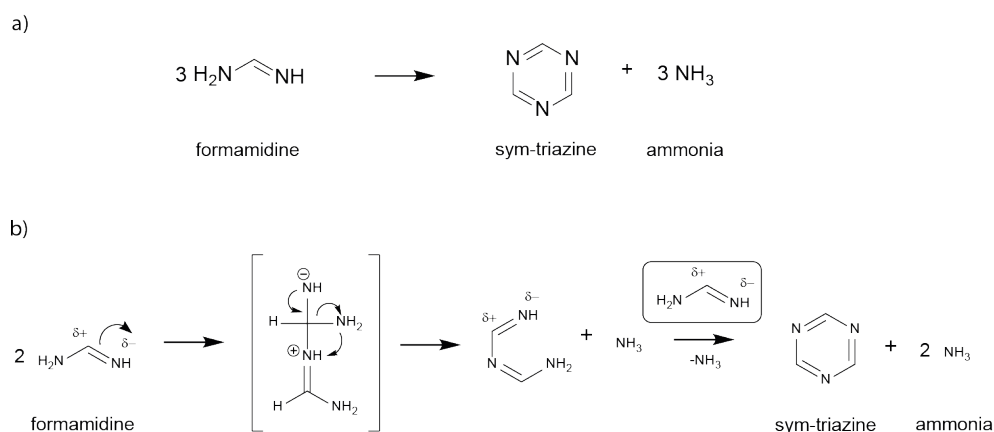
Figure 8.10 – Reaction of formamidine to form sym-triazine. a) Total reaction of formamidine to form sym-triazine and ammonia, b) detailed chemical mechanism of the reaction depicted in a).

8.2.3 Sym-triazine as a precursor?

Sym-triazine appears to be the main molecule forming during the evaporation of FAI. We will now focus on its implication as a product of the evaporation in the VTD system. Sym-triazine has a melting point in between 81-86°C depending on the presence of impurities and evaporates at 114°C. The evaporation process does not lead to any sign of degradation and the vapours produced are stable up to 600°C before degradation into hydrogen cyanide occurs.[298] As a result, one would suspect that once the sym-triazine forms within the system, either during evaporation or during transport to the chamber, the molecule stays pristine during the whole process. Figure 8.11 presents the liquid NMR (^{1}H, ^{13}C, 2D ^{1}H-^{1}H COSY) and FTIR characterisation of a commercial sym-triazine powder (97%, Sigma-Aldrich). For the NMR characterisation, the fresh powder was directly dissolved in DMSO-d6.

^{1}H NMR measurements show mostly a singlet at 9.3-9.4 ppm, which corresponds to the protons attached to the carbon on the heterocycle ring. Several other peaks appear (7-9 ppm and 1.7 ppm). However, integrating the signals compared to the main sym-triazine peak reveals ratios from 1 to 0.06 at best. This suggests that those peaks come from the impurities of the purchased product (purity = 97%) rather than from the sym-triazine molecule itself (Figure 8.11a). ^{13}C NMR data also show one sharp peak at 166 ppm which correspond to the three equivalent carbon atoms present in the heterocycle ring. 2D ^{1}H-^{1}H COSY NMR does not show any cross-peak as each proton are separated by 4 bonds (Figure 8.11b). For FTIR, the sym-triazine powder was dissolved in IPA (0.5M) and spin-coated onto a silicon wafer. The substrate was annealed at 60°C for 10 min to remove traces of IPA. The typical triazine ring vibration (heterocycle vibration) occurs at 824 cm^{-1}. In addition, the aromatic C-N and C=N stretching vibrations appearing in the 1200-1700 cm^{-1} region confirm the presence of the nitrogen substituted aromatic ring (Figure 8.11c).
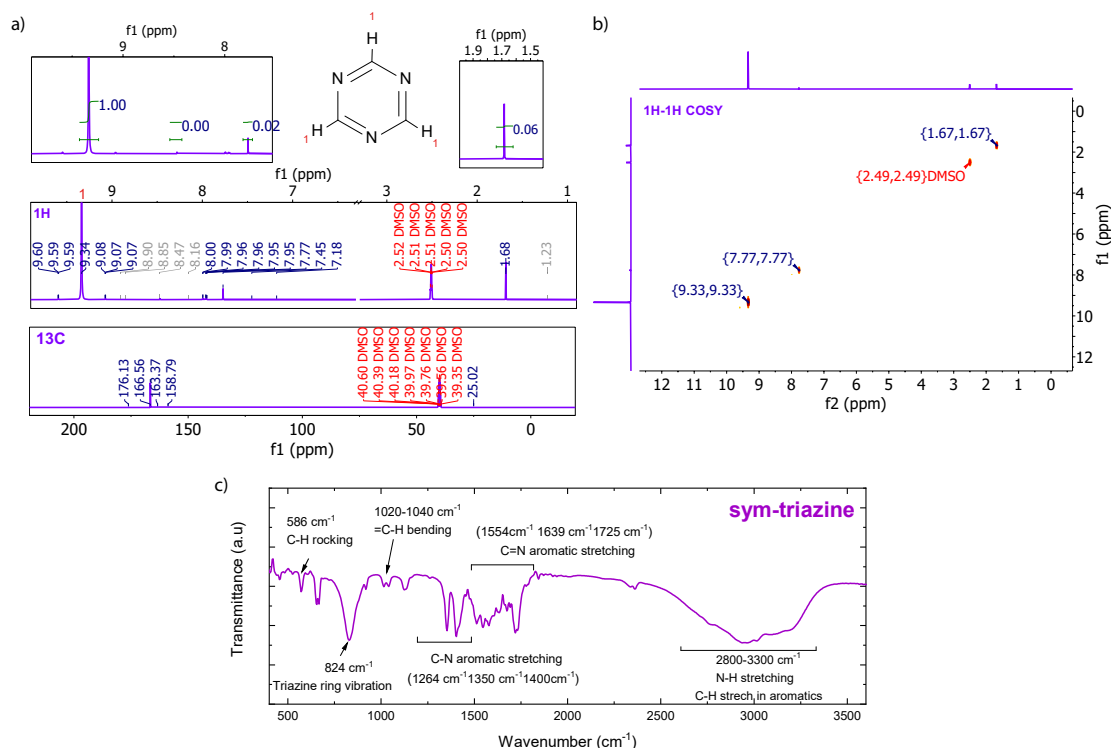
Figure 8.11 – Characterisations of sym-triazine. a) ^{1}H-proton NMR of sym-triazine in DMSO-d6 (middle), ^{13}C-carbon NMR (bottom), b) 2D ^{1}H-^{1}H COSY, c) FTIR data.

To confirm the fact that sym-triazine does not react with PbI_2, a sym-triazine solution (0.5M in IPA) was spin-coated onto a PbI_2 template and annealed at 130°C. Figure 8.12 displays X-ray diffractograms of the fresh $CsBr/PbI_2$ template and after sym-triazine spin-coating. One can see that no difference in between the XRD patterns is observed, indicating that sym-triazine is not reacting with the template. As a next step, an evaporation of sym-triazine was carried out in the VTD system in a similar way as FAI/MAI evaporation ($T_{crucible}$ = 200°C, 800 sccm, $T_{substrate}$ = 80°C , $T_{preheating}$ = 150°C, $T_{gas\ line}$= 200°C, working pressure = 12 mbar, Duration = 2 h). Here the temperature of the substrate was kept at low temperature to try to condense the organic molecule onto the deposition table. Furthermore, a $CsBr/PbI_2$ substrate was also placed onto the deposition table, once again to establish if the substrate would react with the organic molecule(s). Liquid ^{1}H of the condensate and the dissolved $CsBr/PbI_2$ substrate indicate no presence of sym-triazine in both cases (Figure 8.12b), confirming the fact that sym-triazine does not to react with the lead template. The same results were obtained by FTIR spectroscopy (Figure 8.12c): no sym-triazine was detected in the evaporator. These results imply that sym-triazine formed during the evaporation of FAI does not absorb on c-Si or $CsBr/PbI_2$ templates.

The formation of sym-triazine during the process prevents the fabrication of FA-based perovskites. It is of significant importance to either prevent the formation of this molecule
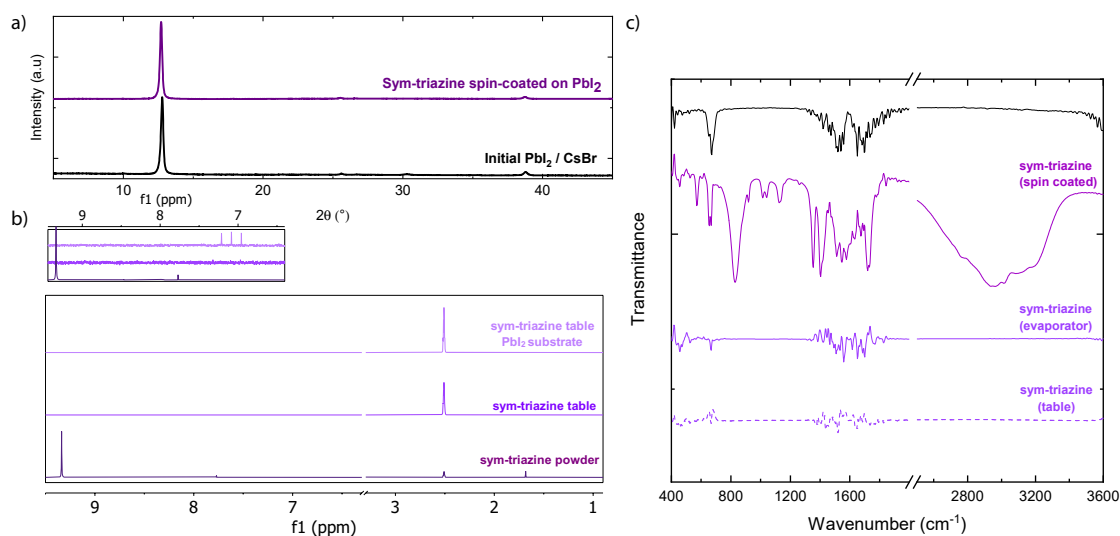
Figure 8.12 – Evaporation of sym-triazine. a) X-ray diffractograms of a PbI$_2$ layer spin-coated with sym-triazine, b) Liquid ^{1}H NMR of the sym-triazine powder, sym-triazine evaporated on the deposition table and corresponding PbI$_2$ layer on the deposition table, c) Corresponding FTIR data.

or to find a way to reverse the reaction to form FA from sym-triazine. We have already seen that preventing the formation of sym-triazine is challenging as the reaction of FAI at high temperatures and low pressures leads to the formation of sym-triazine with a high yield.[297] The latter solution, *i.e.* the reversible reaction from sym-triazine to FA, is more promising to enable the formation of FA-based perovskites. The simplest way to do so is to favour the chemical reaction presented in Figure 8.13a.[299] Primary amines, such as ammonia have been found to cleave the heterocycle ring through a nucleophilic attack of the carbon within the aromatic ring, as shown in Figure 8.13a. Ammonia could be used as a carrier gas (NH$_3$) instead of nitrogen. However, as ammonia is corrosive to metals and o-rings, it currently limits our capability to test this approach.
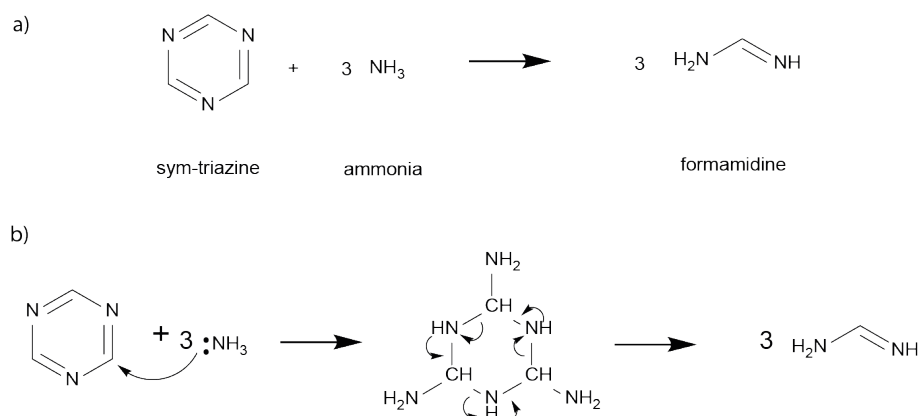

Figure 8.13 – Chemical degradation reaction of sym-triazine by primary amines. a) overall reaction with ammonia as amine source, b) detailed mechanism of the nucleophilic attack of ammonia for the ring cleavage of sym-triazine, resulting in the formation of formamidine.

As similar approach, without having to deal directly with ammonia is to use an ammonium halide NH_4X instead. The reaction of sym-triazine with ammonium chloride (NH_4Cl) in boiling ethanol leads to the formation of FACl.[300] Here we tried to reproduce the same reaction in the vapour phase. To do so, we loaded in the evaporation crucible 1 g of sym-triazine with an additional 1 g of NH_4Cl. The evaporation was done at 200°C with the deposition table at low temperature to condense and characterise the deposited molecule ($T_{crucible}$ = 200°C, 800 sccm, $T_{substrate}$ = 80°C , $T_{preheating}$ = 150°C, $T_{gasline}$= 200°C, P = 12 mbar, duration = 2 h).

Figure 8.14b-c displays the FTIR and ^{1}H NMR data of the condensate. In both cases, we can clearly identify the presence of NH_4Cl as expected from the evaporation of NH_4Cl, which leads to the formation of NH_4^+, NH_3 and HCl. More interestingly, we can also observe in the ^{1}H NMR spectrum the presence of the typical signature of FA, which according to the position of the amine peaks correspond to the FACl molecule. These results indicate that the reaction of sym-triazine with NH_4Cl in the vapour phase is similar to the one occurring in solution.[300] It also underlines the fact that the reaction of sym-triazine to form FA-halide molecule is reversible. These results suggest that formation of a FA-based perovskite layer through the evaporation and ring cleavage of the sym-triazine is possible.
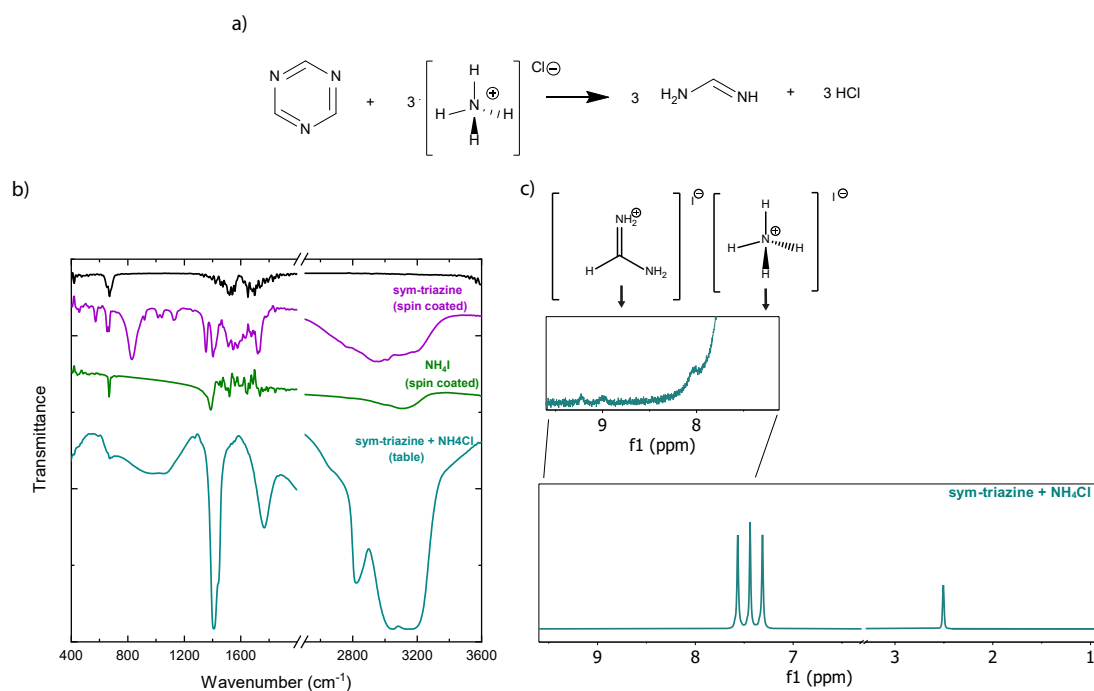

Figure 8.14 – **Reaction of sym-triazine with NH_4Cl.** a) chemical reaction of the formation of FA from sym-triazine and ammonium chloride, b) FTIR measurement of spin-coated sym-triazine and NH_4Cl on a silicon wafer, c) Liquid ^{1}H NMR spectrum of the condensate. The presence of the FACl molecule suggests that the reaction in a) takes place during evaporation or the transport to the chamber.

143

8.3   Conclusion

In this chapter, we investigated the evaporation of FA-halides using the home-built VTD setup described in chapter 6. First, evaporations were carried out by using the evaporation parameters used for MAI in the previous chapter. However, FA-based perovskite layers could not be formed using those parameters. More importantly, no or few traces of FAI could be detected in the deposition chamber after its sublimation. On the other hand, FAI could be detected and FA-based perovskites formed if substrates were placed directly inside the evaporator. Attempts to introduce FA into the deposition chamber by modifying the process parameters (such as crucible temperature, carrier gas flow rate, temperature of the gas line, evaporation of different FA-halides) all failed. Detailed analysis of the FAI evaporation products by TGA-MS reveals that sym-triazine (formed by the trimerisation of three FA molecules) is the main product of the evaporation. And sym-triazine does not react with PbI_2 and does not condense on substrates, irrespective of their temperatures. The molecule is suspected to be formed during evaporation or transport to the chamber. Pathways to prevent the formation of the sym-triazine are discussed and investigated. Amongst them, the reversible reaction of sym-triazine with ammonia or ammonium halide leads to the formation of FA-halides within the deposition chamber. While further work is needed, sym-triazine may be an alternative precursor to produce FA-based solar cells. Owing to its large manufacturing volume and high vapour pressure, sym-triazine thus represents a promising precursor alternative for low-cost, high-throughput vapour-based perovskite solar cells.

9 Vapour transport deposition of perovskites: general conclusions and perspectives

9.1 Conclusions

In the second part of the thesis, we discussed the possibility of replacing the organohalides spin-coating described in chapter 2 by a vapour transport deposition step. VTD appears as a more favourable option in view of industrialising double-side textured perovskite/c-Si tandem cells compared to spin-coating. To do so, we developed a custom-made vapour transport deposition chamber that separates the organohalide evaporation and deposition zones, decoupling evaporation conditions and substrate temperature. Using MAI as organohalide precursor and a PVD-deposited PbI_2 layer, we produced 12%-efficient perovskite solar cells. Thanks to the presence of the showerhead and the large deposition chamber, our system can accommodate up to one industrial 6 inch silicon wafer. In that regard, homogeneous $MaPbI_3$ perovskite layers were formed on 15 x 15 cm^2 ITO substrate. Perovskite layers fabricated with this method were also shown to conformally coat a 6 inch front-side textured c-Si wafer. Switching to a FAI precursor leads to one main issue preventing the conversion to the perovskite: the formation of sym-triazine during the evaporation or transport through the chamber. Here, we discuss different pathways to solve it by upgrading our system.[1]

9.2 Perspectives

Many research laboratories reported the fabrication of FA-based perovskites by vacuum deposition either using co-evaporation from multiple sources in a high vacuum chamber (PVD approach)[242, 301] or by CVD.[252, 264–267] This suggests that the problem encountered here is mostly related to our setup. Most of the FA-based perovskite fabrication routes by PVD or CVD have the substrates relatively close to the source. This enables a high

---

[1]I want to particularly thank Nathanaël Miaz, Cédric Bucher, Quentin Guesnay, Aymeric Schafflützel and Dr. Quentin Jeangros for all their contributions, through new idea, simulations, designs on solidworks, discussions and brainstorming

concentration of organohalides by having either a relatively small reaction chamber such
as a tube furnace (CVD) or by reducing the overall working pressure to increase the
vapour pressure of the organics (PVD). The issues discussed in the previous chapter
(formation of sym-triazine, organohalides loss due to transport, FAI degradation, low
vapour pressure of FAI) are likely to occur in these standard PVD and CVD chambers,
however less dramatically that in our system, as evidence by the fact that perovskite
formation still occurs in the evaporator unit (Figure 8.2). Overall, these issues specific to
our VTD setup call for a modification to the system design, which is discussed in the
next paragraphs.

9.2.1   Design of a new evaporator

A first issue to correct is related to the temperature control of the evaporator. In its
current design, the thermocouple used to control the evaporation temperature is directly in
contact with the crucible. While it is the best way to read its temperature, we found that
the temperature reading might be slightly different from one evaporation to the other due
to the fact that the thermocouple might have a different contact angle with the crucible.
In addition, the thermocouple was found to bend with time. In the new evaporator design
(Figure 9.1) the thermocouple is now directly integrated within the heating unit, which
promises a more reproducible temperature control from one evaporation to another.

We already have discussed the fact that forcing the colder carrier gas directly into the
crucible is problematic. In the new evaporator design, the geometry is tailored so that
the carrier gas picks up the organic vapours without cooling the powder. In turn, this
additionally increases the precision of the temperature control of the powder during the
evaporation. Furthermore, the new evaporator design is smaller. This lighter design also
enables the evaporation unit to cool down more rapidly and thus to reduce the dwell time
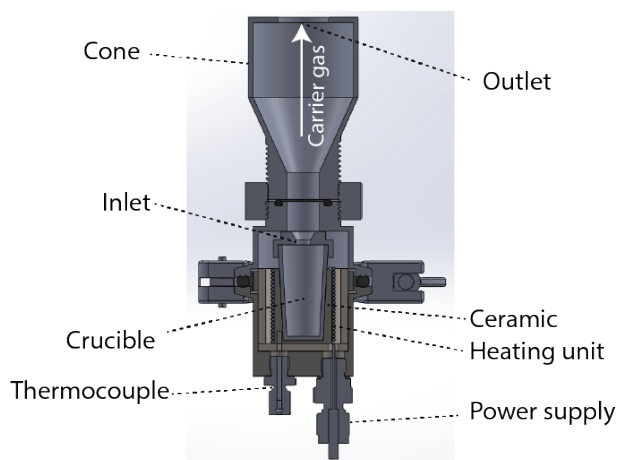in between evaporations.

**Figure 9.1 – Design of a new evaporation
unit.** Cross-section of the new evaporator unit.

9.2.2 Reducing the path length and residence time of the organic towards the chamber

Organohalides transport to the chamber is one of the main issues at this stage as FAI molecules may degrade, form sym-triazine or condense in the tubes. For now, a distance of 1.7 meter separates the evaporator outlet from the chamber inlet. Ideally, we would like to reduce the length of the tube as much as possible. By lifting the evaporator unit at the height of the chamber, the distance from the evaporator to the chamber could be reduced to 0.5 meter. Ideally, the diameter of the tubes should be increased to prevent adsorption and degradation during transport.

9.2.3 Increasing the temperature of the carrier gas before the evaporator

For now, even with the additional heating blanket upstream the evaporator, for a mild carrier flow rate of 800 sccm, the temperature of the gas entering the evaporator barely reaches $65°C$. This temperature is below the sublimation temperature of organohalides, hence reducing evaporation yield. Poor thermal heating in our current system comes from the fact that the residence time of the gas through the preheating unit is short. In the next design, the tortuosity of the gas path will be increased to maximise residence time and hence increase the carrier gas temperature.

9.2.4 Adding a halide source

As we have seen in the section 8.2, exposing $PbBr_2$ to FAI vapours leads to an exchange of halides, which is of major importance for the fabrication of perovskite/c-Si tandem cells. As the discussed in the literature review chapter, the band gap of the perovskite top cell should be on the order of 1.7 eV to reach maximum performance. This mainly implies that bromine should be introduced into the lattice (assuming a caesium content of 10-20%). However, bromine introduction in the $CsBr/PbI_2$ layer during thermal evaporation is cancelled by exposure to the iodine vapour during the CVD step, leading to a lower band gap in the absence of a Br post-treatment. The goal here is to add (an) additional source(s) to the chamber to be able to introduce different halide vapours independently from the organic source. The source will consist of a simplified version of the organic source. Candidate materials include I_2, HI, Br_2, HBr. In addition to band gap tuning, the introduction of halide vapours is interesting if the organics source is halide-free (*e.g.* sym-triazine, formaminidium acetate or simply formamidine). FAI evaporates as FA and HI, which suggests that both FA and HI should be present at the same time at the substrate surface to form the perovskite.[259] As observed in the TGA-MS experiments, FA and I/HI are not present in large quantities which in turn, reduces the probability of the event. This might explain the absence of FAI in the deposition chamber. FA might be

too volatile to stick to the deposition table if no halides are present at the same moment to form FAI. Introducing a halide source in the chamber to increase the vapour pressure of the halide might also facilitate the perovskite formation.

Overall, these reactor modifications (and others) should help achieving the aims of next research projects: making high efficiency perovskite/c-Si cells on 6 inch double-side textured c-Si wafers.

Concluding Remarks

The aim of this thesis was to develop highly efficient monolithic perovskite/c-Si tandems where the perovskite top is as a mere add-on to the c-Si bottom cell. This meant that the perovskite top cell must i) feature a band gap with a complementary absorption profile to c-Si, ii) be compatible with the fabrication constraints imposed by the bottom cells (low thermal budget imposed by SHJs, compatibility with the front-side texture of the c-Si cell), iii) use fabrication methods compatible with a deposition on 6 inch c-Si wafers textured on their front side, while iv) still exhibiting high performance and stability.

Due to the requirement of depositing the perovskite top cell on textured c-Si wafers, traditional wet-chemical perovskite deposition routes were ruled out as the perovskite absorber thickness is typically one order of magnitude thinner than the c-Si pyramidal features it needs to cover. To coat conformally textured c-Si wafers, we developed a sequential hybrid PVD/SP method. The PVD of the inorganic template is primordial to ensure that textured substrates are homogeneously covered over large areas. We found that different c-Si textures yield different PbI_2 morphologies as local shadowing effects during deposition play a critical role. Sharp pyramids yield a porous PbI_2 template that facilitates the infiltration of organohalides and the formation of the perovskite. On the other hand, smoother surface textures result in denser templates and in incomplete perovskite conversion as PbI_2 clusters are observed within valleys. To reach suitable perovskite band gaps for a tandem integration, caesium-halides were co-evaporated with PbI_2 and different ratios of formamidinium iodide and bromine were incorporated during the spin-coating step.

When including such top cells in tandems, the recombination junction was found to have an important role to reduce the impact of defects that may be present in the perovskite top cell and to prevent a dewetting of the small molecule HTL during the perovskite crystallisation process. In that regard, a recombination junction based on nanocrystalline silicon showed a great potential and enabled the fabrication of monolithic 2T perovskite/SHJ tandems with a PCE over 25% when using double-side textured c-Si wafers. The perovskite deposition workflow and recombination junction developed here were transposed to different cell polarities and c-Si bottom cell technologies, *e.g.* cells based on p-type wafers contacted by high-temperature passivating contacts. This

emphasises the versatility of the process flow developed here.

Further improvements in efficiency to reach an efficiency over 30% for such designs include: i) the reduction of parasitic absorption in the front electrode and contact stack (using screen-printed Ag, a wide band gap TCO and by thinning down the thickness of the C_{60}/SnO_2 stack), ii) reducing recombination at the perovskite/charge selective layer interfaces (by doping the charges transport layers and/or introducing passivation layers), iii) increasing the perovskite band gap to reach a higher V_{oc}.

In the second part of this thesis, we replaced the organic spin-coating step by a CVD one. The goal here was to benefit from the large-area deposition capability enabled by vapour-based techniques compared to spin-coating. We introduced a custom-made vapour transport deposition setup to expose the PbI_2 template to organohalide vapours and convert it to the perovskite phase. This reactor can accommodate up to one 6 inch c-Si wafer. Depositing methylammonium iodide with this setup resulted in functional cells and conformal perovskite coatings on 6 inch textured c-Si wafers. On the other hand, depositions with a formamidinium precursor were found to be more challenging due to the formation of sym-triazine as by-product. Still, we could show how sym-triazine can be cleaved to form formamidine again, highlighting that sym-triazine may potentially be used as a new precursor for perovskite fabrication.

To conclude, this research made several key contributions to the field of perovskite solar cells, most notably the first perovskite/c-Si tandem breaking the 25 % efficiency mark thanks to the use of a c-Si bottom textured on both sides, an optically optimised system directly compatible with industrial c-Si process flows. Overall, results obtained here and by the community in general are encouraging regarding the industrialisation of perovskite/c-Si tandems. The record efficiency of these devices is now 29.15% (from 13.8% in 2015), value that will certainly overpass the 30% barrier in the coming years, at least on small active area. Oxford PV recently claimed that they managed to reach tandem efficiencies over 25% with 6 inch c-Si wafers, another important step towards the industrialisation of this technology. Still, several questions remain unanswered such as whether the perovskite top cell can be deposited with a high-yield and throughput comparable to what is achieved in c-Si production lines, maintain manufacturing costs at a minimum, remain efficient when included in industrial modules, and can match the operational stability of c-Si modules with less than 1-2% of relative degradation per year for 20-25 years. The journey before perovskite/c-Si tandems become commercial is still paved with several difficulties, but recent advances, including those emerging from this research, are promising.

Appendices

A Experimental Details

A.1 Perovskite solar cell fabrication

A.1.1 Planar n-i-p solar cells

Glass/FTO (15 Ohm/sq, Solaronix) or Glass/ITO substrates (15 Ohm/sq, Kintec) were cleaned by an oxygen plasma treatment and followed by a UV-Ozone treatment for 15 min.

ETL

chapter 3
First, ≈ 8 nm of C_{60} ($> 99.95\%$, NanoC) was thermally evaporated to form the electron transport layer in a Lesker MiniSPECTROS system, with a substrate temperature of $30°C$ and a base pressure of $< 1.5 \times 10^{-6}$ Torr.

chapter 7
1 nm of LiF ($> 99\%$, Sigma Aldrich) and 6 nm of C_{60} ($> 99.95\%$, NanoC) were thermally evaporated to form the electron transport layer in a home-built evaporation system at a substrate temperature of $30°C$ and a base pressure of $< 1.5 \times 10^{-6}$ Torr. For PCBM cells, PCBM ($> 99.95\%$, NanoC) in solution (10 mg/ml in Chlorobenzene) was spin-coated on top of the FTO substrate at 3000 rpm for 30 s in an inert atmosphere.

Perovskite for MAPbI$_3$ cells

150 nm PbI$_2$ ($> 99.99\%$, Alfa Aesar) was evaporated in a Lesker MiniSPECTROS evaporation system. The PbI$_2$ layer was transformed to the final perovskite phase by spin-coating a solution of methylammonium iodide (0.346 M, Greatcell solar) in ethanol at 3000 rpm for 30 s using dynamic solution dispensing in an inert atmosphere, followed

by annealing (120°C, 30 min in a N_2).

Mixed-cation, mixed-halide perovskite cells

PbI_2 (> 99.99%, Alfa Aesar) and CsI (> 99%, Abcr) were co-evaporated (165 nm for $Cs_xMA_{1-x}PbI_3$ and 180 nm for $Cs_xFA_{1-x}PbI(_{1-y}Br_y)_3$.). The CsI evaporation rate was fixed to 15% of the PbI_2 rate, corresponding to an atomic Cs:Pb ratio of 0.19 (by RBS and EDX). The PbI_2/CsI layer was transformed to the final perovskite phase by spin-coating a solution of methylammonium iodide (0.346M, Dyesol) or a mixture of formamidinium bromide:iodide (2:1 molar ratio, 0.445M, Dyesol) in ethanol at 3000 rpm for 30 s using dynamic solution dispensing in an inert atmosphere, followed by an annealing step ($Cs_xMA_{1-x}PbI_3$: 120°C, 30 min in glovebox, $Cs_xFA_{1-x}PbI(_{1-y}Br_y)_3$: 150°C, 30 min in ambient air, $\approx$ 30%RH). The stoichiometry of the film depends on the template composition, the organohalide concentration in the solution and the spin-coating parameters (*e.g.*. spin speed). The optimal concentration of the organohalide solution required was determined empirically and depends on the PbI_2/CsI template thickness.

HTL

Then, a solution of spiro-OMeTAD in chlorobenzene containing 72.3 mg/mL of spiro-OMeTAD (> 99.5%, Lumtec), 28.8 μl/ml ot 4-tert-butylpyridine (> 96%, TCI), and 17.5 μl/ml of 520 mg/mL lithium bistrifluoromethylsulfonyl imide (> 97.0%, Sigma-Aldrich) in acetonitrile) was spin-coated at 4000 rpm for 30 s.

Opaque and transparent electrodes

For opaque design, 100 nm of gold was evaporated at a rate of 1 Å/s. The active area of the cell was 0.25 cm^2 if not stated otherwise.

The transparent electrode consisted of a 20 nm-thick MoO_x (> 99.98%, Sigma Aldrich) buffer layer deposited by thermal evaporation at a rate of 0.5 Å/s and 100 nm of indium zinc oxide with a resistivity of $\approx$ 55 Ohm/sq deposited by sputtering in a home-built system (4 inch target: 90% In_2O_3 + 10% ZnO; base pressure < 2×10^{-6} mbar; working pressure: 2.2 mbar, power: 70W).[158] Au (130 nm or Ag 130 nm, for 5 x 5 cm^2 tandems) was thermally evaporated through a shadow mask to form the metallic front grid. For the large area tandem cells, the metal fingers shaded about 3.8% of the total aperture area. Finally, an anti-reflective coating ($\approx$ 100 nm of MgF_2, > 99.99%, Umicore) was deposited on the cells by thermal evaporation.

A.1.2 Planar p-i-n solar cells

HTL

First, 12 nm of 2,2',7,7'-tetra(N,N-di-tolyl)amino-9,9-spiro-bifluorene (spiro-TTB, >99%, Lumtec) was thermally evaporated to form the hole transport layer in a home-made evaporation system (base pressure of < 2.0 x 10^{-6} mbar, working pressure of < 3.0 x 10^{-6} mbar, evaporation rate of 0.2 Å/s measured by a quartz crystal monitor, aluminum oxide crucible, power applied of about 40 W, reached with a ramp-up of 10 W/min, substrate holder at room temperature).

Mixed-cation, mixed-halide perovskite cells

The perovskite absorber was then deposited using the sequential two-step PVD/SP method. First, PbI_2 (>99.99%, beads from Alfa Aesar) was co-evaporated with CsBr, CsI and CsCl (>99.99%, Abcr) in a Lesker MiniSPECTROS system (base pressure of < 2 x 10^{-6} mbar, working pressure of < 5 x 10^{-6} mbar, evaporation rate of 1 Å/s for PbI_2 and various ones for Cs-halide, as-measured by quartz crystal monitors, aluminum oxide crucibles, evaporation temperatures of $\approx 325°C$ for PbI_2, reached with a ramp up of $20°C$/min, and of $\approx 400\text{-}480°C$ for Cs-halides, reached with a ramp up of $20°C$/min, substrate holder at $30°C$). Subsequently, a mixture of formamidinium bromide and iodide (various FAI:FABr ratios, reference of 1:2, FAI:FABr), in various molarity (reference of 0.513 M) in ethanol, (Greatcell solar) was spin-coated onto this template layer. This step was performed using dynamic solution dispensing at various spin speed (ref = 4000 rpm) during 30 s in an inert atmosphere. The layers were then annealed at $150°C$ for 30 min in ambient air to crystallise the perovskite absorber.

ETL

An electron-selective stack of LiF (1 nm, 99.98%, Sigma-Aldrich)/C_{60} (15 nm, $> 99.95\%$, NanoC) was then thermally evaporated in a home-made evaporation system without breaking the vacuum in between these two depositions (base pressure of < 2 x 10^{-6} mbar, working pressure of > 3 x 10^{-6} mbar, evaporation rate of 0.1 Å/s for LiF and 0.3 Å/s for C_{60} as-measured by quartz crystal monitors, aluminum oxide crucibles, power applied to the sources of ≈ 180 W for LiF, reached with a ramp-up of 40 W/min, and ≈ 80W for C_{60}, reached with a ramp of 20 W/min, substrate holder at room temperature).

Opaque and transparent electrodes

For opaque design, 120 nm of Ag was thermally evaporated at a rate of 2 Å/s over the surface. The active area of the cell was 0.25 cm^2 if not stated otherwise.

For semitransparent cells, after the C_{60} deposition, a buffer layer of 10 nm of SnO_2 was deposited by atomic layer deposition using an Oxford instrument system at 100°C using tetrakis(dimethylamino)tin and H_2O as precursors. 110 nm of indium zinc oxide (IZO) was then sputtered in a home-built system using a 4-inch target (90% In_2O_3 + 10% ZnO) with an RF power of 70 W (sheet resistance of 27 Ohm/sq). 120 nm of Ag was thermally evaporated at a rate of 2 Å/s over the surface or through a shadow mask to form the front metal grid of 2T tandems. An anti-reflective coating of MgF_2 (100 nm, > 99.99%, Umicore) was thermally evaporated at a working pressure of < 1 x 10^{-5} mbar (base pressure of < 1 x 10^{-5} mbar) at a rate of 2 Å/s as-measured by a quartz crystal monitor. The final tandem cell active area, defined by the size of the IZO front electrode deposited through a shadow mask, was 1.81 cm^2, while the aperture area defined by the inside part of the metal frame was 1.42 cm^2.

During all layer depositions by thermal evaporation, the deposition rate was first stabilised to the targeted value before opening the substrate shutter. All thicknesses in this section are given for KOH-textured crystalline silicon substrates unless stated otherwise. These are determined by dividing the thicknesses deposited on flat glass witness samples by 1.7.

A.1.3   Vapour transport deposition of the organohalides

For cells produced by the sequential PVD/VTD process, the PbI_2 layer was taken out of the glovebox in air and placed onto the VTD deposition table (temperature of 80-160°C). ≈ 1g of fresh methylammonium iodide (Greatcell solar, stored in N_2 atmosphere) was placed in a graphite crucible. The graphite crucible was then placed in the evaporator and sealed. The whole system (evaporator and deposition chamber) was then pumped down to a base pressure of 0.15 mbar (5 min pumping). The carrier gas was then introduced by a mass flow controller (800 sccm, N_2 if not stated otherwise). The temperature of the crucible was then increased to the desired temperature (200°C if not stated otherwise) at a rate of ≈ 10°C/min (10-15 min to reach the setpoint). The crucible temperature profile is provided in Figure 6.4. Evaporations were performed in steady state conditions for ≈ 2-3 hrs. Once the evaporation finished, the temperature control of the evaporator was switched off, the process valve was closed and the substrates removed from the deposition chamber. The system was then pumped down again and flushed with 2800 sccm of N_2 (1500 from evaporator line, 800 from mixing line) to prevent organics condensation in the evaporation and gas transport line until the crucible reached a temperature below 100°C. The perovskite films were transferred back in a glovebox filled with N_2. Any MAI excess was washed away by spin-coating isopropanol (IPA 99%, Sigma-Aldrich) by dynamic spin-coating at 3000 rpm for 30 s. The samples were then annealed for 3 min at 120°C on a temperature-controlled hotplate to remove the IPA excess.

A.2 Silicon solar cell fabrication

A.2.1 (100) silicon texturing by alkaline solution

SHJ bottom cells were fabricated using n-type silicon float-zone wafers with a resistivity of 1-5 Ω and a thickness of 260 μm (before texturing).

For SST, a dielectric etch mask was deposited on one side of the wafer by PEVCD. Single-side texturisation was realised by wafer immersion in a KOH-based solution, followed by dielectric mask removal with a diluted HF solution.

For DST, the entire wafer was immersed in a KOH-based solution, for usually 20 min. To change the pyramid size, prolonged texturing of 40 min and 60 min was performed. Smoothening of the pyramids was done separately with a solution of nitric acid (HNO_3), acetic acid ($C_2H_4O_2$) and hydrofluoridric acid (HF). The wafers were immersed for 5 s, 10 s, 30 s, 60 s to obtain in different smoothenings. After that, the wafers were washed with deionised water.

A.2.2 Silicon heterojunction solar cells (SHJ)

SST SHJ in front emitter configuration

SHJ bottom cells were fabricated using n-type SST c-Si float-zone wafers with a resistivity of 1-5 Ω and a thickness of 280 μm (before texturing). Intrinsic and doped hydrogenated amorphous silicon layers were deposited on both sides of the wafer in a PECVD reactor to passivate the silicon surface and to create charge carrier selective contacts. The SHJ bottom cell was made in the front-emitter configuration, with the n-type contact at the back and the p-type at the front. The back contact consisted of a sputtered TCO/Ag stack. The p+/n+ nc-Si:H recombination junction was deposited in the same PECVD reactor at low temperatures ($< 200°C$) onto the p-type amorphous silicon layer at the front side of the SHJ bottom cell. Trimethylboron and phosphine were added to the silane/hydrogen gas mixture to form the p- and the n-doped layers. The perovskite top cell was deposited directly onto the nc-Si:H recombination junction.

DST SHJ in rear emitter configuration

SHJ bottom cells were fabricated using n-type DST c-Si float-zone wafers with a resistivity of 1-5 Ω and a thickness of 260 μm (before texturing). Intrinsic and doped hydrogenated amorphous silicon layers were deposited on both sides of the wafer by PECVD to passivate the c-Si surface and to create the charge carrier-selective contacts. The SHJ bottom cells were produced by depositing the n-type contact at the front and the p-type contact at the back (rear emitter configuration). The back electrode consisted of a sputtered

ITO/Ag stack. The front side n-type amorphous silicon layer was then capped by the recombination junction, which consisted of either an ITO layer (40-50 nm; 190 Ohm/sq) or an n-type/p-type nc-Si:H layer stack. The former was sputtered, while the latter was deposited in the same PECVD reactor as the amorphous silicon layers (< 200 °C). The processed 4-inch wafers were then laser cut to 2.5 x 2.5 cm substrates.

A.2.3 High temperature passivating contact solar cells (HTPC)

The bottom cell was processed using a fabrication sequence based on full-area deposition and thermal annealing for the formation of the junction.[44] In brief, a p-type SST c-Si wafer, flat on its rear and KOH-etched on its front, was first passivated by growing a chemical silicon oxide (SiO_x) on both sides, before depositing by PECVD n- or p-doped silicon containing a few atomic percent of C (SiC_x) on the front and rear sides of the wafer, respectively. A single annealing step at 850°C then triggered the crystallisation of the doped SiC_x layer and promoted the diffusion of the dopants into the wafer to form the charge carrier selective contacts. A hydrogenation step was then applied to passivate the electronic defects that formed at the SiO_x/c-Si interface upon annealing. A SiN_x:H donor layer was deposited of the wafer by PECVD on both sides, which released atomic hydrogen upon annealing at 450°C. To process the tandem cell, the bottom cell was capped with a p+ nc Si:H layer deposited by PECVD. The doping level and high crystalline fraction of the SiC_x(n), resulting from the annealing step at 850°C, enable the formation of an efficient tunnel recombination junction when combined with the nc-Si(p+):H layer. These features simplify the process in comparison to SHJ, where a nc-Si(n+):H is deposited before the nc-Si(p+):H to provide a low contact resistivity. Subsequently, the perovskite top cell is deposited in the p-i-n configuration in the same manner as presented in the previous section.

A.3 Characterisation techniques

UV-visible spectrophotometry (UV-Vis)

A UV–vis spectrophotometer (PerkinElmer Lambda 900) with an integrating sphere was used to acquire total reflectance, transmittance, and absorbance spectra.

X-ray diffraction (XRD)

XRD measurements were carried out in an Empyrean diffractometer (Panalytical) equipped with a PIXcel-1D detector. The diffraction patterns were measured using a Cu K α radiation (wavelength of 1.54 Å). Samples were measured in air.

Secondary electron microscopy (SEM)

Secondary electron SEM images were acquired with acceleration voltages of 3 keV using either an Everhart-Thornley or an in-lens detector (Zeiss Gemini 2 microscope or Jeol JSM-7500 TFE). Energy Dispersive X-ray (EDX) maps were acquired at 10 keV using a silicon drift detector from Oxford Instruments.

Transmission electron microscopy (TEM)

The microstructure of the perovskite cells and nc-Si:H junction was investigated using TEM.

Cross-sections of the fully textured perovskite/SHJ tandem were prepared for TEM analysis using a focused ion beam workstation (Zeiss NVision 40). Thin TEM lamellae, prepared with a final gallium beam voltage of 2 or 5 kV, were quickly transferred in air (< 2 min) to a transmission electron microscope, either a FEI Tecnai Osiris or a double Cs corrected FEI TITAN Themis. STEM HAADF and BF imaging were combined with energy-dispersive X-ray spectroscopy at an acceleration voltage of 200 kV and a probe current of 100 to 200 pA. EDX fitting was performed using the Cliff-Lorimer method.[152] More details about the sample preparation, the TEM analysis and potential artefacts associated with the technique can be found elsewhere.[183]

In chapter 3, FFTs of high-resolution TEM micrographs and iFFTs of selected Si (111) and (022) reflections were computed with a mask diameter of 0.6 nm^{-1} using an in-house-written Mathematica script. For each individual iFFT, the contrast, brightness and gamma values were adjusted manually to highlight the Si crystallites.

Fourier-Transform Infrared Spectroscopy (FTIR)

FTIR measurements were obtained using a Fourier Transform Infrared (FTIR) spectrometer (Bruker Vertex 80 v) equipped with a RT-DTGS detector and a KBr beamsplitter. The measurements were carried out in ambient atmosphere. The layers were deposited on 240 μm thick DSP wafers.

Raman spectroscopy

Raman spectroscopy was performed using a Monovista CRS+ setup on a-Si:H(i)/a-Si:H(p)/nc-Si:H(p+)/nc-Si:H(n+) stacks deposited on glass. To obtain the crystallinity, the data was fitted and deconvolved using Lorentzians. The crystallinity was defined as the ratio between the area below the curve of the crystalline peaks (at 510 cm^{-1} and 519 cm^{-1}) over the sum of the crystalline and amorphous peaks.

Appendix A. Experimental Details

Atomic force microscopy (AFM)

The Atomic force microscopy (AFM) measurements were taken on a Digital Instruments Nanoscope 3100 system from Bruker using a AdvanceTEC, 45 N/m, (Nanosensors) in air. The samples are mounted on a x,y,z stage. A scan speed of 0.4 Hz was used for the scan range of 5 μm, whereas a scan speed of 0.2 Hz was used for the 50 μm range. Organohalide and perovskite measurements by AFM were taken directly after fabrication to prevent moisture ingress and degradation.

Liquid nuclear magnetic resonance spectrometry (NMR)

^{1}H, ^{13}C, and 2D ^{1}H-^{1}H homonuclear COSY liquid nuclear magnetic resonance spectrometry (NMR) were carried on an AVANCE III HD 400 MHz Spectrometer (Bruker). The samples (organohalide powder or organohalide condensate on a c-Si wafer) were dissolved in 600 μml DMSO-d6 (99.8%, MagniSolv) and transferred in an NMR test tube. 1 μl of hydroiodic acid was added to acidify the solution to prevent proton exchange.

Current density–voltage measurement (J–V)

Current density–voltage (J–V) measurements were performed using a two-lamp (halogen and xenon) class AAA WACOM sun simulator with an AM1.5G irradiance spectrum at 1000 W/m^2. Shadow masks were used to define the illuminated area (0.25 cm^2 for opaque cells and 1.42 cm^2 for tandems) and the cells were measured with a scan rate of 100 mV/s. Maximum power-point tracking was realised through an in-house-written LabVIEW code based on ref.[302]

External quantum efficiency (EQE)

External quantum efficiency (EQE) spectra were obtained using a custom-made spectral response set-up with a lock-in amplifier, using chopped light at a frequency of 232 Hz. For tandem cells, blue and red light biases were used to saturate the complementary sub-cell. Furthermore, a voltage bias of 0.7 V and 1.1 V was applied to measure the sub-cells in short-circuit conditions (0.7 V for the perovskite and 1.1 V for the silicon cell).

Stability tests in chapter 4

The unencapsulated device was measured at 25°C in ambient air (20-30% RH) using a two-lamp (halogen and xenon) class AAA WACOM sun simulator with an AM1.5G irradiance spectrum at 1000 W/m^2. Maximum power-point tracking measurements were performed for 61 hours using an in-house LabVIEW code. J-V measurements were recorded approximatively every 10 hours following the same procedure explained above.

The cells were kept under illumination between MPP and J-V measurements. A tandem cell was encapsulated between two 6 cm x 6 cm x 2 mm glass cover sheets. At the edges, a black butyl rubber edge sealant was applied. To prevent any inflow of the butyl edge sealant at elevated temperature, a frame of white silicone cord was placed on the cell side of the sealant. Ribbons with a conductive adhesive were placed on the front and rear side of the tandem cell to contact it. The encapsulated cell was light-soaked in an ambient atmosphere (20-30% RH) using a Solaronix degradation system at 0.7 sun. During this measurement, the tandem cell was placed on a metal carrier plate with vacuum holes, kept at a controlled temperature of 30°C. The cell was kept at its MPP using an in-house-written algorithm uploaded to an Arduino microcontroller. J-V reverse and forward scans were initially recorded every 5 minutes and, after 30 hours of light soaking, every 30 minutes. The cell was kept under constant illumination.

B Appendix: Supporting Information
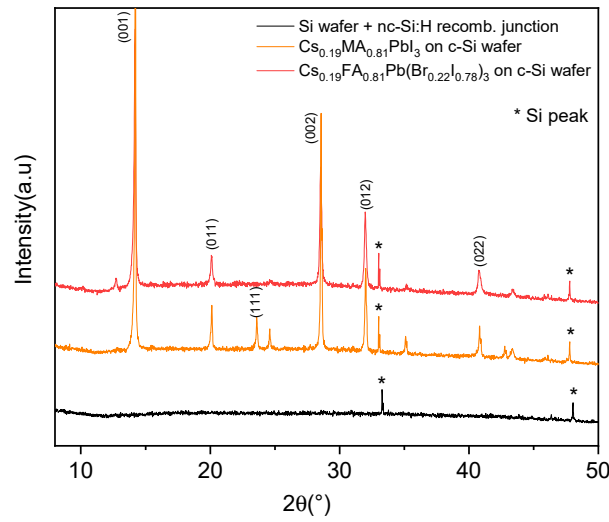
Figure B.1 – **XRD patterns of the $Cs_xMA_{1-x}PbI_3$ and $Cs_xFA_{1-x}PbI(_{1-y}Br_y)_3$ perovskites.** The perovskite layers were deposited on SHJ bottom cells coated with the nc-Si:H recombination junction and C_{60} to provide a substrate for perovskite growth identical to that in fully processed tandem cells. In the $Cs_{0.19}FA_{0.81}PbI(_{0.78}Br_{0.22})_3$ diffractogram (composition determined by RBS), a low-intensity peak appears at $12.7°$ 2θ, which is due to the presence of unconverted PbI_2.

Figure B.2 – *J-V* curve of a rear-side-textured SHJ solar cell. The solar cell is capped with a 100 nm-thick transparent IZO front electrode and a thermally evaporated Ag contact.
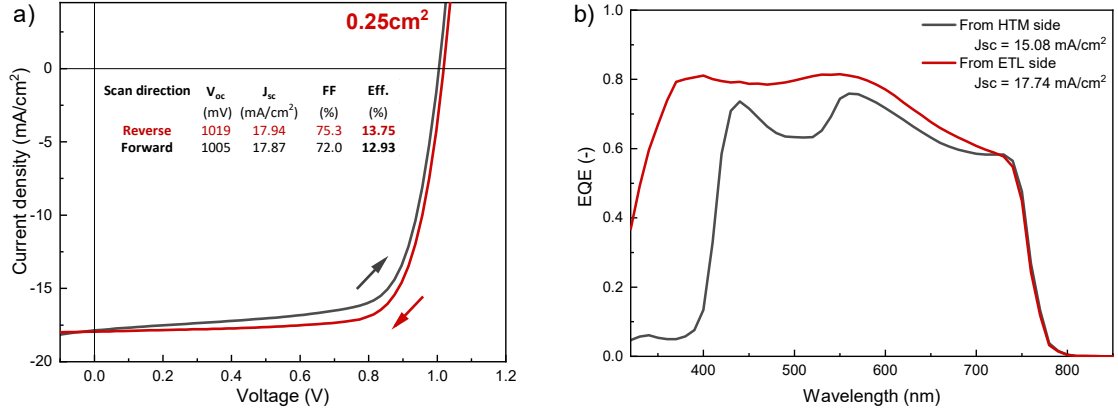
Figure B.3 – Semitransparent n-i-p solar cell characterisation of semitransparent single-junction $Cs_{0.19}MA_{0.81}PbI_3$ perovskite solar cell. a) *J-V* curve with an aperture area of 0.25 cm^2 measured from the ETL side. b) Corresponding external quantum efficiency (EQE) spectra measured from both glass and spiro-OMeTAD sides.
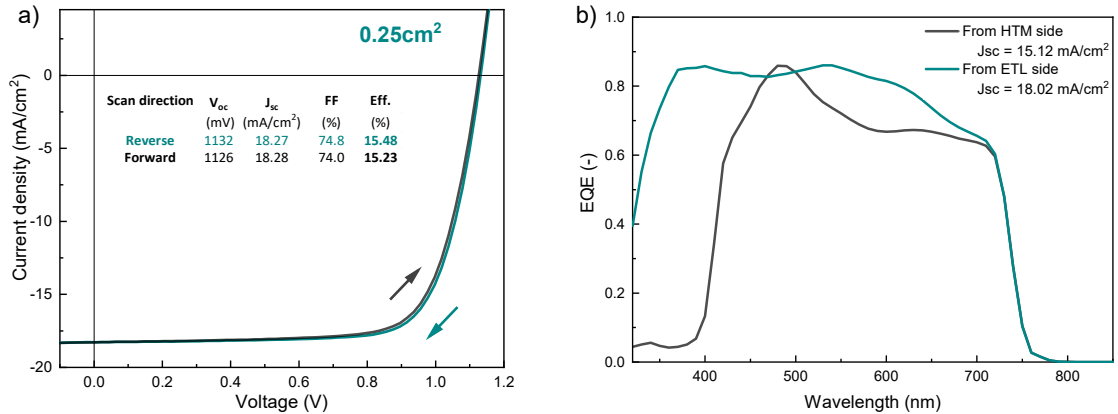
Figure B.4 – Semitransparent n-i-p single-junction $Cs_{0.19}FA_{0.81}PbI(_{0.78}Br_{0.22})_3$ perovskite solar cell. a) *J-V* curve with an aperture area of 0.25 cm^2 measured from the ETL side. b) Corresponding external quantum efficiency (EQE) spectra measured from both glass and spiro-OMeTAD sides.
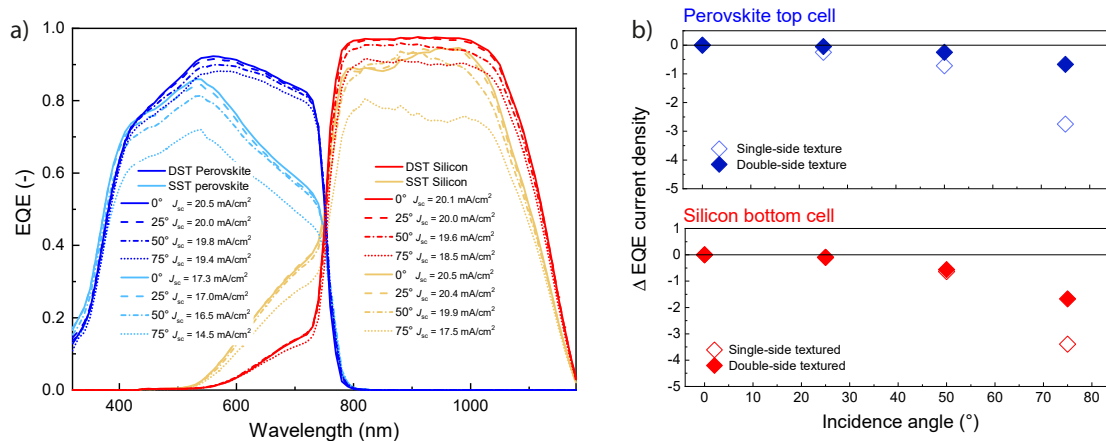
Figure B.5 – Angular optical comparison of DST and SST tandems. a) EQE measurements of DST and SST tandem at different light incident angles, b) Corresponding current density in both sub cells for each angle.
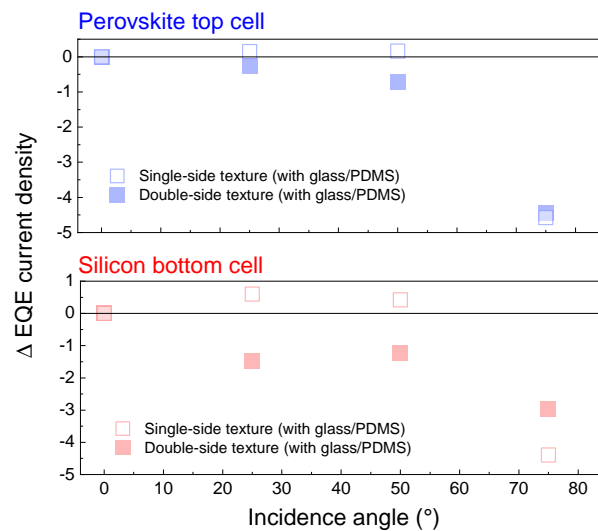
Figure B.6 – Current density losses in both-sub cells depending on light incidence angle Values extracted from EQE measurements. A glass cover glued with PDMS was deposited on top of the tandem and used to simulated the effect of encapsulation.
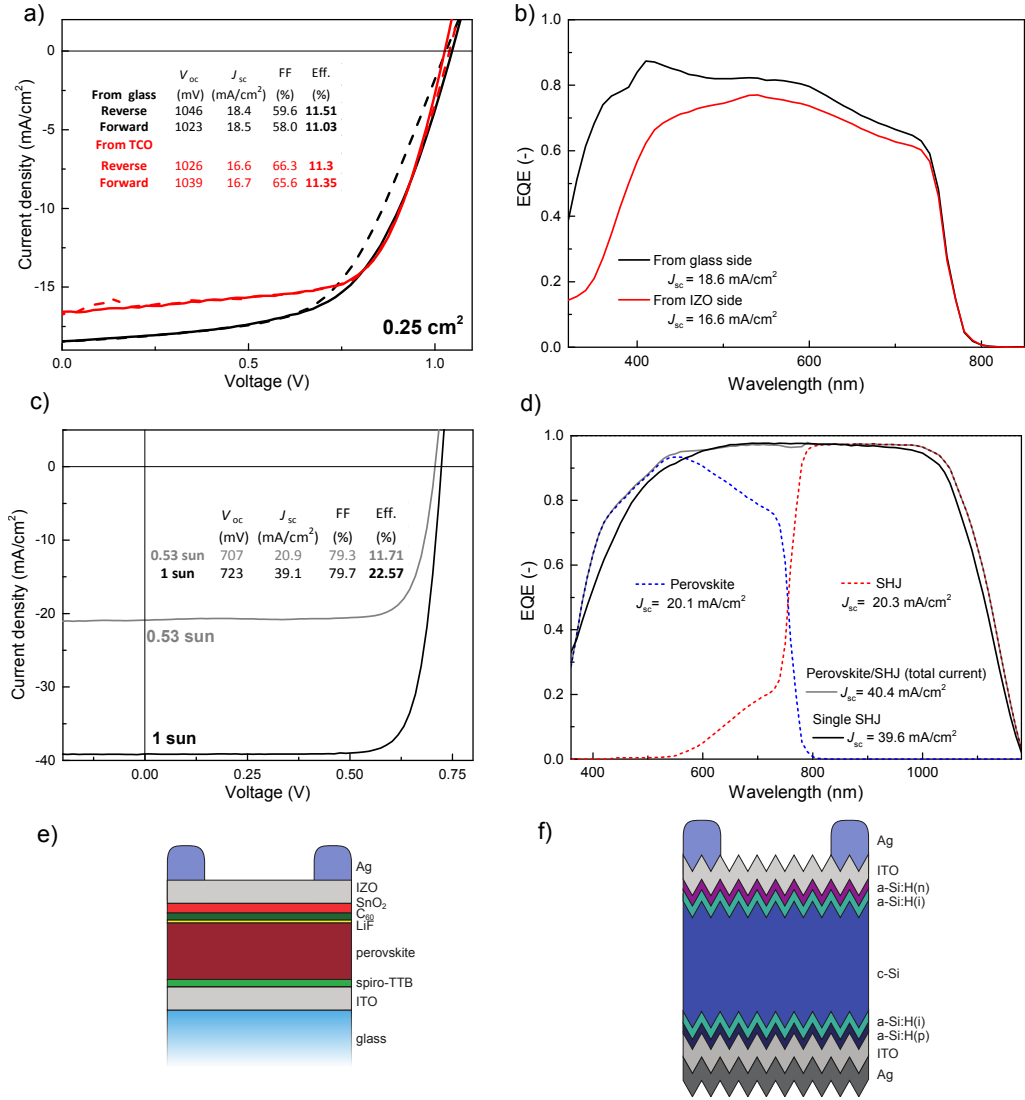
Figure B.7 – **Perovskite and SHJ single-junctions performance.** a) Semitransparent p-i-n single-junction perovskite solar cells (0.25 cm² aperture area) produced with a similar process sequence as presented for the tandem solar cells of chapter 4, b) Corresponding EQE measured from the glass side (black) or the IZO side (red). The low EQE measured from the film side for the single-junction cell is likely to stem from a higher reflectance at the front surface, resulting from the lack of surface texture, and a higher transparency near the absorption edge due to the thinner perovskite absorber (330 nm in the flat configuration compared to 440 nm for the textured case), c) *J-V* curve of a SHJ bottom cell with a 4 cm² aperture area; d) Corresponding EQE curve of the SHJ bottom cell alongside the record monolithic fully textured perovskite/SHJ tandem solar cell shown in Figure 4.15; Schematic views of e) the semitransparent single-junction perovskite solar cell measured in a-b) and f) the SHJ measured in c).

a) plot: current [A] vs voltage [V], with legend $V_{OC} \rightarrow I_{SC}$, $I_{SC} \rightarrow V_{OC}$, steady-state MPP. Fraunhofer ISE, CalLab PV Cells.

b) steady-state MPP: voltage [mV], current [mA], power [mW] vs time/s

c)

Fläche / *Area* (da)[1]:   = (1.419   ±   0.013   ) cm²

[1] : (t) = total area, (ap) = aperture area, (da) = designated illumination area /7/

Kennlinienparameter des Messobjektes unter Standardtestbedingungen (STC) / *IV-curve parameter under Standard Testing Conditions (STC)* :

		Vorwärtsrichtung / forwards scan direction			Rückwärtsrichtung / reverse scan direction			MPP-Tracking / MPP-Tracking		
V_{oc}	=	(1786.0 ±	12.0) mV	(	1788.1 ±	12.0) mV				
I_{SC} (Ed.2 - 2008)	=	(27.71 ±	0.53) mA	(	27.72 ±	0.53) mA				
I_{MPP}	=	24.66	mA		25.03	mA	(	25.15 ±	0.76) mA
V_{MPP}	=	1386.0	mV		1446.5	mV	(	1424.1 ±	25.0) mV
P_{MPP}	=	34.18	mW		36.21	mW	(	35.81 ±	0.96) mW
FF	=	69.06	%		73.06	%				
η	=	24.09	%		25.52	%	(	25.24 ±	0.72) %

Figure B.8 – Certification report for the 25.2% tandem. a) Certified *J-V* curves of the 25.24%-efficient monolithic textured perovskite/SHJ tandem solar cell measured with a scan rate of 100 mV/s; b) Voltage (black), current (red), power (blue) during 700 s MPP tracking; c) Corresponding *J-V* and MPP parameters recorded by CalLab, Fraunhofer ISE (1.419 cm² aperture area).
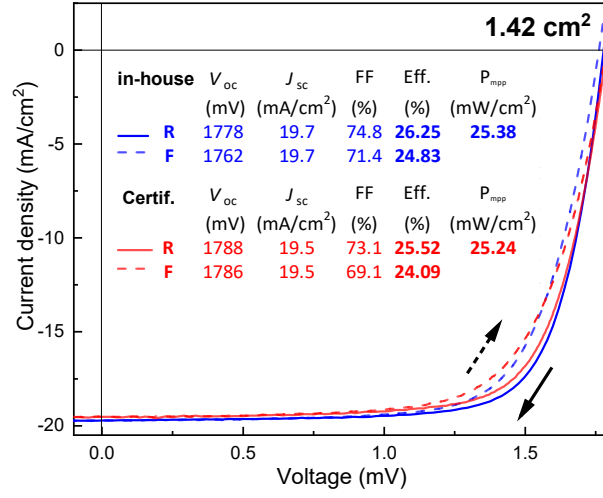
Figure B.9 – **In-house *J-V* characteristics of the record cell.** *J-V* measurements of our best monolithic textured perovskite/SHJ tandem solar cell measured in-house (blue lines) and by CalLab, Fraunhofer ISE (red lines), scanned in reverse (solid line) and forward (dashed line) direction. It is noteworthy to mention that the certification *J-V* measurements have been carried out $\approx$ 4 weeks after our in-house *J-V* measurements.
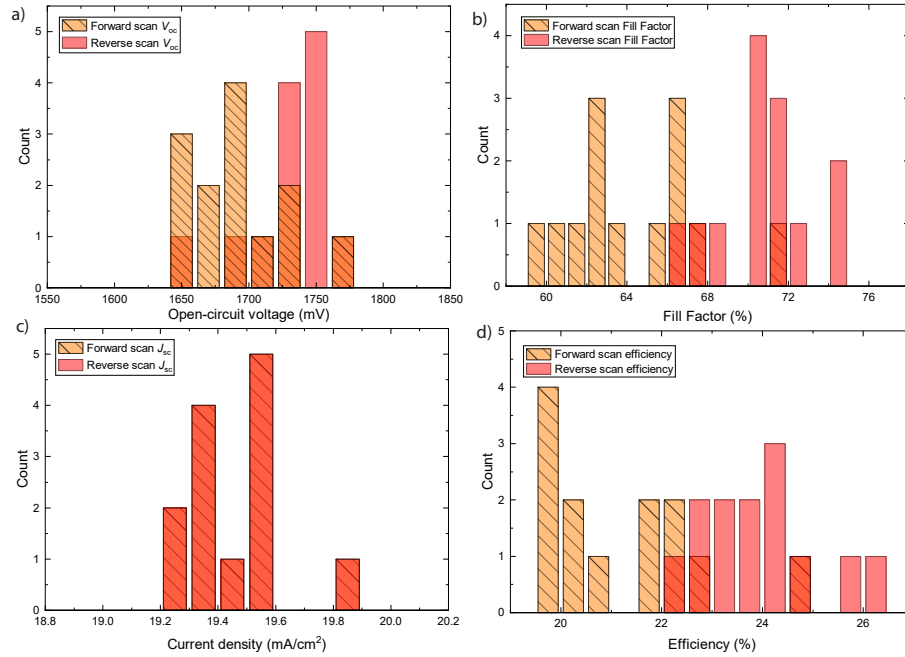
Figure B.10 – **Tandem cell results statistics.** Extracted *J-V* parameters of 13 co-processed monolithic textured perovskite/SHJ tandem solar cells.
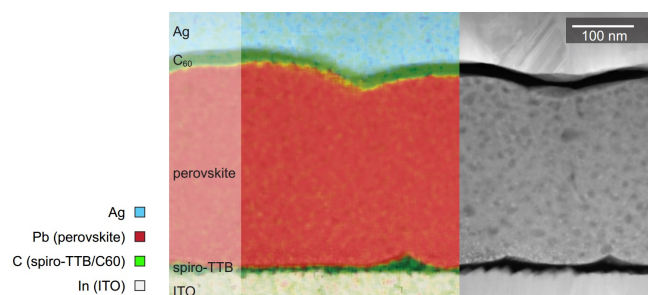
Figure B.11 – Microstructure of a perovskite single-junction solar cell on a flat substrate.
STEM EDX map of selected elements (colored left panel) and corresponding HAADF image (grayscale right panel) of a perovskite single-junction cell deposited on ITO. The spiro-TTB layer remains conformal in a flat configuration. The variations in contrast observed within the perovskite absorber are due to the formation of Pb-rich domains and small voids during the FIB sample preparation process.[183,303]
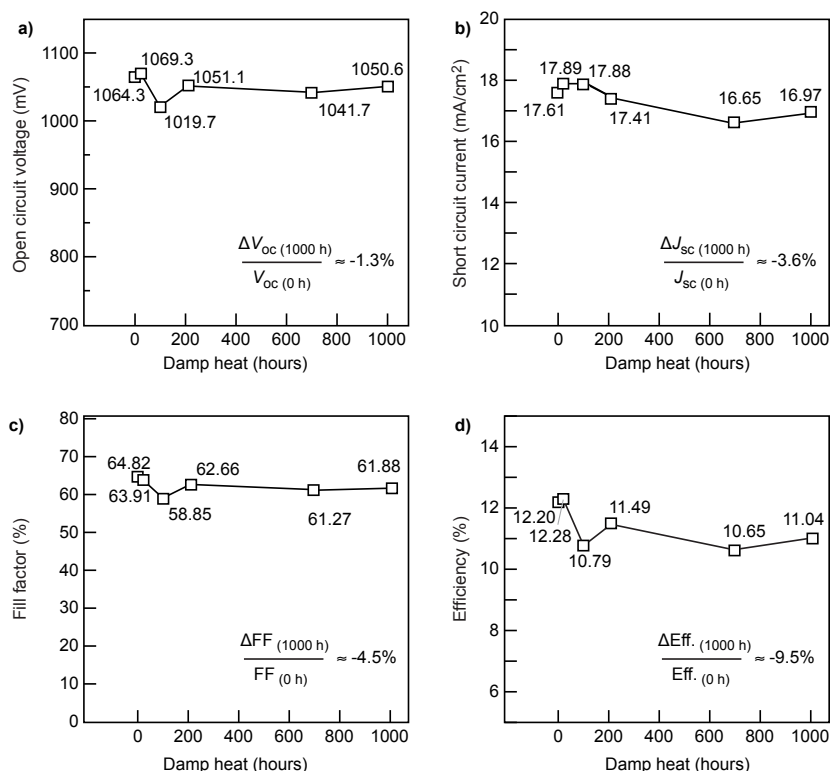
Figure B.12 – Damp heat test on a semitransparent p-i-n perovskite solar cell. a-d) Evolution of the photovoltaic characteristics during damp heat stability testing (85°C in a relative humidity level of 85% for 1000 hours) of an encapsulated planar single-junction perovskite device (glass/glass with edge sealant). The single-junction presented here pass damp heat testing, with <10% efficiency drop after 1000 hours.
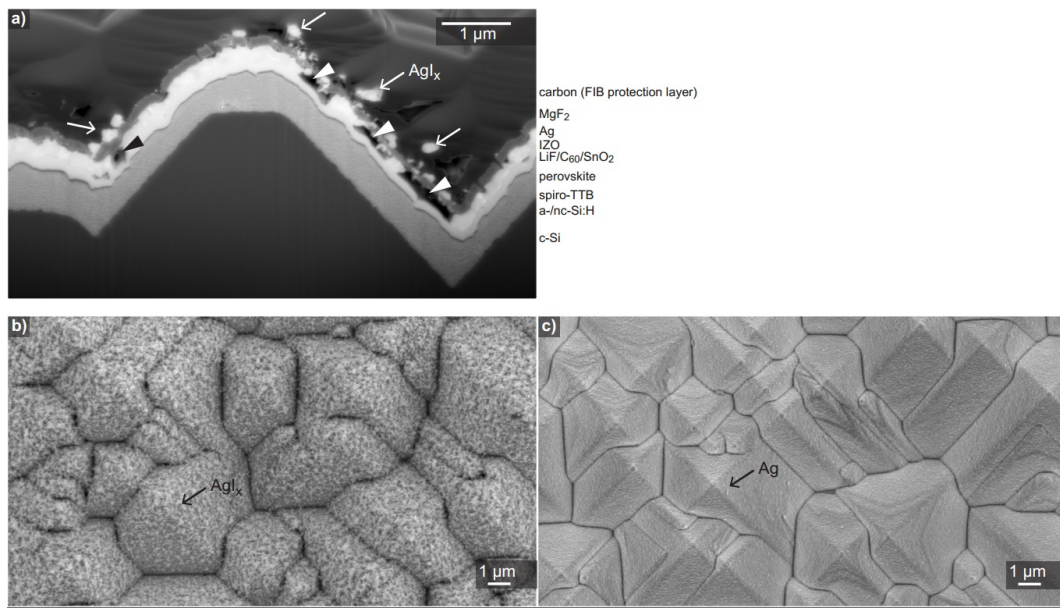
Figure B.13 – Silver halide formation during light soaking. a) SEM image of a FIB-prepared cross section prepared at the position of one Ag front finger after the light soaking experiment shown in Figure 4.18a-b. AgI$_x$ clusters form on the front MgF$_2$ surface (indicated by arrows), leaving voids at the initial position of the Ag layer (arrowheads). SEM top view images taken at the back of the encapsulated device degraded in Figure 4.18c-d, showing b) regions of the Ag back metallization that was exposed to a source of iodine and reacted, giving rise to an inhomogeneous topography (region close to one conductive ribbon) and c) the Ag back metallization that remained intact below the back conductive ribbon.
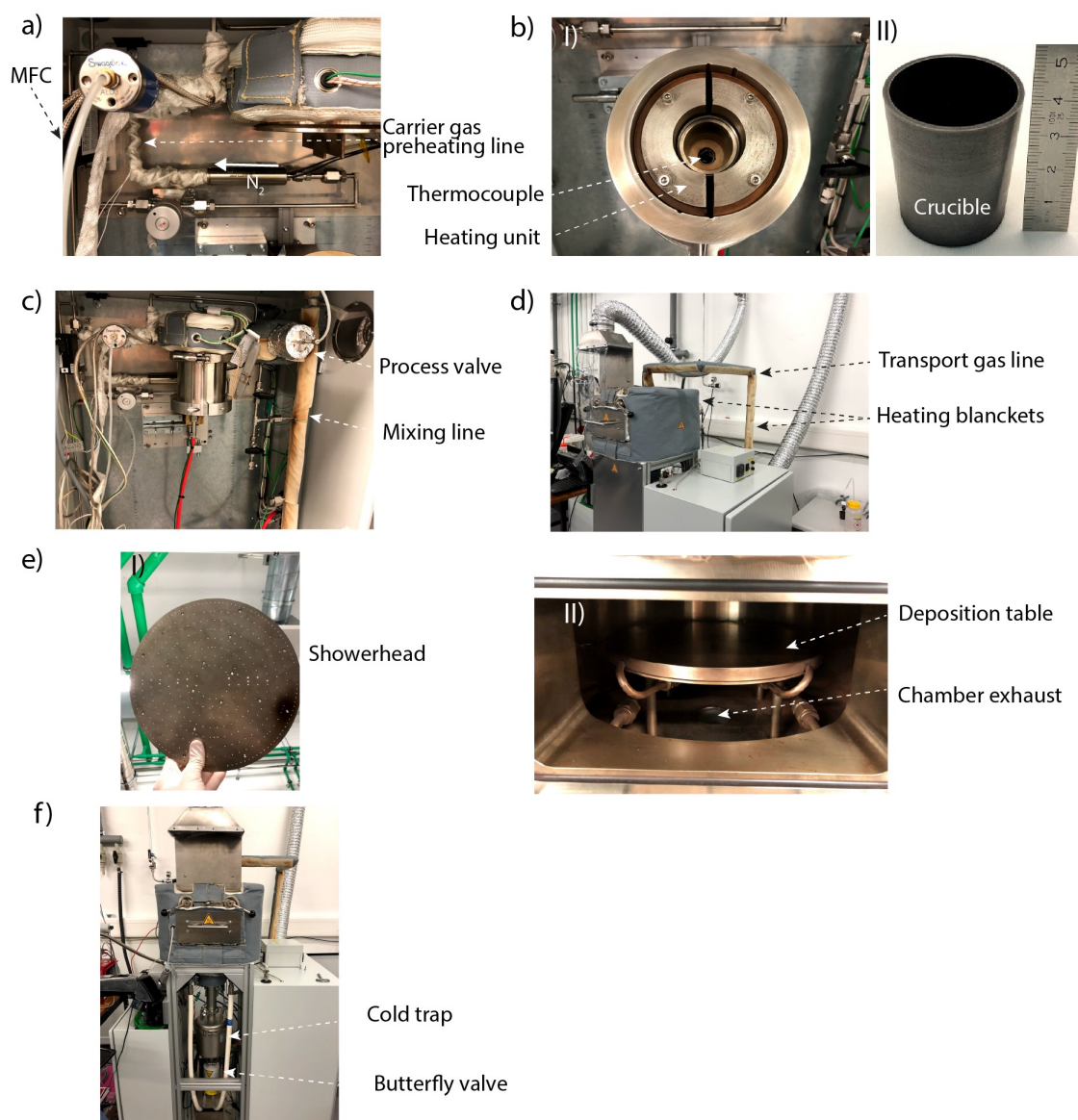
Figure B.14 – Pictures of the different part of the CVD setup. Pictures of a) the carrier gas preheating unit , b) the top of the evaporator I), the crucible II), c) an overall view of the evaporation line with the process and mixing lines, d) side-view with transport gas line, e) showerhead I), chamber view of the deposition table and exhaust, f) front-view of the CVD system with the cold trap and butterfly valve.
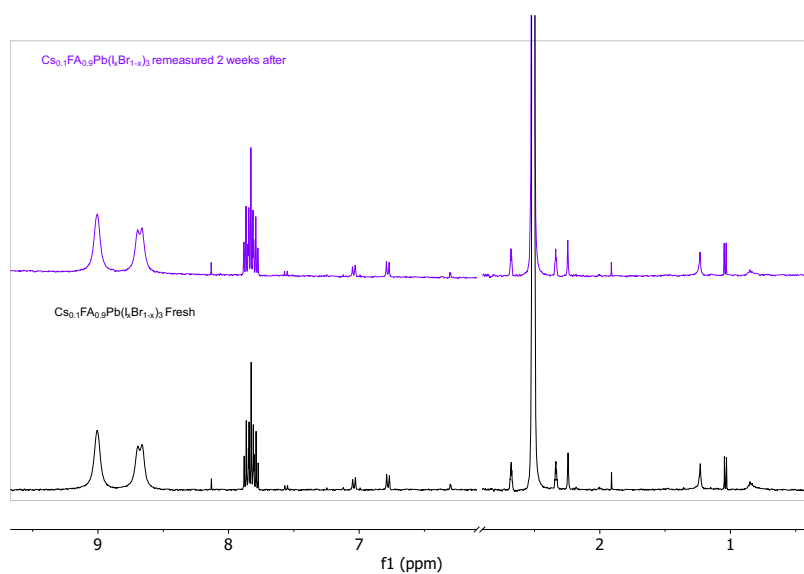
Figure B.15 – Initial liquid ^{1}H NMR of FAPI cell and after 2 weeks aging in the NMR tube. The fresh powder was dissolved in DMSO-d6. One can see that after 2 weeks in the NMR tube, the FA cation stays pristine. The additional peaks arise from protons of the Spiro-TTB molecule.
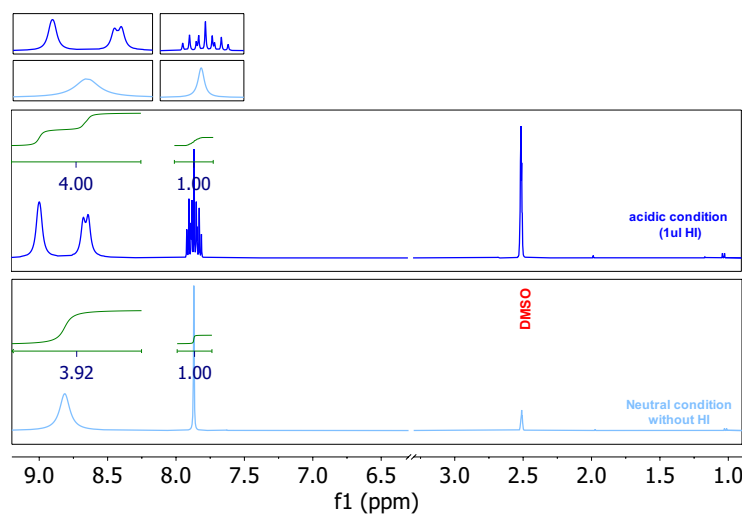
Figure B.16 – Liquid ^{1}H NMR of FAI with and without HI addition. The fresh powder was dissolved in DMSO-d6, 1 μl of HI was added to the NMR tube (dark blue).
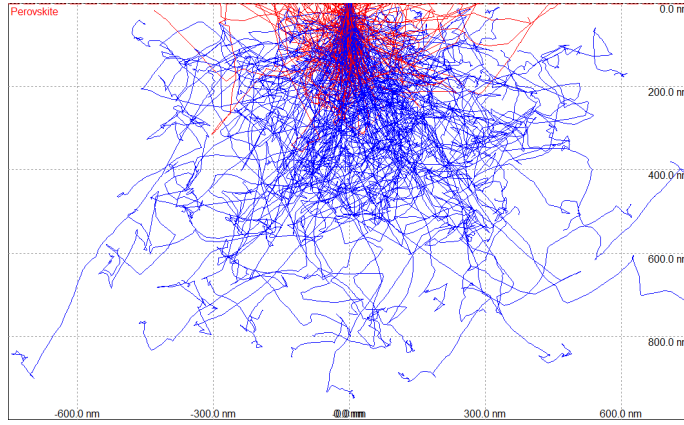
Figure B.17 – **Simulation of the interaction volume of the electron with the perovskite layer at 10 keV.** Data simulation with the Casino simulation software (https://www.gel.usherbrooke.ca/casino/). Acceleration voltage of the electron set to 10 keV, perovskite density defined at 3.7g/cm^3
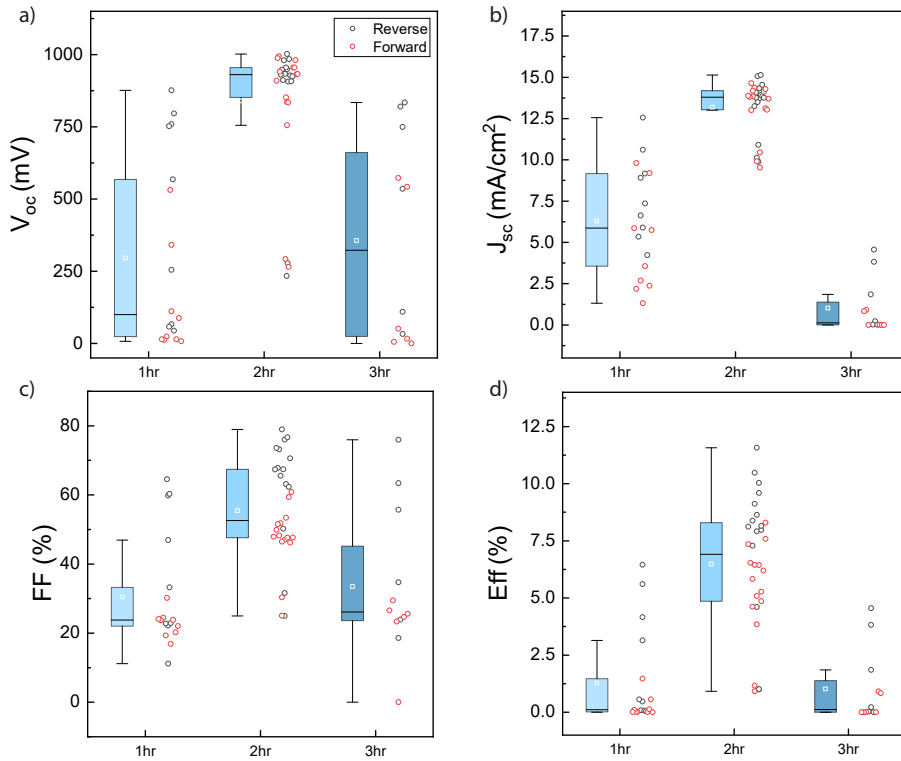
Figure B.18 – **Extracted *J-V* parameters for PVD/CVD cells at 120°C.** 9-12 cells per condition, reverse and froward scans displayed for PVD/CVD cells produced with $T_{crucible} = 200°\text{C}$ and $T_{substrate} = 120°\text{C}$ for 1 to 3 hrs. a) Open-circuit voltage (V_{oc}) b) Short-circuit density (J_{sc}), c) Fill factor (FF) and d) efficiency (Eff).
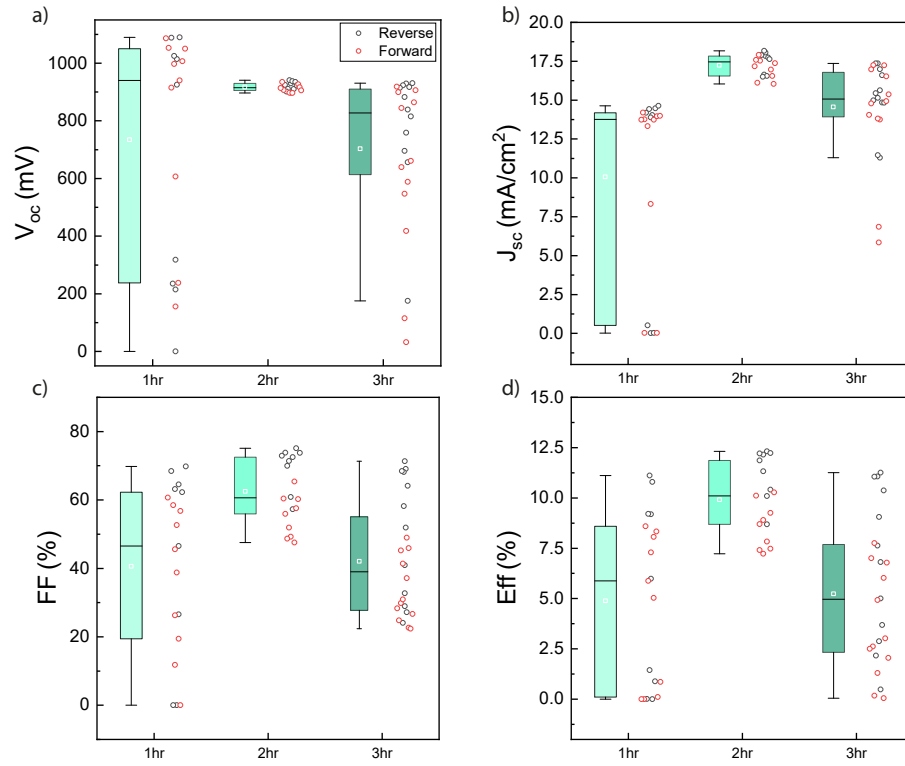
Figure B.19 – **Extracted *J-V* parameters for PVD/CVD cells at 140°C** 9-12 cells per condition, reverse and froward scans displayed for PVD/CVD cells produced with $T_{crucible} = 210°$C and $T_{substrate} = 140°$C for 1 to 3 hrs. a) Open-circuit voltage (V_{oc}) b) Short-circuit density (J_{sc}), c) Fill factor (FF) and d) efficiency (Eff).
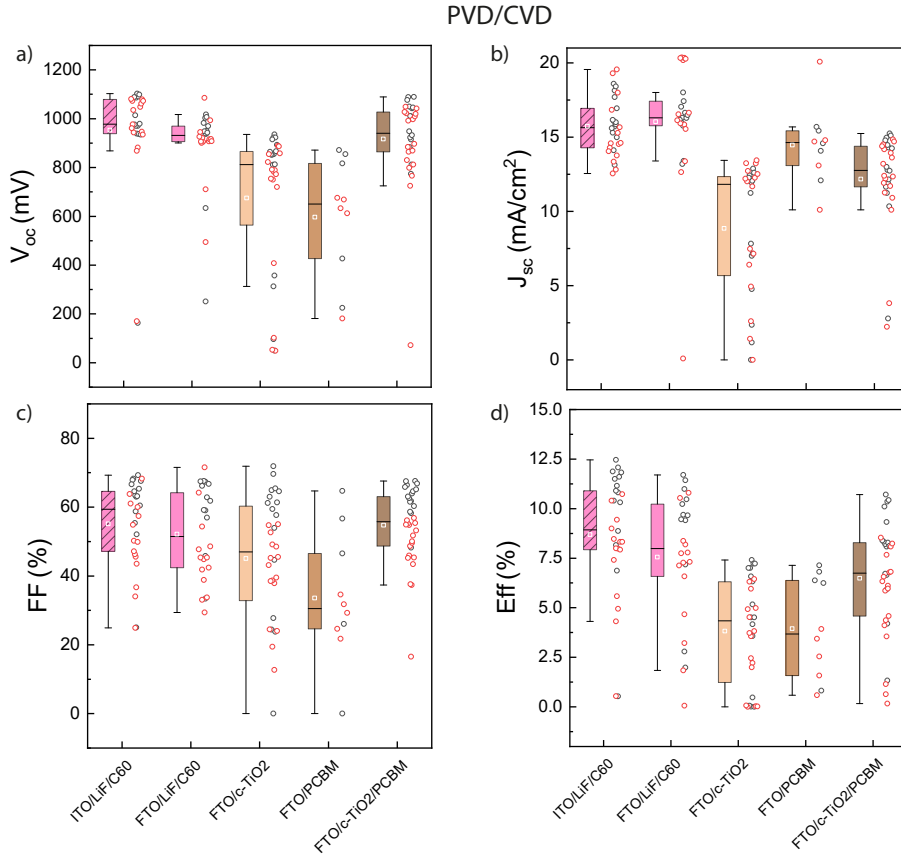
Figure B.20 – **Extracted *J-V* parameters for PVD/CVD cells with different ETLs.** 6-15 cells per condition, reverse and froward scans displayed for PVD/CVD cells produced with $T_{crucible} = 210°$C and $T_{substrate} = 140°$C for 2 hrs. a) Open-circuit voltage (V_{oc}) b) Short-circuit density (J_{sc}), c) Fill factor (FF) and d) efficiency (Eff).
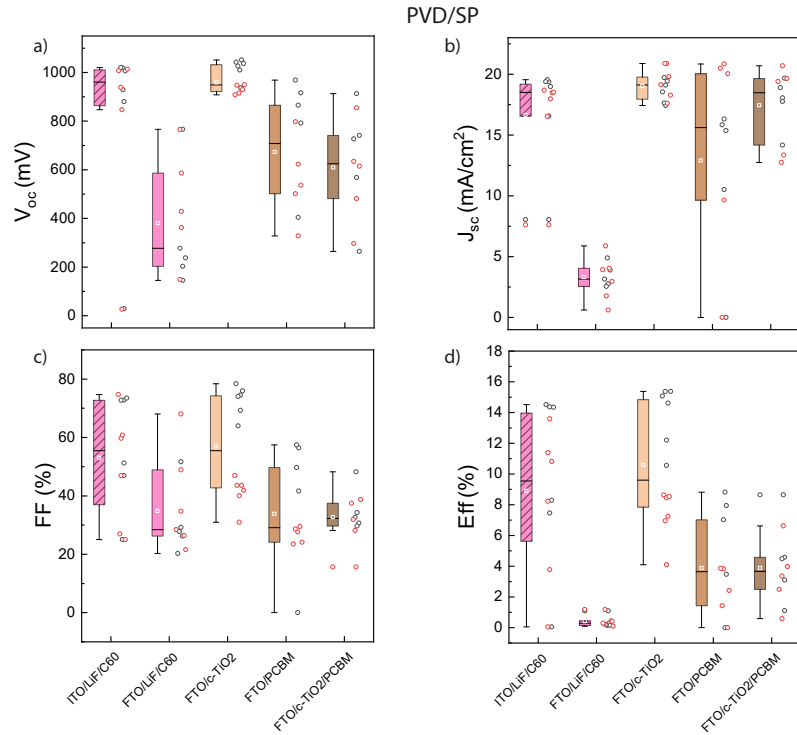
Figure B.21 – Extracted *J-V* parameters for PVD/SP cells with different ETLs. 5-6 cells per condition, reverse and froward scans displayed. a) Open-circuit voltage (V_{oc}) b) Short-circuit density (J_{sc}), c) Fill factor (FF) and d) efficiency (Eff).
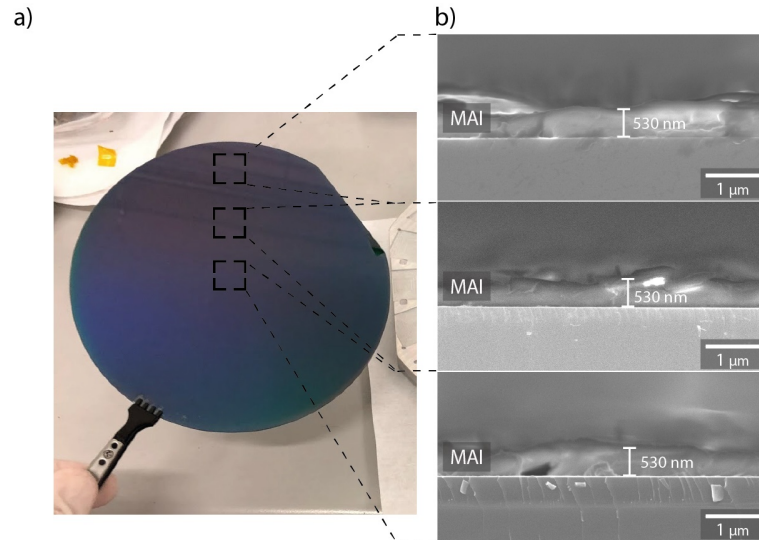
Figure B.22 – Large-scale deposition of MAI. Picture of the methylammonium iodide deposited with the table at 70°C on top of a 6 inch silicon wafer (left), cross-section SEM images taken at the centre (bottom), middle (middle) and edge (top) of the silicon wafer (right).
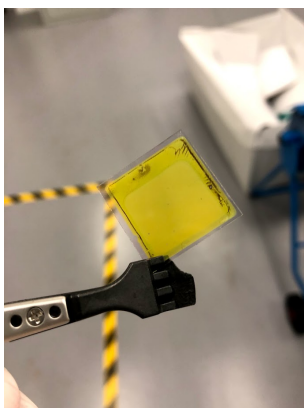
Figure B.23 – **Picture of a MAPbI₃ layer after ALD SnO₂** After an ALD SnO₂ deposition at 100°C (1 h of deposition), the organic cation evaporated and only PbI₂ was left on the substrate.
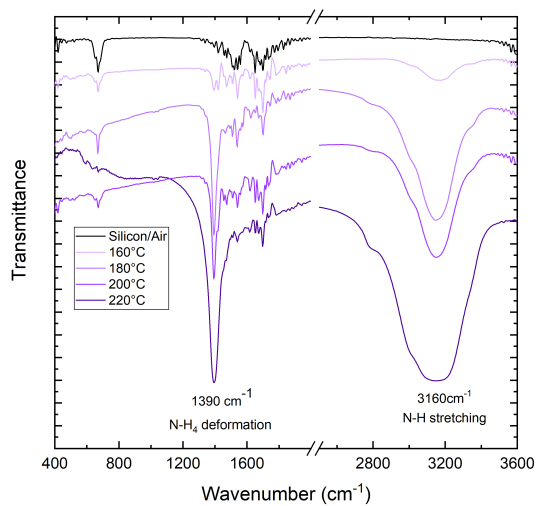
Figure B.24 – **FTIR analysis of FA evaporation at different temperatures without amy carrier gas in the evaporator.** The temperature of the blankets of the evaporator were set to 160°C to enable the condensation of the organohalides. The evaporation was performed for 2 hrs without any carrier gas.
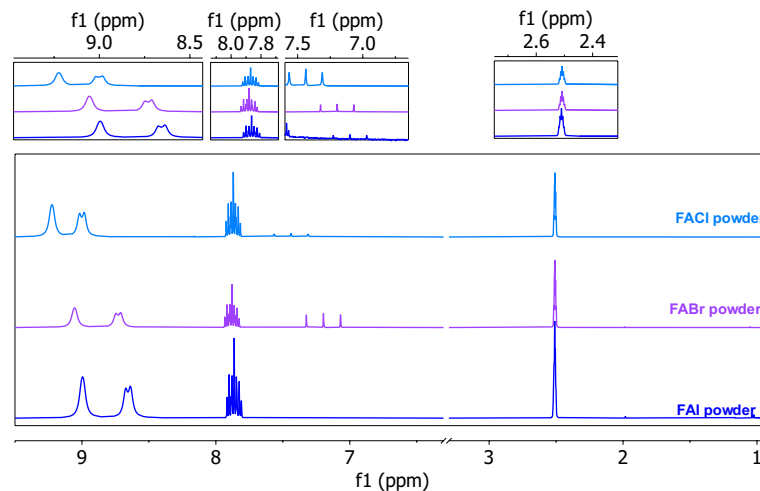
Figure B.25 – **Fresh FAI, FABr and FACl powders analysed by liquid ^{1}H NMR.** The fresh powder was dissolved in DMSO-d6, the chemical shift of the amine group increases with the electronegativity of the halide.
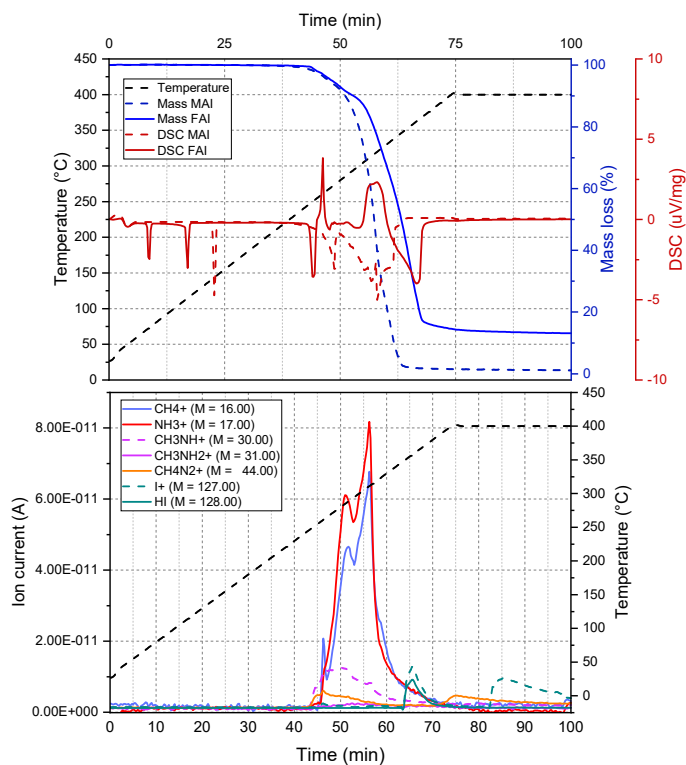
Figure B.26 – **TGA-MS analysis of formaminidium iodide (25-400°C)** TGA-DSC analysis of FAI (25-400°C) (top), MS analysis of FAI (25-400°C) (bottom). Please note that sym-triazine (m/z = 81) and its fragments were not included in that measurement, and thus couldn't be seen. The reason is that sym-triazine was not yet identified at the time of that measurement.

List of Figures

List of Tables

Bibliography

[1] C. Battaglia, A. Cuevas, and S. De Wolf, "High-efficiency crystalline silicon solar cells: status and perspectives," *Energy Environ. Sci.*, vol. 9, no. 5, pp. 1552–1576, 2016.

[2] S. Philipps and W. Warmuth, "Photovoltaics Report 2019.," *Fraunhofer Institute for Solar Energy Systems, ISE*, no. November, pp. 1–49, 2019.

[3] A. Louwen, W. G. J. H. M. van Sark, A. P. C. Faaij, and R. E. I. Schropp, "Reassessment of net energy production and greenhouse gas emissions avoidance after 40 years of photovoltaics development," *Nature Communications*, vol. 7, p. 13728, 2016.

[4] A. Richter, M. Hermle, and S. W. S. Glunz, "Reassessment of the limiting efficiency for crystalline silicon solar cells," *IEEE Journal of Photovoltaics*, vol. 3, no. 4, pp. 1184–1191, 2013.

[5] K. Yoshikawa, W. Yoshida, T. Irie, H. Kawasaki, K. Konishi, H. Ishibashi, T. Asatani, D. Adachi, M. Kanematsu, H. Uzu, and K. Yamamoto, "Exceeding conversion efficiency of 26% by heterojunction interdigitated back contact solar cell with thin film Si technology," *Solar Energy Materials and Solar Cells*, vol. 173, no. April, pp. 37–42, 2017.

[6] W. Shockley and H. J. Queisser, "Detailed balance limit of efficiency of p-n junction solar cells," *Journal of Applied Physics*, vol. 32, no. 3, pp. 510–519, 1961.

[7] S. Essig, C. Allebé, T. Remo, J. F. Geisz, M. A. Steiner, K. Horowitz, L. Barraud, J. S. Ward, M. Schnabel, A. Descoeudres, D. L. Young, M. Woodhouse, M. Despeisse, C. Ballif, and A. Tamboli, "Raising the one-sun conversion efficiency of III-V/Si solar cells to 32.8% for two junctions and 35.9% for three junctions," *Nature Energy*, vol. 2, p. 17144, 2017.

[8] R. Cariou, J. Benick, P. Beutel, N. Razek, C. Flotgen, M. Hermle, D. Lackner, S. W. Glunz, A. W. Bett, M. Wimplinger, and F. Dimroth, "Monolithic Two-Terminal III-V/Si Triple-Junction Solar Cells with 30.2% Efficiency under 1-Sun AM1.5g," *IEEE Journal of Photovoltaics*, vol. 7, no. 1, pp. 367–373, 2017.

[9] F. Sahli, B. B. A. Kamino, J. Werner, M. Bräuninger, B. Paviet-Salomon, L. Barraud, R. Monnard, J. J. P. Seif, A. Tomasi, Q. Jeangros, A. Hessler-Wyser, S. De Wolf, M. Despeisse, S. Nicolay, B. Niesen, C. Ballif, S. D. Wolf, M. Despeisse, S. Nicolay, B. Niesen, and C. Ballif, "Improved optics in monolithic perovskite/silicon tandem solar cells by a nanocrystalline silicon recombination layer," *Advanced Energy Materials*, vol. 8, pp. 1701609–1701609, 2017.

[10] F. Sahli, J. Werner, B. A. Kamino, M. Bräuninger, R. Monnard, B. Paviet-salomon, L. Barraud, L. Ding, J. J. D. Leon, D. Sacchetto, G. Cattaneo, M. Despeisse, M. Boccard, S. Nicolay, Q. Jeangros, B. Niesen, and C. Ballif, "Fully textured monolithic perovskite/silicon tandem solar cells with 25.2% power conversion efficiency," *Nature materials*, vol. 17, pp. 820–826, 2018.

[11] G. Nogay, F. Sahli, J. Werner, R. Monnard, M. Boccard, M. Despeisse, F.-J. Haug, Q. Jeangros, A. Ingenito, and C. Ballif, "25.1%-Efficient Monolithic Perovskite/Silicon Tandem Solar Cell Based on a p-type Monocrystalline Textured Silicon Wafer and High-Temperature Passivating Contacts," *ACS Energy Letters*, vol. 4, pp. 844–845, 2019.

[12] A. Tomasi, F. Sahli, J. P. Seif, L. Fanni, S. M. De Nicolas Agut, J. Geissbuhler, B. Paviet-Salomon, S. Nicolay, L. Barraud, B. Niesen, S. De Wolf, and C. Ballif, "Transparent electrodes in silicon heterojunction solar cells: Influence on contact passivation," *IEEE Journal of Photovoltaics*, vol. 6, no. 1, pp. 17–27, 2016.

[13] J. Werner, L. Barraud, A. Walter, M. Brauninger, F. Sahli, D. Sacchetto, N. Tetreault, B. Paviet-Salomon, S.-J. S.-J. S.-J. Moon, C. Allebé, M. Despeisse, S. Nicolay, S. De Wolf, B. Niesen, and C. Ballif, "Efficient Near-Infrared-Transparent Perovskite Solar Cells Enabling Direct Comparison of 4-Terminal and Monolithic Perovskite/Silicon Tandem Cells," *ACS Energy Letters*, vol. 1, no. 2, pp. 474–480, 2016.

[14] Z. Song, J. Werner, N. Shrestha, F. Sahli, S. De Wolf, B. Niesen, S. C. S. Watthage, A. A. B. Phillips, C. Ballif, R. R. J. Ellingson, and M. M. J. Heben, "Probing Photocurrent Nonuniformities in the Subcells of Monolithic Perovskite/Silicon Tandem Solar Cells," *Journal of Physical Chemistry Letters*, vol. 7, no. 24, pp. 5114–5120, 2016.

[15] Z. Song, J. Werner, S. Watthage, F. Sahli, N. Shrestha, S. De Wolf, B. Niesen, A. Phillips, C. Ballif, R. Ellingson, and M. Heben, "Imaging the Spatial Evolution of Degradation in Perovskite/c-Si Tandem Solar Cells After Exposure to Humid Air," *IEEE Journal of Photovoltaics*, 2017.

[16] M. Mundus, B. Venkataramanachar, R. Gehlhaar, M. Kohlstädt, B. Niesen, W. Qiu, J. Herterich, F. Sahli, M. Bräuninger, J. Werner, J. Hohl-Ebinger, G. Uytterhoeven, U. Würfel, C. Ballif, M. Schubert, W. Warta, and S. Glunz, "Spectrally resolved

nonlinearity and temperature dependence of perovskite solar cells," *Solar Energy Materials and Solar Cells*, vol. 172, 2017.

[17] J. Werner, G. Nogay, F. Sahli, C.-J. T. Yang, M. Bräuninger, G. Christmann, A. Walter, B. Kamino, P. Fiala, P. Löper, S. Nicolay, Q. Jeangros, B. Niesen, and C. Ballif, "Complex Refractive Indices of Cesium-formamidinium-based Mixed Halide Perovskites with Optical Bandgaps from 1.5 to 1.8 eV," *ACS Energy Letters*, vol. 3, pp. 742–747, 2018.

[18] J. Werner, F. Sahli, F. Fu, J. J. Diaz Leon, A. Walter, B. A. Kamino, B. Niesen, S. Nicolay, Q. Jeangros, and C. Ballif, "Perovskite/Perovskite/Silicon Monolithic Triple-Junction Solar Cells with a Fully Textured Design," *ACS Energy Letters*, vol. 3, no. 9, pp. 2052–2058, 2018.

[19] D. A. Jacobs, M. Langenhorst, F. Sahli, B. S. Richards, T. P. White, C. Ballif, K. R. Catchpole, and U. W. Paetzold, "Light Management: A Key Concept in High-Efficiency Perovskite/Silicon Tandem Photovoltaics," *Journal of Physical Chemistry Letters*, vol. 10, no. 11, pp. 3159–3170, 2019.

[20] J. Gao, F. Sahli, C. Liu, D. Ren, X. Guo, J. Werner, Q. Jeangros, S. M. Zakeeruddin, C. Ballif, M. Grätzel, and J. Luo, "Solar Water Splitting with Perovskite/Silicon Tandem Cell and TiC-Supported Pt Nanocluster Electrocatalyst," *Joule*, vol. 3, no. 12, pp. 2930–2941, 2019.

[21] R. A. Razera, D. A. Jacobs, F. Fu, P. Fiala, M. Dussouillez, F. Sahli, T. C. Yang, L. Ding, A. Walter, A. F. Feil, H. I. Boudinov, S. Nicolay, C. Ballif, and Q. Jeangros, "Instability of p-i-n perovskite solar cells under reverse bias," *Journal of Materials Chemistry A*, vol. 8, no. 1, pp. 242–250, 2019.

[22] C. Breyer, D. Bogdanov, A. Aghahosseini, A. Gulagi, M. Child, A. S. Oyewo, J. Farfan, K. Sadovskaia, and P. Vainikka, "Solar photovoltaics demand for the global energy transition in the power sector," *Progress in Photovoltaic Research and applications*, vol. 26, no. 8, pp. 505–523, 2018.

[23] J. Rogelj, M. Den Elzen, N. Höhne, T. Fransen, H. Fekete, H. Winkler, R. Schaeffer, F. Sha, K. Riahi, and M. Meinshausen, "Paris Agreement climate proposals need a boost to keep warming well below 2C," *Nature*, vol. 534, no. 7609, pp. 631–639, 2016.

[24] N. M. Haegel, H. Atwater, T. Barnes, C. Breyer, A. Burrell, Y.-M. Chiang, S. De Wolf, B. Dimmler, D. Feldman, S. Glunz, J. C. Goldschmidt, D. Hochschild, R. Inzunza, I. Kaizuka, B. Kroposki, S. Kurtz, S. Leu, R. Margolis, K. Matsubara, A. Metz, W. K. Metzger, M. Morjaria, S. Niki, S. Nowak, I. M. Peters, S. Philipps, T. Reindl, A. Richter, D. Rose, K. Sakurai, R. Schlatmann, M. Shikano, W. Sinke, R. Sinton, B. Stanbery, M. Topic, W. Tumas, Y. Ueda, J. van de Lagemaat, P. Verlinden, M. Vetter, E. Warren, M. Werner, M. Yamaguchi, and A. W. Bett,

Bibliography

"Terawatt-scale photovoltaics: Transform global energy," *Science*, vol. 364, no. 6443, pp. 836–838, 2019.

[25] Z. J. Yu, J. V. Carpenter, Z. C. Holman, J. V. Carpenter III, and Z. C. Holman, "Techno-economic viability of silicon-based tandem photovoltaic modules in the United States," *Nature Energy.*, p. In Press., 2016.

[26] "Price of PV modules, www.pvinsight.com," 2020.

[27] M. A. Green, E. D. Dunlop, D. H. Levi, J. Hohl-Ebinger, M. Yoshita, and A. W. Ho-Baillie, "Solar cell efficiency tables (version 54)," *Progress in Photovoltaic Research and applications*, vol. 27, no. 7, pp. 565–575, 2019.

[28] G. Conibeer, "Third-generation photovoltaics," *Materials Today*, vol. 10, no. 11, pp. 42–50, 2007.

[29] M. A. Green, *Third generation photovoltaics: advanced solar energy conversion.* 2006.

[30] A. De Vos, "Detailed balance limit of the efficiency of tandem solar cells," *Journal of Physics D: Applied Physics*, vol. 13, no. 5, pp. 839–846, 1980.

[31] W. Ruppel and P. Würfel, "Upper Limit for the Conversion of Solar Energy," *IEEE Transactions on Electron Devices*, vol. 27, no. 4, pp. 877–882, 1980.

[32] J. Werner, "Perovskite / Silicon Tandem Solar Cells : Toward A ordable Ultra-High Efficiency," *EPFL*, vol. Thesis, 2018.

[33] R. Sheng, A. W. Ho-Baillie, S. Huang, M. Keevers, X. Hao, L. Jiang, Y. B. Cheng, and M. A. Green, "Four-Terminal Tandem Solar Cells Using CH3NH3PbBr3 by Spectrum Splitting," *Journal of Physical Chemistry Letters*, vol. 6, no. 19, pp. 3931–3934, 2015.

[34] Z. J. Yu, K. C. Fisher, B. M. Wheelwright, R. P. Angel, and Z. C. Holman, "PVMirror: A New Concept for Tandem Solar Cells and Hybrid Solar Converters," *IEEE Journal of Photovoltaics*, vol. 5, no. 6, pp. 1791–1799, 2015.

[35] H. Zhang, H. Yao, J. Hou, J. Zhu, J. Zhang, W. Li, R. Yu, B. Gao, S. Zhang, and J. Hou, "Over 14% Efficiency in Organic Solar Cells Enabled by Chlorinated Nonfullerene Small-Molecule Acceptors," *Advanced Materials*, vol. 30, no. 28, pp. 1–7, 2018.

[36] NREL Efficiency Chart, "NREL Efficiency Chart."

[37] J. Meier, S. Dubail, R. Fluckiger, D. Fischer, H. Keppner, and A. Shah, "Intrinsic microcrystalline silicon (uc-Si:H) A promising new thin film solar cell material," *IEEE Photovoltaic Specialists Conference*, pp. 409–412, 1994.

[38] M. A. Green, A. Ho-Baillie, and H. J. Snaith, "The emergence of perovskite solar cells," *Nature Photonics*, vol. 8, p. 506, 2014.

[39] H. J. Snaith, "Perovskites: The emergence of a new era for low-cost, high-efficiency solar cells," *Journal of Physical Chemistry Letters*, vol. 4, no. 21, pp. 3623–3630, 2013.

[40] P. Gao, M. Grätzel, and M. K. Nazeeruddin, "Environmental Science Organohalide lead perovskites for photovoltaic applications," *Energy & Environmental Science*, vol. 1, no. c, pp. 2448–2463, 2014.

[41] A. W. Blakers, A. Wang, A. M. Milne, J. Zhao, and M. A. Green, "22.8% Efficient Silicon Solar Cell," *Applied Physics Letters*, vol. 55, no. 13, pp. 1363–1365, 1989.

[42] M. A. Green, "The Passivated Emitter and Rear Cell (PERC): From conception to mass production," *Solar Energy Materials and Solar Cells*, vol. 143, pp. 190–197, 2015.

[43] J. Melskens, B. W. Van De Loo, B. Macco, L. E. Black, S. Smit, and W. M. Kessels, "Passivating Contacts for Crystalline Silicon Solar Cells: From Concepts and Materials to Prospects," *IEEE Journal of Photovoltaics*, vol. 8, no. 2, pp. 373–388, 2018.

[44] G. Nogay, A. Ingenito, E. Rucavado, Q. Jeangros, J. Stuckelberger, P. Wyss, C. Ballif, M. Morales-masis, F.-j. Haug, and L. Philipp, "Crystalline Silicon Solar Cells With Coannealed Electron- and Hole-Selective SiC x Passivating Contacts," *IEEE Journal of PhotovoltaicsJournal of Photovolatics*, vol. 8, no. 6, pp. 1478–1485, 2018.

[45] A. Descoeudres, C. Allebé, N. Badel, L. Barraud, J. Champliaud, G. Christmann, F. Debrot, A. Faes, J. Geissbühler, J. Horzel, A. Lachowicz, J. Levrat, S. Martin De Nicolas, S. Nicolay, B. Paviet-Salomon, L.-L. Senaud, C. Ballif, and M. Despeisse, "Low-temperature processes for passivation and metallization of high- efficiency crystalline silicon solar cells," *Solar Energy*, 2018.

[46] J. Liu, Y. Yao, and S. Xiao, "Review of status developments of high-efficiency crystalline silicon solar cells," *J. Phys D: appl. Phys.*, vol. 51, p. 123001, 2018.

[47] S. De Wolf, A. Descoeudres, Z. C. Holman, and C. Ballif, "High-efficiency Silicon Heterojunction Solar Cells: A Review," *Green*, vol. 2, pp. 7–24, 2012.

[48] M. Taguchi, A. Terakawa, E. Maruyama, and M. Tanaka, "Obtaining a higher voc in HIT cells," *Progress in Photovoltaics: Research and Applications*, vol. 13, no. 6, pp. 481–488, 2005.

[49] Z. C. Holman, A. Descoeudres, S. De Wolf, and C. Ballif, "Record Infrared Internal Quantum Efficiency in Silicon Heterojunction Solar Cells With Dielectric/Metal Rear Reflectors," *IEEE Journal of Photovoltaics*, vol. 3, no. 4, pp. 1243–1249, 2013.

[50] S. De Wolf, H. Fujiwara, and M. Kondo, "Impact of annealing on passivation of a-Si:H / c-Si heterostructures," *Conference Record of the IEEE Photovoltaic Specialists Conference*, pp. 2–5, 2008.

[51] D. Weber, "CH 3 NH 3 PbX 3 , ein Pb(II)-System mit kubischer Perowskitstruktur," *Z. Naturforsch., B: J. Chem. Sci.*, vol. 1445, no. August, pp. 1443–1445, 1978.

[52] C. R. Kagan, D. B. Mitzi, and C. D. Dimitrakopoulos, "Organic-inorganic hybrid materials as semiconducting channels in thin- film field-effect transistors," *Science*, vol. 286, no. 5441, pp. 945–947, 1999.

[53] D. B. Mitzi, "Synthesis, structure, and properties of organic-inorganic perovskites and related materials," in *Progress in Inorganic Chemistry*, 1991.

[54] K. Chondroudis and D. B. Mitzi, "Electroluminescence from an organic-inorganic perovskite incorporating a quaterthiophene dye within lead halide perovskite layers," *Chemistry of Materials*, vol. 11, no. 11, pp. 3028–3030, 1999.

[55] D. B. Mitzi, C. A. Feild, W. T. A. Harrison, and A. M. Guloy, "Conducting tin halides with a layered organic-based perovskite structure," *Nature*, vol. 369, no. June, p. 467, 1994.

[56] A. Kojima, K. Teshima, Y. Shirai, and T. Miyasaka, "Organometal halide perovskites as visible-light sensitizers for photovoltaic cells," *Journal of the American Chemical Society*, vol. 131, no. 17, pp. 6050–6051, 2009.

[57] S. Shi, Y. Li, X. Li, and H. Wang, "Advancements in all-solid-state hybrid solar cells based on organometal halide perovskites," *Materials Horizons*, vol. 2, no. 4, pp. 378–405, 2015.

[58] M. Saliba, T. Matsui, J.-Y. Seo, K. Domanski, J.-P. J.-P. Correa-Baena, M. K. M. Nazeeruddin, S. S. M. Zakeeruddin, W. Tress, A. Abate, A. Hagfeldt, M. Grätzel, and M. Gratzel, "Cesium-containing Triple Cation Perovskite Solar Cells: Improved Stability, Reproducibility and High Efficiency," *Energy Environ. Sci.*, vol. 9, no. 6, p. 1989, 2016.

[59] V. M. Goldschmidt, "Die Gesetze der Krystallochemie.," *Naturwissenschaften*, vol. 14, pp. 477–485, 1926.

[60] Z. Li, M. Yang, J. S. Park, S. H. Wei, J. J. Berry, and K. Zhu, "Stabilizing Perovskite Structures by Tuning Tolerance Factor: Formation of Formamidinium and Cesium Lead Iodide Solid-State Alloys," *Chemistry of Materials*, vol. 28, no. 1, pp. 284–292, 2016.

[61] C. J. Bartel, C. Sutton, B. R. Goldsmith, R. Ouyang, C. B. Musgrave, L. M. Ghiringhelli, and M. Scheffler, "New tolerance factor to predict the stability of perovskite oxides and halides," *Science Advances*, vol. 5, no. 2, pp. 1–10, 2019.

[62] N. Pellet, P. Gao, G. Gregori, T.-y. Yang, M. K. Nazeeruddin, J. Maier, and M. Grätzel, "Mixed-Organic-Cation Perovskite Photovoltaics for Enhanced Solar-Light Harvesting," *Angewandte Chemie*, no. 53, pp. 3151–3157, 2014.

[63] B. Conings, J. Drijkoningen, N. Gauquelin, A. Babayigit, J. D'Haen, L. D'Olieslaeger, A. Ethirajan, J. Verbeeck, J. Manca, E. Mosconi, F. De Angelis, and H. G. Boyen, "Intrinsic Thermal Instability of Methylammonium Lead Trihalide Perovskite," *Advanced Energy Materials*, vol. 5, no. 15, 2015.

[64] M. Kot, K. Wojciechowski, H. Snaith, and D. Schmeißer, "Evidence of Nitrogen Contribution to the Electronic Structure of the CH3NH3PbI3 Perovskite," *Chemistry - A European Journal*, vol. 24, no. 14, pp. 3539–3544, 2018.

[65] P. Umari, E. Mosconi, and F. De Angelis, "Relativistic GW calculations on CH3 NH3 PbI 3 and CH3 NH3 SnI3 Perovskites for Solar Cell Applications," *Scientific Reports*, vol. 4, pp. 1–7, 2014.

[66] W. J. Yin, J. H. Yang, J. Kang, Y. Yan, and S. H. Wei, "Halide perovskite materials for solar cells: A theoretical review," *Journal of Materials Chemistry A*, vol. 3, no. 17, pp. 8926–8942, 2015.

[67] C. Wehrenfennig, M. Liu, H. J. Snaith, M. B. Johnston, and L. M. Herz, "Homogeneous emission line broadening in the organo lead halide perovskite CH3NH3PbI3-xClx," *Journal of Physical Chemistry Letters*, vol. 5, no. 8, pp. 1300–1306, 2014.

[68] S. A. Kulkarni, T. Baikie, P. P. Boix, N. Yantara, N. Mathews, and S. Mhaisalkar, "Band-gap tuning of lead halide perovskites using a sequential deposition process," *Journal of Materials Chemistry A*, vol. 2, no. 24, pp. 9221–9225, 2014.

[69] E. T. Hoke, D. J. Slotcavage, E. R. Dohner, A. R. Bowring, H. I. Karunadasa, and M. D. McGehee, "Reversible photo-induced trap formation in mixed-halide hybrid perovskites for photovoltaics," *Chemical Science*, vol. 6, no. 1, pp. 613–617, 2015.

[70] A. M. Leguy, P. Azarhoosh, M. I. Alonso, M. Campoy-Quiles, O. J. Weber, J. Yao, D. Bryant, M. T. Weller, J. Nelson, A. Walsh, M. Van Schilfgaarde, and P. R. Barnes, "Experimental and theoretical optical properties of methylammonium lead halide perovskites," *Nanoscale*, vol. 8, no. 12, pp. 6317–6327, 2016.

[71] S. De Wolf, J. Holovsky, S. J. Moon, P. Löper, B. Niesen, M. Ledinsky, F. J. Haug, J. H. Yum, and C. Ballif, "Organometallic halide perovskites: Sharp optical absorption edge and its relation to photovoltaic performance," *Journal of Physical Chemistry Letters*, vol. 5, no. 6, pp. 1035–1039, 2014.

[72] S. D. Stranks, G. E. Eperon, G. Grancini, C. Menelaou, M. J. P. Alcocer, T. Leijtens, L. M. Herz, A. Petrozza, and H. J. Snaith, "Electron-Hole Diffusion Lengths Exceeding," *Science*, vol. 342, no. 6156, pp. 341–345, 2013.

[73] A. Miyata, A. Mitioglu, P. Plochocka, O. Portugall, J. T. W. Wang, S. D. Stranks, H. J. Snaith, and R. J. Nicholas, "Direct measurement of the exciton binding energy and effective masses for charge carriers in organic-inorganic tri-halide perovskites," *Nature Physics*, vol. 11, no. 7, pp. 582–587, 2015.

[74] J. M. Ball, M. M. Lee, A. Hey, and H. J. Snaith, "Low-temperature processed meso-superstructured to thin-film perovskite solar cells," *Energy and Environmental Science*, vol. 6, no. 6, pp. 1739–1743, 2013.

[75] G. Xing, N. Mathews, S. S. Lim, Y. M. Lam, S. Mhaisalkar, and T. C. Sum, "Long-Range Balanced Electron- and Hole-Transport Lengths in Organic-Inorganic CH 3 NH 3 PbI 3," *Science*, vol. 342, no. 6960, pp. 498–500, 2013.

[76] H. S. Kim, C. R. Lee, J. H. Im, K. B. Lee, T. Moehl, A. Marchioro, S. J. Moon, R. Humphry-Baker, J. H. Yum, J. E. Moser, M. Grätzel, and N. G. Park, "Lead iodide perovskite sensitized all-solid-state submicron thin film mesoscopic solar cell with efficiency exceeding 9%," *Scientific Reports*, vol. 2, pp. 1–7, 2012.

[77] L. Calió, S. Kazim, M. Grätzel, and S. Ahmad, "Hole-Transport Materials for Perovskite Solar Cells," *Angewandte Chemie - International Edition*, vol. 55, no. 47, pp. 14522–14545, 2016.

[78] J. Y. Jeng, Y. F. Chiang, M. H. Lee, S. R. Peng, T. F. Guo, P. Chen, and T. C. Wen, "CH3NH3PbI3 perovskite/fullerene planar-heterojunction hybrid solar cells," *Advanced Materials*, vol. 25, no. 27, pp. 3727–3732, 2013.

[79] N. J. Jeon, J. H. Noh, Y. C. Kim, W. S. Yang, S. Ryu, and S. I. Seok, "Solvent engineering for high-performance inorganic–organic hybrid perovskite solar cells," *Nat Mater*, vol. 13, no. 9, pp. 897–903, 2014.

[80] J. Burschka, N. Pellet, S.-J. Moon, R. Humphry-Baker, P. Gao, M. K. Nazeeruddin, and M. Grätzel, "Sequential deposition as a route to high-performance perovskite-sensitized solar cells.," *Nature*, vol. 499, no. 7458, pp. 316–320, 2013.

[81] S. G. Li, K. J. Jiang, M. J. Su, X. P. Cui, J. H. Huang, Q. Q. Zhang, X. Q. Zhou, L. M. Yang, and Y. L. Song, "Inkjet printing of CH3NH3PbI3 on a mesoscopic TiO2 film for highly efficient perovskite solar cells," *Journal of Materials Chemistry A*, vol. 3, no. 17, pp. 9092–9097, 2015.

[82] Z. Wei, H. Chen, K. Yan, and S. Yang, "Inkjet printing and instant chemical transformation of a CH3NH3PbI3/nanocarbon electrode and interface for planar perovskite solar cells," *Angewandte Chemie - International Edition*, vol. 53, no. 48, pp. 13239–13243, 2014.

[83] J. H. Kim, S. T. Williams, N. Cho, C. C. Chueh, and A. K. Jen, "Enhanced Environmental Stability of Planar Heterojunction Perovskite Solar Cells Based on Blade-Coating," *Advanced Energy Materials*, vol. 5, no. 4, pp. 2–7, 2015.

[84] S. Razza, F. Di Giacomo, F. Matteocci, L. Cinà, A. L. Palma, S. Casaluci, P. Cameron, A. D'Epifanio, S. Licoccia, A. Reale, T. M. Brown, and A. Di Carlo, "Perovskite solar cells and large area modules (100 cm2) based on an air flow-assisted PbI2 blade coating deposition process," *Journal of Power Sources*, vol. 277, pp. 286–291, 2015.

[85] G. Cotella, J. Baker, D. Worsley, F. De Rossi, C. Pleydell-Pearce, M. Carnie, and T. Watson, "One-step deposition by slot-die coating of mixed lead halide perovskite for photovoltaic applications," *Solar Energy Materials and Solar Cells*, vol. 159, pp. 362–369, 2017.

[86] F. Di Giacomo, S. Shanmugam, H. Fledderus, B. J. Bruijnaers, W. J. Verhees, M. S. Dorenkamper, S. C. Veenstra, W. Qiu, R. Gehlhaar, T. Merckx, T. Aernouts, R. Andriessen, and Y. Galagan, "Up-scalable sheet-to-sheet production of high efficiency perovskite module and solar cells on 6-in. substrate using slot die coating," *Solar Energy Materials and Solar Cells*, vol. 181, no. August 2017, pp. 53–59, 2018.

[87] M. Liu, M. B. Johnston, and H. J. Snaith, "Efficient planar heterojunction perovskite solar cells by vapour deposition.," *Nature*, vol. 501, no. 7467, pp. 395–8, 2013.

[88] O. Malinkiewicz, A. Yella, Y. H. Lee, G. M. Espallargas, M. Graetzel, M. K. Nazeeruddin, and H. J. Bolink, "Perovskite solar cells employing organic charge-transport layers," *Nature Photonics*, vol. 8, no. 2, pp. 128–132, 2014.

[89] C. Tao, S. Neutzner, L. Colella, S. Marras, A. R. Srimath Kandada, M. Gandini, M. D. Bastiani, G. Pace, L. Manna, M. Caironi, C. Bertarelli, and A. Petrozza, "17.6% Stabilized Efficiency in Low-Temperature Processed Planar Perovskite Solar Cells," *Energy and Environmental Science*, vol. 8, no. 8, pp. 2365–2370, 2015.

[90] F. Fu, L. Kranz, S. Yoon, J. Löckinger, T. Jäger, J. Perrenoud, T. Feurer, C. Gretener, S. Buecheler, and A. N. Tiwari, "Controlled growth of PbI2 nanoplates for rapid preparation of CH3NH3PbI3 in planar perovskite solar cells," *Physica Status Solidi (A) Applications and Materials Science*, vol. 212, no. 12, pp. 2708–2717, 2015.

[91] M. T. Hörantner and H. Snaith, "Predicting and Optimising the Energy Yield of Perovskite-on-Silicon Tandem Solar Cells under Real World Conditions," *Energy Environ. Sci.*, pp. 0–34, 2017.

[92] S. A. Altazin, L. Stepanova, J. Werner, B. Niesen, C. Ballif, and B. Ruhstaller, "Design of perovskite / crystalline-silicon monolithic tandem solar cells," *Optics Express*, vol. 26, pp. 579–590, may 2018.

[93] T. Todorov, T. Gershon, O. Gunawan, C. Sturdevant, and S. Guha, "Perovskite-kesterite monolithic tandem solar cells with high open-circuit voltage," *Applied Physics Letters*, vol. 105, p. 173902, 2014.

[94] Q. Han, Y. T. Hsieh, L. Meng, J. L. Wu, P. Sun, E. P. Yao, S. Y. Chang, S. H. Bae, T. Kato, V. Bermudez, and Y. Yang, "High-performance perovskite/ Cu(In,Ga)Se2 monolithic tandem solar cells," *Science*, vol. 361, no. 6405, pp. 904–908, 2018.

[95] M. Jost, T. Bertram, D. Koushik, J. Marquez, M. Verheijen, M. D. Heinemann, E. Köhnen, A. Al-Ashouri, S. Braunger, F. Lang, B. Rech, T. Unold, M. Creatore, I. Lauermann, C. A. Kaufmann, R. Schlatmann, and S. Albrecht, "21.6%-efficient Monolithic Perovskite/Cu(In,Ga)Se2 Tandem Solar Cells with Thin Conformal Hole Transport Layers for Integration on Rough Bottom Cell Surfaces," *ACS Energy Letters*, p. acsenergylett.9b00135, 2019.

[96] D. H. Kim, C. P. Muzzillo, J. Tong, A. F. Palmstrom, B. W. Larson, C. Choi, S. P. Harvey, S. Glynn, J. B. Whitaker, F. Zhang, Z. Li, H. Lu, M. F. van Hest, J. J. Berry, L. M. Mansfield, Y. Huang, Y. Yan, and K. Zhu, "Bimolecular Additives Improve Wide-Band-Gap Perovskites for Efficient Tandem Solar Cells with CIGS," *Joule*, vol. 3, no. 7, pp. 1734–1745, 2019.

[97] S. Gharibzadeh, I. M. Hossain, P. Fassl, B. A. Nejand, T. Abzieher, M. Schultes, E. Ahlswede, P. Jackson, M. Powalla, S. Schäfer, M. Rienäcker, T. Wietler, R. Peibst, U. Lemmer, B. S. Richards, and U. W. Paetzold, "2D/3D Heterostructure for Semi-transparent Perovskite Solar Cells with Engineered Bandgap Enables Efficiencies Exceeding 25% in Four-Terminal Tandems with Silicon and CIGS," *Advanced Functional Materials*, 2020.

[98] G. E. Eperon, T. Leijtens, K. A. Bush, R. Prasanna, T. Green, J. T.-W. Wang, D. P. McMeekin, G. Volonakis, R. L. Milot, R. May, A. Palmstrom, D. J. Slotcavage, R. A. Belisle, J. B. Patel, E. S. Parrott, R. J. Sutton, W. Ma, F. Moghadam, B. Conings, A. Babayigit, H.-G. Boyen, S. Bent, F. Giustino, L. M. Herz, M. B. Johnston, M. D. McGehee, and H. J. Snaith, "Perovskite-perovskite tandem photovoltaics with optimized band gaps," *Science*, vol. 354, no. 6314, pp. 861–865, 2016.

[99] J. Tong, Z. Song, D. H. Kim, X. Chen, C. Chen, A. F. Palmstrom, P. F. Ndione, M. O. Reese, S. P. Dunfield, O. G. Reid, J. Liu, F. Zhang, S. P. Harvey, Z. Li, S. T. Christensen, G. Teeter, D. Zhao, M. M. Al-Jassim, M. F. Van Hest, M. C. Beard, S. E. Shaheen, J. J. Berry, Y. Yan, and K. Zhu, "Carrier lifetimes of >1 ms in Sn-Pb perovskites enable efficient all-perovskite tandem solar cells," *Science*, vol. 364, no. 6439, pp. 475–479, 2019.

[100] R. Lin, K. Xiao, Z. Qin, Q. Han, C. Zhang, M. Wei, M. I. Saidaminov, Y. Gao, J. Xu, M. Xiao, A. Li, J. Zhu, E. H. Sargent, and H. Tan, "Monolithic all-perovskite tandem solar cells with 24.8% efficiency exploiting comproportionation to suppress Sn(ii) oxidation in precursor ink," *Nature Energy*, vol. 4, no. 10, pp. 864–873, 2019.

[101] D. Zhao, C. Wang, Z. Song, Y. Yu, C. Chen, X. Zhao, K. Zhu, and Y. Yan, "Four-Terminal All-Perovskite Tandem Solar Cells Achieving Power Conversion Efficiencies Exceeding 23%," *ACS Energy Letters*, vol. 3, no. 2, pp. 305–306, 2018.

[102] S. E. Sofia, J. P. Mailoa, D. N. Weiss, B. J. Stanbery, T. Buonassisi, and I. M. Peters, "Economic viability of thin-film tandem solar modules in the United States," *Nature Energy*, 2018.

[103] O. Dupré, B. Niesen, S. De Wolf, and C. Ballif, "Field Performance versus Standard Test Condition Efficiency of Tandem Solar Cells and the Singular Case of Perovskites/Silicon Devices," *Journal of Physical Chemistry Letters*, vol. 9, no. 2, pp. 446–458, 2018.

[104] J. P. Mailoa, C. D. Bailie, E. C. Johlin, E. T. Hoke, A. J. Akey, W. H. Nguyen, M. D. McGehee, and T. Buonassisi, "A 2-terminal perovskite/silicon multijunction solar cell enabled by a silicon tunnel junction," *Applied Physics Letters*, vol. 106, no. 12, p. 121105, 2015.

[105] S. Albrecht, M. Saliba, J. P. Correa Baena, F. Lang, L. Kegelmann, M. Mews, L. Steier, A. Abate, J. Rappich, L. Korte, R. Schlatmann, M. K. Nazeeruddin, A. Hagfeldt, M. Grätzel, B. Rech, J. Rg Rappich, L. Korte, R. Schlatmann, M. K. Nazeeruddin, A. Hagfeldt, M. Grätzel D, B. Rech, M. Grätzel, and B. Rech, "Monolithic perovskite/silicon-heterojunction tandem solar cells processed at low temperature," *Energy Environ. Sci.*, vol. 9, no. 1, pp. 81–88, 2016.

[106] J. Werner, C. H. Weng, A. Walter, L. Fesquet, J. P. Seif, S. De Wolf, B. Niesen, and C. Ballif, "Efficient Monolithic Perovskite/Silicon Tandem Solar Cell with Cell Area >1 cm2," *Journal of Physical Chemistry Letters*, vol. 7, no. 1, pp. 161–166, 2016.

[107] F. Fu, T. Feurer, T. P. Weiss, S. Pisoni, E. Avancini, C. Andres, S. Buecheler, and A. N. Tiwari, "High-efficiency inverted semi-transparent planar perovskite solar cells in substrate configuration," *Nature Energy*, vol. 2, no. 1, p. 16190, 2016.

[108] K. A. K. Bush, A. F. A. Palmstrom, Z. Z. Yu, M. Boccard, R. Cheacharoen, J. P. J. Mailoa, D. P. D. McMeekin, R. L. Z. R. Hoye, C. D. C. Bailie, T. Leijtens, I. I. M. Peters, M. C. Minichetti, N. Rolston, R. Prasanna, S. Sofia, D. Harwood, W. Ma, F. Moghadam, H. J. H. Snaith, T. Buonassisi, Z. C. Holman, S. F. S. Bent, and M. D. M. McGehee, "23.6%-Efficient Monolithic Perovskite/Silicon Tandem Solar Cells with Improved Stability," *Nature Energy*, vol. 2, p. 17009, feb 2017.

[109] B. Chen, Z. J. Yu, S. Manzoor, S. Wang, W. Weigand, Z. Yu, G. Yang, Z. Ni, X. Dai, Z. C. Holman, and J. Huang, "Blade-Coated Perovskites on Textured Silicon for 26%-Efficient Monolithic Perovskite/Silicon Tandem Solar Cells," *Joule*, pp. 1–15, 2020.

[110] Y. Hou, E. Aydin, M. De Bastiani, C. Xiao, F. H. Isikgor, D.-J. Xue, B. Chen, H. Chen, B. Bahrami, A. H. Chowdhury, A. Johnston, S.-W. Baek, Z. Huang, M. Wei, Y. Dong, J. Troughton, R. Jalmood, A. J. Mirabelli, T. G. Allen, E. Van Kerschaver, M. I. Saidaminov, D. Baran, Q. Qiao, K. Zhu, S. De Wolf, and E. H.

Sargent, "Efficient tandem solar cells with solution-processed perovskite on textured crystalline silicon," *Science*, vol. 367, no. 6482, pp. 1135–1140, 2020.

[111] I. Y. Choi, C. U. Kim, W. Park, H. Lee, M. H. Song, K. K. Hong, S. I. Seok, and K. J. Choi, "Two-terminal mechanical perovskite/silicon tandem solar cells with transparent conductive adhesives," *Nano Energy*, vol. 65, no. August, p. 104044, 2019.

[112] E. Lamanna, F. Matteocci, E. Calabrò, L. Serenelli, E. Salza, L. Martini, F. Menchini, M. Izzi, A. Agresti, S. Pescetelli, S. Bellani, A. E. Del Río Castillo, F. Bonaccorso, M. Tucci, and A. Di Carlo, "Mechanically Stacked, Two-Terminal Graphene-Based Perovskite/Silicon Tandem Solar Cell with Efficiency over 26%," *Joule*, vol. 4, pp. 1–17, 2020.

[113] J. A. Raiford, R. A. Belisle, K. A. Bush, R. Prasanna, A. F. Palmstrom, M. D. McGehee, and S. F. Bent, "Atomic layer deposition of vanadium oxide to reduce parasitic absorption and improve stability in n-i-p perovskite solar cells for tandems," *Sustainable Energy and Fuels*, no. 6, pp. 1517–1525, 2019.

[114] H. Shen, S. T. Omelchenko, D. A. Jacobs, S. Yalamanchili, D. Yan, P. Phang, T. Duong, Y. Wu, Y. Yin, C. Samundsett, J. Peng, N. Wu, T. P. White, G. G. Andersson, N. S. Lewis, and R. Kylie, "In situ recombination junction between p - Si and TiO 2 enables high efficiency monolithic perovskite / Si tandem cells," *Science Advances*, vol. 4, pp. 1–12, 2018.

[115] J. Lehr, M. Langenhorst, R. Schmager, S. Kirner, U. Lemmer, B. S. Richards, C. Case, and U. W. Paetzold, "Energy yield modelling of perovskite/silicon two-terminal tandem PV modules with flat and textured interfaces," *Sustainable Energy and Fuels*, vol. 2, no. 12, pp. 2754–2761, 2018.

[116] M. Jošt, E. Köhnen, A. B. Morales-Vilches, B. Lipovšek, K. Jäger, B. Macco, A. Al-Ashouri, J. Krč, L. Korte, B. Rech, R. Schlatmann, M. Topič, B. Stannowski, and S. Albrecht, "Textured interfaces in monolithic perovskite/silicon tandem solar cells: Advanced light management for improved efficiency and energy yield," *Energy and Environmental Science*, vol. 11, no. 12, pp. 3511–3523, 2018.

[117] J. Werner, A. Walter, E. Rucavado, S.-J. J. Moon, D. Sacchetto, M. Rienaecker, R. Peibst, R. Brendel, X. Niquille, S. D. Wolf, P. Löper, M. Morales-Masis, S. Nicolay, B. Niesen, C. Ballif, S. De Wolf, P. Löper, M. Morales-Masis, S. Nicolay, B. Niesen, and C. Ballif, "Zinc tin oxide as high-temperature stable recombination layer for mesoscopic perovskite/silicon monolithic tandem solar cells," *Applied Physics Letters*, vol. 109, p. 233902, 2016.

[118] Y. Wu, D. D. Yan, J. Peng, T. Duong, Y. Wan, S. Phang, H. Shen, N. Wu, C. Barugkin, X. Fu, S. Surve, D. Grant, D. Walter, T. T. White, K. K. Catchpole, K. K. Weber, P. Phang, H. Shen, N. Wu, C. Barugkin, X. Fu, S. Surve, D. Walter,

T. T. White, K. K. Catchpole, and K. K. Weber, "Monolithic perovskite/silicon-homojunction tandem solar cell with over 22% efficiency," *Energy & Environmental Science*, vol. 10, pp. 2472–2479, 2017.

[119] R. Fan, N. Zhou, L. Zhang, R. Yang, Y. Meng, L. Li, T. Guo, Y. Chen, Z. Xu, G. Zheng, Y. Huang, L. Li, L. Qin, X. Qiu, Q. Chen, and H. Zhou, "Toward Full Solution Processed Perovskite/Si Monolithic Tandem Solar Device With PCE Exceeding 20%," *Solar RRL*, vol. 1, no. 11, p. 1700149, 2017.

[120] S. Zhu, X. Yao, Q. Ren, C. C. Zheng, S. Li, Y. Tong, B. Shi, S. Guo, L. Fan, H. Ren, C. Wei, B. Li, Y. Ding, Q. Huang, Y. L. Li, Y. Zhao, and X. Zhang, "Transparent electrode for monolithic perovskite/silicon-heterojunction two-terminal tandem solar cells," *Nano Energy*, vol. 45, no. December 2017, pp. 280–286, 2018.

[121] J. Zheng, C. F. J. Lau, H. Mehrvarz, F. J. Ma, Y. Jiang, X. Deng, A. Soeriyadi, J. Kim, M. Zhang, L. Hu, X. Cui, D. S. Lee, J. Bing, Y. Cho, C. Chen, M. A. Green, S. Huang, A. W. Y. W. Ho-Baillie, J. Lau, H. Mehrvarz, F. J. Ma, Y. Jiang, X. Deng, A. Soeriyadi, J. Kim, M. Zhang, L. Hu, X. Cui, D. S. Lee, J. Bing, Y. Cho, C. Chen, M. A. Green, S. Huang, and A. W. Y. W. Ho-Baillie, "Large area efficient interface layer free monolithic perovskite/homo-junction-silicon tandem solar cell with over 20% efficiency," *Energy and Environmental Science*, vol. 11, no. 9, pp. 2432–2443, 2018.

[122] Mark Osborne, "Oxford PV takes record perovskite tandem solar cell to 27.3% conversion efficiency," 2018.

[123] R. L. Z. Hoye, K. A. Bush, F. Oviedo, S. E. Sofia, M. Thway, X. Li, Z. Liu, J. Jean, J. P. Mailoa, A. Osherov, F. Lin, A. F. Palmstrom, V. Bulovic, M. D. McGehee, I. M. Peters, and T. Buonassisi, "Developing a Robust Recombination Contact to Realize Monolithic Perovskite Tandems With Industrially Common p-Type Silicon Solar Cells," *IEEE Journal of Photovoltaics*, vol. 8, pp. 1023–1028, jul 2018.

[124] K. A. Bush, S. Manzoor, K. Frohna, Z. J. Yu, J. A. Raiford, A. F. Palmstrom, H.-P. Wang, R. Prasanna, S. F. Bent, Z. C. Holman, and M. D. McGehee, "Minimizing Current and Voltage Losses to Reach 25%-Efficient Monolithic Two-Terminal Perovskite-Silicon Tandem Solar Cells," *ACS Energy Letters*, p. acsenergylett.8b01201, 2018.

[125] J. Zheng, H. Mehrvarz, F. J. Ma, C. F. J. Lau, M. A. Green, S. Huang, and A. W. Ho-Baillie, "21.8% Efficient Monolithic Perovskite/Homo-Junction-Silicon Tandem Solar Cell on 16 cm2," *ACS Energy Letters*, vol. 3, no. 9, pp. 2299–2300, 2018.

[126] H. Shen, S. T. Omelchenko, D. A. Jacobs, S. Yalamanchili, Y. Wan, D. Yan, P. Phang, T. Duong, Y. Wu, Y. Yin, C. Samundsett, J. Peng, N. Wu, T. P. White, G. G. Andersson, N. S. Lewis, and K. R. Catchpole, "In situ recombination junction between p-Si and TiO2 enables high-efficiency monolithic perovskite/Si tandem cells," *Science Advances*, vol. 4, no. 12, 2018.

Bibliography

[127] OxfordPV, "Oxford PV perovskite solar cell achieves 28% efficiency," 2018.

[128] B. Chen, Z. Yu, K. Liu, X. Zheng, Y. Liu, J. Shi, D. Spronk, P. N. Rudd, Z. Holman, and J. Huang, "Grain Engineering for Perovskite/Silicon Monolithic Tandem Solar Cells with Efficiency of 25.4%," *Joule*, vol. 3, no. 1, pp. 177–190, 2019.

[129] L. Mazzarella, Y.-H. Lin, S. Kirner, A. B. Morales-Vilches, L. Korte, S. Albrecht, E. Crossland, B. Stannowski, C. Case, H. J. Snaith, and R. Schlatmann, "Infrared Light Management Using a Nanocrystalline Silicon Oxide Interlayer in Monolithic Perovskite/Silicon Heterojunction Tandem Solar Cells with Efficiency above 25%," *Advanced Energy Materials*, vol. 1803241, p. 1803241, 2019.

[130] B. A. Kamino, B. Paviet-Salomon, S. J. Moon, N. Badel, J. Levrat, G. Christmann, A. Walter, A. Faes, L. Ding, J. J. Diaz Leon, A. Paracchino, M. Despeisse, C. Ballif, and S. Nicolay, "Low-Temperature Screen-Printed Metallization for the Scale-Up of Two-Terminal Perovskite-Silicon Tandems," *ACS Applied Energy Materials*, vol. 2, no. 5, pp. 3815–3821, 2019.

[131] I. J. Park, J. H. Park, S. G. Ji, M.-A. Park, J. H. Jang, and J. Y. Kim, "A Three-Terminal Monolithic Perovskite/Si Tandem Solar Cell Characterization Platform," *Joule*, pp. 1–12, 2018.

[132] E. Köhnen, M. Jošt, A. B. Morales-Vilches, P. Tockhorn, A. Al-Ashouri, B. Macco, L. Kegelmann, L. Korte, B. Rech, R. Schlatmann, B. Stannowski, and S. Albrecht, "Highly efficient monolithic perovskite silicon tandem solar cells: analyzing the influence of current mismatch on device performance," *Sustainable Energy & Fuels*, vol. 3, no. 8, pp. 1995–2005, 2019.

[133] A. J. Bett, P. S. Schulze, K. M. Winkler, Ö. S. Kabakli, I. Ketterer, L. E. Mundt, S. K. Reichmuth, G. Siefer, L. Cojocaru, L. Tutsch, M. Bivour, M. Hermle, S. W. Glunz, and J. C. Goldschmidt, "Two-terminal Perovskite silicon tandem solar cells with a high-Bandgap Perovskite absorber enabling voltages over 1.8 V," *Progress in Photovoltaic Research and applications*, vol. 28, no. 2, pp. 99–110, 2020.

[134] P. Tockhorn, P. Wagner, L. Kegelmann, J. C. Stang, M. Mews, S. Albrecht, and L. Korte, "Three-Terminal Perovskite/Silicon Tandem Solar Cells with Top and Interdigitated Rear Contacts," *ACS Applied Energy Materials*, vol. 3, no. 2, pp. 1381–1392, 2020.

[135] HZB, "HZB hits 29.15% efficiency with perovskite/silicon tandem cell," 2020.

[136] J. Xu, C. C. Boyd, Z. J. Yu, A. F. Palmstrom, D. J. Witter, B. W. Larson, R. M. France, J. Werner, S. P. Harvey, E. J. Wolf, W. Weigand, S. Manzoor, M. F. A M van Hest, J. J. Berry, J. M. Luther, Z. C. Holman, and M. D. McGehee, "Triple-halide wide-band gap perovskites with suppressed phase segregation for efficient tandems Downloaded from," *Science*, vol. 367, no. March, pp. 1097–1104, 2020.

[137] I. M. Peters, S. Sofia, J. Mailoa, and T. Buonassisi, "Techno-economic analysis of tandem photovoltaic systems," *RSC Advances*, vol. 6, no. 71, pp. 66911–66923, 2016.

[138] Z. Liu, S. E. Sofia, H. S. Laine, M. Woodhouse, S. Wieghold, I. M. Peters, and T. Buonassisi, "Revisiting thin silicon for photovoltaics: A technoeconomic perspective," *Energy and Environmental Science*, vol. 13, no. 1, pp. 12–23, 2020.

[139] S. E. Sofia, H. Wang, A. Bruno, T. Buonassisi, and I. M. Peters, "Cost-Efficiency Trade-off of Silicon Solar Cells for use in Perovskite-Silicon Tandem Modules," *IEEE Journal of Photovoltaics*, vol. 0, no. 1, pp. 0572–0576, 2020.

[140] N. L. Chang, A. W. Y. Ho-Baillie, D. Vak, M. Gao, M. A. Green, and R. J. Egan, "Manufacturing cost and market potential analysis of demonstrated roll-to-roll perovskite photovoltaic cell processes," *Solar Energy Materials and Solar Cells*, vol. 174, no. May 2017, pp. 314–324, 2018.

[141] Z. Li, Y. Zhao, X. Wang, Y. Sun, Z. Zhao, Y. Li, H. Zhou, and Q. Chen, "Cost Analysis of Perovskite Tandem Photovoltaics," *Joule*, pp. 1–14, 2018.

[142] I. Mathews, S. Sofia, E. Ma, J. Jean, H. S. Laine, S. C. Siah, T. Buonassisi, and I. M. Peters, "Economically Sustainable Growth of Perovskite Photovoltaics Manufacturing," *Joule*, pp. 1–18, 2020.

[143] Z. Song, C. Mcelvany, A. B. Phillips, I. Celik, P. Krantz, S. C. Watthage, G. K. Liyanage, D. Apu, and M. Heben, "A technoeconomic analysis of perovskite solar module manufacturing with low-cost materials and techniques," *Energy Environ. Sci.*, 2017.

[144] J. Werner, B. Niesen, and C. Ballif, "Perovskite / silicon tandem solar cells : marriage of convenience or true love story ? An overview," *Accepted in Advanced materials interfaces*, vol. 5, p. 1700731, 2017.

[145] N. M. Haegel, R. Margolis, T. Buonassisi, D. Feldman, A. Froitzheim, R. Garabedian, M. Green, S. Glunz, H.-M. Henning, B. Holder, I. Kaizuka, B. Kroposki, K. Matsubara, S. Niki, K. Sakurai, R. A. Schindler, W. Tumas, E. R. Weber, G. Wilson, M. Woodhouse, and S. Kurtz, "Terawatt-scale photovoltaics: Trajectories and challenges," *Science*, vol. 356, no. 6334, 2017.

[146] J. Qian, M. Ernst, N. Wu, and A. Blakers, "Impact of perovskite solar cell degradation on the lifetime energy yield and economic viability of perovskite/silicon tandem modules," *Sustainable Energy and Fuels*, vol. 3, no. 6, pp. 1439–1447, 2019.

[147] S. De Wolf and M. Kondo, "Nature of doped a-Si:H/c-Si interface recombination," *Journal of Applied Physics*, vol. 105, no. 10, p. 103707, 2009.

[148] N. Pellet, J. Teuscher, J. Maier, and M. Grätzel, "Transforming hybrid organic inorganic perovskites by rapid halide exchange," *Chemistry of Materials*, vol. 27, no. 6, pp. 2181–2188, 2015.

[149] T. Jesper Jacobsson, J. P. Correa-Baena, M. Pazoki, M. Saliba, K. Schenk, M. Grätzel, and A. Hagfeldt, "Exploration of the compositional space for mixed lead halogen perovskites for high efficiency solar cells," *Energy and Environmental Science*, vol. 9, no. 5, pp. 1706–1724, 2016.

[150] M. K. Gangishetty, R. W. Scott, and T. L. Kelly, "Effect of relative humidity on crystal growth, device performance and hysteresis in planar heterojunction perovskite solar cells," *Nanoscale*, vol. 8, no. 12, pp. 6300–6307, 2016.

[151] E. J. Juarez-Perez, L. K. Ono, and Y. Qi, "Thermal degradation of formamidinium based lead halide perovskites into: Sym -triazine and hydrogen cyanide observed by coupled thermogravimetry-mass spectrometry analysis," *Journal of Materials Chemistry A*, vol. 7, no. 28, pp. 16912–16919, 2019.

[152] G. Cliff and G. W. Lorimer, "The quantitative analysis of thin specimens," *Journal of Microscopy*, vol. 103, no. 2, pp. 203–207, 1975.

[153] H. Yu, F. Wang, F. Xie, W. Li, J. Chen, and N. Zhao, "The role of chlorine in the formation process of "CH3NH3PbI3-xClx" perovskite," *Advanced Functional Materials*, vol. 24, no. 45, pp. 7102–7108, 2014.

[154] F. Guo, H. Azimi, Y. Hou, T. Przybilla, M. Hu, C. Bronnbauer, S. Langner, E. Spiecker, K. Forberich, and C. J. Brabec, "High-performance semitransparent perovskite solar cells with solution-processed silver nanowires as top electrodes," *Nanoscale*, vol. 7, no. 5, pp. 1642–1649, 2015.

[155] C. D. Bailie, M. G. Christoforo, J. P. Mailoa, A. R. Bowring, E. L. Unger, W. H. Nguyen, J. Burschka, N. Pellet, J. Z. Lee, M. Grätzel, R. Noufi, T. Buonassisi, A. Salleo, and M. D. McGehee, "Semi-transparent perovskite solar cells for tandems with silicon and CIGS," *Energy and Environmental Science*, vol. 8, no. 3, pp. 956–963, 2015.

[156] K. A. Bush, C. D. Bailie, Y. Chen, A. R. Bowring, W. Wang, W. Ma, T. Leijtens, F. Moghadam, and M. D. McGehee, "Thermal and Environmental Stability of Semi-Transparent Perovskite Solar Cells for Tandems Enabled by a Solution-Processed Nanoparticle Buffer Layer and Sputtered ITO Electrode," *Advanced Materials*, vol. 28, no. 20, pp. 3937–3943, 2016.

[157] P. Löper, S.-J. Moon, S. M. de Nicolas, B. Niesen, M. Ledinsky, S. Nicolay, J. Bailat, J.-H. Yum, S. D. Wolf, and C. Ballif, "Organic–inorganic halide perovskite/crystalline silicon four-terminal tandem solar cells," *Physical Chemistry Chemical Physics*, vol. 17, pp. 1619–1629, 2015.

[158] J. Werner, G. Dubuis, A. Walter, P. Löper, S. J. S.-J. Moon, S. Nicolay, M. Morales-Masis, S. De Wolf, B. Niesen, and C. Ballif, "Sputtered rear electrode with broadband transparency for perovskite solar cells," *Solar Energy Materials and Solar Cells*, vol. 141, p. 407, 2015.

[159] E. Della Gaspera, Y. Peng, Q. Hou, L. Spiccia, U. Bach, J. J. Jasieniak, and Y. B. Cheng, "Ultra-thin high efficiency semitransparent perovskite solar cells," *Nano Energy*, vol. 13, pp. 249–257, 2015.

[160] Y. Yang Michael, Q. Chen, Y. T. Hsieh, T. B. Song, N. D. Marco, H. Zhou, and Y. Yang, "Multilayer Transparent Top Electrode for Solution Processed Perovskite/Cu(In,Ga)(Se,S)2 Four Terminal Tandem Solar Cells," *ACS Nano*, vol. 9, no. 7, pp. 7714–7721, 2015.

[161] S. Pang, D. Chen, C. Zhang, J. Chang, Z. Lin, H. Yang, X. Sun, J. Mo, H. Xi, G. Han, J. Zhang, and Y. Hao, "Efficient bifacial semitransparent perovskite solar cells with silver thin film electrode," *Solar Energy Materials and Solar Cells*, vol. 170, no. February, pp. 278–286, 2017.

[162] P. You, Z. Liu, Q. Tai, S. Liu, and F. Yan, "Efficient Semitransparent Perovskite Solar Cells with Graphene Electrodes," *Advanced Materials*, vol. 27, no. 24, pp. 3632–3638, 2015.

[163] Z. Holman, A. Descoeudres, L. Barraud, F. Fernandez, J. Seif, S. De Wolf, and C. Ballif, "Current Losses at the Front of Silicon Heterojunction Solar Cells," *IEEE Journal of Photovoltaics*, vol. 2, no. 1, pp. 7–15, 2012.

[164] H. Kanda, A. Uzum, A. K. Baranwal, T. A. Peiris, T. Umeyama, H. Imahori, H. Segawa, T. Miyasaka, and S. Ito, "Analysis of Sputtering Damage on I-V Curves for Perovskite Solar Cells and Simulation with Reversed Diode Model," *Journal of Physical Chemistry C*, vol. 120, no. 50, pp. 28441–28447, 2016.

[165] H. Kanda, A. Uzum, H. Nishino, T. Umeyama, H. Imahori, Y. Ishikawa, Y. Uraoka, and S. Ito, "Interface Optoelectronics Engineering for Mechanically Stacked Tandem Solar Cells Based on Perovskite and Silicon," *ACS Applied Materials and Interfaces*, vol. 8, no. 49, pp. 33553–33561, 2016.

[166] F. Fu, T. Feurer, T. Jäger, E. Avancini, B. Bissig, S. Yoon, S. Buecheler, and A. N. Tiwari, "Low-temperature-processed efficient semi-transparent planar perovskite solar cells for bifacial and tandem applications," *Nature Communications*, vol. 6, pp. 1–9, 2015.

[167] F. Fu, T. Feurer, T. Weiss, S. Pisoni, E. Avancini, C. Andres, S. Buecheler, and A. Tiwari, "High-efficiency inverted semi-transparent planar perovskite solar cells in substrate configuration," *Nature Energy*, vol. 2, pp. 1234–1237, 2016.

[168] T. Wahl, J. Hanisch, S. Meier, M. Schultes, and E. Ahlswede, "Sputtered indium zinc oxide rear electrodes for inverted semitransparent perovskite solar cells without using a protective buffer layer," *Organic Electronics*, vol. 54, no. September 2017, pp. 48–53, 2018.

[169] A. J. Bett, P. S. Schulze, K. M. Winkler, Ö. S. Kabakli, I. Ketterer, L. E. Mundt, S. K. Reichmuth, G. Siefer, L. Cojocaru, L. Tutsch, M. Bivour, M. Hermle, S. W. Glunz, and J. C. Goldschmidt, "Two-terminal Perovskite silicon tandem solar cells with a high-Bandgap Perovskite absorber enabling voltages over 1.8 V," *Progress in Photovoltaic Research and applications*, vol. 28, no. 2, pp. 99–110, 2020.

[170] M. Morales-Masis, S. Martin De Nicolas, J. Holovsky, S. De Wolf, and C. Ballif, "Low-Temperature High-Mobility Amorphous IZO for Silicon Heterojunction Solar Cells," *IEEE Journal of Photovoltaics*, vol. 5, no. 5, pp. 1340–1347, 2015.

[171] M. Stolterfoht, C. M. Wolff, J. A. Márquez, S. Zhang, C. J. Hages, D. Rothhardt, S. Albrecht, P. L. Burn, P. Meredith, T. Unold, and D. Neher, "Visualization and suppression of interfacial recombination for high-efficiency large-area pin perovskite solar cells," *Nature Energy*, vol. 3, pp. 847–854, 2018.

[172] W. H. Lee, C. Y. Chen, C. S. Li, S. Y. Hsiao, W. L. Tsai, M. J. Huang, C. H. Cheng, C. I. Wu, and H. W. Lin, "Boosting thin-film perovskite solar cell efficiency through vacuum-deposited sub-nanometer small-molecule electron interfacial layers," *Nano Energy*, vol. 38, no. April, pp. 66–71, 2017.

[173] D. T. Grant, K. R. Catchpole, K. J. Weber, and T. P. White, "Design guidelines for perovskite/silicon 2-terminal tandem solar cells: an optical study," *Optics Express*, vol. 24, p. 1454, 2016.

[174] P. Buehlmann, J. Bailat, D. Dominé, A. Billet, F. Meillaud, A. Feltrin, C. Ballif, D. Domiń, A. Billet, F. Meillaud, A. Feltrin, and C. Ballif, "In situ silicon oxide based intermediate reflector for thin-film silicon micromorph solar cells," *Applied Physics Letters*, vol. 91, no. 14, p. 143505, 2007.

[175] M. Despeisse, G. Bugnon, A. Feltrin, M. Stueckelberger, P. Cuony, F. Meillaud, A. Billet, and C. Ballif, "Resistive interlayer for improved performance of thin film silicon solar cells on highly textured substrate," *Applied Physics Letters*, vol. 96, p. 073507, 2010.

[176] C. Amano, H. Sugiura, A. Yamamoto, and M. Yamaguchi, "20.2% efficiency Al0.4Ga0.6As/GaAs tandem solar cells grown by molecular beam epitaxy," *Applied Physics Letters*, vol. 51, no. 24, pp. 1998–2000, 1987.

[177] G. J. Bauhuis, P. Mulder, and J. J. Schermer, "Ultra-thin, high performance tunnel junctions for III-V multijunction cells," *Progress in Photovoltaic Research and applications*, vol. 22, no. 6, pp. 656–660, 2014.

[178] H. Keppner, U. Kroll, P. Torres, J. Meier, R. Platz, D. Fischer, N. Beck, S. Dubail, J. A. A. Selvan, N. P. Vaucher, M. Goerlitzer, Y. Ziegler, R. Tscharner, C. Hof, M. Goetz, P. Pernet, N. Wyrsch, J. Vuille, J. Cuperus, and A. Shah, "The " Micromorph " cell : a new way to high-efficiency-low- temperature crystalline silicon thin-film cell manufacturing ?," *AIP Conference Proceedings*, vol. 271, no. 1997, pp. 271–281, 2008.

[179] P. Alpuim, V. Chu, and J. P. Conde, "Doping of amorphous and microcrystalline silicon films deposited at low substrate temperatures by hot-wire chemical vapor deposition," *Journal of Vacuum Science & Technology A*, vol. 19, no. 5, pp. 2328–2334, 2001.

[180] G. Nogay, J. P. Seif, Y. Riesen, A. Tomasi, Q. Jeangros, N. Wyrsch, F. J. Haug, S. De Wolf, and C. Ballif, "Nanocrystalline Silicon Carrier Collectors for Silicon Heterojunction Solar Cells and Impact on Low-Temperature Device Characteristics," *IEEE Journal of Photovoltaics*, vol. 6, no. 6, pp. 1654–1662, 2016.

[181] A. Tomasi, B. Paviet-Salomon, Q. Jeangros, J. Haschke, G. Christmann, L. Barraud, A. Descoeudres, J. J. P. Seif, S. Nicolay, M. Despeisse, S. De Wolf, and C. Ballif, "Simple processing of back-contacted silicon heterojunction solar cells using selective-area crystalline growth," *Nature Energy*, vol. 2, no. April, p. 17062, 2017.

[182] J. P. Seif, A. Descoeudres, G. Nogay, S. Hanni, S. M. De Nicolas, N. Holm, J. Geissbuhler, A. Hessler-Wyser, M. Duchamp, R. E. Dunin-Borkowski, M. Ledinsky, S. De Wolf, and C. Ballif, "Strategies for Doped Nanocrystalline Silicon Integration in Silicon Heterojunction Solar Cells," *IEEE Journal of Photovoltaics*, vol. 6, no. 5, pp. 1132–1140, 2016.

[183] Q. Jeangros, M. Duchamp, J. Werner, M. Kruth, R. R. E. Dunin-Borkowski, B. Niesen, C. Ballif, and A. Hessler-Wyser, "In Situ TEM Analysis of Organic-Inorganic Metal-Halide Perovskite Solar Cells under Electrical Bias," *Nano Letters*, vol. 16, no. 11, pp. 7013–7018, 2016.

[184] A. Shah, P. Torres, R. Tscharner, N. Wyrsch, and H. Keppner, "Photovoltaic Technology: The Case for Thin-Film Solar Cells," *Science*, vol. 285, no. 5428, pp. 692–698, 1999.

[185] I. Almansouri, A. Ho-Baillie, S. P. Bremner, and M. A. Green, "Supercharging Silicon Solar Cell Performance by Means of Multijunction Concept," *IEEE Journal of Photovoltaics*, vol. 5, no. 3, pp. 968–976, 2015.

[186] F. C. Hanusch, E. Wiesenmayer, E. Mankel, A. Binek, P. Angloher, C. Fraunhofer, N. Giesbrecht, J. M. Feckl, W. Jaegermann, D. Johrendt, T. Bein, and P. Docampo, "Efficient planar heterojunction perovskite solar cells based on formamidinium lead bromide," *Journal of Physical Chemistry Letters*, vol. 5, no. 16, pp. 2791–2795, 2014.

[187] T. Leijtens, K. A. Bush, R. Cheacharoen, R. Beal, A. R. Bowring, and M. D. McGehee, "Towards enabling stable lead halide perovskite solar cells; interplay between structural, environmental, and thermal stability," *J. Mater. Chem. A*, vol. 5, p. 11483, 2017.

[188] D. P. McMeekin, G. Sadoughi, W. Rehman, G. E. Eperon, M. Saliba, M. T. Horantner, A. Haghighirad, N. Sakai, L. Korte, B. Rech, M. B. Johnston, L. M. Herz, and H. J. Snaith, "A mixed-cation lead mixed-halide perovskite absorber for tandem solar cells," *Science*, vol. 351, no. 6269, pp. 151–155, 2016.

[189] H. Kim, C. M. Gilmore, A. Piqué, J. S. Horwitz, H. Mattoussi, H. Murata, Z. H. Kafafi, and D. B. Chrisey, "Electrical, optical, and structural properties of indium–tin–oxide thin films for organic light emitting devices," *Journal of Applied Physics*, vol. 86, no. 11, p. 6451, 1999.

[190] R. Santbergen, R. Mishima, T. Meguro, M. Hino, H. Uzu, J. Blanker, K. Yamamoto, and M. Zeman, "Minimizing optical losses in monolithic perovskite/c-Si tandem solar cells with a flat top cell," *Optics Express*, vol. 24, no. 18, p. A1288, 2016.

[191] K. Jäger, L. Korte, B. Rech, and S. Albrecht, "Numerical optical optimization of monolithic planar perovskite-silicon tandem solar cells with regular and inverted device architectures," *Optics Express*, vol. 25, no. 12, pp. 473–482, 2017.

[192] B. W. Schneider, N. N. Lal, S. Baker-Finch, T. P. White, K. Masuko, M. Shigematsu, T. Hashiguchi, D. Fujishima, M. Kai, N. Yoshimura, T. Yamaguchi, Y. Ichihashi, T. Yamanishi, T. Takahama, M. Taguchi, E. Maruyama, and S. Okamoto, "Pyramidal surface textures for light trapping and antireflection in perovskite-on-silicon tandem solar cells," *Optics Express*, vol. 22, no. 21, pp. A1422–A1430, 2014.

[193] S. Manzoor, Z. J. Yu, A. Ali, W. Ali, K. A. Bush, A. F. Palmstrom, S. F. Bent, M. D. McGehee, and Z. C. Holman, "Improved light management in planar silicon and perovskite solar cells using PDMS scattering layer," *Solar Energy Materials and Solar Cells*, vol. 173, no. June, pp. 59–65, 2017.

[194] R. Schmager, I. M. Hossain, F. Schackmar, B. S. Richards, G. Gomard, and U. W. Paetzold, "Light coupling to quasi-guided modes in nanoimprinted perovskite solar cells," *Solar Energy Materials and Solar Cells*, vol. 201, no. July, p. 110080, 2019.

[195] L. Mazzarella, M. A. Werth, K. L. Jager, M. Jošt, L. Korte, S. Albrecht, R. Schlatmann, and B. STannowski, "Infrared photocurrent management in monolithic perovskite / silicon heterojunction tandem solar cells by using a nanocrystalline silicon oxide interlayer," *Optics Express (under prublication)*, vol. 26, no. 10, pp. 81–88, 2018.

[196] K. Bittkau, T. Kirchartz, and U. Rau, "Optical design of spectrally selective interlayers for perovskite / silicon heterojunction tandem solar cells," vol. 26, no. 18, pp. 750–760, 2018.

[197] J. H. Heo, S. H. Im, J. H. Noh, T. N. Mandal, C.-S. Lim, J. A. Chang, Y. H. Lee, H.-j. Kim, A. Sarkar, M. K. Nazeeruddin, M. Grätzel, and S. I. Seok, "Efficient inorganic–organic hybrid heterojunction solar cells containing perovskite compound and polymeric hole conductors," *Nature Photonics*, vol. 7, pp. 486–491, may 2013.

[198] H. D. Um, N. Kim, K. Lee, I. Hwang, J. Hoon Seo, Y. J. Yu, P. Duane, M. Wober, and K. Seo, "Versatile control of metal-assisted chemical etching for vertical silicon microwire arrays and their photovoltaic applications," *Scientific Reports*, vol. 5, no. May, pp. 1–11, 2015.

[199] D. H. Macdonald, A. Cuevas, M. J. Kerr, C. Samundsett, D. Ruby, S. Winderbaum, and A. Leo, "Texturing industrial multicrystalline silicon solar cells," *Solar Energy*, vol. 76, no. 1-3, pp. 277–283, 2004.

[200] D. S. Ruby, S. H. Zaidi, S. Narayanan, B. M. Damiani, and A. Rohatgi, "Rie-texturing of multicrystalline silicon solar cells," *Solar Energy Materials and Solar Cells*, vol. 74, no. 1-4, pp. 133–137, 2002.

[201] K. E. BEAN, "no. 2,," *IEEE Transactions on Electron Devices*, no. 10, pp. 1185–1193, 1978.

[202] E. D. Palik, O. J. Glembocki, I. Heard, P. S. Burno, and L. Tenerz, "Etching roughness for (100) silicon surfaces in aqueous KOH," *Journal of Applied Physics*, vol. 70, no. 6, pp. 3291–3300, 1991.

[203] E. Vazsonyi, K. De Clercq, R. Einhaus, E. Van Kerschaver, K. Said, J. Poortmans, J. Szlufcik, and J. Nijs, "Improved anisotropic etching process for industrial texturing of silicon solar cells," *Solar Energy Materials and Solar Cells*, vol. 57, no. 2, pp. 179–188, 1999.

[204] M. Steinert, J. Acker, S. Oswald, and K. Wetzig, "Study on the mechanism of silicon etching in HNO3-rich HF/HNO3 mixtures inf," *Journal of Physical Chemistry C*, vol. 111, no. 5, pp. 2133–2140, 2007.

[205] L. Dong, R. W. Smith, and D. J. Srolovitz, "A two-dimensional molecular dynamics simulation of thin film growth by oblique deposition," *Journal of Applied Physics*, vol. 80, no. 10, pp. 5682–5690, 1996.

[206] J. Yin, H. Qu, J. Cao, H. Tai, J. Li, and N. Zheng, "Vapor-assisted crystallization control toward high performance perovskite photovoltaics with over 18% efficiency in the ambient atmosphere," *Journal of Materials Chemistry A*, vol. 4, no. 34, pp. 13203–13210, 2016.

[207] M. Becker and M. Wark, "Recent Progress in the Solution-Based Sequential Deposition of Planar Perovskite Solar Cells," *Crystal Growth and Design*, vol. 18, no. 8, pp. 4790–4806, 2018.

[208] F. Fu, L. Kranz, S. Yoon, J. Lockinger, T. Jager, J. Perrenoud, T. Feurer, C. Gretener, S. Buecheler, and A. N. Tiwari, "Controlled growth of PbI2 nanoplates for rapid preparation of CH3NH3PbI3 in planar perovskite solar cells," *Physica Status Solidi (A) Applications and Materials Science*, vol. 212, no. 12, pp. 2708–2717, 2015.

[209] M. I. El-Henawey, R. S. Gebhardt, M. M. El-Tonsy, and S. Chaudhary, "Organic solvent vapor treatment of lead iodide layers in the two-step sequential deposition of CH3NH3PbI3-based perovskite solar cells," *Journal of Materials Chemistry A*, vol. 4, no. 5, pp. 1947–1952, 2016.

[210] T. Liu, Q. Hu, J. Wu, K. Chen, L. Zhao, F. Liu, C. Wang, H. Lu, S. Jia, T. Russell, R. Zhu, and Q. Gong, "Mesoporous PbI2 Scaffold for High-Performance Planar Heterojunction Perovskite Solar Cells," *Advanced Energy Materials*, vol. 6, no. 3, pp. 1–7, 2016.

[211] A. Parretta, A. Sarno, P. Tortora, H. Yakubu, P. Maddalena, J. Zhao, and A. Wang, "Angle-dependent reflectance measurements on photovoltaic materials and solar cells," *Optics Communications*, vol. 172, no. 1, pp. 139–151, 1999.

[212] L. Ba, T. Wang, J. Wang, and W. Shen, "Perovskite/c-Si Monolithic Tandem Solar Cells under Real Solar Spectra: Improving Energy Yield by Oblique Incident Optimization," *Journal of Physical Chemistry C*, vol. 123, no. 47, pp. 28659–28667, 2019.

[213] E. Unger, E. Hoke, C. Bailie, W. Nguyen, A. Bowring, T. Heumüller, M. Christoforo, and M. McGehee, "Hysteresis and transient behavior in current–voltage measurements of hybrid-perovskite absorber solar cells," *Energy & Environmental Science*, vol. 7, no. 11, pp. 3690–3698, 2014.

[214] C. Eames, J. Frost, P. Barnes, B. O'Regan, A. Walsh, and M. Islam, "Ionic transport in hybrid lead iodide perovskite solar cells," *Nature Communications*, vol. 6, p. 7497, jun 2015.

[215] C. Li, S. Tscheuschner, F. Paulus, P. Hopkinson, J. Kießling, A. Köhler, Y. Vaynzof, and S. Huettner, "Iodine Migration and its Effect on Hysteresis in Perovskite Solar Cells," *Advanced Materials*, vol. 28, pp. 2446–2454, mar 2016.

[216] I. Levine, P. Nayak, J. Wang, N. Sakai, S. Van Reenen, T. Brenner, S. Mukhopadhyay, H. Snaith, G. Hodes, and D. Cahen, "Interface-dependent ion migration/accumulation controls hysteresis in MAPbI3 solar cells," *Journal of Physical Chemistry C*, vol. 120, no. 30, pp. 16399–16411, 2016.

[217] I. Levine, P. K. Nayak, J. T. W. Wang, N. Sakai, S. Van Reenen, T. M. Brenner, S. Mukhopadhyay, H. J. Snaith, G. Hodes, and D. Cahen, "Interface-dependent ion migration/accumulation controls hysteresis in MAPbI3 solar cells," *Journal of Physical Chemistry C*, vol. 120, no. 30, pp. 16399–16411, 2016.

[218] C. Müller, T. Glaser, M. Plogmeyer, M. Sendner, S. Döring, A. A. Bakulin, C. Brzuska, R. Scheer, M. S. Pshenichnikov, W. Kowalsky, A. Pucci, and R. Lovrinčić, "Water Infiltration in Methylammonium Lead Iodide Perovskite: Fast and Inconspicuous," *Chemistry of Materials*, vol. 27, no. 22, pp. 7835–7841, 2015.

[219] K. Domanski, E. A. Alharbi, A. Hagfeldt, M. Grätzel, and W. Tress, "Systematic investigation of the impact of operation conditions on the degradation behaviour of perovskite solar cells," *Nature Energy*, vol. 3, no. January, pp. 1–7, 2018.

[220] Y. Kato, L. K. Ono, M. V. Lee, S. Wang, S. R. Raga, and Y. Qi, "Silver Iodide Formation in Methyl Ammonium Lead Iodide Perovskite Solar Cells with Silver Top Electrodes," *Advanced Materials Interfaces*, vol. 2, no. 13, pp. 2–7, 2015.

[221] Y. Han, S. Meyer, Y. Dkhissi, K. Weber, J. Pringle, U. Bach, L. Spiccia, and Y.-B. Cheng, "Degradation observations of encapsulated planar CH3NH3PbI3 perovskite solar cells at high temperatures and humidity," *J. Mater. Chem. A*, vol. 3, no. 15, pp. 8139–8147, 2015.

[222] A. Alberti, I. Deretzis, G. Pellegrino, C. Bongiorno, E. Smecca, G. Mannino, F. Giannazzo, G. Condorelli, N. Sakai, T. Miyasaka, C. Spinella, and A. La Magna, "Similar Structural Dynamics for the Degradation of CH3NH3PbI3 in Air and in Vacuum," *ChemPhysChem*, vol. 16, no. 14, pp. 3064–3071, 2015.

[223] M. Morales-masis, S. D. Wolf, R. Woods-robinson, J. W. Ager, and P. C. Ballif, "Transparent Electrodes for Efficient Optoelectronics," 2017.

[224] J. Xu, C. C. Boyd, Z. J. Yu, A. F. Palmstrom, D. J. Witter, B. W. Larson, R. M. France, J. Werner, S. P. Harvey, E. J. Wolf, W. Weigand, S. Manzoor, M. F. Van Hest, J. J. Berry, J. M. Luther, Z. C. Holman, and M. D. McGehee, "Triple-halide wide-band gap perovskites with suppressed phase segregation for efficient tandems," *Science*, vol. 367, no. 6482, pp. 1097–1104, 2020.

[225] J. Diekmann, P. Caprioglio, D. Rothhardt, M. Arvind, T. Unold, T. Kirchartz, D. Neher, and M. Stolterfoht, "Pathways towards 30% efficient perovskite solar cells," *arxiv*, 2019.

[226] M. T. Hörantner, T. Leijtens, M. E. Ziffer, G. E. Eperon, M. G. Christoforo, M. D. McGehee, and H. J. Snaith, "The Potential of Multijunction Perovskite Solar Cells," *ACS Energy Letters*, vol. 2, pp. 2506–2513, oct 2017.

[227] Z. Yang, A. Rajagopal, C. C. Chueh, S. B. Jo, B. Liu, T. Zhao, and A. K. Jen, "Stable Low-Bandgap Pb–Sn Binary Perovskites for Tandem Solar Cells," *Advanced Materials*, vol. 28, no. 40, pp. 8990–8997, 2016.

[228] S. Gu, R. Lin, Q. Han, Y. Gao, H. Tan, and J. Zhu, "Tin and Mixed Lead–Tin Halide Perovskite Solar Cells: Progress and their Application in Tandem Solar Cells," *Advanced Materials*, vol. 1907392, pp. 1–16, 2020.

[229] A. M. Igual-Muñoz, A. Castillo, C. Dreessen, P. P. Boix, and H. J. Bolink, "Vacuum-Deposited Multication Tin-Lead Perovskite Solar Cells," *ACS Applied Energy Materials*, 2020.

[230] M. G. Walter, E. L. Warren, J. R. McKone, S. W. Boettcher, Q. Mi, E. A. Santori, and N. S. Lewis, "Solar water splitting cells," *Chemical Reviews*, vol. 110, no. 11, pp. 6446–6473, 2010.

[231] J. D. Holladay, J. Hu, D. L. King, and Y. Wang, "An overview of hydrogen production technologies," *Catalysis Today*, vol. 139, no. 4, pp. 244–260, 2009.

[232] J. Luo, J. H. Im, M. T. Mayer, M. Schreier, M. K. Nazeeruddin, N. G. Park, S. D. Tilley, H. J. Fan, and M. Grätzel, "Water photolysis at 12.3% efficiency via perovskite photovoltaics and Earth-abundant catalysts," *Science*, vol. 345, no. 6204, pp. 1593–1596, 2014.

[233] W. H. Cheng, M. H. Richter, M. M. May, J. Ohlmann, D. Lackner, F. Dimroth, T. Hannappel, H. A. Atwater, and H. J. Lewerenz, "Monolithic Photoelectrochemical Device for Direct Water Splitting with 19% Efficiency," *ACS Energy Letters*, vol. 3, no. 8, pp. 1795–1800, 2018.

[234] J. Jia, L. C. Seitz, J. D. Benck, Y. Huo, Y. Chen, J. W. D. Ng, T. Bilir, J. S. Harris, and T. F. Jaramillo, "Solar water splitting by photovoltaic-electrolysis with a solar-to-hydrogen efficiency over 30%," *Nature Communications*, vol. 7, no. May, pp. 1–6, 2016.

[235] A. Nakamura, Y. Ota, K. Koike, Y. Hidaka, K. Nishioka, M. Sugiyama, and K. Fujii, "A 24.4% solar to hydrogen energy conversion efficiency by combining concentrator photovoltaic modules and electrochemical cells," *Applied Physics Express*, vol. 8, no. 10, 2015.

[236] N. J. Jeon, H. Na, E. H. Jung, T.-y. Y. Yang, Y. G. Lee, G. Kim, H.-w. W. Shin, S. Il Seok, J. Lee, J. Seo, S. I. Seok, J. Lee, and J. Seo, "A fluorene-terminated hole-transporting material for highly efficient and stable perovskite solar cells," *Nature Energy*, vol. 3, no. 8, pp. 682–689, 2018.

[237] Q. Jiang, Y. Zhao, X. Zhang, X. Yang, Y. Chen, Z. Chu, Q. Ye, X. Li, Z. Yin, and J. You, "Surface passivation of perovskite film for efficient solar cells," *Nature Photonics*, vol. 13, no. 7, pp. 460–466, 2019.

[238] Y. Chen, L. Zhang, Y. Zhang, H. Gao, and H. Yan, "Large-area perovskite solar cells-a review of recent progress and issues," *RSC Advances*, vol. 8, no. 19, pp. 10489–10508, 2018.

[239] A. Priyadarshi, L. J. Haur, P. Murray, D. Fu, S. Kulkarni, G. Xing, T. C. Sum, N. Mathews, and S. G. Mhaisalkar, "A large area (70 cm2) monolithic perovskite solar module with a high efficiency and stability," *Energy and Environmental Science*, vol. 9, no. 12, pp. 3687–3692, 2016.

[240] Y. Hu, S. Si, A. Mei, Y. Rong, H. Liu, X. Li, and H. Han, " Stable Large-Area (10 10 cm 2) Printable Mesoscopic Perovskite Module Exceeding 10% Efficiency ," *Solar RRL*, vol. 1, no. 2, p. 1600019, 2017.

[241] S. Razza, F. Di Giacomo, F. Matteocci, L. Cinà, A. L. Palma, S. Casaluci, P. Cameron, A. D'Epifanio, S. Licoccia, A. Reale, T. M. Brown, and A. Di Carlo, "Perovskite solar cells and large area modules (100 cm2) based on an air flow-assisted PbI2 blade coating deposition process," *Journal of Power Sources*, vol. 277, pp. 286–291, 2015.

[242] J. Borchert, R. L. Milot, J. B. Patel, C. L. Davies, A. D. Wright, L. Martínez Maestro, H. J. Snaith, L. M. Herz, and M. B. Johnston, "Large-Area, Highly Uniform Evaporated Formamidinium Lead Triiodide Thin Films for Solar Cells," *ACS Energy Letters*, vol. 2, no. 12, pp. 2799–2804, 2017.

[243] R. Swartwout, M. T. Hoerantner, and V. Bulović, "Scalable Deposition Methods for Large-area Production of Perovskite Thin Films," *Energy & Environmental Materials*, vol. 2, no. 2, pp. 119–145, 2019.

[244] J. K. Hwang, S. W. Lee, W. Lee, S. Bae, K. Cho, S. Kim, S. Lee, J. Y. Hyun, Y. Kang, H. S. Lee, and D. Kim, "Conformal perovskite films on 100 cm2 textured silicon surface using two-step vacuum process," *Thin Solid Films*, vol. 693, no. 2019, p. 137694, 2020.

[245] M. L. Petrus, J. Schlipf, C. Li, T. P. Gujar, N. Giesbrecht, P. Müller-Buschbaum, M. Thelakkat, T. Bein, S. Hüttner, and P. Docampo, "Capturing the Sun: A Review of the Challenges and Perspectives of Perovskite Solar Cells," *Advanced Energy Materials*, vol. 7, no. 16, pp. 1–27, 2017.

[246] J. Ávila, C. Momblona, P. P. Boix, M. Sessolo, and H. J. Bolink, "Vapor-Deposited Perovskites: The Route to High-Performance Solar Cell Production?," *Joule*, pp. 1–12, 2017.

[247] L. K. Ono, Y. Qi, and J. Accepted, "Progress on Novel Perovskite Materials and Solar Cells with Mixed Cations and Halide Anions .," *ACS Applied Materials & Interfaces*, 2017.

[248] T. Abzieher, J. A. Schwenzer, S. Moghadamzadeh, F. Sutterluti, I. M. Hossain, M. Pfau, E. Lotter, M. Hetterich, B. S. Richards, U. Lemmer, M. Powalla, and U. W. Paetzold, "Efficient All-Evaporated pin-Perovskite Solar Cells: A Promising Approach Toward Industrial Large-Scale Fabrication," *IEEE Journal of Photovoltaics*, vol. 9, no. 5, pp. 1249–1257, 2019.

[249] A. G. Aberle, "Thin-film solar cells," *Thin Solid Films*, vol. 517, no. 17, pp. 4706–4710, 2009.

[250] H. Li, K. Kim, B. Hallam, B. Hoex, S. Wenham, and M. Abbott, "POCl3 diffusion for industrial Si solar cell emitter formation," *Frontiers in Energy*, vol. 11, no. 1, pp. 42–51, 2017.

[251] G. Longo, C. Momblona, M. G. I. La Placa, L. Gil-Escrig, M. Sessolo, and H. J. Bolink, "Fully Vacuum Processed Wide Bandgap Mixed Halide Perovskite Solar Cells," *ACS Energy Letters*, vol. 3, pp. 214–219, 2018.

[252] M. R. Leyden, Y. Jiang, and Y. Qi, "Chemical vapor deposition grown formamidinium perovskite solar modules with high steady state power and thermal stability," *Journal of Materials Chemistry A*, vol. 4, no. 34, pp. 13125–13132, 2016.

[253] P. Fan, D. Gu, G. X. Liang, J. T. Luo, J. L. Chen, Z. H. Zheng, and D. P. Zhang, "High-performance perovskite CH3 NH3 PbI3 thin films for solar cells prepared by single-source physical vapour deposition," *Scientific Reports*, vol. 6, no. July, pp. 1–9, 2016.

[254] W. A. Dunlap-Shohl, E. T. Barraza, A. Barrette, K. Gundogdu, A. D. Stiff-Roberts, and D. B. Mitzi, "MAPbI3 Solar Cells with Absorber Deposited by Resonant Infrared Matrix-Assisted Pulsed Laser Evaporation," *ACS Energy Letters*, vol. 3, no. 2, pp. 270–275, 2018.

[255] X. Zhu, D. Yang, R. Yang, B. Yang, Z. Yang, X. Ren, J. Zhang, J. Niu, J. Feng, and S. F. F. Liu, "Superior stability for perovskite solar cells with 20% efficiency using vacuum co-evaporation," *Nanoscale*, vol. 9, no. 34, pp. 12316–12323, 2017.

[256] J. Borchert, H. Boht, W. Fränzel, R. Csuk, R. Scheer, and P. Pistor, "Structural investigation of co-evaporated methyl ammonium lead halide perovskite films during growth and thermal decomposition using different PbX2 (X = I, Cl) precursors," *Journal of Materials Chemistry A*, vol. 3, no. 39, pp. 19842–19849, 2015.

[257] L. K. Ono, S. Wang, Y. Kato, S. R. Raga, and Y. Qi, "Fabrication of semi-transparent perovskite films with centimeter-scale superior uniformity by the hybrid deposition method," *Energy and Environmental Science*, vol. 7, no. 12, pp. 3989–3993, 2014.

[258] J. Borchert, I. Levchuk, L. C. Snoek, M. U. Rothmann, R. Haver, H. J. Snaith, C. J. Brabec, L. M. Herz, and M. B. Johnston, "Impurity Tracking Enables Enhanced Control and Reproducibility of Hybrid Perovskite Vapor Deposition," *ACS Applied Materials & Interfaces*, vol. 11, no. 32, pp. 28851–28857, 2019.

[259] M. J. Baekbo, O. Hansen, I. Chorkendorff, P. C. Vesborg, M. J. Bækbo, O. Hansen, I. Chorkendorff, and P. C. Vesborg, "Deposition of methylammonium iodide: Via evaporation-combined kinetic and mass spectrometric study," *RSC Advances*, vol. 8, no. 52, pp. 29899–29908, 2018.

[260] Q. Chen, H. Zhou, Z. Hong, S. Luo, H.-s. S. Duan, H.-h. H. Wang, Y. Liu, G. Li, and Y. Yang, "Planar Heterojunction Perovskite Solar Cells via Vapor-Assisted Solution Process," *Journal of the American Chemical Society*, vol. 136, no. 2, pp. 622–625, 2014.

[261] M. Leyden, L. Ono, S. Raga, Y. Kato, S. Wang, and Y. Qi, "High performance perovskite solar cells by hybrid chemical vapor deposition," *Journal of Materials Chemistry A*, vol. 2, no. 44, pp. 18742–18745, 2014.

[262] P. Luo, Z. Liu, W. Xia, C. Yuan, J. Cheng, and Y. Lu, "Uniform, stable, and efficient planar-heterojunction perovskite solar cells by facile low-pressure chemical vapor deposition under fully open-air conditions," *ACS Applied Materials and Interfaces*, vol. 7, no. 4, pp. 2708–2714, 2015.

[263] Y. Peng, G. Jing, and T. Cui, "A hybrid physical-chemical deposition process at ultra-low temperatures for high-performance perovskite solar cells," *Journal of Materials Chemistry A*, vol. 3, no. 23, pp. 12436–12442, 2015.

[264] M. R. Leyden, M. V. Lee, S. R. Raga, and Y. Qi, "Large formamidinium lead trihalide perovskite solar cells using chemical vapor deposition with high reproducibility and tunable chlorine concentrations," *Journal of Materials Chemistry A*, vol. 3, no. 31, pp. 16097–16103, 2015.

[265] Y. Jiang, M. M. R. Leyden, L. Qiu, S. Wang, L. K. L. Ono, Z. Wu, E. E. J. Juarez-Perez, and Y. Qi, "Combination of Hybrid CVD and Cation Exchange for Upscaling Cs-Substituted Mixed Cation Perovskite Solar Cells with High Efficiency and Stability," *Advanced Functional Materials*, vol. 28, no. 1, p. 1703835, 2017.

[266] L. Luo, Y. Zhang, N. Chai, X. Deng, J. Zhong, F. Huang, Y. Peng, Z. Ku, and Y. B. Cheng, "Large-area perovskite solar cells with CsxFA1xPbI3yBry thin films deposited by a vapor-solid reaction method," *Journal of Materials Chemistry A*, vol. 6, no. 42, pp. 21143–21148, 2018.

[267] L. Qiu, S. He, Y. Jiang, D. Y. Son, L. K. Ono, Z. Liu, T. Kim, T. Bouloumis, S. Kazaoui, and Y. Qi, "Hybrid chemical vapor deposition enables scalable and stable Cs-FA mixed cation perovskite solar modules with a designated area of 91.8 cm2 approaching 10% efficiency," *Journal of Materials Chemistry A*, vol. 7, no. 12, pp. 6920–6929, 2019.

[268] M. T. Hoerantner, E. L. Wassweiler, H. Zhang, A. Panda, M. Nasilowski, A. Osherov, R. Swartwout, A. E. Driscoll, N. S. Moody, M. G. Bawendi, K. F. Jensen, and V. Bulović, "High-Speed Vapor Transport Deposition of Perovskite Thin Films," *ACS Applied Materials and Interfaces*, vol. 11, no. 36, pp. 32928–32936, 2019.

[269] S. Sanders, D. Stümmler, P. Pfeiffer, N. Ackermann, G. Simkus, M. Heuken, P. K. Baumann, A. Vescan, and H. Kalisch, "Chemical Vapor Deposition of Organic-

Inorganic Bismuth-Based Perovskite Films for Solar Cell Application," *Scientific Reports*, vol. 9, no. 1, pp. 1–8, 2019.

[270] S. Ngqoloda, C. J. Arendse, T. F. Muller, P. F. Miceli, S. Guha, L. Mostert, and C. J. Oliphant, "Air-stable hybrid perovskite solar cell by sequential vapor deposition in a single reactor," *ACS Applied Energy Materials*, 2020.

[271] T. Du, N. Wang, H. Chen, H. Lin, and H. He, "Comparative study of vapor- and solution-crystallized perovskite for planar heterojunction solar cells," *ACS Applied Materials and Interfaces*, vol. 7, no. 5, pp. 3382–3388, 2015.

[272] P. Luo, Z. Liu, W. Xia, C. Yuan, J. Cheng, and Y. Lu, "A simple in situ tubular chemical vapor deposition processing of large-scale efficient perovskite solar cells and the research on their novel roll-over phenomenon in J-V curves," *Journal of Materials Chemistry A*, vol. 3, no. 23, pp. 12443–12451, 2015.

[273] G. Li, J. Y. Ho, M. Wong, and H. S. Kwok, "Low cost, high throughput and centimeter-scale fabrication of efficient hybrid perovskite solar cells by closed space vapor transport," *Physica Status Solidi - Rapid Research Letters*, vol. 10, no. 2, pp. 153–157, 2016.

[274] M. M. Tavakoli, L. Gu, Y. Gao, C. Reckmeier, J. He, A. L. Rogach, Y. Yao, and Z. Fan, "Fabrication of efficient planar perovskite solar cells using a one-step chemical vapor deposition method," *Scientific Reports*, vol. 5, no. August, pp. 1–9, 2015.

[275] P. Luo, Z. Liu, W. Xia, C. Yuan, J. Cheng, C. Xu, and Y. Lu, "Chlorine-conducted defect repairment and seed crystal-mediated vapor growth process for controllable preparation of efficient and stable perovskite solar cells," *Journal of Materials Chemistry A*, vol. 3, no. 45, pp. 22949–22959, 2015.

[276] Y. Peng, G. Jing, and T. Cui, "High-performance perovskite solar cells fabricated by vapor deposition with optimized PbI2 precursor films," *RSC Advances*, vol. 5, no. 116, pp. 95847–95853, 2015.

[277] R. Sheng, A. Ho-Baillie, S. Huang, S. Chen, X. Wen, X. Hao, and M. A. Green, "Methylammonium lead bromide perovskite-based solar cells by vapor-assisted deposition," *Journal of Physical Chemistry C*, vol. 119, no. 7, pp. 3545–3549, 2015.

[278] P. S. Shen, J. S. Chen, Y. H. Chiang, M. H. Li, T. F. Guo, and P. Chen, "Low-Pressure Hybrid Chemical Vapor Growth for Efficient Perovskite Solar Cells and Large-Area Module," *Advanced Materials Interfaces*, vol. 3, no. 8, pp. 1–8, 2016.

[279] A. Ioakeimidis, C. Christodoulou, M. Lux-Steiner, and K. Fostiropoulos, "Effect of PbI2 deposition rate on two-step PVD/CVD all-vacuum prepared perovskite," *Journal of Solid State Chemistry*, vol. 244, pp. 20–24, 2016.

[280] A. Ng, Z. Ren, Q. Shen, S. H. Cheung, H. C. Gokkaya, S. K. So, A. B. Djurišić, Y. Wan, X. Wu, and C. Surya, "Crystal Engineering for Low Defect Density and High Efficiency Hybrid Chemical Vapor Deposition Grown Perovskite Solar Cells," *ACS Applied Materials and Interfaces*, vol. 8, no. 48, pp. 32805–32814, 2016.

[281] M. M. Tavakoli, S. M. Zakeeruddin, M. Grätzel, and Z. Fan, "Large-Grain Tin-Rich Perovskite Films for Efficient Solar Cells via Metal Alloying Technique," *Advanced Materials*, vol. 30, no. 11, pp. 1–9, 2018.

[282] G. Tong, H. Li, G. Li, T. Zhang, C. Li, L. Yu, J. Xu, Y. Jiang, Y. Shi, and K. Chen, "Mixed cation perovskite solar cells by stack-sequence chemical vapor deposition with self-passivation and gradient absorption layer," *Nano Energy*, vol. 48, no. 2017, pp. 536–542, 2018.

[283] E. J. Juarez-Perez, Z. Hawash, S. R. Raga, L. K. Ono, and Y. Qi, "Thermal degradation of CH3NH3PbI3 perovskite into NH3 and CH3I gases observed by coupled thermogravimetry-mass spectrometry analysis," *Energy and Environmental Science*, vol. 9, no. 11, pp. 3406–3410, 2016.

[284] D. P. Nenon, J. A. Christians, L. M. Wheeler, J. L. Blackburn, E. M. Sanehira, B. Dou, M. L. Olsen, K. Zhu, J. J. Berry, and J. M. Luther, "Structural and chemical evolution of methylammonium lead halide perovskites during thermal processing from solution," *Energy and Environmental Science*, vol. 9, no. 6, pp. 2072–2082, 2016.

[285] W. T. Van Gompel, R. Herckens, G. Reekmans, B. Ruttens, J. D'Haen, P. Adriaensens, L. Lutsen, and D. Vanderzande, "Degradation of the Formamidinium Cation and the Quantification of the Formamidinium-Methylammonium Ratio in Lead Iodide Hybrid Perovskites by Nuclear Magnetic Resonance Spectroscopy," *Journal of Physical Chemistry C*, vol. 122, no. 8, pp. 4117–4124, 2018.

[286] O. J. Weber, B. Charles, and M. T. Weller, "Phase behaviour and composition in the formamidinium-methylammonium hybrid lead iodide perovskite solid solution," *Journal of Materials Chemistry A*, vol. 4, no. 40, pp. 15375–15382, 2016.

[287] J. Coates, "Encyclopedia of Analytical Chemistry -IInterpretation of Infrared Spectra, A Practical Approach," *Encyclopedia of Analytical Chemistry*, pp. 1–23, 2004.

[288] J. B. Patel, R. L. Milot, A. D. Wright, L. M. Herz, and M. B. Johnston, "Formation Dynamics of CH3NH3PbI3 Perovskite Following Two-Step Layer Deposition," *Journal of Physical Chemistry Letters*, vol. 7, no. 1, pp. 96–102, 2016.

[289] A. Cabana and C. Sandordy, "The infrared spectra of solid methylammonium halides," *Speetroohknica Acta*, vol. 18, pp. 843–861, 1962.

[290] S. Petit, D. Righi, and J. Madejová, "Infrared spectroscopy of NH4+-bearing and saturated clay minerals: A review of the study of layer charge," *Applied Clay Science*, vol. 34, no. 1-4, pp. 22–30, 2006.

[291] E. J. Juarez-Perez, Z. Hawash, S. R. Raga, L. K. Ono, and Y. Qi, "Thermal degradation of CH 3 NH 3 PbI 3 perovskite into NH 3 and CH 3 I gases observed by coupled thermogravimetry -mass spectrometry analysis Experimental Section Synthesis of CH 3 NH 3 PbI 3 single crystals," 2016.

[292] S. Wang, L. K. Ono, M. R. Leyden, Y. Kato, S. R. Raga, M. V. Lee, and Y. Qi, "Smooth perovskite thin films and efficient perovskite solar cells prepared by the hybrid deposition method," *Journal of Materials Chemistry A*, vol. 3, no. 28, pp. 14631–14641, 2015.

[293] Z. Song, S. C. Watthage, A. B. Phillips, B. L. Tompkins, R. J. Ellingson, and M. J. Heben, "Impact of Processing Temperature and Composition on the Formation of Methylammonium Lead Iodide Perovskites," *Chemistry of Materials*, vol. 27, no. 13, pp. 4612–4619, 2015.

[294] K. B. Lohmann, J. B. Patel, M. U. Rothmann, C. Q. Xia, R. D. J. Oliver, L. M. Herz, H. J. Snaith, and M. B. Johnston, "Control over Crystal Size in Vapor Deposited Metal-Halide Perovskite Films," *ACS Energy Letters*, vol. 5, pp. 710–717, 2020.

[295] M. Senthilkumar, J. Mathiyarasu, J. Joseph, K. L. Phani, and V. Yegnaraman, "Electrochemical instability of indium tin oxide (ITO) glass in acidic pH range during cathodic polarization," *Materials Chemistry and Physics*, vol. 108, no. 2-3, pp. 403–407, 2008.

[296] R. A. Kerner and B. P. Rand, "Electrochemical and Thermal Etching of Indium Tin Oxide by Solid-State Hybrid Organic-Inorganic Perovskites," *ACS Applied Energy Materials*, vol. 2, no. 8, pp. 6097–6101, 2019.

[297] F. C. Schaefer, I. Hechenbleikner, G. A. Peters, and V. P. Wystrach, "Synthesis of the sym-Triazine System. I. Trimerization and Cotrimerization of Amidines," *Journal of the American Chemical Society*, vol. 81, no. 6, pp. 1466–1470, 1959.

[298] C. Grundmann, "New Methods in Preparative Organic Chemistry Syntheses with s-Triazine," *Angewandte Chemie - International Edition*, vol. 2, no. 6, p. 309, 1963.

[299] C. Grundmann and A. Kreutzberger, "Triazines. XIII. The Ring Cleavage of s-Triazine by Primary Amines. A New Method for the Synthesis of Heterocycles," *Journal of the American Chemical Society*, vol. 77, no. 24, pp. 6559–6562, 1956.

[300] C. Grundmann and R. Rätz, "Triazines. XVI. A New Synthesis for 1,2,4-Triazoles," *Journal of Organic Chemistry*, vol. 21, no. 9, pp. 1037–1038, 1956.

[301] L. Gil-Escrig, C. Momblona, M. G. La-Placa, P. P. Boix, M. Sessolo, and H. J. Bolink, "Vacuum Deposited Triple-Cation Mixed-Halide Perovskite Solar Cells," *Advanced Energy Materials*, vol. 8, no. 14, pp. 1–6, 2018.

[302] Y.-T. Hsiao and C.-H. Chen, "Maximum power tracking for photovoltaic power system," *Conference Record of the 37th 2002 IEEE Industry Applications Conference*, vol. 2, no. 2002, pp. 1035–1040, 2002.

[303] V. Srot, M. Gec, P. van Aken, J. Jeon, and M. Čeh, "Influence of TEM specimen preparation on chemical composition of Pb(Mg1/3Nb2/3)O3-PbTiO3 single crystals," *Micron*, vol. 62, pp. 37–42, 2014.

List of acronyms

2T   2-terminal

4T   4-terminal

AFM Atomic force microscopy

Al-BSF Aluminium-Back surface field

ALD Atomic layer deposition

BOS Balance-of-system

C$_{60}$ Buckminsterfullerene

c-Si Crystalline silicon

CVD Chemical vapour deposition

DSP Double-side polished

DST Double-side textured

EDX Energy-dispersive X-ray spectroscopy

E$_g$ Band gap

ETL Electron transport layer

EQE External quantum efficiency

FA   Formamidinium cation

FABr Formamidinium bromide

FAI   Formamidinium iodide

FF   Fill factor

FIB   Focused ion beam

FTIR Fourier-transform infrared spectroscopy

FTO Fluorinated tin oxide

HTL Hole transport layer

HTPC High-temperature passivating contact

IBC Interdigitated back-contacted

IR Infradred

ITO Indium tin oxide

IZO Indium zinc oxide

J-V Current-Voltage measurements

J_{sc} Short-circuit density

LCOE Levelized cost of electricity

MA Methylammonium cation

MAI Methylammonium iodide

MALI Methylammonium lead triiodide

MoO_x Molybdenum oxide

MPP Maximum power point

nc-Si:H Hydrogenated nanocrystalline silicon

NIR Near-infrared

NMR Nuclear magnetic resonance spectroscopy

OVPD Organic vapour deposition

PbI_2 Lead iodide

PCBM Phenyl-C_{61}-butyric-acid-methyl-ester

PCE Power conversion efficiency

PECVD Plasma enhance chemical vapour deposition

PERC Passivated emitter and rear cell

PTAA Poly(triarylamine)

PV Photovoltaic

PVD Physical vapour deposition

SEM Scanning electron microscopy

SHJ Silicon heterojunction

SP Solution-processing

Spiro-OMeTAD
    2,2',7,7'-Tetrakis-(N,N-di-4-methoxyphenylamino)-9,9'-spirobifluorenes

Spiro-TTB 2,2,7,7-Tetra(N,N-di-p-tolyl)amino-9,9-spirobifluorene

SST Single-side textured

STC Standard test conditions

TCO Transparent conductive oxide

TEM Transmission electron microscopy

TmPyPB 1,3,5-Tri[(3-pyridyl)-phen-3-yl]benzene

UV/Vis Ultraviolet/Visible spectroscopy

V_{oc} Open-circuit voltage

VTD Vapour transport deposition

XRD X-ray diffraction

Contributions & CV

Publications as first author

* contributed equally

1. <u>F. Sahli</u>, B. A. Kamino, J. Werner, M. Bräuninger, B. Paviet-Salomon, L. Barraud, R. Monnard, J. P. Seif, A. Tomasi, Q. Jeangros, A. Hessler-Wyser, S. De Wolf, M. Despeisse, S. Nicolay, B. Niesen and C. Ballif, *"Improved optics in monolithic perovskite/silicon tandem solar cells by a nanocrystalline silicon recombination layer"*, Advanced Energy Materials, (2017).

2. <u>F. Sahli</u>*, J. Werner*, B. A. Kamino, M. Bräuninger, B. Paviet-Salomon, L. Barraud, R. Monnard, J. P. Seif, A. Tomasi, Q. Jeangros, A. Hessler-Wyser, S. De Wolf, M. Despeisse, S. Nicolay, B. Niesen and C. Ballif, *"Fully textured monolithic perovskite/silicon tandem solar cells with 25.2% power conversion efficiency"*, Nature Materials, (2018).

3. G. Nogay*, <u>F. Sahli</u>*, J. Werner, R. Monnard, M. Boccard, M. Despeisse, F-J. Haug, Q. Jeangros, A.Ingenito and C. Ballif, *"25.1%-Efficient Monolithic Perovskite/Silicon Tandem Solar Cell Based on a p -type Monocrystalline Textured Silicon Wafer and High-Temperature Passivating"*, ACS Energy Letters, (2019).

4. <u>F. Sahli</u>, N. Miaz, N. Salsi, C. Bucher, A. Schafflützel, Q. Guesnay, L. Duchêne, Q. Jeangros, B. Niesen and C. Ballif., *"Chemical and organic vapour deposition of methylammonium lead iodide perovskite solar cells"*, (manuscript under preparation).

Publications as co-author

1. A. Tomasi, <u>F. Sahli</u>, J. P. Seif, L. Fanni, S. Martin de Nicolas Agut, J. Geissbühler, B. Paviet-Salomon, S. Nicolay, L. Barraud, B. Niesen, S. De Wolf and C. Ballif *"Transparent electrodes in silicon heterojunction solar cells: Influence on contact passivation"*, IEEE Journal of Photovoltaics, (2016).

2. J. Werner, L. Barraud, A. Walter, M. Brauninger, <u>F. Sahli</u>, D. Sacchetto, N.

Tetreault, B. Paviet-Salomon, S.-J. Moon, C. Allebe, M. Despeisse, S. Nicolay, S. De Wolf, B. Niesen and C. Ballif, *"Efficient near-infrared-transparent perovskite solar cells enabling direct comparison of 4 terminal and monolithic perovskite/silicon tandem cells"*, ACS Energy Letters, (2016).

3. Z. Song, J. Werner, N. Shrestha, F. Sahli, S. De Wolf, B. Niesen, S. C. Watthage, A. B. Phillips, C. Ballif, R. J. Ellingson and M. J. Heben *"Probing photocurrent nonuniformities in the subcells of monolithic perovskite/silicon tandem solar cells"*, The journal of physical chemistry letters, (2016).

4. Z. Song, J. Werner, S. C. Watthage, F. Sahli, N. Shrestha, S. De Wolf, B. Niesen, A. B. Phillips, C. Ballif, R. J. Ellingson and M. J. Heben *"Imaging the spatial evolution of degradation in perovskite/Si tandem solar cells after exposure to humid air"*, IEEE Journal of Photovoltaics, (2017).

5. M. Mundus, B. Venkataramanachar, R. Gehlhaar, M. Kohlstaedt, B. Niesen, W. Qiu, J. Philipp Herterich, F. Sahli, M. Bräuninger, J. Werner, J. Hohl-Ebinger, G. Uytterhoeven, U. Wuerfel, C. Ballif, M. C. Schubert, W. Warta and S. W Glunz *"Spectrally resolved nonlinearity and temperature dependence of perovskite solar cells"*, Solar Energy Materials and Solar Cells, (2017).

6. J. Werner, G. Nogay, F. Sahli, T. C. J. Yang, M. Brauninger, G. Christmann, A. Walter, B. A. Kamino, P. Fiala, P. Loper, S. Nicolay, Q. Jeangros, B. Niesen and C. Ballif *"Complex refractive indices of cesium–formamidinium-based mixed-halide perovskites with optical band gaps from 1.5 to 1.8 eV"*, ACS Energy Letters, (2018).

7. J. Werner, F. Sahli, F. Fu, J. J. D. Leon, A. Walter, B. A. Kamino, B. Niesen, S. Nicolay, Q. Jeangros and C. Ballif *"Perovskite/perovskite/silicon monolithic triple-junction solar cells with a fully textured design"*, ACS Energy Letters, (2018).

8. D. A. Jacobs, M. Langenhorst, F. Sahli, B. S. Richards, T. White, C. Ballif, K. R. Catchpole and U. W. Paetzold *"Light Management: A Key Concept in High-Efficiency Perovskite/Silicon Tandem Photovoltaics"*, The journal of physical chemistry letters, (2019).

9. J. Gao, F. Sahli, C. Liu, D. Ren, X. Guo, J. Werner, Q. Jeangros, S. M. Zakeeruddin, C. Ballif, M. Grätzel and J. Luo *"Solar Water Splitting with Perovskite/Silicon Tandem Cell and TiC-Supported Pt Nanocluster Electrocatalyst"*, Joule, (2020).

R. A. Z. Razera, D. A. Jacobs, F. Fu, P. Fiala, M. Dussouillez, F. Sahli, T. C. J. Yang, L. Ding, A. Walter, A. F. Feil, H. I. Boudinov, S. Nicolay, C. Ballif and Q. Jeangros, *"Instability of p–i–n perovskite solar cells under reverse bias"*, Journal of Materials Chemistry A, (2020).

226

Oral Presentations

1. <u>F. Sahli</u>, B. A. Kamino, J. Werner, M. Bräuninger, B. Paviet-Salomon, L. Barraud, R. Monnard, J. P. Seif, A. Tomasi, Q. Jeangros, A. Hessler-Wyser, S. De Wolf, M. Despeisse, S. Nicolay, B. Niesen and C. Ballif, *"Improved optics in monolithic perovskite/silicon tandem solar cells by a nanocrystalline silicon recombination layer"*, Hybrid and Organic Photovoltaics (HOPV) conference, Lausanne (Switzerland), (2017).
Abstract and Oral presentation

2. <u>F. Sahli</u>, J. Werner, B. A. Kamino, M. Bräuninger, B. Paviet-Salomon, L. Barraud, R. Monnard, J. P. Seif, A. Tomasi, Q. Jeangros, A. Hessler-Wyser, S. De Wolf, M. Despeisse, S. Nicolay, B. Niesen and C. Ballif, *"Hybrid sequential deposition process for fully textured monolithic perovskite/silicon tandem solar cells"*, World Conference on Photovoltaic Energy Conversion (WCPEC-7), Hawaii (USA), (2018).
Abstract and Oral presentation
Best student paper award

3. <u>F. Sahli</u>, G. Nogay, J. Werner, F. Fu, A. Walter, S. Rafizadeh, V. Paratte, R. Monnard, B. A. Kamino, P. Fiala, T. C.-J. Yang, M. Bräuninger, R. A. Z. Razera, M. Despeisse, S. Nicolay, A. Ingenito, M. Boccard, Q. Jeangros and C. Ballif, *"Perovskite/Silicon Monolithic Tandem Based on a P-type High-temperature Tolerant Silicon Bottom Cell"*, Hybrid and Organic Photovoltaics (HOPV) conference, Rome (Italy), (2019).
Abstract and Oral presentation

4. <u>F. Sahli</u>, G. Nogay, J. Werner, F. Fu, A. Walter, S. Rafizadeh, V. Paratte, R. Monnard, B. A. Kamino, P. Fiala, T. C.-J. Yang, M. Bräuninger, R. A. Z. Razera, M. Despeisse, S. Nicolay, A. Ingenito, M. Boccard, Q. Jeangros and C. Ballif, *"High-Efficiency Monolithic Perovskite/Silicon Tandem Solar Cells"*, European Photovoltaic Solar Energy Conference (EU-PVSEC) , Marseille (France), (2019).
Abstract and Oral presentation

Poster Presentation

1. <u>F. Sahli</u>, B. A. Kamino, J. Werner, M. Brauninger, B. Paviet-Salomon, L. Barraud, R. Monnard, J. P. Seif, A. Tomasi, Q. Jeangros, A. Hessler-Wyser, S. De Wolf, M. Despeisse, S. Nicolay, B. Niesen and C. Ballif, *"Improved optics in monolithic perovskite/silicon tandem solar cells by a nanocrystalline silicon recombination layer"*, Perovskite Solar cells and Optoelectronics (PSCO) conference, Oxford (UK), (2017).
Abstract and Poster

Florent Sahli

Chemical engineer

- Rue des Marronniers 11, 1800 Vevey
- +41 73 324 01 91
- florent.sahli@gmail.com
- Swiss
- 01.04.1991 (29 years old)

Professional Experiences

03.2016 - 06.2020

PhD in chemistry and chemical engineering
EPFL, Institute of Micro-engineering, PV-LAB, Neuchâtel (CH)
- Development of highly efficient Perovskite/Silicon tandem solar cells
- Nanofabrication and thin films characterization
- Development of vapor-based deposition system
- World record efficiency for perovskite/silicon tandem solar cell
- Awards: Chemistry Travel Awards, best student paper award (IEEE conference)

06.2015 - 01.2016

Research & development engineer (civil service)
Antenna technologies, R&D department, Geneva (CH)
- Optimization of water treatment device (electrochlorination)
- Introduce chemical and environmental safety procedures for customers and technical operators
- Technical support and economic consulting for a disinfectant production plant in Burkina Faso and Guinea

10.2014 - 04.2015

Research Associate (civil service)
EPFL, Institute of Micro-engineering, PV-LAB, Neuchâtel (CH)
- Optimization of Transparent Conductive Oxides (TCOs)/amorphous silicon interface for high-efficiency silicon solar cells

09.2013 - 02.2014

Bioprocess Engineer (intern)
Novartis AG, R&D department, Basel (CH)
- Development and optimization of high-density cell culture perfusion processes using next-generation cell retention devices
- Scale-down of cell retention systems for a platform full-scale process feasibility study

Education

03.2016 - 06.2020

PhD in Chemistry and Chemical Engineering
EPFL, Photovoltaics and thin film electronics Laboratory (PVlab)

09.2012 - 07.2014

Master degree in Chemical Engineering and Biotechnology
EPFL/University of California, Davis (master thesis)

09.2009 - 06.2012

Bachelor degree in Chemistry and Chemical Engineering
EPFL/University of Helsinki (3rd year - Erasmus)

Languages

French (Native)
English (C1)
German (A2)

228